Relativistic Scattering of Solitons in Nonlinear Field Theory

by

Benjamin Gutierrez

B.Sc., Universidad Nacional Autonoma de Mexico 2002

A THESIS SUBMITTED IN PARTIAL FULFILLMENT OF
THE REQUIREMENTS FOR THE DEGREE OF

DOCTOR OF PHILOSOPHY

in

The Faculty of Graduate Studies

(Physics)

THE UNIVERSITY OF BRITISH COLUMBIA

(Vancouver)

May 2013

ABSTRACT

This thesis presents results from numerical studies of the dynamics of three classical nonlinear field theories, each of which possesses stable, localized solutions called solitons. We focus on two of the theories, known as Skyrme models, which have had application in various areas of physics. The third, which treats a complex scalar field, is principally viewed as a model problem to develop solution techniques. In all cases, time dependent, nonlinear partial differential equations in several spatial dimensions are solved computationally. Simulation of high energy collisions of the solitons is of particular interest.

The solitons of the complex scalar field theory are known as Q-balls and carry a charge Q. We investigate the scattering of these objects, reproducing previous findings for collisions where the Q-balls have charge of the same sign. We obtain new results for interactions where the Q-balls have opposite charge, and for scattering of Q-balls against potential obstructions.

The chief contributions of this thesis come from simulations performed within the context of a Skyrme model in two spatial dimensions. This is a multi-scalar theory with solitons known as baby skyrmions. We concentrate on the rich phenomenology seen in high-energy scattering of pairs of these objects, each of which has a topological charge that can be either positive or negative. We extend the understanding of the role of different parameters of the model in governing the outcome of head-on and off-axis collisions.

The study of instabilities seen in previous simulations of Skyrme models is of central interest. Our results confirm that the governing partial differential equations become of mixed hyperbolic-elliptic type for interactions at sufficiently high-energy, as originally suggested by Crutchfield and Bell [1]. We present strong evidence for the loss of energy conservation and smoothness of the dynamical fields in these instances. This supports the conclusion that the initial value problem at hand becomes ill-posed, so that the observed instabilities result from the nature of the equations themselves, and are not numerical artifacts.

Finally, we present preliminary results for the typical phenomenology seen in head-on scattering

of solitons in the Skyrme model in three spatial dimensions.

PREFACE

The identification of the research area and specific problems addressed in this thesis was made by the author in consultation with the research supervisor. All parts of the research, including the analysis of data, were carried out by the author.

TABLE OF CONTENTS

LIST OF TABLES

LIST OF FIGURES

LIST OF ABBREVIATIONS

AMR: Adaptive Mesh Refinement.

AMRD: Adaptive Mesh Refinement Driver.

CN: Crank-Nicholson numerical scheme.

FDA: Finite Difference Approximation.

KO: Kreiss-Oliger dissipation.

MAPLE: a general-purpose commercial computer algebra system.

MPI: Message Passing Interface.

NGS: Newton-Gauss-Seidel Relaxation Technique.

ODE: Ordinary Differential Equation.

ODEPACK: A collection of Fortran solvers for the initial value problem for ODE systems.

PAMR: Parallel Adaptive Mesh Refinement: refers to set of libraries written by Frans Pretorius.

PDE: Partial Differential Equation.

RNPL: Rapid Numerical Prototyping Language.

TRE: Truncation Error Estimate.

ACKNOWLEDGEMENTS

I would like to express my deepest and most sincere gratitude to my supervisor, Matthew W. Choptuik, for all his support and patience during all these years. I would like to thank the members of my graduate committee: Jeremy S. Heyl, Moshe Rozali and William G. Unruh. I owe a special debt of gratitude to Fernando Quevedo, who has always provided me guidance and support. My special gratitude to Frans Pretorius for his continuous advise and his generous share of the Woodhen facility, and to Luis Lehner, for his hospitality at the Perimeter Institute. I also want to thank Doug Bonn, Rebecca Trainor, Roman Baranowski, Timothy Yuswack, Dario Nuñez and Tonatiuh Matos for all their kind support and help.

I would like to thank UBC for the UGF Scholarship I was awarded. This research was supported by NSERC, CIFAR, and the Westgrid, Scinet and Clumeq consortia. Likewise, I would like to thank Gerhard Huisken and the Albert Einstein Institute for their hospitality and support during my visit in 2008.

I want to thank my family, my mother Blanca, my sister Karla and Jean Vincent, for their continuous love and support, without whom none of this would have been possible.

Finally, special thanks to my friends and colleges Anand, Arman, Bruno, Daniel Lindstrom, Daoyan, Federico, Fernando Herrejon, Hendrik, Hissam, Jason, Lucia Hernandez, Martha, Miguel Angel, Miguel Lerma, Naayeli and Silvestre.

DEDICATION

This thesis is dedicated to the loving memory of my father, Benjamin, and my friend Gustavo. They are very much missed.

CHAPTER 1

INTRODUCTION

The study of nonlinear wave equations arising from classical field theories is among the most active and exciting areas of mathematical physics. An especially interesting feature of many of these equations is that they admit solutions describing localized concentrations of energy known as solitons. It is widely accepted that the identification of solitons is one of the most important discoveries in nonlinear science [2, 3].

As we shall see, there are many different classes of solitons. Historically, the first to be studied in detail are governed by time-dependent partial differential equations having the property that dispersion is counterbalanced by nonlinearities. In this case the solitonic solutions are persistent, particle-like solitary waves that have remarkable stability properties [4, 5, 2]. Famously, the first report of this type of soliton was published by Russell in 1845, and described the observation of stable, large amplitude solitary water waves generated by a horse-drawn boat in a narrow channel [6]. The first documented search for a mathematical model that could explain these waves was made by Boussinesq and Rayleigh in the 1870s [7], and in 1895 Korteweg and De Vries showed that a nonlinear hydrodynamic equation—the celebrated KdV equation—had solutions corresponding to Russell's observations [2].

Despite this and some other early work[1] the investigation of complex nonlinear systems did not begin in earnest until the 1950s, when computer resources started to be sufficient to allow direct assault on otherwise intractable problems. Particularly notable in this regard are the 1953 numerical experiments of one-dimensional lattices by Fermi, Pasta and Ulam [8, 9] that produced surprising results that were in apparent contradiction with statistical mechanics. The lattice model was further considered by Zabusky and Kruskal in the 1960s [10], who found that in the continuum limit the dynamics of the lattice was governed by the KdV equation. Furthermore, they discovered that the results of Fermi *et al* [8, 9] were explained by the existence of KdV solitons and showed that the solitary waves could propagate through one another without disturbing each other's shape.

[1] Here, Frenkel and Kontorova's model for crystal dislocation is especially worth mentioning [7, 2].

They also found that the collisions preserved the localized energy density of each wave. Indeed, it was in the work of Zabusky and Kruskal that the term "soliton"—intended to emphasize the particle-like properties of the waves—first appeared [2, 10].

Since that time, stable localized solutions of wave-type equations arising in many disciplines have been identified [11, 4]. These include biology (neural pulses), plasma physics, ferromagnets (domain walls), superfluids (vortices) and nonlinear optics (solitary electromagnetic pulses) [12, 11, 4, 2]. Perhaps the most spectacular examples are found in the Earth's atmosphere (tornadoes) and in the ocean (tsunamis), although it is still debated whether the latter are really solitons [13].

This thesis is focused on the study of nonlinear classical field theories called Skyrme models, which have solitonic solutions aptly named *skyrmions* [14, 15, 16, 17, 4]. The dynamical behaviour of skyrmions is rich and complicated, and can only be examined in detail by numerical means. We thus aim to use computational techniques to probe some of the phenomenology of the models, as well as to investigate some interesting mathematical features that will be subsequently described. As we will discuss, Sykrme models have physical applications, but this aspect of the theories will not be our main concern. Rather, we adopt the view that, in the context of nonlinear science, understanding the dynamical nature of skyrmions—and, in particular, interactions between them—is a worthy pursuit in its own right.

We consider two specific Skyrme theories. One is the original model proposed by Skyrme in which the fields have dependence on all three spatial dimensions and time. The other, known as the baby-Skyrme model, is closely related to the first, but is restricted to two spatial dimensions. Because of the reduced dimensionality, calculations in the baby-Skyrme theory are much less computationally expensive than those in the full model. Primarily for this reason, the bulk of the computations described in this thesis involve the baby-Skyrme model.

Since the equations of motion that govern the Skyrme systems are quite complicated, we found it useful to begin our numerical work by considering an even simpler model field-theory that describes the evolution of a complex scalar field with a non-trivial potential. This model also has localized solutions—known as Q-balls—that can be interpreted as solitons. We use this theory primarily to develop a computational approach and infrastructure that is then applied to the studies of the Skyrme systems. As a consequence of a particular symmetry of this theory, Q-balls carry a conserved Nöther charge Q [18], which can either positive, or negative. In spite of the role of Q-balls as a model problem for this work, we found novel results on the interaction of Q-ball pairs where

each soliton carries a charge Q of opposite sign—an issue so far absent from the literature—and on the scattering of Q-balls against potential obstructions. We will elaborate on this aspect in Chap. 3.

All of the theories that we study are governed by sets of partial differential equations (PDEs) of evolutionary type, and thus we must formulate and solve initial-value problems[2]. Assuming well-posedness—a concept which is crucial to our studies, and which will be discussed in more detail in Sec. 1.5.2—if we specify smooth initial data, we can expect a unique solution. We will be especially interested in evolutions describing two initially-separated solitons that subsequently collide (or otherwise interact), and where the relative initial speed (boost factor) between the solitons is viewed as a control parameter. Attention will further be concentrated on cases where the boost factor is large, so that—since our models are all Lorentz-invariant—we say that the dynamics is in the ultrarelativistic regime.

1.1 Skyrme Model in Three Spatial Dimensions

The Skyrme model provides a description of nuclear matter in which only meson fields appear explicitly. Nucleons (the proton and the neutron) then emerge precisely as skyrmions [19, 20], i.e. as collective excitations of mesons [16, 21]. Although the model superficially appears to describe bosonic matter, a key property that provides physical plausibility is that quantization of the skyrmion is consistent only if the associated quantum state has spin-1/2, i.e. if it is a fermion [20, 15, 16].

Skyrmions share some of the properties seen in the "classical" solitons mentioned previously, including localization [3, 4, 5, 2, 22]. However, they do not necessarily preserve their shape after interacting with one another: in particular they can merge, annihilate or radiate energy. Nonetheless, in this work we follow Coleman [23] and Vachaspati [24] and use the term soliton to refer to a *static, localized* classical lump.

The Skyrme model is usually presented in terms of an $SU(2)$-valued field, U, with a Lagrangian density [25, 26, 20, 27],

$$\mathcal{L} = \frac{F_\pi^2}{16}\mathrm{Tr}(\partial_\mu U \partial_\mu U^\dagger) + \frac{1}{32e^2}\mathrm{Tr}\left[(\partial_\mu U)\,U^\dagger, (\partial_\mu U)\,U^\dagger\right]^2 , \tag{1.1}$$

[2]Strictly speaking we must deal with initial-boundary-value problems, since our computational domains do not extend to spatial infinity.

where the Greek indices $\mu, \nu \ldots = 0, 1, 2, 3$ run over the dimensions of spacetime, while $\dagger$ and Tr denote the adjoint and trace operators respectively. In addition, F_π is taken to be the pion weak decay constant [28], and e is a dimensionless real parameter. We observe that (1.1) includes an ordinary kinetic term, and a second term which is fourth order in the derivatives of the fields. The latter is required for the existence of static skyrmions[3] [31, 32, 33]. Its functional form is not arbitrary, but is the most general fourth order term compatible with *chiral* symmetry. This symmetry is observed in nuclear phenomenology, and it treats "left-handed" and "right-handed" particles independently. In other words, chiral transformations do not "mix" left and right-handed particles, so a left-handed particle can not be mapped into a right-handed, or vice versa. The inclusion of a potential (or mass term) in the Lagrangian is optional, and we have not added one in our work.

We can write U and $U^\dagger$ in terms of a four component real-valued vector representation of $SU(2)$ [25, 26, 20, 27] (see Sec. 5.2), by defining $\phi_a(x^\mu) \equiv (\phi_1(x^\mu), \phi_2(x^\mu), \phi_3(x^\mu), \phi_4(x^\mu))$. We then have

$$\mathcal{L} = \frac{1}{2}\partial_\mu\phi_a\partial^\mu\phi_a + \frac{1}{4}(\partial_\mu\phi_a\partial^\mu\phi_a)^2 - \frac{1}{4}(\partial_\mu\phi_a\partial_\nu\phi_a)(\partial^\mu\phi_b\partial^\nu\phi_b) + \lambda_{\mathrm{LM}}(\phi_a\phi_a - 1)\,. \tag{1.2}$$

Here the Latin indices $a, b, \ldots = 1, 2, 3, 4$ label the components of the fields and obey an Einstein summation convention (see Sec. 1.8). The parameters F_π and e have been scaled away by means of a change of our units of energy ($F_\pi/4e$) and length ($2/eF_\pi$) [20]. Chiral invariance of (1.2) requires that the ϕ_a satisfy the *chiral* constraint $\phi_a\phi_a = \phi_1^2 + \phi_2^2 + \phi_3^2 + \phi_4^2 = 1$, which is enforced by the addition of a Lagrange multiplier (λ_{LM}) term to (1.2) (see Chap. 5 for details). The equations of motion derived from the Lagrangian density (1.2) are

$$(1 + \partial_\mu\phi_a\partial^\mu\phi_a)\,\Box\phi_a + \partial_\mu\partial_\nu\phi_b\partial^\mu\phi_b\partial^\nu\phi_a - \partial^\mu\phi_b\partial^\nu\phi_b\partial_\mu\partial_\nu\phi_a - \Box\phi_b\partial^\nu\phi_b\partial_\nu\phi_a + \lambda_{\mathrm{LM}}\phi_a\,, \tag{1.3}$$

where $\Box \equiv \partial^\alpha\partial_\alpha$ is the usual wave (d'Almbertian) operator.

[3] The Hobart-Derrick argument [29, 15, 30, 31] provides a criteria for the existence of minimal energy static solutions, according to the dimensionality and field content of the model. We discuss this topic in detail in (D.1).

1.1.1 Topological Solutions

A novel feature of skyrmions is that they possess a particular type of conserved quantity known as a *topological charge*, [23, 24, 31, 16, 34], and thus are examples of what are known as topological solitons [4]. This concept can be understood in the following way. The space of physical configurations of the theory can be divided into a number (finite or infinite) of topologically disconnected sub-regions. Although all configurations evolve according to the same equations of motion, they satisfy different boundary conditions. A configuration can be viewed as a map from physical space to the internal space of the theory, and maps corresponding to configurations in different sub-regions can not be deformed into each other *continuously*. In other words, the configurations have distinct *homotopies* [16, 24, 21]. In general, every sub-region can be labelled with an integer, or topological invariant, which is precisely the topological charge [15, 16, 35].

In theories with topological solitons, the ground state is *degenerate*; that is, distinct field states, known as *vacuums*, can have the same minimum energy[5]. This means that in different spatial regions of the domain, the configuration may tend to different vacuum states, with infinite energy barriers separating the regions. Skyrme was the first to realize the significance of the topological charge in a physically motivated model [16], identifying it (for the case of his theory) as the *baryon number*, B [35],

$$B = \frac{1}{2\pi^2}\int \epsilon_{\alpha\beta\gamma\delta}\epsilon_{\nu\rho\sigma}\phi_a\partial^\nu\phi_\beta\partial^\rho\phi_\gamma\partial^\sigma\phi_\delta \;\; d^3x\,, \tag{1.4}$$

(where $\epsilon_{\alpha\beta\gamma\delta}$ and $\epsilon_{\nu\rho\sigma}$ are anti-symmetric Levi-Civita symbols [36]). He thus provided a interpretation for the (classical) conservation of B based on topological concepts [6].

The Lagrangian density (1.2) defines one example of a general class of theories known as *sigma models*, which are scalar field theories with multiple field components [37], and whose Lagrangian densities can be written in the form

$$\mathcal{L}_\sigma = g_{ab}(\phi_a)\partial^\mu\phi^a\partial_\mu\phi^b\,. \tag{1.5}$$

Here $\phi_a(x^\mu)$ are the scalar field components, and g_{ab} is the metric of the so-called target space. If

[4] The archetypal example of a simple model with topological solitons is a single real scalar field in 1+1 dimensions, with a quartic potential, known as the *ϕ^4-theory* [24]

[5] In quantum field theory, the vacuum refers to a state with no particle content. It is common in the literature to abuse this language and refer to the ground state, even in a purely classical theory, as the vacuum.

[6] The baryon number B allows us to define an anti-skyrmion: a skyrmion has a baryon number $B > 0$, while an *anti-skyrmion* is a skyrmion with baryon number $-B$.

$g_{ab} = g_{ab}(\phi_a)$, the sigma model is *nonlinear*.

The first application of sigma models in physics was to describe, not surprisingly, chiral interactions. Specifically, Gell-Mann and Levy [37] introduced a fourth non-physical field, σ, along with the three pions π^+, π^-, π^0, to expand the symmetry group of strong interactions, with the aim to describe the phenomenology of strange particles (the so called chiral modification [14, 15, 16]). Again, the fields satisfy a constraint, $\sigma^2+(\pi^+)^2+(\pi^-)^2+(\pi^0)^2 = 1$, to ensure that chiral symmetry was always satisfied.

A sigma model (or wave map) defines a map between Lorentzian flat space-time, and a Riemannian target space (i.e. the target space is smooth and equipped with a metric function), such that the fields can be viewed as taking values on the target space. While properties such as chiral invariance are interesting to the physicist, the mapping between spaces provides much of the motivation for their study by mathematicians. As we will discuss in detail in subsequent chapters, the target spaces of the Skyrme theories considered in this thesis are S^2 (baby Skyrme model) and S^3 ("full" Skyrme model).

1.1.2 Historical Background

During the 1950's and early 1960's, solitons emerged as obvious candidates for modelling entities such as monopoles, kinks and domain walls [23, 24, 31, 34]. Not surprisingly, the concept was taken even further, with the suggestion that what were previously viewed as fundamental fields could themselves be solitons of some underlying self-organizing structures, with properties that emerge from the more basic degrees of freedom [29, 38]. In 1961, and following this trend, Skyrme was the first to propose a topological model for nuclear matter [14, 16]. It is important to note that at that time understanding of hadrons—particles that interact through the strong nuclear force—was basically limited to the interaction of pions and nucleons. In 1962, Perring and Skyrme hypothesized that an elementary solitonic solution of the sine-Gordon equation might be relevant to hadron physics [39, 40], and the skyrmion is the direct descendant of these ideas [14, 16, 4, 17].

In the late 60's and early 70's, deep inelastic scattering at high energy revealed that hadrons had an underlying substructure. Quantum chromodynamics (QCD) successfully described the observed phenomenology, and largely sidelined Skyrme's approach for several decades [15, 41]. However, QCD turned out to be very difficult to solve in the strong coupling regime (low energies), even when numerical (lattice) methods were adopted. Attention thus turned to simpler phenomenological

models, including Skyrme's, that could provide reasonably accurate descriptions of low-energy hadron physics. Such models exploit the fact that since quarks are confined it is possible to eliminate degrees of freedom not directly relevant to phenomenology, while still retaining many of the fundamental symmetries of QCD (Lorentz, chiral, etc.) [42]. The resulting *effective* models, cast in terms of pion fields, simplified calculations at the expense of providing an incomplete (approximate) physical picture.

At the beginning of the 1980's, Witten [43, 44] discovered that the Skyrme approach is equivalent to QCD in the large N_c limit (where N_c is the number of colors), with baryons being identified as quantized states of the classical soliton solutions. This realization sparked a resurgence of interest in the Skyrme model as an effective theory of pions (mesons), and specifically how to describe baryons and their interactions within the formulation.

1.1.3 Applications

A discussion of the calculation of low-energy observables of baryons including comparison to experimental data can be found in [17, 42, 45]. The calculations of baryonic structure by Adkins, Nappi and Witten [44] based on the Skyrme model achieved an accuracy of the order of $20 - 30\%$. Later calculations on bound two-baryon systems produced similar results [17]. More recent phenomenological work is based on the chiral quark-soliton model (χ_{QSM}), which is an extended version of the original Skyrme theory [45]. Additionally, and although controversial, claims of the observation of a pentaquark state Θ^+ [46] in the mid 2000s brought renewed focus on low energy QCD and the relative merits of constituent-quark versus solitonic interpretations of light baryons.

We conclude this brief synopsis of the Skymre model by noting that many excellent reviews of the subject are available, including [15, 16, 17, 46, 47, 48, 49, 27, 50, 28, 51, 52, 41, 53]

1.2 The Skyrme Model in Two Spatial Dimensions

As mentioned before, the baby-Skyrme model (also known as the pseudo-Skyrme model) is an analog of the original Skyrme model, but in this case the fields depend on *two* spatial dimensions plus time [20, 35, 54]. Interestingly enough, this theory also has stable localized solitonic solutions, which are known as *baby skyrmions*.

The Lagrangian density of the model [31, 35, 55, 56], which is similar to its three dimensional

counterpart (1.2), is given by

$$\mathcal{L} = \frac{1}{2}\partial_\mu\phi_a\partial^\mu\phi_a + \frac{1}{4}(\partial_\mu\phi_a\partial^\mu\phi_a)^2 - \frac{1}{4}(\partial_\mu\phi_a\partial_\nu\phi_a)(\partial^\mu\phi_b\partial^\nu\phi_b) + V(\phi_a)\,. \tag{1.6}$$

Once again, Latin indices $a, b, \ldots = 1, 2, 3$ label the components of the fields, while Greek indices label the dimensions of spacetime, $\mu, \nu \ldots = 0, 1, 2$. Analogously to the three dimensional model, the first term in (1.6) is an ordinary kinetic term for a $O(3)$ sigma model, the second and third terms are fourth order in the derivatives, and an additional *potential term* $V(\phi_a)$—which breaks the manifest $O(3)$ symmetry—is included [31, 32, 33]. Besides the reduced dimensionality of the baby theory with respect to the full three dimensional model, the key differences between the two are: (1) (1.6) describes the dynamics of a *three* component vector field, $\phi_a \equiv (\phi_1, \phi_2, \phi_3)$, rather that the four component field appearing in (1.2). (2) Correspondingly, in this case the *chiral* constraint is $\phi_a\phi_a = \phi_1^2 + \phi_2^2 + \phi_3^2 = 1$. (3) The existence of non-trivial static solutions in the baby Skyrme model *requires* the Lagrangian density to have both the fourth order terms and the potential term (See App. D.1) [31, 32, 33]. The functional form of the latter defines the overall properties of the model [35], and we will elaborate on our choice of potential function in Chap. 4.

The equations of motion derived from (1.6) are

$$\begin{aligned}(1 + \partial_\mu\phi_a\partial^\mu\phi_a)\,\Box\phi_a \quad &+ \quad \partial_\mu\partial_\nu\phi_b\partial^\mu\phi_b\partial^\nu\phi_a - \partial^\mu\phi_b\partial^\nu\phi_b\partial_\mu\partial_\nu\phi_a - \Box\phi_b\partial^\nu\phi_b\partial_\nu\phi_a \\ &+ \quad \lambda_{\rm LM}\phi_a - \frac{dV(\phi_a)}{d\phi_a} = 0\,.\end{aligned} \tag{1.7}$$

As in the case of the full model, $\lambda_{\rm LM}$ is a Lagrange multiplier introduced to enforce the chiral constraint.

1.2.1 Historical Background

Interest in two-dimensional sigma models has its roots in the work of Belavin and Polyakov (1975) [33, 57], who pointed out the presence of non-trivial static solutions in an $O(3)$ model of ferromagnets. Further work focused on their use as toy models for Yang-Mills theories and supersymmetry [58, 59]. The direct ancestor of the baby-Skyrme model is the $O(3)$ theory written in terms of complex variables, and is known as the $\mathbb{CP}^1$ model [60]. The theory also possesses non-trivial localized (albeit unstable) solutions that are referred to as $\mathbb{CP}^1$ lumps [20]. Subsequent

work by Leese [61] introduced modifications to the theory, which has *static* stable solutions known as Q-lumps (in analogy with the Q-balls that we will subsequently describe). In view of these developments, Wilczek and Zee [58, 57] suggested that a two dimensional sigma model could be interpreted as a toy model for skyrmions. Finally, we note that the term "baby skyrmion" first appeared in the literature in the 1994 work of Piette, Schroers and Zakrzewski [55].

1.2.2 Applications

Progress in the understanding of ferromagnetic materials and liquid crystals led to the realization that the two dimensional baby-Skyrme model is not just a toy theory, but can describe real physics, such as that seen in ferromagnetic quantum Hall systems [20, 62, 63, 64, 65, 66]. In that context, baby skyrmions correspond to texture (extended) excitations in the spin density which have been observed in the laboratory [67].

1.3 Q-balls in Two Dimensions

The term Q-ball was coined by Coleman [68, 69, 70] to refer to stable, localized (solitonic) solutions of a relativistic complex scalar field theory with a nonlinear quartic potential. Here we note that supersymmetric models of the type proposed to exist in nature generally have a field content that includes several scalars [18]. In particular, this is the case for the Minimal Supersymmetric Standard Model (MSSM), which has both baryonic and leptonic Q-ball solutions [71, 18, 72]. In addition, Q-balls have been suggested as possible *fossil* dark matter in the universe, and have also been postulated to be trapped in the interiors of gravitationally-compact astrophysical objects [73].

Q-ball type solutions also appear in nonlinear Schrödinger systems (e.g. Gross-Pitaevskii), where they can be used, for example, to describe Bose-Einstein condensates of weakly interacting atoms in harmonic traps [74, 75]. They also arise in planar models of the quantum-Hall effect (Maxwell-Chern-Simons Q-balls) [76]. Other examples include non-Abelian Q-balls, spinning Q-balls and Q-rings [77].

Despite their possible physical relevance, in this work we regard our study of Q-balls primarily as a "warm up" problem that allows us to develop our computational methods and infrastructure.

The Q-ball model we consider is described by the Lagrangian density for a complex scalar field,

ϕ, in two spatial dimensions [18, 78, 79, 80],

$$\mathcal{L} = \partial_\mu \phi \partial^\mu \phi^* - U(|\phi|^2)\,, \tag{1.8}$$

where Greek indices range over $0, 1, 2$. Due to the invariance of the Lagrangian density under the $U(1)$ symmetry transformation, $\phi \to \phi e^{i\alpha}$, the theory has a conserved Nöether current, J^μ (see Sec. 3.2 for details). The corresponding conserved charge, Q, is given by

$$Q = \int d^2x \;\; J^0 = \frac{1}{2i} \int d^2x \;\; (\phi^* \partial^0 \phi - \phi \partial^0 \phi^*)\,. \tag{1.9}$$

We emphasize that, in contrast to the Skyrme model, Q (1.9) is not a topological invariant [18, 78].

1.3.1 Existence of Q-ball Solutions

There are certain requirements that the potential $U(\sigma)$ in (1.8) must satisfy in order for the model to admit Q-ball configurations. These will be discussed in detail in Sec. 3.2 and App. B.2. In our study, we have used a polynomial potential for which Q-ball solutions are known to exist [18, 78, 81]. Specifically, we take

$$U(|\phi^2|) = \frac{1}{2} m^2 |\phi|^2 - \frac{1}{3} \alpha |\phi|^3 + \frac{1}{4} \beta |\phi|^4\,, \tag{1.10}$$

where m, α and β are positive real-valued parameters. Using this form for the potential, and performing suitable rescalings that are described in Sec. 3.2, the equations of motion derived from (1.8) read

$$\ddot{\phi} - \nabla^2 \phi + \phi - |\phi| \phi + B |\phi|^2 \phi = 0\,. \tag{1.11}$$

Here, an overdot denotes differentiation with respect to time, $|\phi|$ is the modulus of the complex scalar field ϕ, ∇^2 is the usual Laplacian operator in the plane, and B is another positive real-valued parameter.

1.4 Overview of Previous Numerical Work

1.4.1 Skyrme Model in Three Spatial Dimensions

As discussed previously, the Skyrme model provides an effective-field framework in which to perform calculations relevant to nuclear physics phenomenology. The first attempts to solve the Skyrme equations of motion numerically aimed to calculate nucleon-nucleon scattering amplitudes [82], where atomic nuclei were viewed as semi-classical bound states of solitons [83]. Additional pioneering work was due to Verbaarschot, Walhout and Wambach [84] (1986), who carried out calculations of head-on collisions of skyrmions in axisymmetry (1986), and Allder, Koonin, Seki and Sommermann [85] (1987), who performed the first truly three dimensional numerical calculations of skyrmion-skyrmion collisions (i.e. in three dimensional Cartesian coordinates), although the interactions studied were still head-on. In an attempt to reproduce the properties of the deuteron, Crutchfield, Snyderman and Brown [83] (1992) simulated the classical evolution of bound-states of skyrmions. The same year, Sommermann, Seki, Larson and Koonin [86] carried out the first three dimensional simulation of baryon–anti-baryon annihilation in the Skyrme model [86]. Wambach [28] provides a review about the Hamiltonian formulation of the model that was popular at that time, as well as the numerical techniques employed during the 1980's and early 1990's.

In an influential study, Battye and Sutcliffe [25] (1996) considered the scattering of multi-soliton skyrmions—minimal energy solutions that describe a bound state of multiple skyrmions. The latter work represents the beginning of what one might call the "modern era" of the field, since most subsequent work (including this thesis) has adopted the Lagrangian formulation of the equations of motion that they presented. The same authors [26] (2001) showed that the numerical evolution of clusters of static skyrmions can lead to end states resembling the complex structures known as fullerenes that are observed in large carbon molecules [26]. Other relevant work involving the numerical solution of the Skyrme field equations includes Amado *et al* [87] (1999) and Halasz *et al* [88] (2000). Both of these papers focus on the stabilization the skyrmion by means of vector meson fields.

A more thorough discussion of relevant numerical work is given in Sec. 5.3.

1.4.2 Skyrme Model in Two Spatial Dimensions

The literature concerning the numerical study of the baby Skyrme model is very rich and goes back to the works of Leese, Peyrard and Zakrzewski on the scattering of $\mathbb{CP}^1$ lumps and Q-lumps (see Sec. 4.5) [89, 90]. During the 1990s there was a plethora of investigations that explored the properties of different variations of the model, each defined by the specific potential function under consideration. Among the main contributors here were Sutcliffe [91], Peyrad *et al* [92], Piette [93, 55], Kudryavtsev *et al* [56] and Weidig [35]. The versatility of the baby-Skyrme model was further illustrated by the work of Dwyer and Rajagopal [94], who employed it as a toy model for more sophisticated physics—namely electroweak solitons.

Once more, we will provide additional details about these previous studies in a subsequent section (Sec. 4.5).

1.4.3 Observed Instabilities in the Skyrme Model

Over the years, one of the most interesting and challenging aspects of simulations of the Skyrme model is that instabilities have often been encountered in numerical evolutions. This has been the case for both the full three-dimensional and baby models [85, 86, 88]. In an effort to improve stability, some authors introduced artificial viscosity in their implementations [84], or used discrete time steps that seemed unnaturally small. Although such strategies proved useful in many cases, there remained evidence of instabilities that were *not* associated (at least completely) with the numerical approximations being employed *per se* [85].

In 1991, Crutchfield and Bell [1] suggested two possible causes of the latter type of instability. The first was due to an inadequate enforcement of the chiral constraint when a leap-frog time-evolution scheme was adopted. The second, and far more consequential, was associated with a possible loss of hyperbolicity—and thus well-posedness (see Sec. 1.5.2)—of the field equations [1, 26, 25, 95]. Specifically, the authors argued that evolution of certain types of initial data would lead to the development of regions in the solution domain where, heuristically, the equations would become of mixed hyperbolic-elliptic type. Thus, for such initial conditions, one could not expect solutions to exist, and, in fact, "instabilities" of the type that had been reported in some investigations were precisely what one would expect from numerical calculations. Crutchfield and Bell further posited that a loss of hyperbolicity could actually be *expected* on physical grounds, since the Skyrme model is a low energy effective theory [1, 26], and is thus, by definition, incomplete. In

particular, they noted that the model would not be suitable to describe high energy regimes. The presumed loss of hyperbolicity is of concern since, among other things, it would determine the limits of the application of the Skyrme model as an approximation to QCD and chiral interactions [96]. Such behaviour is also highly interesting from a mathematical point of view.

1.4.4 Q-balls in Two Spatial Dimensions

There is also significant literature on the numerical computation of Q-ball collisions. Particularly notable is the pioneering work of Battye and Sutcliffe [72] who adopted polynomial potentials and solved the full nonlinear equations of motion in one, two and three dimensions plus time. Their studies established the complex nature of Q-ball dynamics, including fragmentation and charge transfer. Using the same type of potential, Axenides *et al.* [18] classified the general outcome of Q-ball scattering as a function of the velocity of initial approach. In contrast, work by Multamaki and Iiro considered Q-ball scattering using potentials with a functional form inspired by phenomenological models, principally the Minimal Supersymmetric Standard Model (MSSM) [81, 97, 79]. We will review this literature in more detail in Sec. 3.5.1.

Another aspect of Q-ball dynamics that we find interesting is their scattering by potential obstructions. Numerical experiments of this type of interaction using topological solitons are numerous, see e.g. Collins and Zakrzewski [98]. However, to our knowledge the only numerical study of Q-ball–obstruction scattering is due to Al-Alawi and Zakrzewski [99], and this paucity of results inspired the calculations we describe in Sec. 3.7.

1.5 Aims of This Thesis

1.5.1 Phenomenology of General Collisions

We emphasize once more that this work is motivated by the rich and complex dynamics of the scattering of skyrmions and Q-balls, both in two and three spatial dimensions. One of our primary objectives is to use large scale numerical computations to study the nature of the nonlinear interactions of these solitons. All of the field theories that we simulate are characterized by large parameter spaces (especially when details of the initial data are taken into account), and our survey of these spaces can not be comprehensive. We thus consider what we feel are representative calculations with the hope that they can provide general insight into the phenomenology (collisions) on

which we focus.

1.5.2 High Energy Collisions and Hyperbolicity

We are also very interested in better understanding the nature of the instabilities observed in previous numerical evolutions of the Skyrme equations of motion. Specifically, we wish to investigate the possible breakdown of hyperbolicity and well-posedness postulated by Crutchfield and Bell [1] that was sketched above (Sec. 1.4.3).

Since we feel that the results from our study of this issue are among the most significant contributions of this thesis, it is worth spending some time at this point to be more specific about what we mean by hyperbolicity. Intuitively, hyperbolicity is associated with finite speeds for the propagation of signals, such as is the case for solutions of ordinary (linear) wave equations. The rigorous definition of hyperbolicity (see e.g. [100]), is expressed as an algebraic condition on the (constant) coefficients on the system of partial differential evolution equations written in first-order-in time form (see App. C.1)[7]. Full details aside, the key idea is that a hyperbolic PDE system represents a *well-posed initial value problem* [101]. This means that, at least for some amount of time[8], the evolution of initial data having suitable smoothness properties will result in a unique solution. Furthermore, well-posedness means that the solution depends continuously on the (smooth) initial data and its derivatives, so that the future developments of two initial configurations that differ slightly only diverge slightly as the evolutions proceed, and (at least locally) in direct proportion to the initial separation of the data. In contrast, when a problem is ill-posed (i.e *not* well-posed), the difference between the evolution of "nearby" initial states will have *no* bound as a function of time (no matter how short a time interval is considered), and there will be *no* solution for given initial data.[9]

In the case of a relativistic theory, such as the Skyrme model, Lorentz invariance may give the impression that hyperbolicity (which, again, we heuristically associate with causality) is guaranteed. Indeed, for so called semi-linear equations—in which the coefficients appearing in the principal part

[7]Specifically, the coefficients of a first order PDE system are used to construct a *principal symbol* matrix, P. If P has only real eigenvalues, the system is hyperbolic. However, the extent of the degeneracy of the eigenvalues and linear independence of the eigenvectors of P determine if the system is weakly, strongly or strictly hyperbolic. Only the latter two guarantee well-posedness of the initial value problem. See App. C.1 for details.

[8]We add this caveat since there are systems of evolution equations that have well-posed initial value problems, but for which sufficiently "strong" initial data leads to blow-up of the solution in finite time [102, 103, 104, 105].

[9]Note that ill-posed behaviour is different than the sensitivity to initial conditions seen in chaotic systems, for example. In the latter case we still expect that the difference in solutions evolving from nearby states will remain small (i.e. bounded in time) provided that the evolution time is sufficiently short.

of the PDEs do not depend on the solution itself—a result due to Hawking [106] implies that if the energy-momentum tensor of the theory satisfies a relation known as the dominant energy condition (DEC) [96], then energy cannot flow superluminaly. Here we note that Gibbons [96] has shown that the energy momentum tensor of the Skyrme model satisfies the DEC. However, Wong [95] points out that since the Skyrme equations are only quasi-linear—i.e. the coefficients in the principal part *do* depend on the solution—the requirement of the DEC alone might not be sufficient to rule out the existence of superluminal propagation of signals (as encountered in the case of elliptic equations). In fact, in [95], Wong rigorously establishes some conditions under which the Skyrme model will lose hyperbolicity. However, his results are highly mathematical, and their precise relationship to previous numerical work, and our own, are not clear to us at this time.

We should note that the the breakdown of hyperbolicity is not unheard of in evolution equations associated with physical systems. The situation here may be analogous to the case of other PDEs, such as the Tricomi equation of gasdynamics, where trans-sonic flow triggers instabilities that signal a breakdown in hyperbolicity.

Gibbons [96], as well as Crutchfield and Bell [1], state that the loss of pure hyperbolicity is likely to occur when the kinetic energy of the field configuration exceeds the potential energy. This is expected to occur in situations such as the high-velocity scattering of two skyrmions, or in skyrmion-anti-skyrmion annihilation. We thus concentrate much of our effort on the simulation of such processes.

1.6 Summary of Numerical Approach and Methodology

We have implemented a computational infrastructure that provides automation and flexibility in the development of finite difference codes for the approximate solution of hyperbolic time dependent PDEs. We test this infrastructure using the complex scalar field model given its simplicity relative to the Skyrme models (1.6) and (1.2). We consistently use second order (in the mesh spacing) approximations to discretize our PDEs and, in particular, use a centred two time-step discretization to treat time derivatives. The discrete nonlinear equations that result from the finite-differencing are solved using relaxation techniques. A key aspect of our codes is the incorporation of parallel adaptive mesh refinement (AMR). Here we make use of a set of libraries written by Pretorius [107, 108] that implement the Berger and Oliger AMR algorithm [109]. Full details of our numerical

methods, along with a description of the diagnostic tools that we have used, are given in in Chap. 2.

1.7 Summary of Thesis

In this section we briefly summarize the organization and main contributions of this work.

Chap. 2 is devoted to an in-depth description of the computational infrastructure and the numerical techniques that constitute the core of our methodology.

In Chap. 3 we investigate the scattering of Q-balls as a model problem to develop and test the infrastructure. We perform adaptive (AMR) calculations that reproduce previously reported phenomenology for collisions of Q-balls having the same charge [18]. We also carry out similar experiments for oppositely-charged Q-ball collisions which, so far as we know, have not been reported previously. Next, we investigate the dynamics of Q-balls as a function of the charge itself, finding, for example, that right-angle scattering is completely absent if the configurations have small enough charge. We conclude by studying the scattering of Q-balls against potential obstructions, observing final states that represent combinations of transmission and reflection of the solitons.

The main contributions of the thesis are described in Chap. 4, which details the adaptive (and non-adaptive), convergent numerical evolutions that we have performed within the context of the baby-Skyrme model. We focus on two types of head-on collisions: one involving two baby skyrmions, and the other using one skyrmion and one antiskyrmion. Both of these processes display rich dynamical behaviour. Some instances of more general grazing (i.e. off-axis) collisions are also modeled, further adding to our understanding of skyrmion scattering.

Our most novel results involve the investigation of the transition from pure-hyperbolic to mixed hyperbolic-elliptic behaviour in Skymre models, posited by Crutchfield and Bell [1, 26, 95], and described above. We find strong evidence that evolutions of initial configurations describing collisions of baby skyrmions with sufficiently large relative boosts become ill-posed. Specifically, we observe a loss of conservation of energy and smoothness of the dynamical fields, with indications that both of these deficits worsen as the finite-difference mesh scale decreases.[10] For certain types of collisions, we determine specific parameter settings at which the lack of well-posedness sets in. We also show that evolution of generic smooth initial data specifically designed to have kinetic energy significantly greater than potential leads to a breakdown of hyperbolicity.

[10] Additionally, in App. C.2 we provide some corroborating evidence for loss of hyperbolicity that is based on a linearized mode analysis of the equations of motion.

In terms of the computational approach itself, we find that the simple method that we use to enforce the chiral constraint, as well as the specific finite-difference adopted, results in an improvement of stability relative to some earlier numerical work [85, 84]. Most importantly, through careful analysis of convergence properties, we establish that our approximate results *do* tend to the desired continuum solutions as the mesh spacing tends to zero (and in those cases where the evolution is apparently well-posed).

Chap. 5 describes preliminary results from simulations of the head-on scattering of skyrmions in three spatial dimensions, and where AMR is employed. Although our computer resources are insufficient to establish definitive convergence behaviour (for which non-adaptive computations had to be used), the phenomenology that we observe is consistent with previous studies [85, 28, 26].

Finally, Chap. 6 provides a further summary of our results and a discussion of possible future research avenues and applications of our codes.

1.8 Notation and Conventions

We adopt the following index notations. Latin letters such as $a, b, c, \ldots$ denote field components, while Greek indices $\mu, \nu, \ldots$ run over the spacetime values $0, 1, 2, 3$ (where 0 is the time index). Latin letters such as $i, j, k, \ldots$ range over the spatial dimensions. The Einstein summation convention applies to all types of indices. For example,

$$\partial_\mu \phi_a \partial^\mu \phi_a \equiv \sum_{a=1}^{N} \sum_{\mu=0}^{d} \partial_\mu \phi_a \partial^\mu \phi_a \,, \tag{1.12}$$

where N is the number of field components of the tensor, and d (sometimes D) is the number of spatial dimensions. For the specific models considered we have: $d = 2$, $N = 1$ for Q-balls; $d = 2$, $N = 3$ for baby skyrmions and $d = 3$, $N = 4$ for skyrmions. The metric signature is $(-, +, +, +)$ and we denote the flat metric by $\eta_{\mu\nu}$. Since all of our calculations are carried out in flat spacetime, $\eta_{\mu\nu}$ is used to raise and lower all spacetime indices. Geometric units are used throughout this thesis: in particular, the speed of light in vacuum is $c = 1$. When we speak of a model being $2 + 1$ or $3 + 1$ (equivalently 2D or 3D), we mean that the fields have dependence on 2 or 3 spatial dimensions plus time, respectively. The usual vector cross product is denoted by $\times$.

The ordinary derivative of the function $\phi = \phi(t, x, y, z)$ with respect to a spatial coordinate x

is denoted variously

$$\frac{\partial \phi}{\partial x} \equiv \partial_x \phi \equiv \phi_x \,, \tag{1.13}$$

while for the time coordinate, t, we have

$$\frac{\partial \phi}{\partial t} \equiv \partial_t \phi \equiv \phi_t \equiv \dot{\phi} \,. \tag{1.14}$$

For functions of a single variable, we will also use the prime notation. E.g. if we have $\phi = \phi(r)$, then

$$\phi' \equiv \frac{d\phi}{dr} \,. \tag{1.15}$$

We need to stress that here and below—and due to our use of superscripts for other purposes—we will often adopt a notation whereby ϕ^1, ϕ^2 and ϕ^3 (and similarly π^1, π^2 and π^3), rather than ϕ_1, ϕ_2 and ϕ_3, denote field components.

For the baby-Skyrme model (Chap. 4), we fix units so that $F_\pi = \kappa = 1$. F_π then has dimensions of energy and κ and $1/\mu$ have dimensions of length. Similarly, for the Skyrme model (Chap. 5), the parameters F_π and e are scaled away by choosing suitable units of energy ($F_\pi/4e$) and length ($2/eF_\pi$) [20]. We note that κ^{-2} in the baby-Skyrme model is the analogue of e in the full theory.

CHAPTER 2

NUMERICAL METHODS

This chapter is devoted to the description of the numerical techniques used to solve the time dependent partial differential equations that govern the various models of interest in this thesis. We begin with a discussion of elementary concepts of finite difference approximation (FDA) (Sec. 2.1), which is the discretization technique used to compute all of our numerical solutions. This is followed by a description of the relaxation algorithm used to solve the discrete equations that result from the finite difference process (Sec. 2.3), and a discussion of our use of Kreiss-Oliger dissipation (Sec. 2.2) for the stabilization/regularization of our difference schemes. The chapter concludes with an overview of our specific approach to (parallel) adaptive mesh refinement (Sec. 2.4). We note that much of the discussion below closely follows the style and conventions of [110, 111], and Chap. 4 of [112].

2.1 Finite Difference Basics

The solution of a partial differential equation via finite differencing first requires the discretization of the domain of the problem. Let $u(t, x, y, z)$ be a solution of a certain partial differential equation (PDE) on a continuum spatial domain. In 3D[11] we discretize this domain using N_x, N_y and N_z points in the x, y and z directions respectively, resulting in sets of discrete coordinates that we label x_i, $i = 1, \ldots, N_x$, y_j, $j = 1, \ldots, N_y$ and z_k, $k = 1, \ldots, N_z$. We restrict attention to so-called *uniform meshes*, which means that the spatial domain is an ordered set of points, (x_i, y_j, z_k), where the separation between contiguous points in any coordinate direction is some constant, h. Specifically we have

$$x_{i+1} - x_i = h, \qquad y_{j+1} - y_j = h, \qquad z_{k+1} - z_k = h\,. \tag{2.1}$$

[11] The discussion here focuses on the case of 3 spatial dimensions: the restriction to 2 space dimensions is straightforward and should be clear to the reader.

We will refer to h variously as the mesh spacing, the grid spacing, or the discretization scale.

The specific grid points making up the mesh are easily determined from the coordinate ranges defining the continuum domain. Thus, for

$$x_{\min} \leq \quad x \quad \leq x_{\max}, \tag{2.2}$$

$$y_{\min} \leq \quad y \quad \leq y_{\max}, \tag{2.3}$$

$$z_{\min} \leq \quad z \quad \leq z_{\max}, \tag{2.4}$$

the grid points are

$$x_i \quad = \quad x_{\min} + (i-1)\,h, \qquad\qquad i = 1 \ldots N_x, \tag{2.5}$$

$$y_j \quad = \quad y_{\min} + (j-1)\,h, \qquad\qquad j = 1 \ldots N_y, \tag{2.6}$$

$$z_k \quad = \quad z_{\min} + (k-1)\,h, \qquad\qquad k = 1 \ldots N_z, \tag{2.7}$$

such that

$$x_1 = x_{\min} \qquad \text{and} \qquad x_{N_x} = x_{\max}, \tag{2.8}$$

$$y_1 = y_{\min} \qquad \text{and} \qquad y_{N_y} = y_{\max}, \tag{2.9}$$

$$z_1 = z_{\min} \qquad \text{and} \qquad z_{N_z} = z_{\max}. \tag{2.10}$$

There are therefore a total of $N_g = N_x \times N_y \times N_z$ points in the mesh. The time domain, which without loss of generality we take to be

$$0 \leq t \leq t_{\max}, \tag{2.11}$$

is similarly discretized using time steps of size Δt, resulting in a set of N_t discrete time values, denoted t^n and defined by

$$t^n \equiv n\Delta t,\ n = 0, 1, \ldots N_t, \tag{2.12}$$

where N_t, Δt and $t_{\max}$ must satisfy $N_t \Delta t = t_{\max}$.

We make one further demand on our finite difference discretization, which is that whenever

we consider a fixed problem (specific model parameters, initial data etc.), but vary the spatial and temporal mesh spacings, h and Δt—as we will do when investigating the convergence of our numerical solutions—we keep the so-called *Courant number*, λ, defined by

$$\lambda = \frac{\Delta t}{h}, \tag{2.13}$$

fixed. This means that we can always view our finite difference solutions as being characterized by a *single* discretization scale, h.

Having defined our discrete domain (FD mesh, FD grid), we can introduce discrete functions, or *grid functions*, which are defined on the mesh, and which are to approximate their continuum counterparts. Here, and in subsequent chapters, we will denote grid function values—either individually or as a whole—in a variety of ways. The first is to use a standard finite difference notation whereby u^n_{ijk} denotes a single grid function value with

$$u^n_{ijk} \approx u(t^n, x_i, y_j, z_k)\,. \tag{2.14}$$

In instances where the subscript notation for the spatial grid indices could become confusing, we will use $u^n(i,j,k)$ to label the same value. At times it will be convenient to refer to all of the grid function values defined at a specific discrete time, t^n, and we will use u^n for that purpose. Finally, and more abstractly, when referring to the grid function values as a whole (i.e. all values defined on the spatio-temporal mesh), we will use the notation u^h. Here the superscript emphasizes that we are considering the discrete case with a finite difference mesh that is dependent on a single, fundamental control parameter, namely the discretization scale, h.

The problems we wish to solve are generally expressed as systems of hyperbolic partial differential equations (PDEs). Let L represent a set of m differential operators acting on a vector, u, of m unknown dependent functions: $u = (u_1, \ldots, u_m)$. Then any of our systems of interest can be cast in the form

$$Lu - f = 0\,. \tag{2.15}$$

Here—and again specializing to the $3+1$ case, each u_i is a function of the independent variables, that is, $u_i = u_i(t,x,y,z)$ for $i = 1 \ldots m$. Similarly f is a vector of m *source functions*, with $f_i = f_i(t,x,y,z)$. We note that a unique solution of (2.15) will require the specification of initial

and boundary conditions: an appropriate treatment of these conditions is implicit in what follows. For simplicity, we now restrict our discussion to the case when $m = 1$ (a scalar equation), but we emphasize that the development is equally applicable to the general case.

In the finite difference approach to the solution of (2.15) we replace

1. L by a *finite difference approximation*, L^h (also an operator),
2. u and f with grid functions u^h and f^h respectively.

These replacements then yield the following finite difference version of (2.15):

$$L^h u^h - f^h = 0\,. \tag{2.16}$$

We observe that (2.16) will generally represent a system of algebraic equations—linear or nonlinear, dependent on the nature of L^h and the (suppressed) discrete boundary conditions—in the grid function values, u^h.

The difference between the finite difference solution u^h and the continuum solution u defines the *solution error*,

$$e^h \equiv u - u^h\,. \tag{2.17}$$

We note that e^h is sometimes referred to as the "truncation error" (see e.g. [109]), but, as will be discussed shortly, we reserve that nomenclature for a different quantity. The relation between h and the solution error is a crucial aspect of any finite difference approximation. Fundamentally, we want $e^h \to 0$ as $h \to 0$, a behaviour known as *convergence* of the finite difference scheme. The following definitions of convergence are obviously equivalent:

$$\begin{aligned} \lim_{h\to 0} e^h &= 0\,, \\ \lim_{h\to 0} u^h &= u\,. \end{aligned}$$

The *order of accuracy* of a FDA measures how quickly the solution error decreases as a function of h. Specifically, the solution of a FDA shows convergence of order p if

$$\lim_{h\to 0} e^h = O(h^p)\,, \tag{2.18}$$

where p is an non-negative integer, and is then said to be p-th order accurate. In this thesis we

have aimed to construct difference solutions that are second order accurate, i.e. with $e^h = O(h^2)$.

In the numerical solution of finite difference equations resulting from the discretization of time dependent PDEs, the computation generally proceeds discrete time step by discrete time step. That is, we can write (2.16) in the schematic form

$$Q_1 u^{n+1} = Q_0 \left(u^n, u^{n-1}, u^{n-2}, \ldots, u^{n-r} \right) , \quad n = r, r+1, \ldots \tag{2.19}$$

where Q_1 and Q_0 are operators (again, linear or nonlinear, depending on the nature of the PDEs and the difference scheme). Given initial conditions

$$u^n = u_0^n , \quad n = 0 \ldots r , \tag{2.20}$$

where the u_0^n are specified quantities, (2.19) provides the means to successively determine the grid function values at discrete times $t^n = t^{r+1}, t^{r+2}, \ldots t^{N_t}$. Equation (2.19) tells us that the advanced solution values, u^{n+1}, depend on the most recently computed values, u^n, and those at a further r time-levels. However, it is also important to note that the operator Q_1 may be such that the individual advanced-time unknowns u_{ijk}^{n+1} are coupled in a nontrivial fashion. When this is the case, we say that the scheme is *implicit*. On the other hand, if there is no such coupling, then we may be able to write down explicit expressions for each u_{ijk}^n in terms of previously computed values (i.e. values defined at earlier time steps), and the scheme itself is said to be *explicit*. We note that the total number of time levels of data (i.e. $r+2$) that appears in (2.19) provides another characterization of the finite difference method: in particular, an approximation which couples a total of k time levels is often known as a k-level scheme. In Sec. 2.1.3 below we will briefly consider two specific and illustrative discretizations of the 1D wave equation, one a three-level explicit method, the other a two-level implicit scheme.

When implicit difference schemes are employed—which is the case for the systems studied in this dissertation—it may be desirable (or essentially necessary in the nonlinear case) from a computational standpoint to solve the algebraic equations defined by (2.16) or (2.19) using an iterative process. That is, we introduce another grid function, $\tilde{u}^h$, which is to be initialized in some fashion, and with $\tilde{u}^h \to u^h$ in the limit of infinite iteration (assuming, of course, that the iteration

converges).[12] Associated with $\tilde{u}^h$ is another important quantity, the *residual*, r^h, defined by

$$r^h \equiv L^h \tilde{u}^h - f^h \,, \tag{2.21}$$

and which thus quantifies by how much the current estimate of the discrete solution fails to satisfy the difference equations. Clearly, the iterative procedure of determining u^h can be equivalently viewed as the process of driving the residual to 0.

A final basic notion that we will need is that of the truncation error associated with a finite difference scheme. Given the FDA (2.16), and the *continuum* solution, u, of the PDE being approximated, the truncation error is defined by

$$\tau^h \equiv L^h u - f^h \,. \tag{2.22}$$

The difference scheme is said to be *consistent*, if and only if

$$\lim_{h \to 0} \tau^h = 0 \,, \tag{2.23}$$

and consistency is a necessary condition for convergence. Paralleling the above discussion of the solution error, e^h, we say that a finite difference scheme is p-th order accurate if

$$\lim_{h \to 0} \tau^h = O(h^p) \,, \tag{2.24}$$

where p is again a non-negative integer. Finally, the Lax equivalence theorem [113]—originally proven for linear difference equations, but expected to hold for the PDEs and difference schemes studied in this thesis—states that given consistency, *stability* is a necessary and sufficient condition for convergence. Although stability is a crucial issue in the solution of time dependent PDEs using finite difference methods, we will not employ any rigorous definitions of the concept here. appeal to the intuitive notion that a difference scheme for a time dependent problem is stable if the solutions generated by the time iteration do not "blow up", unless the continuum solutions themselves do. [13]

[12] We note that we are abusing notation a bit here, in that $\tilde{u}^h$ should more properly be denoted $\tilde{u}^{n+1}$, $n = r, r+1, \ldots$.

[13] However, for completeness we have included a standard definition of the stability of a numerical scheme in A.1

2.1.1 Richardson Expansions and Convergence Tests

So far it is not possible to say anything about the solution error, e^h, since it involves the continuum solution, u, which is of course unknown. However, two important observations provide insight about the functional form of the solution error. The first is that the form of the truncation error, τ^h, defined by (2.22) can always be inferred from the FDA and the differential equations (2.15) (typically by means of a Taylor expansion) [111]. In particular, over a century ago Richardson [114] noted that a completely centred (we will discuss the notion of centering below) $O(h^2)$ FDA defined on a uniform mesh would have truncation error, τ^h, of the form

$$\tau^h = h^2\tau_2(t,x) + h^4\tau_4(t,x) + h^6\tau_6(t,x) + \dots \tag{2.25}$$

Richardson then conjectured the second key point, which is that the solution error, e_h, in this case would be of the form

$$e^h = h^2 e_2(t,x) + h^4 e_4(t,x) + h^6 e_6(t,x) + \dots \tag{2.26}$$

where e_2, e_4, e_6, are continuum error functions, i.e. having no h-dependence.

Provided that such an expansion exists, we have a powerful method for investigating the convergence properties of finite difference solutions. For example, assume that we have an FDA which is $O(h^2)$ accurate (as is the case for the discretizations considered in this thesis). We then consider performing computations using fixed initial data, but with uniform grids having resolutions h, $2h$ and $4h$ respectively. We then have

$$u^h = u + h^2 e_2 + h^4 e_4 + \dots \tag{2.27}$$

$$u^{2h} = u + (2h)^2 e_2 + (2h)^4 e_4 + \dots \tag{2.28}$$

$$u^{4h} = u + (4h)^2 e_2 + (4h)^4 e_4 + \dots \tag{2.29}$$

We now combine these solutions to define a convergence factor, $Q^h(t)$, which we can use to measure the rate at which the numerical solutions are approaching the continuum one. [14] Specifically, we define

$$Q^h(t) \equiv \frac{\|u^{4h} - u^{2h}\|_2}{\|u^{2h} - u^h\|_2}, \tag{2.30}$$

[14] The Q^h notation is standard in the numerical relativity literature. In this work it should not be confused with the conserved Nöether charge of the Q-ball solitons, Q.

where $\|\cdot\|_2$ is the l_2 norm,

$$\|u^h\|_2 = \left[\frac{\sum_{i=1}^{n} |u_i^h|^2}{n}\right]^{1/2} . \tag{2.31}$$

Here, our definition of $\|\cdot\|_2$ includes division by the number of grid points so that the norm is relatively independent of the mesh resolution used.

Substituting the expansions (2.29) in (2.30), we easily see that the convergence factor as $h \to 0$ should be

$$\lim_{h\to 0} Q^h(t) = \frac{12h^2 \|e_2\|}{3h^2 \|e_2\|} = 4\,. \tag{2.32}$$

In practice, it is an easy task to compute Q^h (modulo resource limitations when fine meshes are used), and observing values that are close to what is expected provides confidence that the numerical solutions *are* convergent. However, it is important to stress that this type of convergence test does *not* establish that the numerical solutions are tending to the *correct* continuum solution. It is for this reason that we consider the independent residual tests, described in Sec. 2.1.4, to be so vital.

2.1.2 Construction of Finite Difference Approximations

There are various means to construct a finite difference approximation for a given differential system. Arguably, the most straightforward approach uses Taylor series expansion. For the sake of exposition, we first restrict attention to the one-dimensional case—extension to additional dimensions is straightforward.

We thus consider a uniform mesh of grid points at locations x_i where $x_i = x_{i-1} + h$ and h is the mesh spacing. We again adopt the notation $u_i \equiv u(x_i)$ where u is the continuum function that satisfies the differential equation to be solved approximately.

By Taylor series expansion we then have (for example)

$$u_{i-1} = u_i - h\mathcal{D}_x u_i + \frac{1}{2}h^2\mathcal{D}_x^2 u_i - \frac{1}{6}h^3\mathcal{D}_x^3 u_i + O(h^4) \tag{2.33}$$

$$u_i = u_i \tag{2.34}$$

$$u_{i+1} = u_i + h\mathcal{D}_x u_i + \frac{1}{2}h^2\mathcal{D}_x^2 u_i + \frac{1}{6}h^3\mathcal{D}_x^3 u_i + O(h^4) \tag{2.35}$$

where $\mathcal{D}_x$, $\mathcal{D}_x^2$, $\mathcal{D}_x^3$, ... are the first-, second-, third-order, etc. derivative operators.

We can now take linear combinations of the above expressions (as well as expansions for

u_{i+2}, u_{i-2} etc.) to generate finite difference approximations for various derivatives. For example, from (2.33) and (2.35) we have

$$u_{i+1} - u_{i-1} = 2h\mathcal{D}_x u_i + O(h^3) \tag{2.36}$$

which yields the $O(h^2)$ FDA for the first derivative:

$$\mathcal{D}_x u_i = \frac{u_{i+1} - u_{i-1}}{2h} + O(h^2)\,. \tag{2.37}$$

This type of FDA is known as a *centred* approximation, since the grid locations of the function values used in the approximation are symmetric with respect to x_i. This approximation can be used at all x_i, except for the first and last mesh points. At these locations, and to maintain $O(h^2)$ accuracy, so-called *forward* and *backward* formulae can be used:

$$\mathcal{D}_x u_i = \frac{-3u_i + 4u_{i+1} - u_{i+2}}{2h} + O(h^2), \qquad \mathcal{D}_x u_i = \frac{3u_i - 4u_{i-1} + u_{i-2}}{2h} + O(h^2). \tag{2.38}$$

We can also construct first order forward and backward approximations to the first derivative from the Taylor expansions:

$$\mathcal{D}_x u_i = \frac{u_{i+1} - u_i}{h} + O(h), \qquad \mathcal{D}_x u_i = \frac{u_i - u_{i-1}}{h} + O(h) \tag{2.39}$$

Approximations to higher differential-order operators can be constructed either using the Taylor expansion approach we just illustrated, or by nesting formulae for lower differential-order operators. For example, from the Taylor series expansions (2.33–2.35) we find the standard $O(h^2)$ centred approximation of the second derivative:

$$\mathcal{D}_x^2 u_i = \frac{u_{i+1} - 2u_i + u_{i-1}}{h^2} + O(h^2). \tag{2.40}$$

On the other hand, using the nesting approach—which is particularly useful for some multi-

dimensional operators—we have

$$\frac{\partial^2 u_{ij}}{\partial x \partial y} = \frac{\partial}{\partial x}\left(\frac{\partial u_{ij}}{\partial y}\right) = \frac{1}{2h_x}\left[\left(\frac{\partial u}{\partial y}\right)_{i+1,j} - \left(\frac{\partial u}{\partial y}\right)_{i-1,j}\right] + O(h_x^2) \tag{2.41}$$

$$\frac{\partial^2 u_{ij}}{\partial x \partial y} = \frac{u_{i+1,j+1} - u_{i+1,j-1} - u_{i-1,j+1} + u_{i-1,j-1}}{4h_x h_y} + O\left(h_x^2, h_y^2\right)$$

2.1.3 Explicit and Implicit Schemes for the Wave Equation

We have already defined the notions of explicit and implicit FDAs for the case of time dependent PDEs, but in an abstract manner (Sec. 2.1). Here we discuss specific examples of such schemes which, for the implicit case, has the added benefit of introducing the time-discretization method used throughout this thesis.

We thus consider the wave equation

$$\phi(t,x)_{tt} = \phi_{xx} \tag{2.42}$$

where, without loss of generality, we have set the propagation speed to unity. (Here and below we will often used ϕ to denote a fundamental field, while π will be used for the time derivative of that field, i.e. $\pi \equiv \phi_t$.) Using (2.40) to approximate both the temporal and spatial derivatives, and again noting that we will always take $\Delta t = \lambda h$, where λ is to be held fixed as $h \to 0$, we have the following $O(h^2)$ approximation of (2.42):

$$\frac{u_i^{n+1} - 2u_i^n + u_i^{n-1}}{(\lambda h)^2} = \frac{u_{i+1}^n - 2u_i^n + u_{i-1}^n}{h^2}\,. \tag{2.43}$$

The structure of the grid points that are involved in this approximation—the so-called *stencil* of the FDA—is shown in Fig. 2.1. We note that the scheme is three-level and is fully-centred, both in space and in time. The scheme (2.43) is explicit since we can explicitly solve for the advanced time unknowns, u_i^{n+1}, from the retarded values u_i^n and u_i^{n-1}:

$$u_i^{n+1} = 2u_i^n - u_i^{n-1} + \lambda^2(u_{i+1}^n - 2u_i^n + u_{i-1}^n)\,. \tag{2.44}$$

We now turn to an FDA for (2.42) which we call the Crank-Nicholson scheme since it uses the same type of temporal discretization proposed by Crank and Nicholson in the 1940's [115] in the

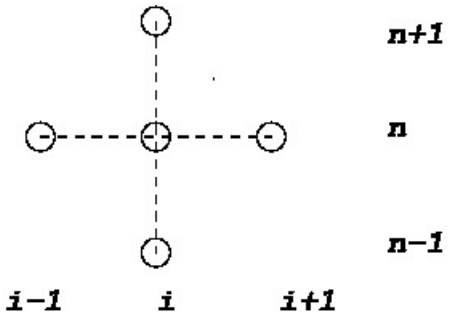

Figure 2.1: Finite difference stencil for fully-centred $O(h^2)$ approximation of the wave equation (2.42).

context of the solution of diffusion equations.

We first rewrite (2.42) in first-order-in-time form by introducing the auxiliary variable π defined, as noted above, by

$$\pi \equiv \phi_t \,. \tag{2.45}$$

Eqn. (2.42) can then be recast as the system:

$$\phi_t = \pi \,, \tag{2.46}$$

$$\pi_t = \phi_{xx} \,. \tag{2.47}$$

As illustrated in Fig. 2.2, the Crank-Nicholson scheme involves two time levels. Like the approximation (2.43) it is also fully centred in time, but in this instance the centering is at a "fictitious" time, $t^{n+1/2}$, indicated by the solid dot in the figure. The centred time discretization is based on the observation that for any grid function u_j^n we have

$$\frac{u_j^{n+1} - u_j^n}{\Delta t} = [u_t]_j^{n+1/2} + O(\Delta t^2) \,. \tag{2.48}$$

In order to complete the discretization of (2.46) we need an $O(h^2)$ approximation for $\pi_j^{n+1/2}$. This is achieved by simply averaging the values of π_j^n and π_j^{n+1}. Similarly, for the spatial derivative that appears in (2.47), second order accuracy in time as well as in space is accomplished by averaging the $O(h^2)$ approximation of ϕ_{xx} applied at each of the two time levels. The full Crank-Nicholson

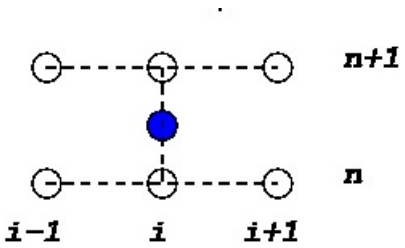

Figure 2.2: Finite difference stencil for $O(h^2)$ Crank-Nicholson approximation of the wave equation (2.42) written in the first-order-in-time form (2.46–2.47).

scheme then reads:

$$\frac{\phi_i^{n+1} - \phi_i^n}{\lambda h} = \frac{\pi_i^{n+1} + \pi_i^n}{2}, \tag{2.49}$$

$$\frac{\pi_i^{n+1} - \pi_i^n}{\lambda h} = \frac{1}{2}\left[\frac{\phi_{i+1}^{n+1} - 2\phi_i^{n+1} + \phi_{i-1}^{n+1}}{h^2} + \frac{\phi_{i+1}^n - 2\phi_i^n + \phi_{i-1}^n}{h^2}\right]. \tag{2.50}$$

We observe that, as the term implicit implies, equations (2.49) and (2.50) have non-trivial couplings among various of the advanced-time unknowns, ϕ_j^{n+1} and π_j^{n+1}, and to advance the solution from t^n to t^{n+1} we must solve a *system* of equations—linear in this case—at least approximately.

As mentioned previously, we use the Crank-Nicholson approach to discretize all of the evolution equations studied in this thesis.

2.1.4 Independent Residual Evaluation

As discussed above, we can use convergence tests to establish whether a sequence of finite difference solutions computed with the same initial data, but using grids with different mesh spacings, is converging to some continuum function in the limit $h \to 0$. However, we also noted that these tests by themselves do not guarantee that that function is the desired solution of the underlying differential equations

Particularly for complex systems of PDEs it is very easy to make one or more mistakes—such as coding a specific term incorrectly in the finite difference implementation—that will lead to precisely the case of convergence to the wrong continuum solution. In order to detect such errors and, ultimately, to provide very strong evidence for convergence to a correct solution, we use the technique of *independent residual evaluation* [116, 117].

The independent residual method involves the construction of a finite difference discretization of the PDEs which is distinct from (independent of) the one used to generate the fundamental discrete approximation, u^h, of those PDEs. To illustrate the technique we again consider a general set of PDEs written in the abstract form

$$Lu = 0\,, \tag{2.51}$$

with an associated finite difference approximation

$$L^h u^h = 0\,. \tag{2.52}$$

We note that, without loss of generality, we have suppressed the source functions used in (2.15) and (2.16) in the above two equations. We now introduce a second discretization of (2.51)

$$\tilde{L}^h \tilde{u}^h = 0\,. \tag{2.53}$$

The difference operator $\tilde{L}^h$ is distinct from L^h and consequently $\tilde{u}^h$ is different from u^h. Now, in the independent residual approach we do not solve (2.53) for $\tilde{u}^h$, rather we *apply* the second difference operator, $\tilde{L}^h$, to the discrete solution, u^h (which we *do* compute from (2.52)) in order to establish convergence.

To see how this works, we note that $\tilde{L}^h$ can be expanded as

$$\tilde{L}^h = L + h^2 E_2 + \ldots \tag{2.54}$$

where we have assumed that $\tilde{L}^h$ is an $O(h^2)$ approximation of L. Here E_2 is a differential operator that, in general, will involve higher-order derivatives than those appearing in L, and whose form can be deduced from the truncation error of the scheme. Assuming that L^h is also a second-order approximation, then we can further expect u^h to have the expansion (see Sec. 2.1.1)

$$u^h = u + h^2 e_2 + \ldots \tag{2.55}$$

where e_2 is a continuum function (no h-dependence). We now consider the action of $\tilde{L}^h$ on u^h—this defines the independent residual. Using the above two expansions, and assuming that L is linear

(a similar argument works in the nonlinear case) we have

$$\begin{aligned} I_u^h \equiv \tilde{L}^h u^h &= \left(L + h^2 E_2 + \ldots\right)\left(u + h^2 e_2 \ldots\right) \\ &= Lu + h^2 L e_2 + h^2 E_2 u + \ldots \qquad (2.56) \\ &= h^2 \left(L e_2 + E_2 u\right) + \ldots \qquad (2.57) \end{aligned}$$

where I_u^h denotes the independent residual and in the last step we have used the original PDE itself, $Lu = 0$. The key observation is that if u^h *is* converging to the correct solution, then the computed independent residual $I_u^h \equiv \tilde{L}^h u^h$ will vanish as $h \to 0$ (in this case, from (2.57), as an $O(h^2)$ quantity). On the other hand, if u^h was converging, but not to the exact solution, then we would have an expansion of the form

$$u^h = v + h^2 f_2 + \ldots \qquad (2.58)$$

where v would not satisfy $Lv = 0$. Indeed, since v would be some essentially arbitrary (smooth) function, then the action of the differential operator on it would yield some other smooth function, w, i.e. we would have $Lu = w$. The leading order terms corresponding to (2.57) would then be

$$w + h^2 \left(L f_2 + e_2 v\right) \qquad (2.59)$$

so that as $h \to 0$ we would find that the independent residual would be an $O(1)$ quantity.

It should be clear from the above that it is *extremely* unlikely that the basic finite difference solution, u^h, could be tending to some fixed function other than u as $h \to 0$, but with I_u^h still vanishing in that limit. Thus, if we find that this residual is going to 0 in the limit of infinitesimal mesh spacing, we can be very confident that our finite difference values are converging to the desired continuum solution.

It is important to note that $\tilde{L}^h$ is used strictly in an applicative fashion: again, we never solve for the corresponding difference solution $\tilde{u}^h$. This means that we do not have to be concerned with issues such as the stability, or computational complexity, in solving (2.53). Furthermore, $\tilde{L}^h$ need not be the same order as L. If, for example, $\tilde{L}^h$ is first-order accurate, while L^h is second order, then $I_u^h \equiv \tilde{L}^h u^h$ will also be $O(h)$ but will still tend to 0 as $h \to 0$ if and only if $u^h \to u$.

The major wrinkle in the use of independent residuals is that if we find that I_u^h does not vanish

as $h \to 0$, then we do not know if there is a problem with the original discretization (2.52) or with the independent one (2.53). It is thus crucial that (2.53) be constructed and implemented in as error-free a manner as possible. Use of symbolic manipulation can be very useful in this context, since it enables the discretization process used to generate $\tilde{L}^h$ to be automated from a high level specification of the PDEs. If the latter is not easily determined to be manifestly correct by inspection, it is often possible—as is done in this thesis—to derive the PDEs using symbolic techniques.

In terms of specifics of the construction of $\tilde{L}^h$, we note that we can, for example, use backwards or forwards difference approximations of derivatives should centred approximations be used for L^h. Again the accuracy order of $\tilde{L}^h$ is not important: all we require is that it be a consistent approximation to L.

2.2 Kreiss-Oliger Dissipation

There is another effect associated with finite difference discretization that has bearing on the work described in this thesis. For illustrative purposes let us again consider the simple wave equation (2.42). We can consider the decomposition of the solution, $\phi(t, x)$, into Fourier modes. Because the PDE is non-dispersive, all modes propagate with the same speed. When one uses a finite difference approximation—such as (2.43)—of the equation, one finds that this is not the case: the discrete solution, $\phi^h \equiv \phi_i$, has a non-trivial dispersion relation. In particular, the high frequency components of the finite difference solution travel more slowly than the low frequency ones, and for some schemes the highest frequency components do not propagate at all. Most importantly for us, the high frequency components of ϕ_i—and the fact that they travel too slowly—can often lead to instability (blow-ups) of the finite difference solution. This effect tends to be exacerbated for nonlinear systems. Moreover, the use of adaptive mesh refinement of the type described in Sec. 2.4, and used in this thesis, can magnify this problem.

Now, since the high frequency modes are not treated properly by the FDA, and since they can be problematic, it can be argued that it is a good idea to modify the difference scheme so that the highest frequency components *are* dissipated. This is a strategy that is commonly used in the difference solution of hyperbolic PDEs.

The specific approach we use for incorporating dissipation is originally due to Kreiss and

Oliger [118] (hereafter often abbreviated KO) and we will illustrate it here with a simple example

We first consider a difference operator, $D_{\rm KO}$, whose action on an arbitrary difference solution, u_i, in one spatial dimension is given by

$$D_{\rm KO}u_i \equiv \frac{\epsilon}{16}\left(u_{i-2} - 4u_{i-1} + 6u_i - 4u_{i+1} + u_{i+2}\right) . \tag{2.60}$$

Here ϵ is an adjustable positive constant whose role will be discussed below. We now perform a Fourier transform on $u_i \equiv (x_i)$, yielding a transformed solution, $\tilde{u}(\xi)$, where $\xi \equiv k\Delta x \equiv kh$ is the dimensionless wave number with corresponding frequency k. Note that from Nyquist's theorem we have that the highest frequency that can be represented on the mesh is $\xi_{\rm max} = \pi$. A straightforward calculation shows that the transform, $\tilde{D}_{\rm KO}$, of $D_{\rm KO}$ has the following action on $\tilde{u}(\xi)$:

$$\tilde{D}_{\rm KO}\tilde{u}(\xi) = \epsilon \sin^4(\frac{\xi}{2})\tilde{u}(\xi) . \tag{2.61}$$

We thus see that $D_{\rm KO}$ acts as a high-pass filter. For high frequency components, where $\xi \to \pi$, $\tilde{D}_{\rm KO}\tilde{u}(\xi) \to \tilde{u}(\xi)$, while for low frequencies, where $\xi \to 0$ we have $\tilde{D}_{\rm KO}\tilde{u}(\xi) \to 0$.

Consider now the simple evolution equation (sometimes known as the advection equation)

$$u_t = au_x , \tag{2.62}$$

where the constant a is the single characteristic speed. We discretize (2.62) using the centred $O(h^2)$ explicit scheme

$$\frac{u_i^{n+1} - u_i^{n-1}}{2\lambda h} = a\frac{u_{i+1}^n - u_{i-1}^n}{2h} . \tag{2.63}$$

Here, as usual, $\lambda \equiv \Delta t/\Delta x \equiv \Delta t/h$. Solving for the most-advanced-time unknowns, u_i^{n+1}, we have

$$u_i^{n+1} = u_i^{n-1} + a\lambda\left(u_{i+1}^n - u_{i-1}^n\right) . \tag{2.64}$$

Now, to add KO dissipation to this scheme we apply $D_{\rm KO}$ to the most retarded values, u_i^{n-1}, and then *subtract* the result from the right hand side of (2.64). This yields

$$u_i^{n+1} = u_i^{n-1} + a\lambda\left(u_{i+1}^n - u_{i-1}^n\right) - \frac{\epsilon}{16}\left(u_{i-2}^{n-1} - 4u_{i-1}^{n-1} + 6u_i^{n-1} - 4u_{i+1}^{n-1} + u_{i+2}^{n-1}\right) , \tag{2.65}$$

The subtraction effectively converts the operation of $D_{\rm KO}$ to a *low-pass* filter on the solution, which is precisely what we want for effective dissipation of high-frequency components.

We note that the addition of KO dissipation does not change the order of accuracy of the difference scheme. To see this, we observe that when written in the form (2.64), where we have multiplied the fundamental form (2.63) by $\Delta t \equiv \lambda h$, the per-step truncation error is now $O(h^3)$. At the same time we have

$$D_{\rm KO} u_i^{n-1} = h^4 (u_{xxxx})_i^{n-1} + O(h^6),$$

and

$$D_{\rm KO} u_i^{n} = h^4 (u_{xxxx})_i^{n} + O(h^5) = O(h^4), \tag{2.66}$$

so (2.65) is an $O(h^2)$ approximation of (2.62) as well.

The application of $D_{\rm KO}$ to the most-retarded time values in (2.65) is motivated from considerations of stability. Depending on the specifics of the difference scheme, it may be possible to effectively apply the operator to other time levels (including more than one level). Additionally, for Crank-Nicholson schemes $D_{\rm KO}$ can often be applied as a filter on the u_i^{n+1} values, once they have been updated from the basic form of the difference equations. This is the approach we have generally used in this thesis.

Finally, the value of the parameter ϵ is typically restricted to the range $0 < \epsilon < 1$, with increasing values of ϵ corresponding to more dissipation. For sufficiently large values of ϵ one can expect the overall scheme to become unstable.

2.3 Newton-Gauss-Seidel Relaxation

As discussed in Sec. 2.1.3, Crank-Nicholson differencing requires the solution of systems of equations to determine advanced time values. If the finite difference mesh has n_g points, and there are n_f grid functions per point, then there are a total of $N = n_g n_f$ unknowns to be determined at each time step. Clearly, the FDA—including differencing of both the interior equations (the PDEs themselves) as well as any boundary conditions—should yield N equations. If the equations of motion are nonlinear, as is the case for the models studied here, then we have the additional complication that the system of algebraic equations to be solved is also nonlinear.

In this thesis, we use the simple but effective technique of one-step point-wise Newton-Gauss-Seidel (NGS) relaxation to solve these nonlinear systems. It is best to first consider the case when $n_f = 1$, so that there is a single grid function. We denote the collection of N advanced time-unknowns by

$$U_I\,, \quad I = 1, 2, \ldots N\,. \tag{2.67}$$

It is then convenient to arrange the U_I into a length-N vector, $\mathbf{U}$

$$\mathbf{U} \equiv [U_1, U_2, \ldots, U_N]\ . \tag{2.68}$$

The equations that need to be solved at each time step can then be written in the form

$$\mathbf{F}\,[\mathbf{U}] = [F_1(U_1, U_2, \ldots, U_N), F_2(U_1, U_2, \ldots, U_N), \ldots F_N(U_1, U_2, \ldots, U_N)] = \mathbf{0} \tag{2.69}$$

The NGS algorithm proceeds as follows. We first note that the procedure is iterative. We start with some initial estimate $\mathbf{U}^{(0)}$ for the advanced-time solution—typically using the values from the previous time step—and then generate a sequence of approximations

$$\mathbf{U}^{(0)} \to \mathbf{U}^{(1)} \to \mathbf{U}^{(2)} \to \ldots \to \mathbf{U}^{(m)} \to \mathbf{U}^{(m+1)} \to \ldots \tag{2.70}$$

until some convergence criteria is achieved. Each relaxation sweep that takes $\mathbf{U}^{(m)}$ to $\mathbf{U}^{(m+1)}$ involves a pass through all of the points in the finite difference mesh. In the current case, since $n_f = 1$, those points can also be labelled by the index I in (2.67), and we will assume that we visit the points in the order $I = 1, 2, \ldots, N$. We now view the I-th component of (2.69) as a *single* nonlinear equation with unknown $U_I^{(m+1)}$ whose value we wish to update. We thus have

$$F_I(U_I^{(m+1)};\ U_1^{(m+1)}, U_2^{(m+1)}, \ldots U_{I-1}^{(m+1)}, U_{I+1}^{(m)}, \ldots, U_N^{(m)}) = 0\,, \tag{2.71}$$

or simply

$$F_I(U_I^{(m+1)}) = 0\,. \tag{2.72}$$

In going from (2.71) to (2.72) we observe that we are considering all of the unknowns other than $U^{(m+1)}$ to be "frozen" as we perform the update. Furthermore the frozen values will correspond

to the current iteration $(m+1)$ for unknowns with indices J, such that $J < I$ and iteration (m) otherwise. (This use of "most recently updated" values is what we mean by Gauss-Seidel iteration.) As the nomenclature suggests, the actual update is now accomplished using the familiar Newton technique. Specifically we have

$$U_I^{(m+1)} = U_I^{(m)} - \delta U_I = U_I^{(m)} - \frac{F_I(U^{(m)})}{J_{II}}\,, \tag{2.73}$$

where the "diagonal Jacobian element", J_{II}, is [15]

$$J_{II} \equiv \left.\frac{\partial F_I}{\partial U_I}\right|_{U_I = U_I^{(m)}}\,. \tag{2.74}$$

Once we have updated U_I via (2.73), we move on to the next unknown U_{I+1}, i.e. we do *not* perform additional Newton steps on the scalar equation (2.73) The restriction of the update to a single Newton step for a single unknown at a single point is what is meant by "one-step point-wise".

The NGS method was originally used for the solution of FDAs of *elliptic* systems, where the convergence of the method—which gets worse as $h \to 0$—is so slow as to render it useless. This is not the case for FDAs of hyperbolic PDEs, where acceptable convergence can usually be achieved in just a few complete sweeps (arguably as few as 2, see [119]), and with the number of sweeps needed independent of h. In the work described subsequently we have typically used 2–5 sweeps.

For the case of multiple grid functions, i.e. when $n_g > 1$, there are two natural ways of extending the scheme. The first is to update each of the grid function values at each grid point separately, with all other values frozen. This means that the Newton step continues to be applied to scalar equations. The second method is to update the n_g function values at each point simultaneously (this is sometimes known as *collective* relaxation). A Newton step for a system of n_g equations is then needed, which in turn requires the evaluation of the $n_g \times n_g$ Jacobian matrix of that system. As discussed in more detail in the subsequent two chapters, this is the approach that we have adopted in our calculations.

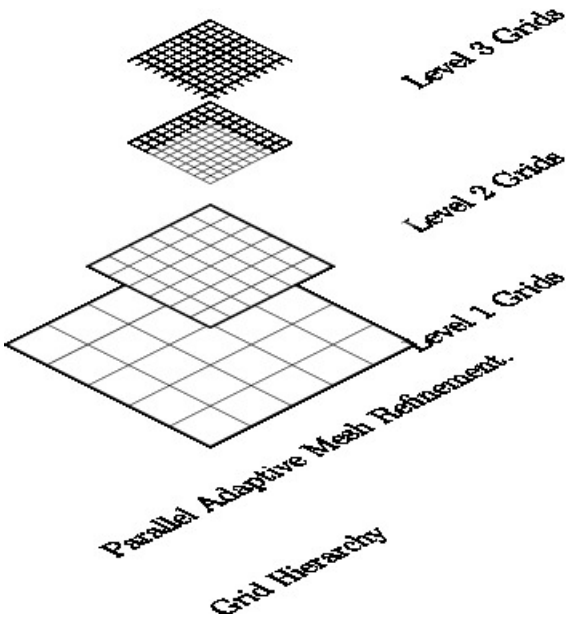

Figure 2.3: A typical grid hierarchy with $L_f = 3$. Child grids are contained inside parent grids, and their boundaries are parallel to each other.

2.4 Adaptive Mesh Refinement

The dynamics of nonlinear field theories often span a wide range of time and space scales. Phenomena in some regions of the computational domain may need a fine grid to be resolved properly, while a coarser spacing may be enough in other areas. Use of a single uniform grid with a meshing sufficiently small to accurately treat the smallest-scale features can then be very inefficient and, particularly for calculations in multiple space dimensions, may in fact be computationally prohibitive. One solution to this problem, which is used in many areas of computational science, is to adopt a single non-uniform grid which is constructed to provide an appropriate (local) mesh spacing throughout the domain. However, for problems such as those considered in this thesis, the regions needing higher (or lower) resolution are not known *a priori* and will generically evolve in tandem with the solution itself.

This last consideration (and others) has prompted the development of methods that are collectively known as adaptive mesh refinement (AMR) techniques. In this work we use a specific AMR methodology due to Berger and Oliger [109] that was designed for the solution of hyperbolic systems, and which has now been coded in one form or another by many researchers and research

[15]The full Jacobian is associated with the system (2.69) and has elements $J_{KL} \equiv \partial F_K / \partial U_L$.

groups.

In particular, Pretorius has implemented a version of the Berger and Oliger algorithm in the form of two C libraries called AMRD (for Adaptive Mesh Refinement Driver) and PAMR (for Parallel Adaptive Mesh Refinement) [120, 121, 107, 108]. These libraries are designed so that a user can incorporate AMR into his/her finite difference calculations in a straightforward fashion, without having to be concerned with most of the details of the AMR algorithm per se. Importantly, the libraries produce code that can be run on massively parallel architectures and, again, the user is freed from the non-trivial task of code parallelization.

We will not discuss the Berger and Oliger algorithm, nor Pretorius' implementation of it, in full detail here. Rather, we will provide a summary of the approach and refer the interested reader to [120, 109, 121, 107, 108] and references therein for more information. We also note that our synopsis closely follows the presentation of [120, 121, 107, 108].

Key features of the Berger and Oliger algorithm include the following;

1. The capability for a (finest) mesh spacing that varies from place to place in the solution domain is achieved through the use of a hierarchy of uniform grids. The hierarchy consists of a pre-specified number, L_f, of levels of discretization, labelled by L, so that $L = 1, 2, \ldots, L_f$. Each level is characterized by a constant mesh spacing, h_L, which satisfies $h_L = h_{L-1}/2$. [16] (See Fig. 2.4 for an example with $L_f = 3$.) $L = 1$ defines the coarsest level of discretization, and at this level there is a *single* uniform grid (called the base grid) that covers the entire domain. At subsequent levels $L = 2, ...L_f$ there may be multiple grids, each of which has boundaries which are aligned with those of the base grid (i.e. non-rotated with respect to the underlying coordinate system). Each grid at level $L = 2$ or higher must be properly contained within a single level $L - 1$ grid. The latter is known as the parent of the former and, conversely, the former is a child of the latter.

2. There are distinct time steps, Δt_L, associated with each level, which also satisfy $\Delta t_L = \Delta t_{L-1}/2$: i.e. refinement is performed in time as well as in space.

3. Evolution of the finite difference solution from one time step to the next is done recursively by level. First, we assume that the solution on all grid levels is defined at the same discrete

[16] By this condition we say that the hierarchy has a "refinement factor of 2". In the original Berger and Oliger work other integer-valued refinement factors were allowed, but Pretorius' implementation makes the restriction to 2.

time. To initiate the stepping cycle, the coarse grid solution ($L = 1$) is first advanced, using the same discrete equations that would be used in a *unigrid* (i.e. non-adaptive) computation. Then a step on all level $L = 2$ grids is performed, again using the fundamental discretized equations of motion, except that for those boundaries that do not coincide with physical boundaries, boundary values are computed via interpolation in the parental grid (the desire to perform interpolation rather than extrapolation motivates taking the coarse grid step first). If there are any $L = 3$ grids the $L = 2$ process is repeated, otherwise an additional $L = 2$ step is taken, which brings $L = 2$ into time-synchronization with $L = 1$. An overall time-cycle is then complete and a new one can begin. It is also important to note that whenever level $L-1$ has been integrated to the same time as level L, level L grid function values are overwritten by child values defined at the same spatial locations.

The process sketched here is easily and naturally extended in recursive fashion for arbitrary L_f and is described in full detail in the references given above.

4. The composition of the hierarchy—i.e. how many levels of discretization are required and where the various grids should be located—is determined dynamically using local truncation error (TRE) estimates as will be described subsequently. These estimates are periodically generated on all levels except $L = L_f$, and then regions requiring refinement are identified, clustered into grids, and a new hierarchy is constructed. For any refined level, $L = 2, \ldots, L_f$, the initialization of grid function values in the new structure will generally involve a combination of copying old values from the same level, and interpolation of level $L - 1$ values. We note that this process will also automatically derefine regions where resolution requirements become less stringent.

Truncation error estimates are computed with a procedure completely analogous to that used in adaptive-step-size ODE integrators. For the purpose of illustration, let L^h be a second order two-level difference operator and $u(t, x)$ the *continuum* solution of the corresponding differential system. Then the *local* (one-step) truncation error, τ, is defined by

$$u(t + \lambda h, x) - L^h u(t, x) = \tau + O(h^3) \tag{2.75}$$

where h is the spatial grid spacing and we have again assumed that the temporal spacing satisfies

$\Delta t = \lambda h$ with λ constant as $h \to 0$. If we evolve another time step we have

$$u(t + 2\lambda h, x) - [L^h]^2 u(t, x) = 2\tau + O(h^3) \tag{2.76}$$

We now consider a 2:1 coarsening of the finite difference grid, and use the corresponding difference operator, L^{2h}, defined on that grid, to advance the solution. We find

$$u(t + 2\lambda h, x) - L^{2h} u(t, x) = 2^{2+1}\tau + O(h^3) = 8\tau + O(h^3) \tag{2.77}$$

Subtracting (2.77) from (2.76) and manipulating, we obtain the following estimate for τ

$$\tau \approx \frac{[L^h]^2 u(t, x) - L^{2h} u(t, x))}{6} \tag{2.78}$$

Provided that we can Richardson-expand the finite difference approximation, u^h, as

$$u^h(t, x) = u(t, x) + h^2 e_2(t, x) + \ldots \tag{2.79}$$

(see Sec. 2.1.1), then it easy to argue that, to the same order of approximation, we can replace $u(t, x)$ with u^h in (2.78). Pretorius' implementation uses a minor modification of this procedure which is especially straightforward to code within the context of the overall Berger and Oliger algorithm. His approach does, however, require that the entire domain be covered by a single $L = 2$ grid (in addition to the base $L = 1$ grid) whenever $L_f > 2$.

The overall placement of grids is controlled by a single parameter, the truncation error threshold, $\tau_{\max}$, which is user-adjustable. Regions where the estimated τ exceeds $\tau_{\max}$ will be covered with finer grids, whereas areas where τ is below the threshold will experience derefinement. For cases such as ours where there are multiple grid functions, the overall truncation error estimate is some function, such as the ℓ_2 norm, of the individual estimates.

In addition to $\tau_{\max}$ and L_f, there are a number of additional parameters which control an AMR calculation. Among these are

1. n_{regrid}, which specifies the frequency of regridding,

2. w_{buffer}, which gives the number of grid points along any and all coordinate directions that a region flagged as having high truncation error is extended prior to the recomposition of the

grid hierarchy.

We will discuss the significance of these parameters in more detail in Sec. 3.6, which describes some specific AMR computations.

We again note that the AMRD/PAMR infrastructure provides for parallel execution and we have used this facility extensively in the calculations described below (we typically run on 64-128 cores). Since we used this feature strictly in a black-box capacity we will not discuss it here: details are provided in [107, 108].

The use of Berger and Oliger AMR is not without cost. There is some computational overhead associated with the (re-)construction of the grid hierarchy, as well as with the various inter-level operations. More seriously, the finite difference solutions tend to systematically develop unphysical high frequency components at those locations where grid function values are interpolated in parental meshes [121]. The use of dissipation can help in this regard, but treatment of this problem remains an active research topic.

If we assume the execution time on any mesh to be proportional to the number of grid points it contains, then the expected speedup of an AMR run can be estimated by comparing the total number of points on all levels $L = 1...L_f$ of our hierarchy with the number of points for a uniform grid with resolution at level L_f. Clearly, significant speedup is only achieved when the filling factors of fine grids shrink sufficiently rapidly that the finest-level grids do not occupy a large part of the computational domain.

CHAPTER 3

RELATIVISTIC SCATTERING OF Q-BALLS IN $2+1$ DIMENSIONS

3.1 Introduction

In this chapter we describe our implementation of a code to perform numerical experiments of the scattering of Q-ball solutions in $2+1$ dimensions. The objective is to use the relatively simple model of a complex scalar field with a quartic potential to develop an infrastructure to study highly boosted matter collisions in more complicated theories. In particular, the latter include the Skyrme models which are discussed in the next two chapters. Following an introduction to Q-balls, Sec. 3.3 presents a derivation of the dynamical equations of motion for a complex scalar field, as well as the specific implementation of the numerical methods—described in the previous chapter—that we use to approximately solve them. We then discuss the generation of suitable initial data for stationary and boosted Q-balls (Sec. 3.3.4 and 3.3.3). Code validation strategies—including convergence testing, consistency checks and monitoring of conserved quantities—are developed in Sec. 3.4. Secs. 3.5–3.7 detail the results of our investigations of head-on Q-ball collisions, and interactions between Q-balls and potential obstructions. Finally, Sec. 3.8 concludes the chapter with a summary of our experiences.

3.2 Planar Q-balls

Let us begin by considering the general features of Q-balls in 2 spatial dimensions, following [78, 79, 80, 18]. The model is described by the $U(1)$ invariant Lagrangian density

$$\mathcal{L} = \partial_\mu \phi \partial^\mu \phi^* - U(|\phi|^2)\,. \tag{3.1}$$

The complex scalar field possesses a conserved Nöether current, a consequence of the symmetry under the transformation $\phi \to \phi e^{i\alpha}$,

$$J^\mu = \frac{1}{2i}(\phi^* \partial^\mu \phi - \phi \partial^\mu \phi^*)\,, \tag{3.2}$$

with a corresponding conserved charge, Q, for any configuration of ϕ given by

$$Q = \int d^2x \;\; J^0 = \frac{1}{2i}\int d^2x \;\; (\phi^* \partial^0 \phi - \phi \partial^0 \phi^*)\,. \tag{3.3}$$

The energy, E, (which is also conserved) is defined by

$$E = \int d^2x \;\; \left[\frac{1}{2}|\dot{\phi}|^2 + \frac{1}{2}|\nabla\phi|^2 + U(|\phi|^2)\right], \tag{3.4}$$

where we have adopted the notation $\dot{\phi} \equiv \partial_t \phi$ for time differentiation. As discussed in more detail in B.2, one can argue for the existence of Q-ball solutions—i.e. stable, stationary, localized "solitons"—through energetic arguments in which the energy is minimized subject to a constraint derived from the expression (3.3) for the conserved charge, Q. The constraint is incorporated in the Lagrangian using a Lagrange multiplier, and the energy minimization is performed at fixed charge. Heuristically, if the energetic balance favours the creation of a Q-ball instead of a more-or-less freely propagating configuration (in other words, if $E < mQ$, where m is the mass parameter for the field), then we expect the resulting soliton to be stable.

When Q-balls are considered in the context of particle physics (i.e. in quantum field theory), the particulars of the potential are often dictated by renormalization considerations [69]. Since we are only considering classical dynamics, and since we are not attempting to perform a study of Q-balls that is comprehensive in any way, we adopt a specific potential form for which Q-balls are known to exist [18, 78, 81]. Specifically, we take

$$U(\phi^2) = \frac{1}{2}m^2|\phi|^2 - \frac{1}{3}\alpha|\phi|^3 + \frac{1}{4}\beta|\phi|^4\,, \tag{3.5}$$

where m, α and β are positive real-valued parameters. Without loss of generality we can perform the rescalings $\phi \to \phi/\alpha$ and $x \to mx$. Doing this, and then substituting (3.5) in (3.1), we have

$$\mathcal{L} = \frac{1}{2}\partial_\mu\phi^*\partial^\mu\phi - \frac{1}{2}|\phi|^2 + \frac{1}{3}A|\phi|^3 - \frac{1}{4}B|\phi|^4\,. \tag{3.6}$$

The (rescaled) values, A and B, can now be viewed as dimensionless control parameters for the theory. In particular, the specific values of A and B that are chosen can ultimately determine if Q-ball solutions exist or not, and will also have an impact on the overall dynamical behaviour of the model. Again, since our principal goal here is to gain experience with nonlinear theories admitting solitons, we have made no attempt to make any survey of the phenomenology as a function of A and/or B. Rather, for our numerical experimentation, and following [18], we will set $A = 1$ and $B = 0.5$. The reader should also note that in the formal development that follows, we will tend to drop explicit mention of A (since it has been set to unity), but will not do so for B.

With $A = 1$, the equation of motion obtained by varying the Lagrangian density (3.6) (see B.1) is

$$\ddot{\phi} - \nabla^2\phi + \phi - |\phi|\phi + B|\phi|^2\phi = 0\,, \tag{3.7}$$

where we again emphasize that an overdot denotes differentiation with respect to time.

Derrick's theorem (Sec. D.1 and [122]) provides some insight into necessary conditions that a field theory must satisfy in order for it to admit stable, time-independent solutions: in general these conditions depend on both the spatial dimensionality, D, of the theory, and the specific field content. For the current case, where $D = 2$, and the matter is a single complex scalar field with a polynomial potential, the theorem implies that there can be *no* stable, *static* solutions. On the other hand, the theorem does *not* exclude *stationary* configurations, i.e. solutions with "internal" dynamics, but where, for example, the energy distribution is static. Motivated by this observation, and by fact that ϕ is complex, we seek circularly-symmetric stationary solutions of the form

$$\phi(r,t) = \sigma(r)\ \ e^{i\omega t}\,, \tag{3.8}$$

where $r \equiv \sqrt{x^2+y^2}$ and $\sigma(r)$, which is real and strictly positive, will be referred to as the *profile function*. The conserved charge then becomes

$$Q = 2\pi\omega \int_0^{+\infty} r\ dr\ \ \sigma(r)^2\,. \tag{3.9}$$

Substitution of (3.8) into the equation of motion (3.7) yields

$$\nabla^2\sigma(r) + (\omega^2 - 1)\sigma(r) + A\sigma^2(r) - B\sigma^3(r) = 0\,, \tag{3.10}$$

or

$$\frac{d^2\sigma(r)}{dr^2} + \frac{1}{r}\frac{d\sigma(r)}{dr} + \sigma(r)(\omega^2 - 1) + A\sigma^2(r) - B\sigma^3(r) = 0\,. \tag{3.11}$$

(3.11) is to be viewed as an eigenvalue problem. For any given central value, $\sigma_0 \equiv \sigma(0)$, of the profile function, a solution satisfying the appropriate boundary conditions—specified below—will only exist for specific values of $\omega \equiv \omega(\sigma_0)$.

As with other eigenvalue problems of this type we in fact expect a countable infinity of solutions that it this case can be labelled conveniently by the number of times that the profile function crosses the $\sigma = 0$ axis. In our studies we will restrict attention to the case where there are no such crossings, or what one might view as "ground state" profile functions.

3.2.1 Solution of the Q-ball ODE

We first introduce an auxiliary variable, $u(r) \equiv d\sigma/dr$, and recast (3.11) in the form:

$$\begin{aligned} \frac{d\sigma}{dr} &= u\,, \\ \frac{du}{dr} &= -\frac{1}{r}u - \sigma(r)(\omega^2 - 1) - A\sigma^2(r) + B\sigma^3(r)\,. \end{aligned} \tag{3.12}$$

As just discussed, (3.12) is to be viewed as a boundary-eigenvalue problem. The boundary conditions are

$$\frac{d\sigma}{dr}(0) \equiv u(0) = 0, \tag{3.13}$$

which is required for regularity at the origin, and

$$\lim_{r\to\infty} \sigma(r) = 0\,, \tag{3.14}$$

which is needed for the total energy of the Q-ball to be finite.[17] Solution of the ODE system (3.12), subject to the boundary conditions (3.13) and (3.14), is achieved by treating the system as an initial

[17] More properly, we need to demand that $\sigma(r)$ decays sufficiently rapidly as $r \to \infty$ to maintain finite energy. However, the configurations that are found with the simple condition $\lim_{r\to\infty}\sigma(r) = 0$ satisfy this requirement.

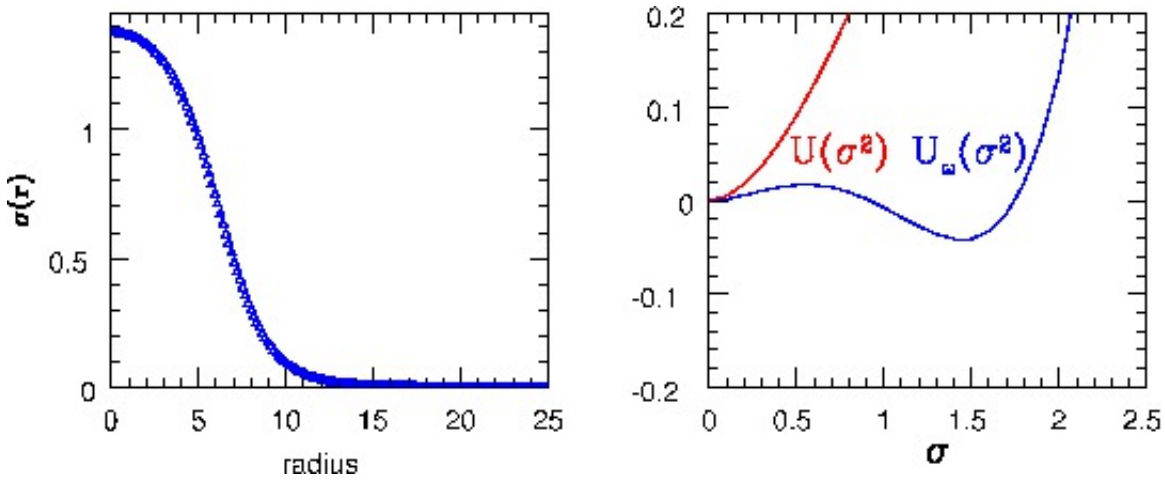

Figure 3.1: This figure displays a typical Q-ball radial profile function, $\sigma(r)$ (left), and the associated bare and effective potentials, $U(\sigma^2)$ and $U_\omega(\sigma^2)$, (right), respectively. (See App. B.2) for a discussion of the effective potential interpretation of Q-ball solutions.) As discussed in the text, $\sigma(r)$ is computed using a shooting technique. Here, with $\sigma_0 = 1.375$, $A = 1$ and $B = 0.5$, we find $\omega \approx 0.7739293$. We note that the plots are actually comprised of subsets of discrete collections of points, r_p, $p = 1, \ldots, N$, where N is of the order of 1300, $r_1 = 0$ and $r_N \equiv r_{\max} \approx 300$ (i.e. only a small portion of the radial integration domain is shown here). The LSODA error tolerance is of the order of 1.0×10^{-9} which guarantees that the error in the profile function $\sigma(r)$ is much smaller than the error of the evolved finite difference solutions that we subsequently generate. Note the rapid falloff of $\sigma(r)$ once $r \gtrsim 15$. This is typical of Q-ball configurations for this potential and justifies the view of Q-balls as "solitonic" (particle-like) entities.

value problem, and using shooting. Specifically, the initial values are $\sigma(0) = \sigma_0$ and $u(0) = 0$. Then, for given σ_0, ω is iteratively adjusted until (3.14) is satisfied. Also implicit in this process is the requirement that $\sigma(r)$ have no zero-crossings. We also note that to compute the central value of du/dr, we apply L'Hopital's rule to the first term of (3.12) which yields

$$\frac{d^2\sigma}{dr^2}(0) = \frac{du}{dr}(0) = \frac{1}{2}\left((\omega^2 - 1)\sigma_0 - \sigma_0^2 + B\sigma_0^3\right) . \tag{3.15}$$

Our shooting technique is a standard one [123, 124]. For any given σ_0, successive estimates, $\tilde{\omega}$, of the desired eigenvalue $\omega = \omega(\sigma_0)$ are generated, based on the observation that depending on whether $\tilde{\omega} < \omega$ or $\tilde{\omega} > \omega$, the behaviour of $\sigma(r)$ as we integrate to large r will tend to be distinct. On one hand, we find that σ diverges to $\pm\infty$, while on the other σ becomes oscillatory. Starting from an initial bracket $[\omega_-, \omega_+]$, such that $\omega_- < \omega < \omega_+$—and which is generally easy to locate through experimentation—we can then use a bisection search [124] to successively narrow the bracket until the eigenvalue $\omega \approx \tilde{\omega}$ has been computed to some specified tolerance. Depending

σ_0	ω
0.05	0.9896261
0.2	0.9593800
0.5	0.9033547
1.0	0.8250378
1.3	0.7858791
1.35	0.7785407
1.375	0.7739293

Table 3.1: This table lists selected central values, σ_0, of the Q-ball profile function, along with the associated eigenvalues, $\omega(\sigma_0)$, computed using the shooting method described in the text.

on the values of the parameters σ_0, A and B, and the desired maximum radius of integration $r_{\max}$, it may not always be possible to determine $\tilde{\omega}$ (even by iterating to machine precision) which satisfies $\lim_{r\to r_{\max}} \sigma(r) = 0$. In such cases it is straightforward to truncate $\sigma(r)$ at some relatively large distance, and then fit to an exponentially decreasing tail function. The integration of the ODEs is performed by the LSODA routine, one of several robust solvers contained in the ODEPACK package [125] of Fortran-callable procedures.

Table 3.1 enumerates a number of (σ_0, ω) pairs that were computed using our shooting algorithm, and a typical profile function $\sigma(r)$ (along with the potential $V(|\phi|)$) is shown in Fig. 3.1. To summarize, for a specific potential (which in our case is fixed by the specification of the constants A and B), we can compute an entire family of (ground state) Q-balls, which are characterized (labelled) by σ_0, and which have corresponding eigenfrequencies, $\omega = \omega(\sigma_0)$.

3.3 Equations of Motion

We now return to the time-dependent equation of motion (3.7),

$$\ddot{\phi} - \nabla^2\phi + \phi - |\phi|\phi + B|\phi|^2\phi = 0\,, \tag{3.16}$$

where an overdot again denotes differentiation with respect to time. For the purposes of our numerical treatment of the model, it is convenient to express ϕ in terms of its real and imaginary components, ϕ_1 and ϕ_2, respectively, each of which is to be viewed as an independent real-valued dynamical field. Thus, restricting attention to the $2+1$ case, and adopting the usual Cartesian

coordinates (t, x, y) we set

$$\phi(t, x, y) \equiv \phi_1(t, x, y) + i\phi_2(t, x, y)\,, \tag{3.17}$$

with the modulus, $|\phi|$, of the field given by

$$|\phi| = \sqrt{\phi_1^2 + \phi_2^2}\,. \tag{3.18}$$

With the above definitions, we can take the real and imaginary parts of (3.16) to derive the evolution equations for ϕ_1 and ϕ_2:

$$\ddot{\phi}_1 - \nabla^2\phi_1 + \phi_1 - |\phi|\phi_1 + B|\phi|^2\phi_1 = 0\,, \tag{3.19}$$

$$\ddot{\phi}_2 - \nabla^2\phi_2 + \phi_2 - |\phi|\phi_2 + B|\phi|^2\phi_2 = 0\,. \tag{3.20}$$

We intend to use a two time-level Crank-Nicholson scheme for the finite difference treatment of the above equations. In order to eliminate the second order time derivatives (which would require a minimum of three discrete time levels) we introduce auxiliary fields π_1 and π_2, defined by

$$\pi_a(t, x, y) = \frac{\partial\phi_a}{\partial t}, \qquad a = 1, 2\,. \tag{3.21}$$

Using these definitions, the equation of motion for the scalar field can be written as the following system of 4 first-order-in-time evolution equations:

$$\begin{aligned}
\frac{\partial\phi_1}{\partial t} &= \pi_1 \qquad\qquad \frac{\partial\phi_2}{\partial t} = \pi_2 \\
\frac{\partial\pi_1}{\partial t} &- \frac{\partial^2\phi_1}{\partial x^2} - \frac{\partial^2\phi_1}{\partial y^2} + \phi_1 - |\phi|\phi_1 + B|\phi|^2\phi_1 = 0 \\
\frac{\partial\pi_2}{\partial t} &- \frac{\partial^2\phi_2}{\partial x^2} - \frac{\partial^2\phi_2}{\partial y^2} + \phi_2 - |\phi|\phi_2 + B|\phi|^2\phi_2 = 0\,.
\end{aligned} \tag{3.22}$$

These equations must be supplemented with appropriate boundary values and initial conditions. The former are discussed in App. E, the latter in Sec. 3.3.3 below.

ϕ	$\frac{\phi_{ij}^{n+1}+\phi_{ij}^{n}}{2}$
ϕ_t	$\frac{\phi_{ij}^{n+1}-\phi_{ij}^{n}}{\Delta t}$
ϕ_{xx}	$\frac{1}{2}\left[\frac{\phi_{i+1,j}^{n+1}-2\phi_{i,j}^{n+1}+\phi_{i-1,j}^{n+1}}{\Delta x^2}+\frac{\phi_{i+1,j}^{n}-2\phi_{i,j}^{n}+\phi_{i-1,j}^{n}}{\Delta x^2}\right]$

Table 3.2: Crank-Nicholson (CN) two-(space) dimensional finite difference stencils used to convert the differential equations to difference equations for any of the four dynamical variables ϕ_a or π_a, $a = 1, 2$. Here we use the notation $\phi_{ij}^n \equiv \phi_{i,j}^n \equiv \phi(t^n, x_i, y_j)$. We remind the reader that we use (component) finite difference grids that are characterized by a single discretization scale, h, so that $\Delta x = \Delta y = h$, and $\Delta t = \lambda h$, where λ is the Courant number. Each of the above expressions is a second order ($O(h^2)$) approximation to its continuum counterpart, and is centred at $(t^{n+1/2}, x_i, y_j)$.

3.3.1 Finite Difference Approach

We proceed to discretize the equations of motion (3.23) using a second order, Crank-Nicholson finite difference scheme. As described in the previous chapter, we use finite difference grids which are characterized by a single discrete scale, h, so that $\Delta x = \Delta y = h$, and $\Delta t = \lambda h$, where λ is the Courant number.[18]

Using the finite difference stencils summarized in Table 3.2 and adopting the notation $\phi^n(i, j) \equiv \phi(t^n, x_i, y_j)$ for grid functions, we can express the difference approximations of (3.23) in residual form. For the ϕ fields we have

$$\begin{aligned} \phi_1^{\rm res}(i,j) &\equiv \tfrac{\pi_1^{n+1}(i,j)+\pi_1^{n}(i,j)}{2} - \tfrac{\phi_1^{n+1}(i,j)-\phi_1^{n}(i,j)}{\Delta t}\,, \\ \phi_2^{\rm res}(i,j) &\equiv \tfrac{\pi_2^{n+1}(i,j)+\pi_2^{n}(i,j)}{2} - \tfrac{\phi_2^{n+1}(i,j)-\phi_2^{n}(i,j)}{\Delta t}\,, \end{aligned} \tag{3.23}$$

[18] As discussed in Chap.2, when we use adaptive mesh refinement (AMR) each of the component grids in the grid hierarchy satisfies these conditions for some h_L, where L labels the level of the grid in the hierarchy and $h_L = h_{L-1}/2$.

and for the π fields,

$$\begin{aligned}
\pi_1^{\rm res}(i,j) \quad &\equiv \tfrac{\pi_1^{n+1}(i,j)-\pi_1^n(i,j)}{\Delta t} \\
&- \quad \frac{1}{2}\left[\frac{\phi_1^{n+1}(i+1,j)-2\phi_1^{n+1}(i,j)+\phi_1^{n+1}(i-1,j)}{\Delta x^2}\right] \\
&- \quad \frac{1}{2}\left[\frac{\phi_1^{n}(i+1,j)-2\phi_1^{n}(i,j)+\phi_1^{n}(i-1,j)}{\Delta x^2}\right] \\
&- \quad \frac{1}{2}\left[\frac{\phi_1^{n+1}(i,j+1)-2\phi_1^{n+1}(i,j)+\phi_1^{n+1}(i,j-1)}{\Delta y^2}\right] \\
&- \quad \frac{1}{2}\left[\frac{\phi_1^{n}(i,j+1)-2\phi_1^{n}(i,j)+\phi_1^{n}(i,j-1)}{\Delta y^2}\right] \\
&+ \quad \phi_1^n(i,j) - |\phi^n(i,j)|\phi_1^n(i,j) + B|\phi^n(i,j)|^2\phi_1^n(i,j)\,, \qquad (3.24)
\end{aligned}$$

$$\begin{aligned}
\pi_2^{\rm res}(i,j) \quad &\equiv \tfrac{\pi_2^{n+1}(i,j)-\pi_2^n(i,j)}{\Delta t} \\
&- \quad \frac{1}{2}\left[\frac{\phi_2^{n+1}(i+1,j)-2\phi_2^{n+1}(i,j)+\phi_2^{n+1}(i-1,j)}{\Delta x^2}\right] \\
&- \quad \frac{1}{2}\left[\frac{\phi_2^{n}(i+1,j)-2\phi_2^{n}(i,j)+\phi_2^{n}(i-1,j)}{\Delta x^2}\right] \\
&- \quad \frac{1}{2}\left[\frac{\phi_2^{n+1}(i,j+1)-2\phi_2^{n+1}(i,j)+\phi_2^{n+1}(i,j-1)}{\Delta y^2}\right] \\
&- \quad \frac{1}{2}\left[\frac{\phi_2^{n}(i,j+1)-2\phi_2^{n}(i,j)+\phi_2^{n}(i,j-1)}{\Delta y^2}\right] \\
&+ \quad \phi_2^n(i,j) - |\phi^n(i,j)|\phi_2^n(i,j) + B|\phi^n(i,j)|^2\phi_2^n(i,j)\,. \qquad (3.25)
\end{aligned}$$

We emphasize that the process of computing a solution to the discrete equations is equivalent to driving all of the residual quantities defined above to 0. We also note that each of the above finite difference equations is naturally associated with the grid point (x_i, y_j).

As also discussed in Chap. 2, we solve the discrete equations using a point-wise Newton-Gauss-Seidel scheme. This means that we sweep through the mesh, visiting each grid point $(x_i, y_j) \equiv (i, j)$ in turn, and updating the four grid function values associated with that point by taking a single Newton step applied to the 4 nonlinear equations defined by (3.23-3.25). We observe that the difference equations couple values defined at (i, j) to the nearest neighbours $(i + 1, j)$, $(i - 1, j)$, $(i, j + 1)$ and $(i, j - 1)$. The Gauss-Seidel nomenclature refers to the fact that in our point-wise

updates we always use the most recently computed (updated) values of those neighbour values in the Newton step. This process is schematically illustrated in Fig. 3.3. Black points have already been updated, while white points still hold "old" values for the grid functions. The points at the physical boundaries (red) are updated according to the boundary condition selected (see App. E).

The Newton step to simultaneously (collectively) update the 4 unknowns defined at (i, j) requires the construction of the 4×4 Jacobian matrix. The elements of this matrix are defined by

$$\begin{aligned}
J_{11} &= \frac{\partial \phi_1^{\text{res}}}{\partial \phi_1} \quad J_{12} = \frac{\partial \phi_1^{\text{res}}}{\partial \phi_2} \quad J_{13} = \frac{\partial \phi_1^{\text{res}}}{\partial \pi_1} \quad J_{14} = \frac{\partial \phi_1^{\text{res}}}{\partial \pi_2} \\
J_{21} &= \frac{\partial \phi_2^{\text{res}}}{\partial \phi_1} \quad J_{22} = \frac{\partial \phi_2^{\text{res}}}{\partial \phi_2} \quad J_{23} = \frac{\partial \phi_2^{\text{res}}}{\partial \pi_1} \quad J_{24} = \frac{\partial \phi_2^{\text{res}}}{\partial \pi_2} \\
J_{31} &= \frac{\partial \pi_1^{\text{res}}}{\partial \phi_1} \quad J_{32} = \frac{\partial \pi_1^{\text{res}}}{\partial \phi_2} \quad J_{33} = \frac{\partial \pi_1^{\text{res}}}{\partial \pi_1} \quad J_{34} = \frac{\partial \pi_1^{\text{res}}}{\partial \pi_2} \\
J_{41} &= \frac{\partial \pi_2^{\text{res}}}{\partial \phi_1} \quad J_{42} = \frac{\partial \pi_2^{\text{res}}}{\partial \phi_2} \quad J_{43} = \frac{\partial \pi_2^{\text{res}}}{\partial \pi_1} \quad J_{44} = \frac{\partial \pi_2^{\text{res}}}{\partial \pi_2}
\end{aligned} \tag{3.26}$$

where we have suppressed the (i, j) indexing, noting that all quantities in the above are evaluated at the point (i, j). We then solve the linear system

$$\begin{pmatrix} J_{11} & J_{12} & J_{13} & J_{14} \\ J_{21} & J_{22} & J_{23} & J_{24} \\ J_{31} & J_{32} & J_{33} & J_{34} \\ J_{41} & J_{42} & J_{43} & J_{44} \end{pmatrix} \begin{pmatrix} \delta\phi_1(i,j) \\ \delta\phi_2(i,j) \\ \delta\pi_1(i,j) \\ \delta\pi_2(i,j) \end{pmatrix} = \begin{pmatrix} \phi_1^{\text{res}}(i,j) \\ \phi_2^{\text{res}}(i,j) \\ \pi_1^{\text{res}}(i,j) \\ \pi_2^{\text{res}}(i,j) \end{pmatrix} \tag{3.27}$$

using the direct solver `DGESV` from the LAPACK package [126] to obtain the corrections $\delta\phi$ and $\delta\pi$. Using the corrections, the unknowns are updated via

$$\begin{pmatrix} \phi_1(i,j) \\ \phi_2(i,j) \\ \pi_1(i,j) \\ \pi_2(i,j) \end{pmatrix} := \begin{pmatrix} \phi_1(i,j) \\ \phi_2(i,j) \\ \pi_1(i,j) \\ \pi_2(i,j) \end{pmatrix} - \begin{pmatrix} \delta\phi_1(i,j) \\ \delta\phi_2(i,j) \\ \delta\pi_1(i,j) \\ \delta\pi_2(i,j) \end{pmatrix} \tag{3.28}$$

When our code that implements this solution process is run in parallel, each processor updates its designated portion of the finite difference grid (or grids when adaptive mesh refinement is also used), and then a *global* l_2 norm (see 2.31) of the residuals through the entire computational domain

is calculated. If this norm is larger than the specified convergence criteria, another Newton-Gauss-Seidel sweep is performed. Once convergence is achieved we advance the discrete time from t^n to t^{n+1}. A pseudo-code version of the full time-stepping algorithm is given in Figure 3.2.

3.3.2 Implementation Strategy

As a first step, a prototype serial unigrid (i.e. non-parallel, non-adaptive) code was developed using RNPL (Rapid Numerical Prototyping Language [127]). Since the continuum and finite difference equations are relatively simple, RNPL can handle the full generation of residual-evaluating and update routines routines automatically, and thus a minimum of coding is required.[19] This prototype runs as a single computer process (again, with no parallelization) and it established the feasibility of the approach.

Our parallel, adaptive production code still uses RNPL, but the core driver is written using the AMRD (Adaptive Mesh Refinement Driver) / PAMR (Parallel Adaptive Mesh Refinement) infrastructure [120, 107, 108] that was mentioned briefly in Chap. 2. These packages constitute a set of routines layered on top of the Message Passing Interface (MPI) library, which itself provides low-level parallel functionality. AMRD/PAMR is designed so that a user is shielded from most of the details of both the parallelization and adaptive-mesh capabilities of a finite difference code. The key user input comes in the form of various hook functions which perform operations such as evaluating the finite difference residuals or effecting an update sweep to (ultimately) advance the solution from one discrete time to the next. Our main driver (written in C) uses the supplied AMRD/PAMR routines, but also incorporates a few specific MPI calls for miscellaneous tasks, such as gathering contributions to conserved quantities from each parallel sub-domain (each processor).

We also note that we developed our own software infrastructure that was designed to tackle more complicated problems than the relatively simple equations governing a complex scalar field in $2+1$ dimensions. For example, the continuum equations of motion are derived using a Maple [128] script, as well as a Maple-based tensor-manipulation package, TensorV6 [129]. Maple is also used to replace the continuum derivatives with finite difference expressions, as well as to generate the corresponding residuals and Jacobian matrix. These last quantities are converted to Fortran 77 using the *codegen* and *CodeGeneration* Maple functions. The initialization routines are generated using RNPL, while the evolution routines are typically written directly in Fortran 77.

[19] It should be noted, however, that RNPL does not implement collective relaxation—rather single Newton-step -Gauss-Seidel updates are applied pointwise, and to each *individual* (scalar) equation at every point in turn.

1: **for** $t^n = \Delta t, 2\Delta t, \ldots$ **do**
2: **for** $i = 1$ to Nx **do**
3: **for** $j = 1$ to Ny **do**
4: Set initial estimate for the solution vector $\boldsymbol{\phi_b^{(0)}} \equiv [\phi_1^{(0)}, \phi_2^{(0)}, \pi_1^{(0)}, \pi_2^{(0)}]^T$
5: Calculate the 4×4 Jacobian matrix $\boldsymbol{J_{ab}}$ and the residual vector $\boldsymbol{B_a}$ at this point using nearest neighbour values (some new, some old)
6: Solve $\boldsymbol{J_{ab}\, \delta_b \phi = B_a}$ for the update $\boldsymbol{\delta_b \phi} = [\delta\phi_1^{(0)}, \delta\phi_2^{(0)}, \delta\pi_1^{(0)}, \delta\pi_2^{(0)}]^T$ using `DGESV` and obtain a new estimate $\boldsymbol{\phi}_b^{\rm new} = \boldsymbol{\phi}_b^{(0)} - \boldsymbol{\delta_b \phi}$
7: **end for**
8: **end for**
9: Calculate the l_2 norm of the residuals using the new guess $\boldsymbol{\phi_b^{\rm new}}$ (This is a global norm for all subdomains used by the parallel infrastructure)
10: **if** l_2 norm of the residuals $<$ tolerance **then**
11: Convergence achieved
12: Goto 17
13: **else**
14: $\boldsymbol{\phi}_b^{(0)} = \boldsymbol{\phi}_b^{\rm new}$
15: Goto 2
16: **end if**
17: **end for**

Figure 3.2: Time stepping algorithm for Q-ball evolution

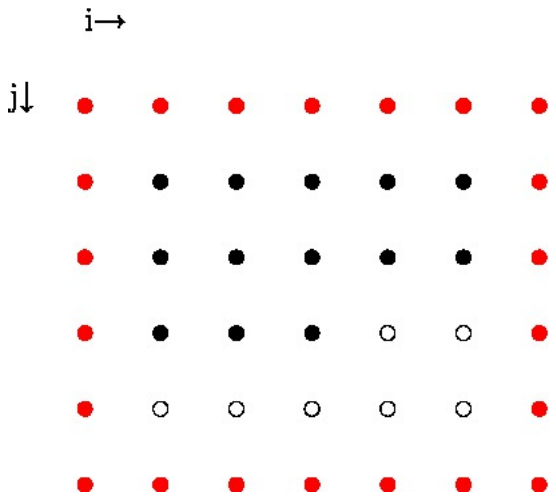

Figure 3.3: Gauss-Seidel update of the two dimensional finite difference mesh. The update proceeds from left to right and top to bottom. Grid function values are coupled to their nearest neighbours, which include points already updated during the sweep (black) and points with old values (white). The points at the physical boundaries (red) are updated according to the boundary condition selected (see App. E).

This strategy of using symbolic computing and script-based automation for code generation provides us with a high degree of confidence in the correctness of our residual and Jacobian elements, while minimizing both the overall amount of coding required as well as the number of implementation errors. We stress that since the tools we have developed have very few "hard-wired" components, the infrastructure is not restricted in any way to the problem currently under consideration. In particular, our tools can be readily used to solve other hyperbolic problems in a relatively straightforward fashion, and with a high degree of confidence. Again, the core of any specific implementation is a main driver that is written in C, and which incorporates all of the numerical subroutines—typically produced using Maple or RNPL, but also possibly coded by hand.

3.3.3 Interpolation and Translation of Q-ball Data

In order to evolve Q-ball initial data, we must set corresponding values for $\phi_a^0(i,j)$ and $\pi_a^0(i,j)$, $a = 1, 2$. We remind the reader that our finite difference domain is comprised of $N_x \times N_y$ grid points and that (i,j) denotes the point with coordinates (x_i, y_j). For the case when the Q-ball is at rest in the (t,x,y) coordinate system, this process is very easy to accomplish using interpolation. We first specify a location (x_c, y_c) at which we wish to center the Q-ball, and which need not coincide with a grid point. For each (i,j) pair we compute the distance, $r_{ij} = \sqrt{(x_i - x_c)^2 + (y_j - y_c)^2}$, of the grid point from the Q-ball center. We then use a polynomial interpolation routine that implements Neville's algorithm [124] to compute $\sigma(i,j)$ from the σ_p values. The routine allows the order of the interpolation to be adjusted, and through trial and error we determined fifth order to be adequate.

Once the values $\sigma(i,j)$ are in hand, we can initialize the dynamical fields. For a single Q ball at rest, we can assume without loss of generality that the scalar field is purely real at the initial

```
1: for  i = 1 to N_x do
2:    for  j = 1 to N_y do
3:       Calculate interpolation radius r_ij = sqrt((x_i - x_c)^2 - (y_j - y_c)^2)
4:       Interpolation routine computes the value σ(r_ij) = σ(i,j)
5:    end for
6: end for
```

Figure 3.4: Interpolation and translation of the Q-ball soliton to (x_c, y_c).

time. For the ϕ_a we thus have

$$\phi_1^0(i,j) = \sigma(i,j)\,, \tag{3.29}$$

$$\phi_2^0(i,j) = 0\,. \tag{3.30}$$

For the π_a we have (recalling the ansatz (3.8))

$$\pi_1^0 = 0\,, \tag{3.31}$$

$$\pi_2^0 = \omega \cdot \sigma(i,j)\,. \tag{3.32}$$

3.3.4 Boosted Initial Data

To provide a Q-ball with some velocity at $t = 0$, we apply a Lorentz transformation (or Lorentz boost) in the x direction. In Cartesian coordinates this transformation takes the form

$$t' = \gamma(t + vx) \quad x' = \gamma(x + vt) \quad y' = y \tag{3.33}$$

and their inverse transformations,

$$t = \gamma(t' - vx') \quad x = \gamma(x' - vt') \quad y = y' \tag{3.34}$$

where γ is the *boost factor*, and which is a key control parameter in most of the computations described in the thesis. Primed and unprimed quantities correspond to the rest and laboratory frames, respectively, and we continue to work in units where $c = 1$. In the rest frame the complex field is (again from the Q-ball ansatz (3.8))

$$\phi'(t', x', y') = \sigma(x', y') \exp(i\omega t') = \phi_1' + i\phi_2'\,, \tag{3.35}$$

The real and imaginary components of ϕ', in the rest frame, are thus given by

$$\phi_1'(t', x', y') = \sigma(x', y') \cos\omega t' \qquad \phi_2'(t', x', y') = \sigma(x', y') \sin(\omega t'), \tag{3.36}$$

and their time derivatives π',

$$\pi_1'(t',x',y') = \frac{\partial \phi_1'}{\partial t'} = -\omega\phi_2' \qquad \pi_2'(t',x',y') = \frac{\partial \phi_2'}{\partial t'} = \omega\phi_1' \,. \tag{3.37}$$

We now "boost" the coordinates according to the transformations (3.33), and since the ϕ_1 and ϕ_2 are scalars we can write,

$$\begin{aligned}
\phi_1(t,x,y) &= \phi_1'(t',x',y') = \sigma(x',y')\cos(\omega t') = \sigma(\gamma[x+vt],y)\cos(\omega[\gamma(t+vx)]),\\
\phi_2(t,x,y) &= \phi_2'(t',x',y') = \sigma(x',y')\sin(\omega t') = \sigma(\gamma[x+vt],y)\sin(\omega[\gamma(t+vx)]),\\
\pi_1(t,x,y) &= \frac{\partial \phi_1}{\partial t}(t,x,y) = \frac{\partial \phi_1'}{\partial t}(t',x',y'),\\
\pi_2(t,x,y) &= \frac{\partial \phi_2}{\partial t}(t,x,y) = \frac{\partial \phi_2'}{\partial t}(t',x',y')\,.
\end{aligned} \tag{3.38}$$

Since $t' = t'(t,x,y)$, $x' = x'(t,x,y)$ and $y' = y'(t,x,y)$, the derivatives transform as components of (co)-vectors,

$$\begin{aligned}
\pi_1(t,x,y) &= \frac{\partial \phi_1'}{\partial t}(t'(t,x,y),x'(t,x,y),y'(t,x,y)) = \frac{\partial \phi_1'}{\partial t'}\frac{\partial t'}{\partial t} + \frac{\partial \phi_1'}{\partial x'}\frac{\partial x'}{\partial t} + \frac{\partial \phi_1'}{\partial y'}\frac{\partial y'}{\partial t}\,,\\
\pi_2(t,x,y) &= \frac{\partial \phi_2'}{\partial t}(t'(t,x,y),x'(t,x,y),y'(t,x,y)) = \frac{\partial \phi_2'}{\partial t'}\frac{\partial t'}{\partial t} + \frac{\partial \phi_2'}{\partial x'}\frac{\partial x'}{\partial t} + \frac{\partial \phi_2'}{\partial y'}\frac{\partial y'}{\partial t}\,.
\end{aligned} \tag{3.39}$$

Again, using the inverse transformations (4.31), equations (3.39) simplify to:

$$\pi_1 = \frac{\partial \phi_1'}{\partial x'}\gamma v + \frac{\partial \phi_1'}{\partial t'}\gamma\,, \tag{3.40}$$

$$\pi_2 = \frac{\partial \phi_2'}{\partial x'}\gamma v + \frac{\partial \phi_2'}{\partial t'}\gamma\,, \tag{3.41}$$

Substituting equation (3.36) in the first term of (3.40) we obtain,

$$\frac{\partial \phi_1'}{\partial x'}(t',x',y') = \frac{\partial}{\partial x'}\left(\sigma(x',y')\cos(\omega t'))\right) = \cos(\omega[\gamma(t+vx)])\frac{\partial \sigma(\gamma[x+vt],y)}{\partial x'} \tag{3.42}$$

Using (3.37) in the second term of (3.40) yields,

$$\frac{\partial \phi_1'}{\partial t'}(t',x',y') = -\omega\phi_2' = -\omega\phi_2 \tag{3.43}$$

and similarly for $\partial\phi_2'/\partial t'$ in (3.41).

The coordinates in the rest frame corresponding to the initial time ($t = 0$) in the laboratory (boosted) frame are given by transformations (4.31),

$$t' = \gamma v x \qquad x' = x\gamma \qquad y' = y, \tag{3.44}$$

We interpolate in $\sigma(x', y')$ (obtained from LSODA) the values of $\sigma(\gamma x, y)$ in the lab frame. We actually accomplish this using $r' = \sqrt{x'^2 + y'^2}$, given that in the rest frame, $\sigma(x', y')$ is a circularly symmetric function $\sigma(r')$.

Collecting results from above, we have the following initial values for a boosted Q-ball:

$$\begin{aligned}
\phi_1^0 &= \sigma(\gamma x, y)\cos(\omega\gamma v x)\,, \\
\phi_2^0 &= \sigma(\gamma x, y)\sin(\omega\gamma v x)\,, \\
\pi_1^0 &= \left(\frac{\partial\sigma(\gamma x, y)}{\gamma\partial x}\right)\cos(\omega\gamma v x)\gamma v - \omega\phi_2\gamma\,, \\
\pi_2^0 &= \left(\frac{\partial\sigma(\gamma x, y)}{\gamma\partial x}\right)\sin(\omega\gamma v x)\gamma v + \omega\phi_1\gamma\,.
\end{aligned} \tag{3.45}$$

Here, the derivatives $\partial\sigma/\partial x$ in the last two equations are calculated numerically.

3.4 Code Validation

In this section we test the convergence and consistency of the solutions generated by our code by means of the computation of convergence factors (eqn. (2.30)) for: 1) smooth Gaussian data, 2) a stationary Q-ball, and 3) a boosted Q-ball. We also monitor the conservation of the Nöether charge, Q, of Q-ball solutions, and demonstrate that independent residuals converge as expected. We will show the results of these tests for two of the four dynamical functions of our model, namely ϕ_1 and π_1. However, we emphasize that their counterparts ϕ_2 and π_2 converge in the same manner. Our runs implement two types of boundary conditions: Sommerfeld outgoing and Dirichlet (reflective) conditions (see App. E). For testing purposes there is no particular reason to prefer one or the other.

3.4.1 Natural Scales of Length and Time

In finite difference computations, specification of a particular grid resolution, h, is in itself largely meaningless if not accompanied with a specification of natural, or characteristic, scales of length, L, and time, T, associated with the solution under study. Clearly, we want to have $h \ll L$ and $h \ll T$ to ensure that the finite difference solutions are close to their continuum counterparts, and this is especially true for the relatively low-order approximations we use here and throughout this thesis. In the current case, a natural length scale is set by the size of the Q-balls, while the reciprocal of the eigenfrequency, ω, sets a time scale.

We restrict our calculations below to Q-balls corresponding to the profile function shown in Fig. 3.1, which, we recall, is computed with parameters $A = 1.0$, $B = 0.5$, $\sigma_0 = 1.375$ and $\omega = 0.7739293$. The associated oscillation time scale is thus $2\pi\omega \approx 8$. It is desirable that our numerical experiments last significantly longer than this time, and this is the case. We selected this particular Q-ball solution partly since it has been previously studied extensively in the literature [18], so we can compare at least some of our results with prior work in a direct manner.

Returning to the issue of finite difference resolution, we note that the diameter of our Q-ball is ≈ 30 in our units. A typical evolution of a non-boosted configuration will be performed in a 40×40 box, where we adopt the nomenclature that an "$X \times Y$ box" means our discrete spatial domain is $0 \leq x \leq X$, $0 \leq y \leq Y$. For a resolution of 513×513, which we consider moderate, we thus have $h = 40/512 = 0.078$. This means that the Q-ball is spanned by about 380 points in each coordinate direction. For boosted data, this number of points is reduced along the boost direction (the x direction), by the boost factor γ and is, of course, one of the reasons that we require increasing resolution as the boost velocity increases in order to maintain the same accuracy.

3.4.2 Computation of the Conserved Charge, Q

We calculate the total charge, Q, after every update of the grid functions. When the code is run in parallel, the domain is divided in subregions, each of which is assigned to a certain processor. We thus first compute the charge density, q, at every point of the subdomain. From (3.3) we calculate

$$q = \phi_1 \, \pi_2 - \phi_2 \, \pi_1 \,, \tag{3.46}$$

which is discretized trivially as

$$q(i,j) = \phi_1(i,j)\pi_2(i,j) - \phi_2(i,j)\pi_1(i,j)\,. \tag{3.47}$$

We integrate this function, using a second order trapezoidal rule, to obtain the total charge per subdomain,

$$Q_{\rm sub} = \frac{\Delta x\,\Delta y}{4} \sum_{i,j}^{N_x-1,N_y-1} \left(q_{i,j} + q_{i+1,j} + q_{i,j+1} + q_{i+1,j+1}\right)\,, \tag{3.48}$$

where Δx and Δy are the grid spacings of the two-dimensional mesh as usual. Finally, one of the processors gathers the $Q_{\rm sub}$ from every subdomain, and sums the contributions to yield the final value of Q. Care needs be taken to select correct limits for i and j in the summation in (3.48), in order to avoid double-summing contributions due to the use of ghost points in the parallel decomposition of the computational domain. We also note that our ability to calculate Q is limited to unigrid (non-adaptive) calculations, since the coding required for the adaptive case is beyond the scope of the current project.

3.4.3 Independent Residual Evaluators

As discussed in Chap. 2, the use of independent residual evaluators is a powerful and general technique to demonstrate the convergence of finite difference solutions to continuum solutions of the PDEs under consideration. Our specific independent residual evaluators are constructed as follows. For the ϕ_a variables, we replace the Crank-Nicholson approximation with the following expression, which is first order accurate in time:

$$I_{\phi_a}(i,j) = \frac{\phi_a(i,j)^{n+1} - \phi_a(i,j)^n}{\Delta t} - \pi_a(i,j)^{n+1}\,. \tag{3.49}$$

For the π_a unknowns, we use a first order forward approximation for the second spatial derivatives of the ϕ_a:

$$\begin{aligned} I_{\pi_a}(i,j) &= \frac{\pi_a^{n+1}(i,j) - \pi_a^n(i,j)}{\Delta t} - \left[\frac{\phi_a^{n+1}(i,j) - 2\phi_a^{n+1}(i+1,j) + \phi_a^{n+1}(i+2,j)}{\Delta x^2}\right] \\ &- \left[\frac{\phi_a^{n+1}(i,j) - 2\phi_a^{n+1}(i,j+1) + \phi_a^{n+1}(i,j+2)}{\Delta y^2}\right] \\ &+ \left(\frac{dV^{n+1}(i,j)}{d|\phi^{n+1}(i,j)|} + \frac{dV^n(i,j)}{d|\phi^n(i,j)|}\right)\,. \end{aligned} \tag{3.50}$$

where

$$\frac{dV^{n+1}(i,j)}{d|\phi^{n+1}(i,j)|} = \phi_a^{n+1}(i,j) - |\phi^{n+1}(i,j)|\phi_a^{n+1}(i,j) + B|\phi^{n+1}(i,j)|)^2\phi_a^{n+1}(i,j)\,, \tag{3.51}$$

and $a = 1, 2$. As with the residuals (3.23)–(3.25) that define the governing finite difference system itself, these quantities should vanish in the limit $h \to 0$, provided that our finite difference solutions *are* converging to the appropriate continuum solutions. However, convergence is expected to be only *first order* in the mesh spacing for any of the independent residuals. Again, we emphasize that the stability of the independent discretization is not an issue, since we are not using the expressions (3.49)–(3.50) to evolve any quantities.

3.4.4 Gaussian Initial Data

As a first step in the validation of our finite difference code, we consider the evolution of some generic, smooth initial data. To this end we prepare an initial configuration where the component scalar fields are Gaussian pulses of the form,

$$\begin{aligned}
\phi_1(0, x_i, y_j) &= A_1 \exp\left[-\left(\frac{x_i - x_c}{40}\right)^2 - \left(\frac{y_j - y_c}{3}\right)^2\right], \\
\phi_2(0, x_i, y_j) &= A_1 \exp\left[-\left(\frac{x_i - x_c}{40}\right)^2 - \left(\frac{y_j - y_c}{3}\right)^2\right],
\end{aligned} \tag{3.52}$$

where A_1, A_2, x_c and y_c are parameters, and where

$$\pi_1(0, x_i, y_j) = 0 \qquad \pi_2(0, x_i, y_j) = 0\,. \tag{3.53}$$

This type of initial data is known as *time symmetric* since evolution backwards in time will generate the same dynamics as evolution forwards in time.

Fig. 3.5 shows the evolution of the modulus $|\phi|$ of the complex field for the above initial configuration. The main dynamical behaviour that is observed in ϕ is a quasi-periodic oscillation of the modulus, accompanied by outgoing radiation of circular (due to the symmetry of the initial conditions) waves. The component fields, ϕ_1 and ϕ_2, as well as their time derivatives, execute roughly sinusoidal oscillations at any given spatial location.

Convergence factors for the fields ϕ_1 and π_1 are shown in Fig. 3.6. We observe $Q^h \to 4$ as $h \to 0$,

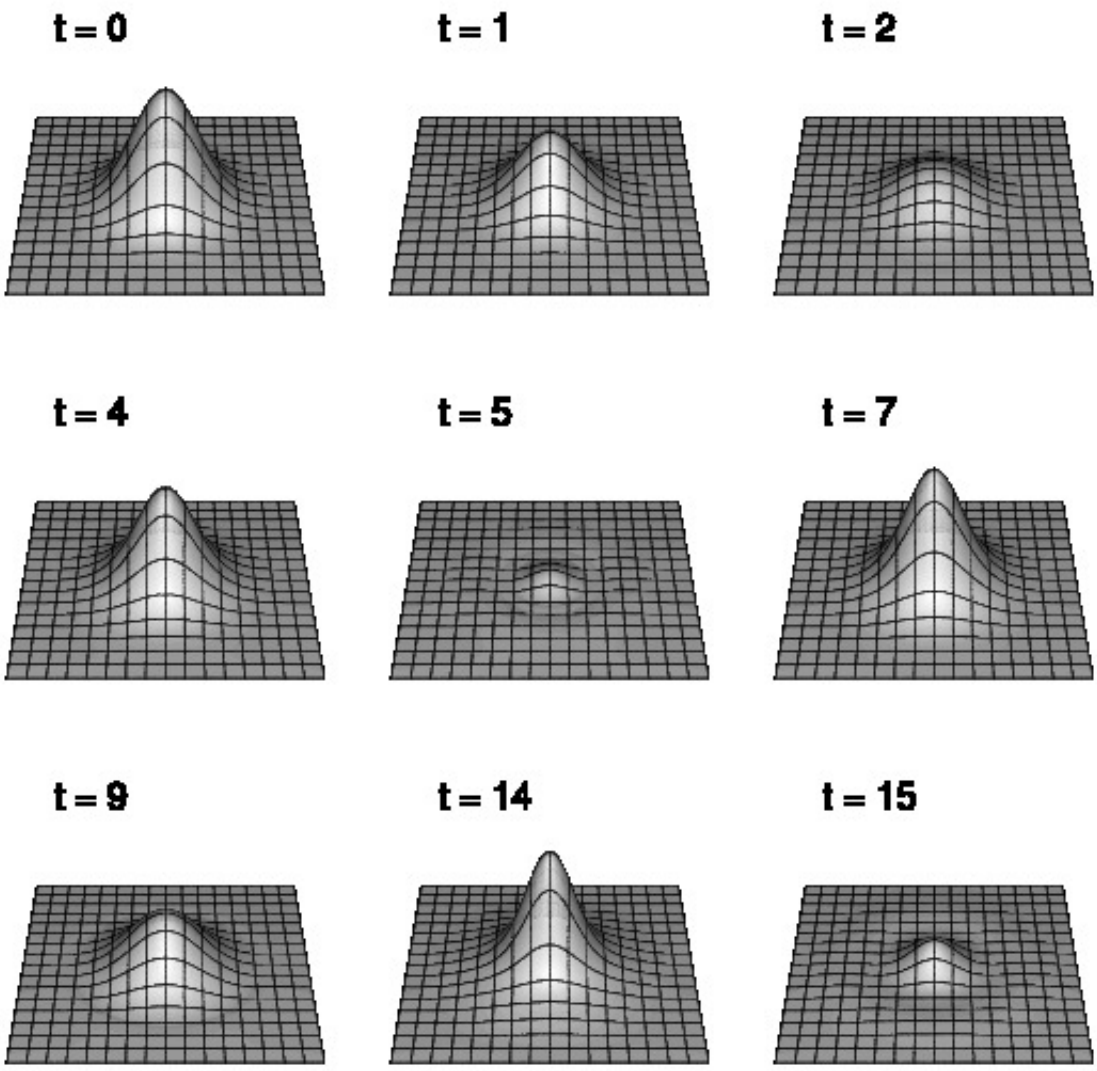

Figure 3.5: Evolution of the complex scalar field modulus $|\phi|$ for smooth Gaussian initial data of the form (3.52) with $A_1 = A_2 = 0.25$. The displayed results come from a unigrid (non-adaptive) calculation with 513×513 resolution, on a 50×50 box (so each square in the figure has an edge length of 1.25), and Courant number $\lambda = 0.2$. Both the real and imaginary Gaussian components of the field, and the modulus, $|\phi|$, are confined to a circle of diameter ≈ 28, so the pulse is resolved by about 290 points in each coordinate direction. The maximum amplitude of the modulus $|\phi|$ is ≈ 0.35. We do not use Kreiss-Oliger dissipation for this calculation, i.e. $\epsilon_{\rm KO} = 0$. The wave packet oscillates, and dissipates some charge quasi-periodically in (circular) outgoing waves.

signalling the expected second order convergence.[20] The small bumps that are seen in the plots, especially at lower resolution appear to be correlated with times when much of the corresponding field is passing through a value of zero. In this instance, the computation of the convergence factor can be expected to be relatively irregular and, in any case, all indications are that these fluctuations die away with increasing resolution.

Fig. 3.7 shows the results of the independent residual test for the functions ϕ_1 and π_1 using four distinct resolutions, h_L, $L = 1, 2, 3, 4$, where $h_L = h_{L-1}/2$. It is crucial to note that here, and in all other plots of this type that follow in this thesis, the residual norms have been rescaled by factors of 2^{L-1} so that coincidence of the resulting plots indicates the expected first order convergence of the residuals. We note that the oscillatory nature of the fields is also evident from this test. Finally, we observe that the choice between reflective (Dirichlet) or outgoing radiation boundary conditions (those used here) did not seem to affect convergence appreciably for this type of initial data.

3.4.5 Stationary Q-ball and Stability

In this section we analyze our code's convergence properties for the case of initial data describing a single Q-ball located at the centre of the computational domain, and at rest in the coordinate system. As mentioned previously, the Q-ball we use is calculated using parameters $A = 1.0$, $B = 0.5$, $\sigma_0 = 1.375$ and $\omega = 0.7739293$, resulting in an oscillation time of the component fields of about 8. The numerical grid spans a 50×50 box, and, again, the diameter of the Q-ball is about 30 units. We compute using a Courant number, $\lambda = 0.2$ and Kreiss-Oliger dissipation parameter $\epsilon_{\rm KO} = 0.0$, since dissipation was not necessary for this test. We also describe a cursory investigation of the dynamical stability of the Q-ball by integrating initial data that represents, in some sense, a perturbation of the configuration.

Fig. 3.8 shows the evolution of the modulus $|\phi|$ for a period of time corresponding to about 8 oscillations of the component fields ϕ_1 and ϕ_2. To "eye-ball" accuracy at least, $|\phi|$ is time-independent as expected.

Convergence factors for ϕ_1 and π_1 are displayed in Fig. 3.10. As was the case for Gaussian initial data, these plots provide strong evidence that the code is $O(h^2)$ accurate. In particular,

[20] The apparent lack of convergence at early times (also seen in many other convergence plots that follow in this and the subsequent two chapters) is due to the fact that the solution is initialized with identical data, so that the convergence factor—which amounts to 0/0—is formally undefined at the initial time, and is arbitrarily set to 0.

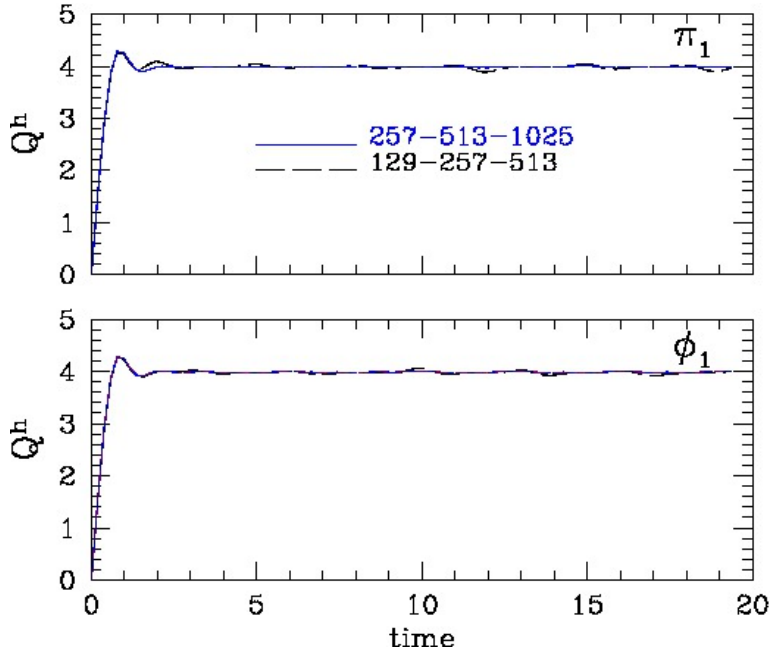

Figure 3.6: Convergence factors for smooth Gaussian initial data for the fields ϕ_1 and π_1. Details of the calculation are given in Fig. 3.5. We observe second-order convergence in both fields.

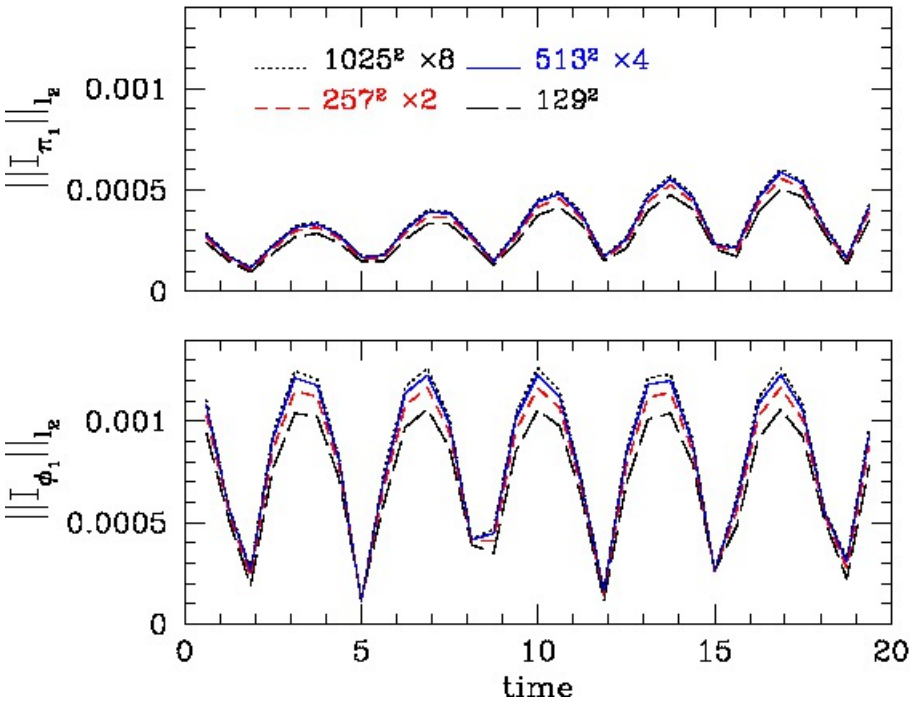

Figure 3.7: Independent residual test for Gaussian initial data. Plotted are the rescaled l_2 norms of the independent residuals of ϕ_1 and π_1 for the calculation described in Fig. 3.5 (see the text for a description of the rescaling). The near-coincidence of the curves demonstrates the expected first-order convergence of the residuals.

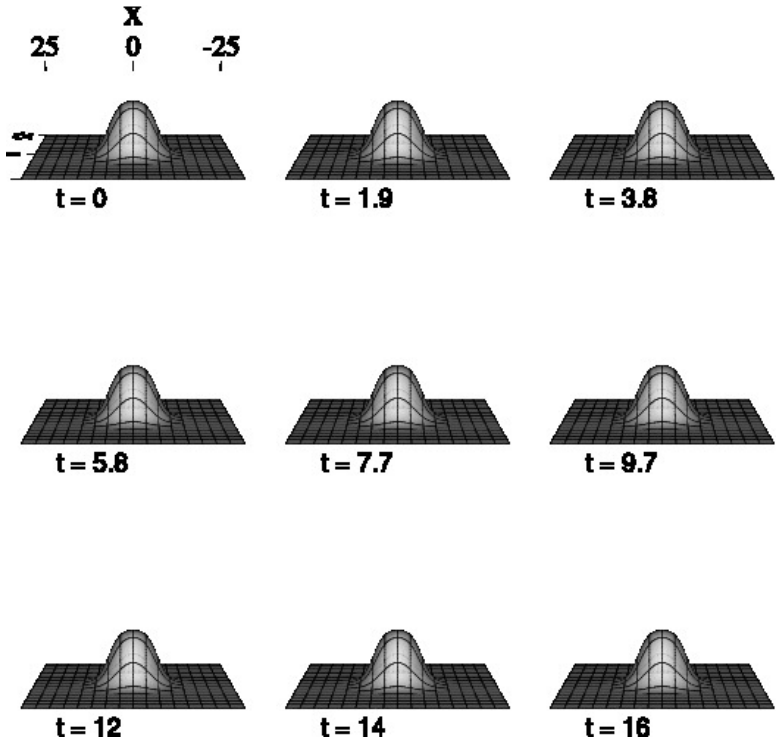

Figure 3.8: Evolution of the modulus $|\phi|$ for stationary Q-ball data. The box domain is of dimensions 50×50, with a Courant number of $\lambda = 0.2$, and a dissipation parameter of $\epsilon_{\rm KO} = 0.0$. Visually, at least, ϕ is time-independent.

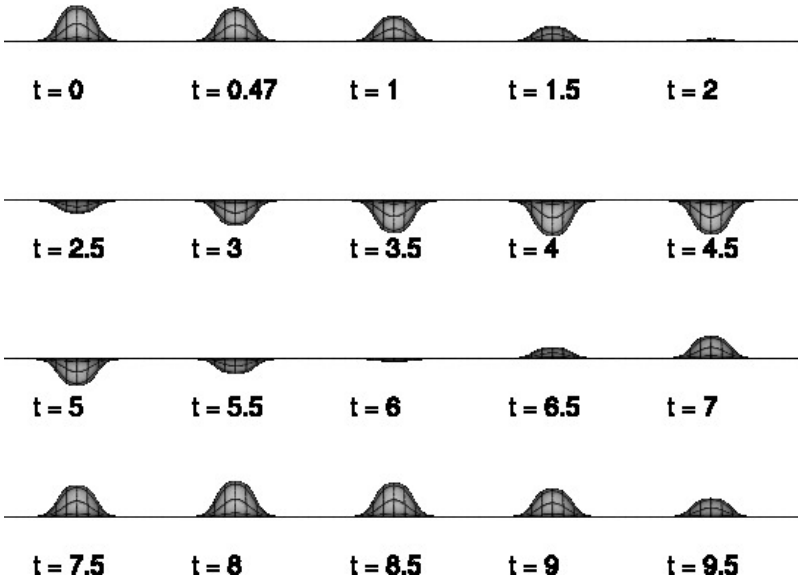

Figure 3.9: Evolution of the real component ϕ_1 of the stationary Q-ball field. Both components are oscillatory functions. For $\omega \approx 0.77$ we have a period of $T \approx 8$, consistent with the two zero crossings at $t \approx 2$ and $t \approx 6$ observed in the plot. The impact of the zero crossings on convergence of the solution can be seen in the plots of the independent residuals for the calculation (Fig. 3.11). The parameters for the run are listed in the caption of the previous figure.

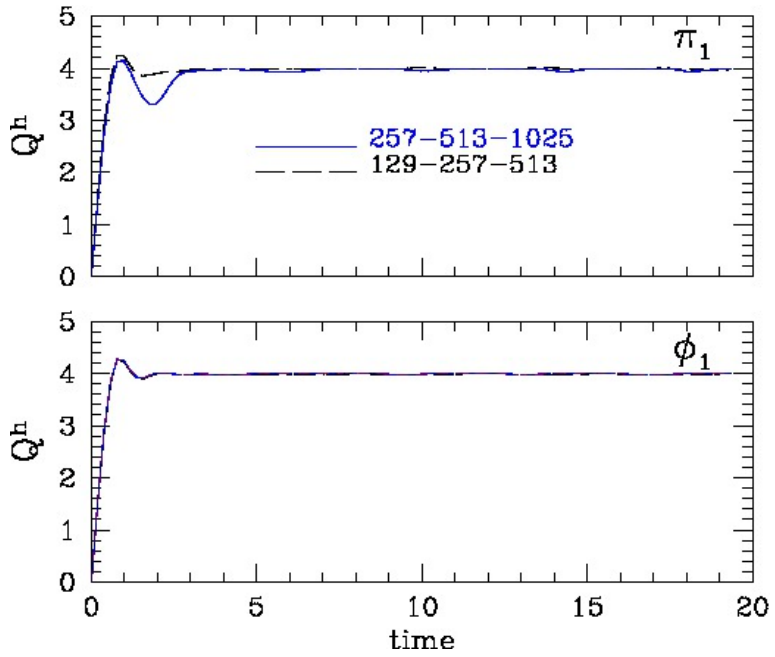

Figure 3.10: Convergence factors for the fields ϕ_1 and π_1 for the evolution of the stationary Q-ball shown in Fig. 3.8. Second order convergence is observed.

note that, modulo the early time behaviour—which can again be attributed to the fact that the initial data is identical on all meshes—the convergence improves (Q^h is closer to 4) as $h \to 0$.

Fig. 3.11 plots the rescaled independent residuals for ϕ_1 and π_1. As previously, the near-coincidence of the curves demonstrates that the residuals are first-order convergent in the mesh spacing. We note that the oscillations in the l_2-norm of the independent residuals occur at about twice the frequency of the Q-ball field components themselves. This is due to the positive definite character of the l_2-norm, whose oscillation only reflects the change of magnitude regardless the sign of the ϕ_1 or π_1 components. While the latter perform positive and negative excursions to maximum amplitude, comprising one cycle, the l_2-norm reflects this as two positive excursions.

Fig. 3.12 shows the results of the computation of the conserved charge Q at various resolutions. At any given mesh scale, there appears to be a roughly linear "dissipation" of charge with time, but there is clearly convergence to charge conservation as $h \to 0$. Indeed, and as investigated in more detail, the charge is apparently converging as $O(h^3)$ rather than the naively expected $O(h^2)$. This behaviour is not understood at this time, although we suspect that it is at least partly dependent on our combined use of a Crank-Nicholson evolution scheme and the trapezoidal integration rule (3.48) for the computation of the total charge. To further investigate this effect,

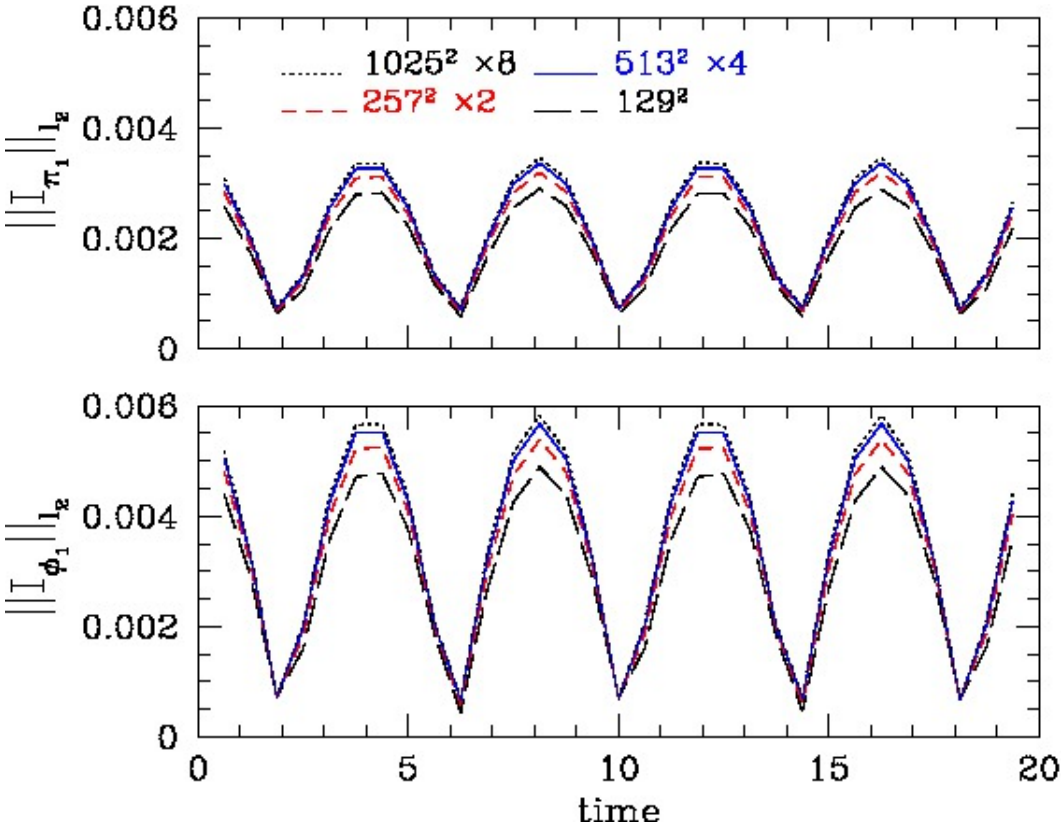

Figure 3.11: Rescaled l_2-norms of the independent residuals of ϕ_1 and π_1 for the evolution of the stationary initial data shown in Fig. 3.8. The near-coincidence of the graphs signals first order convergence, which is consistent with the order of the finite difference approximation of the independent residual. This coincidence constitutes strong evidence for convergence to the correct continuum solution. The period of oscillation in the l_2-norm of the independent residuals is half that of the Q-ball field components themselves. This is a consequence of the positive definite nature of the l_2-norm of the residuals.

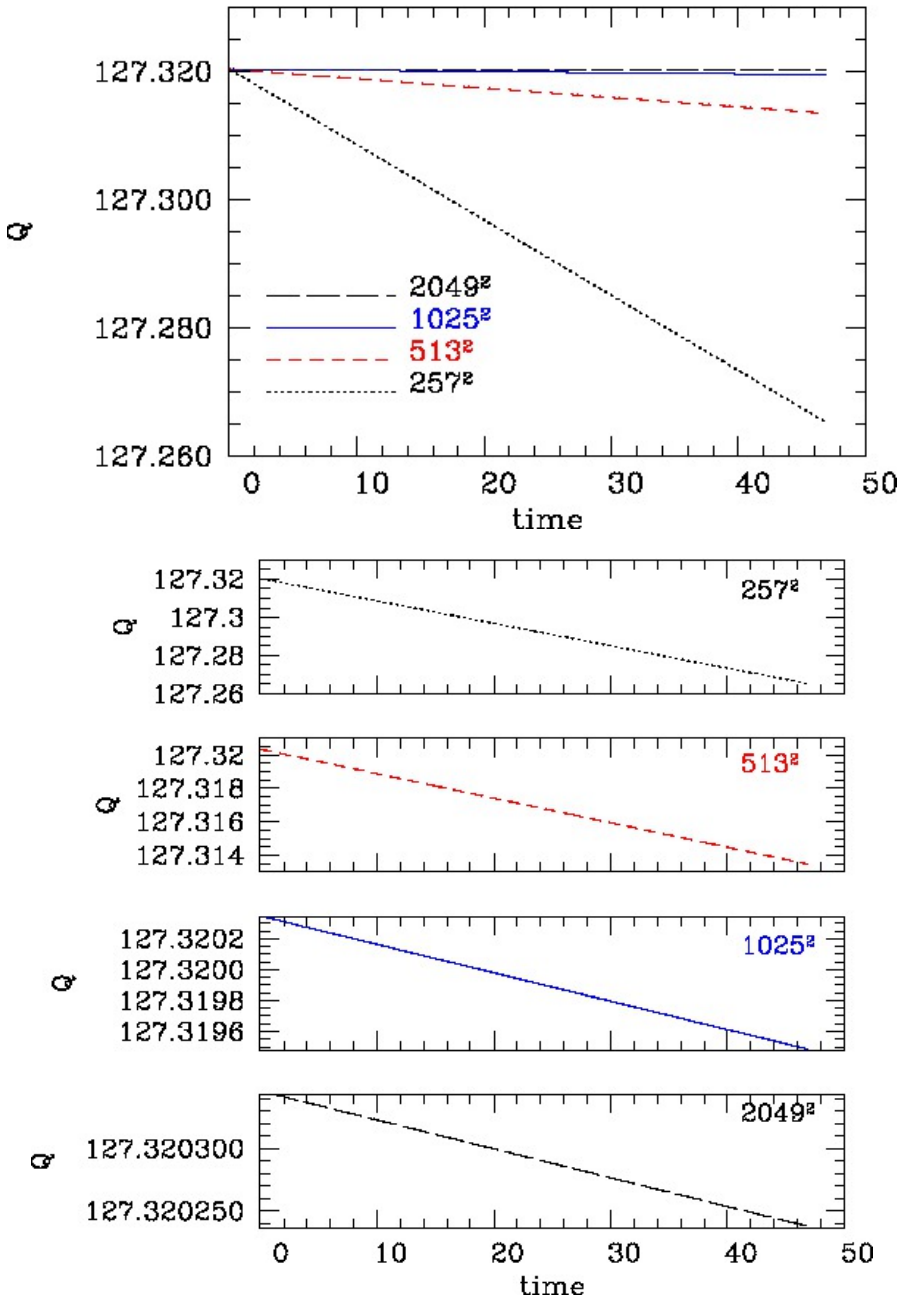

Figure 3.12: Resolution-dependence of the evolution of the computed total charge, Q, using stationary initial data. As with the calculation described in the last few figures, a 50×50 computational box was used and the Courant number was $\lambda = 0.2$. The top plot shows that the calculated Q converges to conservation as $h \to 0$, while the bottom 4 plots show details for each resolution used. We found that the conserved charge Q exhibits better-than-second-order convergence, possibly $O(h^3)$. We suspect that this feature may be due to our combined use of a Crank-Nicholson time-stepping scheme and a trapezoidal integration rule for computing Q.

we integrated the modulus $|\phi|$ of the complex field on each subdomain, using the same trapezoidal rule as (3.48),

$$|\phi|_{\rm sub} = \sum_{i,j} = \frac{\Delta x\ \Delta y}{4} \left(|\phi|_{i,j} + |\phi|_{i+1,j} + |\phi|_{i,j+1} + |\phi|_{i+1,j+1}\right) . \tag{3.54}$$

Results from this integration also converge as $O(h^3)$.

To test the dynamical stability of our Q-ball we approximated (through trial and error) the numerically computed profile, $\sigma(r)$, shown in Fig. 3.1, with the closed form *trial* function,

$$\sigma_{\rm trial}(r) = \frac{4\ \arctan(\exp(-0.75(r-6)))}{4.5} . \tag{3.55}$$

As can be seen from Fig. 3.13 we can view $\sigma_{\rm trial}$ as a perturbation of $\sigma(r)$, but we also emphasize that we have not made any attempt to make the notion of perturbation precise. Given $\sigma_{\rm trial}$ we initialize the dynamical fields using (3.30)–(3.32) with $\sigma(r) \to \sigma_{\rm trial}(r)$. When this data is evolved we find that the modulus $|\phi|$ oscillates slightly at early times, but then eventually settles into a stationary state very close to the Q-ball defined by $\sigma(r)$. This provides evidence that our soliton is indeed stable under small (but finite) perturbations. Additional analysis of the convergence of the charge and the integrated field modulus for this computation yield the same rates of convergence as the computation using the true Q-ball profile.

3.4.6 Boosted Q-ball

We are ultimately interested in studying collisions of Q-balls in the ultrarelativistic regime, that is when two Q-balls collide with a large relative velocity. As a preliminary step towards this goal, we investigate our code's convergence properties for initial data describing a single boosted Q-ball, prepared as described in Sec. 3.3.4. Apart from Fig. 3.16, we will restrict attention here to the case of a small boost, $\gamma = 1.15$, but will consider Q-balls with larger boosts in subsequent sections. We note that a principal and rather obvious observation is that due to effects such as Lorentz contraction along the boost direction, calculations for larger γ require increased grid resolution for fixed accuracy. Equivalently, we expect and observe that at fixed resolution the convergence of our code degrades with increasing γ. This provides a major motivating factor for our use of AMR in such calculations, since maintaining constant accuracy through the use of an increasingly fine mesh

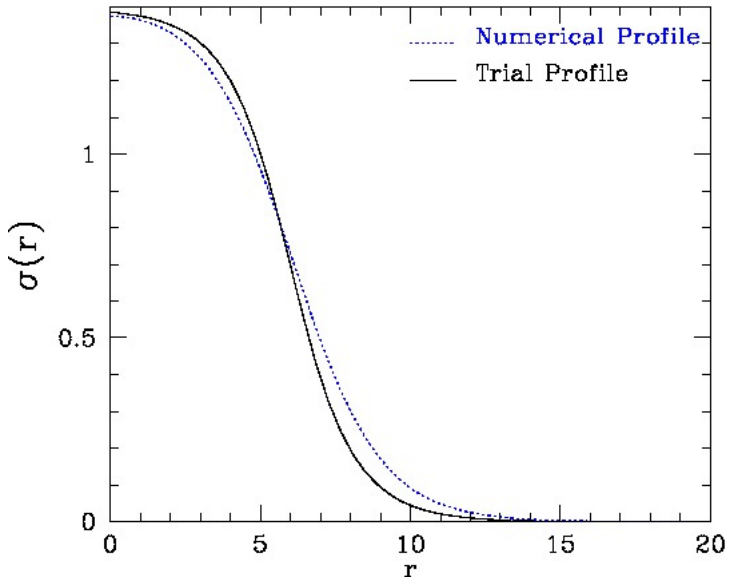

Figure 3.13: Numerical and trial profile functions used to test dynamical stability of a stationary Q-ball solution.

spacing *globally* is computationally expensive (not to mention wasteful).

Our convergence and independent residual tests for a boosted Q-ball were performed in a 40×40 box, with $\lambda = 0.4$, and $\epsilon_{\rm KO} = 0.5$ (we also tried increasing $\epsilon_{\rm KO}$ to 0.6 and 0.7, which did not appreciably affect the results). Fig. 3.14 shows the convergence factors for ϕ_1 and π_1, while Fig. 3.15 shows the evolution of the l_2 norms of the independent residuals for those fields. Once more we observe second order convergence of the dynamical grid functions and first order convergence of the independent residuals, as expected.

As for the non-boosted case, we apparently have $O(h^3)$ convergence of the total charge, but in this instance we also seem to have the same rate of convergence for the integrated modulus of the scalar field. The source of this last behaviour also remains a mystery. However, we must emphasize that as for the case of the "superconvergence" of the charge, this is of course not indicative of any defect in the code.

Finally, Fig. 3.16 shows the evolution of $|\phi|$ for our usual Q-ball data, but where a more substantial boost, $\gamma = 2.4$, has been applied in the x-direction. Although not apparent from the plots, the lab-frame shape of the Q-ball (as projected into the x–y plane) is elliptical due to Lorentz contraction. Again, to visual accuracy, there is no change in the overall shape of the Q-ball (as defined by $|\phi|$) as it propagates through the computational domain.

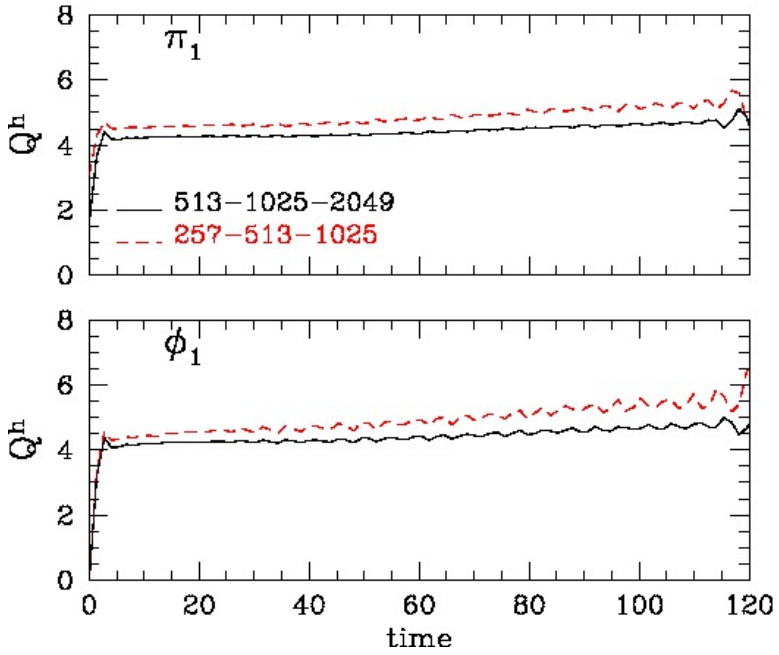

Figure 3.14: Convergence factors for the fields ϕ_1 and π_1 for a $\gamma = 1.15$ boosted Q-ball, displaying second order convergence. The computational box was 40×40, a Courant number $\lambda = 0.4$ was used and Sommerfeld (outgoing radiation) boundary conditions were applied. The Q-ball begins to leave the domain at $t \approx 120$ resulting in the increased fluctuations in the Q^h at that time.

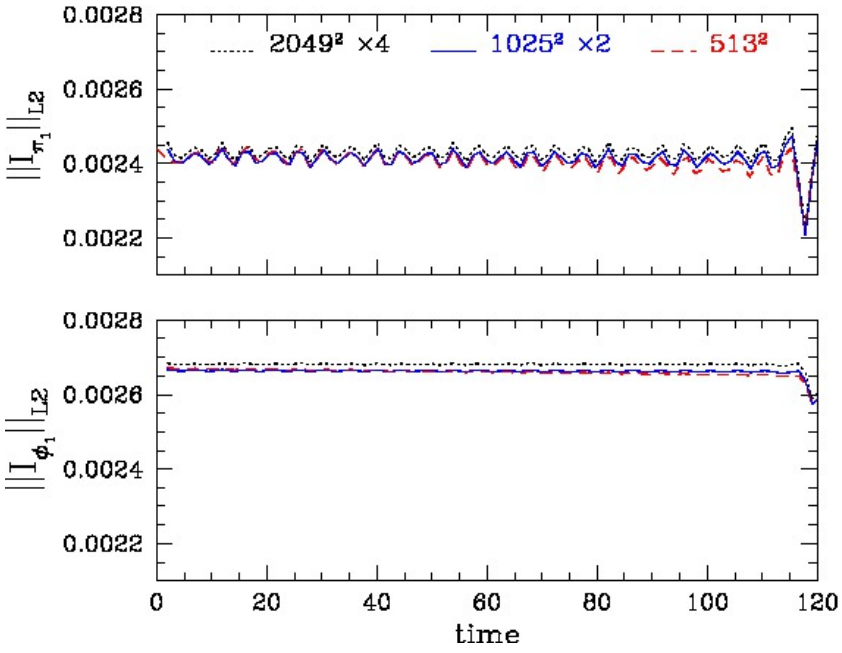

Figure 3.15: Independent residual test for the computation described in the caption of Fig. 3.14. The expected first order convergence is observed.

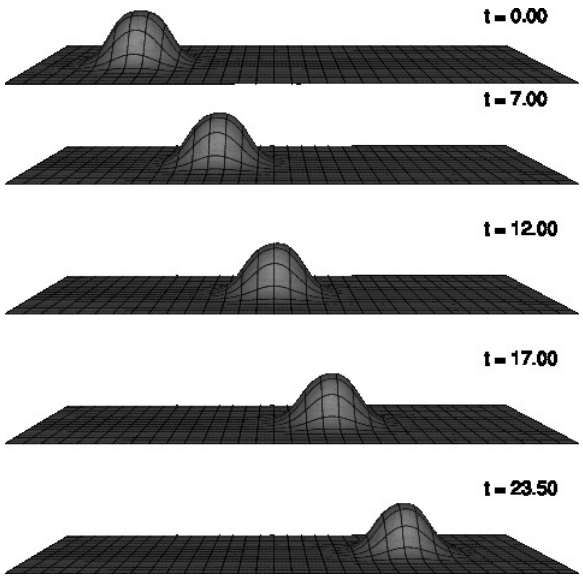

Figure 3.16: Evolution of the modulus $|\phi|$ for a boosted Q-ball with $\gamma = 2.4$. The calculation was performed on a 60×60 box using a 513×513 mesh, $\lambda = 0.3$, and Sommerfeld boundary conditions. In the x-y plane the Q-ball has an elliptical profile: due to Lorentz contraction its diameter in the x direction is ≈ 12.5 units, while its y-diameter is ≈ 30. The latter is, of course, the same as its diameter in the rest frame. (See Fig. 3.17 for a more extreme and visible example of the Lorentz contraction.) The soliton travels unscathed towards the boundary of the computational domain.

To summarize the last three subsections, we have subjected our finite difference code to a comprehensive set of tests and have found that it displays the expected rate of convergence in the mesh spacing and, through the use of independent residual evaluation, are confident that the solutions that are generated are indeed good approximations to continuum solutions of the governing PDEs. We now proceed to use the code to investigate various phenomena related to Q-ball scattering.

3.5 Head-on Scattering of Q-balls

We first consider an analysis of the head-on collision of two Q-balls, with an emphasis on the ultrarelativistic regime. We continue to use Q-balls defined by a single profile function $\sigma(r)$ and associated eigenfrequency ω (the same ones used in all of the calculations described thus far in this chapter). However, as we will shortly describe in more detail, for any Q-ball having total charge Q, we can construct a configuration with the opposite charge $-Q$ by taking $\omega \to -\omega$ in the ansatz (3.8). As we will see, the dynamics of the collisions is dependent on the relative sign

of the total charges of the Q-balls. The issue of Q-ball scattering in $2+1$ dimensions is one that has been studied in the literature, and we review the main findings of this previous work in the next subsection. Our main result, which is consistent with the prior studies, is that high-energy collisions of Q-balls is primarily elastic (solitonic) in nature. In particular for large γ, we observe that the scattering is almost entirely forward in nature, with the two Q-balls passing through one another and emerging essentially unscathed.

3.5.1 General Features of Q-ball Scattering: Previous Work

Past work has focused mostly on low energy scattering. This regime is germane for standard cosmological and astrophysical scenarios, where, for example, Q-balls are considered dark matter candidates (relics from the early universe), or as exotic matter trapped within neutron stars. The most comprehensive study of Q-ball appears to be due to Battye and Sutcliffe [72]. The highest velocity (given to each Q-ball) they analyzed was $v = 0.8$ ($\gamma = 1.6$) and for this data they reason that the Q-balls pass through one another so quickly that they do not have time to interact. The calculations were performed on a uniform grid having 200×200 points, with $h = 0.2$ and $\lambda = 0.25$, and with a second order finite difference scheme that employed a time-explicit update. Similar work by Axenides *et al.* [18] was performed with a 300×300 grid and $h = 0.3$. They do not specify the order of the discretization scheme they used to approximate the spatial derivatives. However, they do mention the use of fourth order Runge-Kutta for the time discretization (also explicit). The highest velocity they considered was $v = 0.7$ ($\gamma = 1.4$).

This previous work [18, 72] established the following facts about head-on Q-ball collisions:

- There is a region of low velocities, $0 < v \leq 0.3$, where we observe that Q-balls with the same charge undergo right angle scattering (similar to that of topological solitons): scattering is consistent with the fact that Q-balls with the same charge repel one another. In contrast, Q-balls with opposite charge fuse into a oscillatory state, consistent with the mutual attraction of the pair in this case.

- For the intermediate range of velocities $0.3 < v \leq 0.7$, scattering of Q-balls of the same charge produces a much richer mixed end state—sometimes referred as *fragmentation*—with both forward and right angle scattering. The size of the ejected Q-balls depends on the initial velocity. If $v \approx 0.3$, the forward scattered Q-balls are small, and those scattering at right

angles are larger. As the velocity tends to $v \approx 0.7$, the situation is reversed. Sometimes a small residual Q-ball is left in the center of the interaction region. We were able to reproduce one of these events at $v = 0.5$ ($\gamma = 1.15$), which is shown in Fig. 3.32.

- For larger velocities—above $v = 0.7$ ($\gamma = 1.4$)— Q-balls of the same charge simply forward scatter, emerging from the collision mostly unscathed, and then propagate away from one another. An example of a collision at $v = 0.7$ is shown in Fig. 3.33.

Q-balls of opposite charge are not mentioned for the intermediate and high velocity regions. The above phenomenology appears to hold for a variety of polynomial potentials, including the one adopted here. However, numerical work by Multamäki and Vilja [97], who adopted a more phenomenologically inspired logarithmic potential, did not show evidence of right angle scattering, even though the velocities used seem to be quite low ($v \approx 0.01$).

It is worth noting that none of the above cited works discuss the convergence of their codes, nor do they monitor the behaviour of conserved quantities. We thus feel that the work described here (and throughout this thesis) represents the use of a more rigorous methodology for the numerical analysis than prior research.

It is also worth mentioning that, beyond the Q-ball model considered here, there have been many other numerical studies of the dynamics of interacting scalar fields that have bearing on our work. For example, in [130] it has been shown that scalar fields with only potential interactions behave like free fields during high-energy colisions: their "free-passage" through each other is quite similar to what we see in our high-speed Q-ball collisions. In addition, there has been extensive investigations of oscillons [131, 132] which are long-lived metastable configurations of a single *real* scalar field with a non-linear polynomial self-interaction potential.

3.5.2 Unigrid Calculations of Q-ball Collisions

In this section we summarize typical results of our simulation of relativistic Q-ball collisions, obtained using the unigrid operation of our code. Subsequent sections will describe our experience with similar calculations performed using AMR. In addition, as our interest here is primarily in illustrating the convergence of the code, and in determining typical resolutions that are required to observe good convergence, we will largely focus attention on two specific scenarios. We also continue to use the same profile function, $\sigma(r)$, that has been adopted for all of the calculations

thus far in this chapter.

The first scenario is the head-on collision of two Q-balls with equal charges, both in magnitude and sign. We will refer to this configuration as a Q^+ Q^+ collision, where $Q_1 = Q_2 = Q^+ = Q$. This unigrid (non-adaptive) calculation was performed at $\gamma = 1.6$ ($v = 0.8$). Fig. 3.18 shows the Convergence factors Q^h of the component field ϕ_1 and its derivative, π_1. The graphs show second order convergence as $h \to 0$. The box domain has dimensions 50×50, a Courant number of $\lambda = 0.2$ and the boundary conditions are of Dirichlet type. No dissipation is used ($\epsilon_{\rm KO} = 0.0$). The independent residual tests for this calculation are shown in Fig. 3.19, which display first-order convergence. The evolution of the charge Q is shown in Fig. 3.20.

The second scenario is the head-on collision of two Q-balls with equal and opposite charges, $Q_1 = Q^+ = Q$ and $Q_2 = Q^- = -Q$, respectively. We will refer to this set-up as a Q^+ Q^- collision. Fig. 3.17 compares the initial-time field modulus, $|\phi|(0, x, y)$, for Q^+ Q^- configurations with no boost (left) and with $\gamma = 2.41$ (right). The Lorentz contraction of the Q-balls, which are centred at $(-20, 0)$ and $(20, 0)$, is evident in the plot of the boosted data.

Figs. 3.22 and 3.23 show the results of convergence and independent residual tests, respectively, for a series of calculations performed with these boosted initial conditions, but a larger value of $\gamma = 2.4$ ($v = 0.91$). The computations were done on a 60×60 box with $\lambda = 0.2$ and $\epsilon_{\rm KO} = 0.5$, Similarly to the first scenario, Dirichlet boundary conditions were used. The plots indicate second order convergence of the difference scheme and first order convergence of the independent residuals. However, it is also clear from comparison with Figs. 3.10 and 3.11 that significantly more resolution is required here, relative to the case of a single Q-ball at rest, to see "good" convergence (e.g. Q^h nearly 4). This is to be expected, of course, since evolution of even a single boosted Q-ball requires larger field gradients to be resolved (compared to the non-boosted case), and the interaction of the two solitons places even more demands on the finite difference approximation. Evidence for this last observation can be seen in the fluctuations of the convergence factors and independent residuals starting at $t \approx 25$.

Fig. 3.21 shows the time evolution of the field modulus $|\phi|$ from this calculation. In accord with previous simulations (although none of the published work describes collisions with γ as large as 2.4), the interaction of the Q-balls can clearly be described as principally a forward-scattering process. In addition, there is little deformation of the individual Q-balls as a result of the collision; i.e. the interaction is largely solitonic.

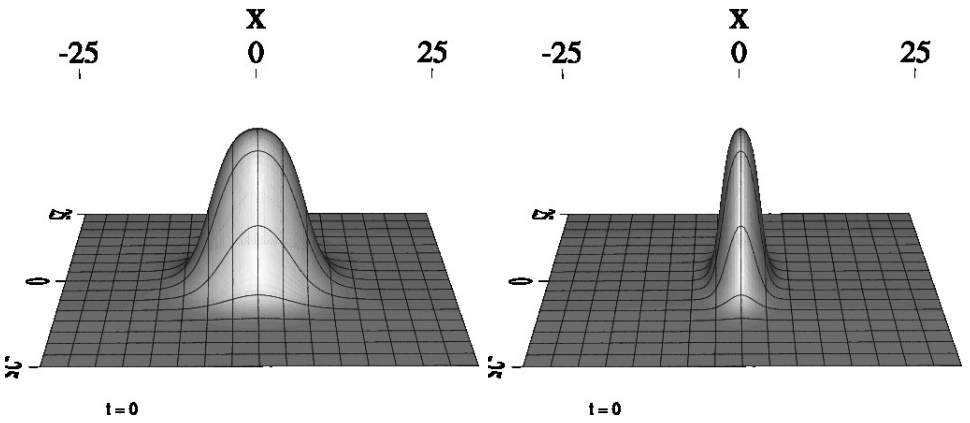

Figure 3.17: This figure illustrates the significant Lorentz contraction of the initial Q-ball configuration for some of our scattering experiments. The modulus, $|\phi|$, of the complex scalar field is plotted. The left Q-ball is at rest, with a diameter of about ≈ 30 units (given a radius of ≈ 15 units from Fig. 3.1). The right one is boosted to $\gamma = 2.41$, and we can see that its diameter in the x direction has contracted to about 12.5 units. The contraction can be computed from the relation $l = l_0/\gamma$, where l is the length in the laboratory reference frame, and l_0 is the length at rest (proper length). This relativistic effect is largely responsible for the need for higher resolutions at high boosts (for fixed accuracy).

We performed simulations of similar head-on collisions with boosts as large as $\gamma = 7$, and using a maximum (unigrid) resolution of 2049×2049. All of these calculations exhibited essentially the same elastic forward-scattering of the Q-balls.

We also experimented with off-axis collisions, in which each Q-ball was given a boost of equal magnitude in the x-direction, but where the initial centres of the Q-balls were offset by b units in the y direction, so that b represents the usual *impact parameter*. Results from a typical calculation with $\gamma = 2.4$ and $b = 10$—which yields a grazing collision—are shown in Fig. 3.24. As with the head-on case, the individual Q-balls emerge from the collision largely unscathed. The charge density, Q, of a similar calculation, this time with $b = 8$ and $\gamma = 1.09$, is shown in Fig. 3.25. A head-on collision at this value of γ ends in right-angle scattering, and it is interesting to note that a small deviation from $b = 0$ completely changes the outcome of the scattering.

3.6 AMR Calculations of Q-ball Collisions

We now discuss the results from calculations of the sort described in the previous section, but where we enable the AMR capability of our code (provided by the AMRD/PAMR infrastructure, as described in Sec. 2.4). As usual, we are interested in convergence properties, and computing Q^h

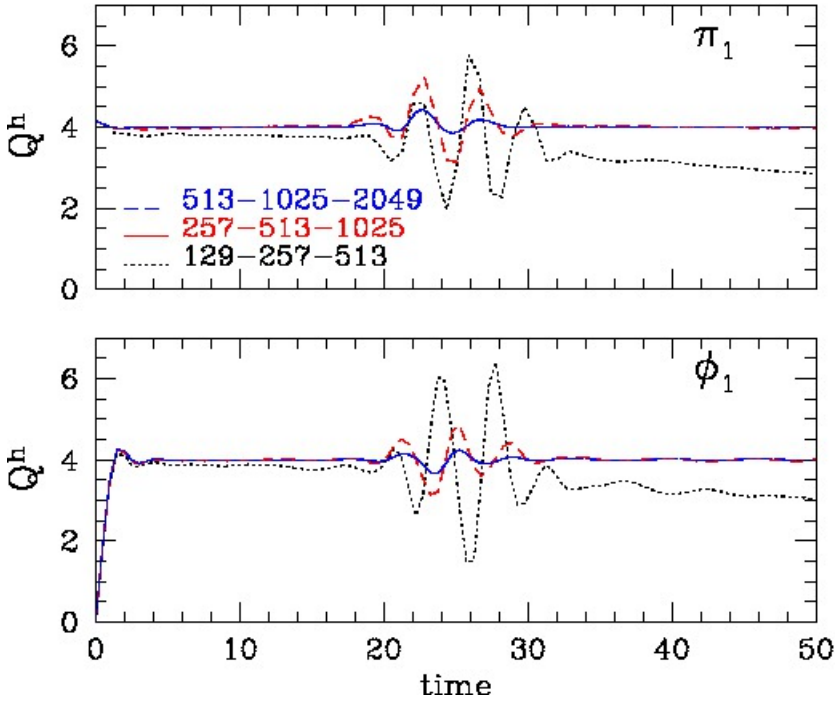

Figure 3.18: Convergence factors, Q^h, for a head-on Q^+ Q^+ collision with $\gamma = 1.6$ ($v = 0.8$). The graphs show second order convergence as $h \to 0$. Results are from unigrid computations using a domain 50×50 and a Courant number $\lambda = 0.2$. The boundary conditions are Dirichlet and no dissipation is used ($\epsilon_{\rm KO} = 0.0$).

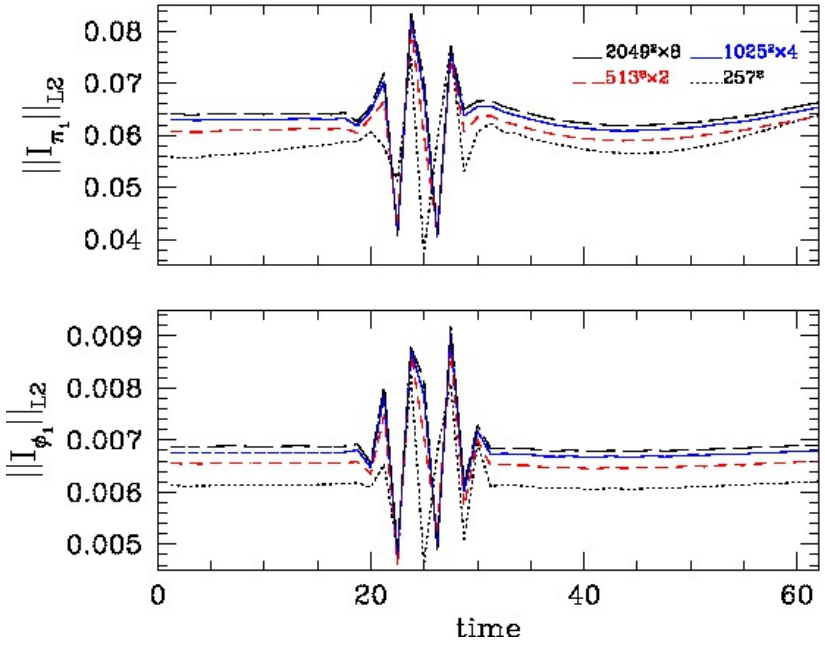

Figure 3.19: Rescaled l_2 norms of the independent residuals for π_1 and ϕ_1 from the Q^+ Q^+ head-on collision described in the caption of the previous figure (Fig. 3.18). The plots show the expected linear convergence as $h \to 0$.

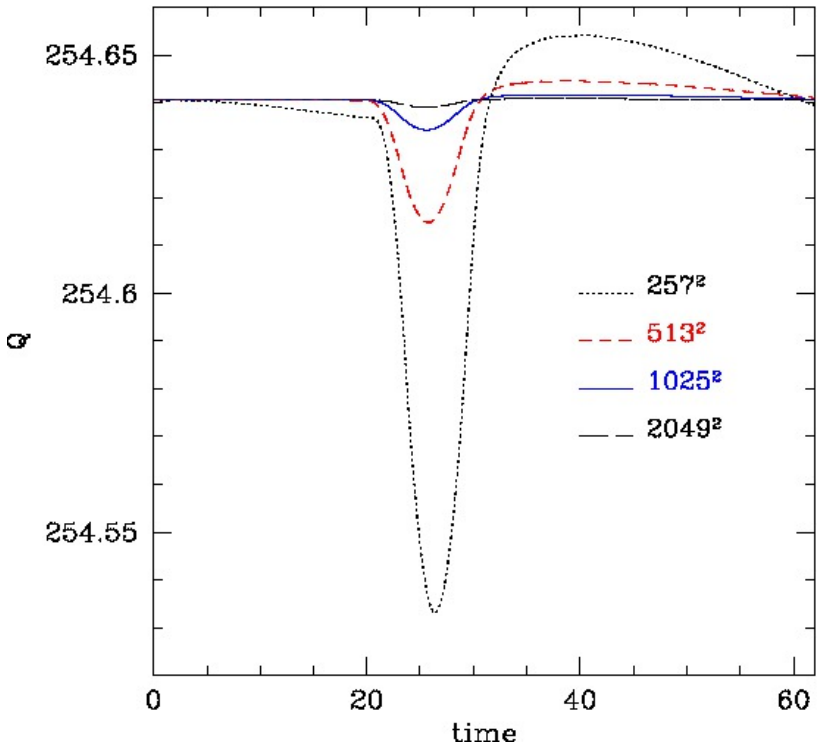

Figure 3.20: Evolution of the computed total charge, Q, for the Q^+ Q^+ collision described in Figs. 3.18. Convergence is evident as $h \to 0$, and we find that the rate of convergence is quadratic, as expected.

for adaptive calculations is more involved than it is for the unigrid case. The complications arise from the fact that the grid pattern in space and time is determined dynamically and automatically by the code, in an attempt to keep a measure of the local solution error (which, following Berger and Oliger, we will tend to call the local truncation error) below some specified threshold. Recall that the mesh refinement algorithm starts with some base grid, having mesh spacing h, that covers the entire computational domain. In order to perform a basic three-level convergence test we will need the results from calculations that use base grids with spacings h, $h/2$ and $h/4$, and we further require that the regridding patterns be the same for all of the computations. This last restriction ensures that the $h/2$ and $h/4$ calculations *are* true $2:1$ and $4:1$ refinements, respectively, of the computation carried out at scale h. To achieve such a set of computations we make use of a feature implemented in AMRD/PAMR and described in Sec. 2.3.9 of [121]. The code is first run in fully adaptive mode, with a base mesh spacing h, and a record of the regridding pattern is saved in a script. For the $h/2$ and $h/4$ calculations, the adaptivity is disabled and the regridding operations

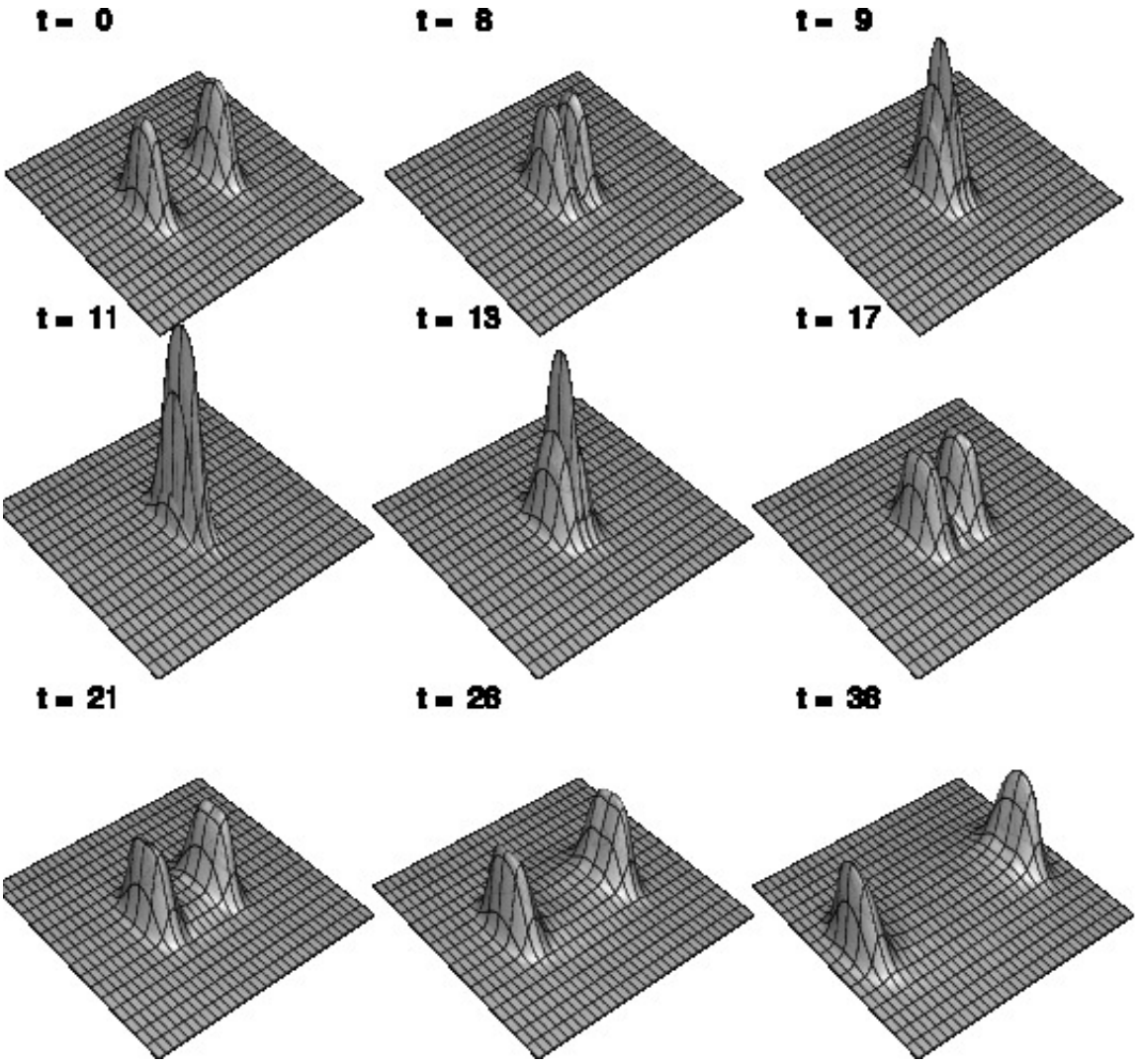

Figure 3.21: Evolution of the modulus $|\phi|$ for a Q^+ Q^- collision with $\gamma = 2.4$. This data comes from a unigrid run on a 50×50 domain, with a mesh resolution of 513×513. The Courant number was $\lambda = 0.2$ and the dissipation parameter was $\epsilon_{\rm KO} = 0.4$. At the level of detail visible in the plot the solitons emerge from the interaction unscathed.

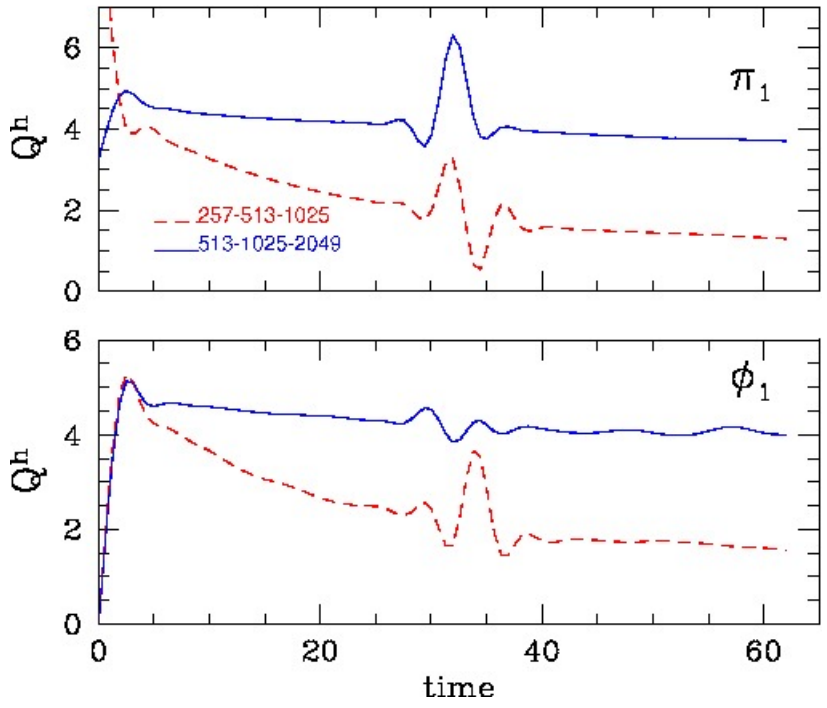

Figure 3.22: Computed convergence factors for the head-on Q^+ Q^- collision described in Fig. 3.21. We observe $O(h^2)$ convergence as $h \to 0$.

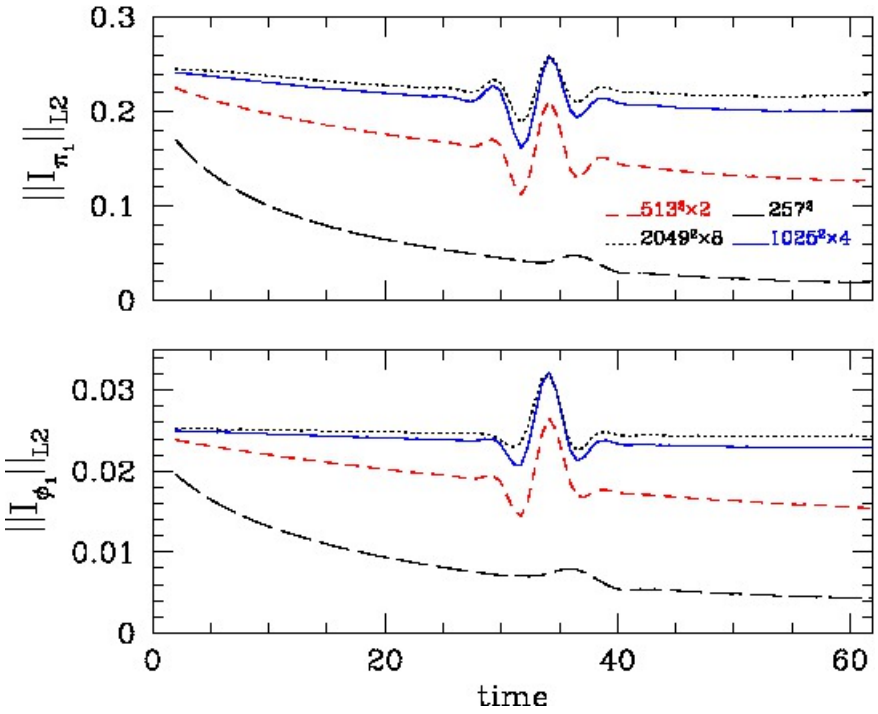

Figure 3.23: Rescaled l_2-norms of the independent residuals for the fields π_1 and ϕ_1 from the $\gamma = 2.4$, Q^+ Q^- collision described in Fig. 3.21. Again, the plots show the expected linear convergence as $h \to 0$.

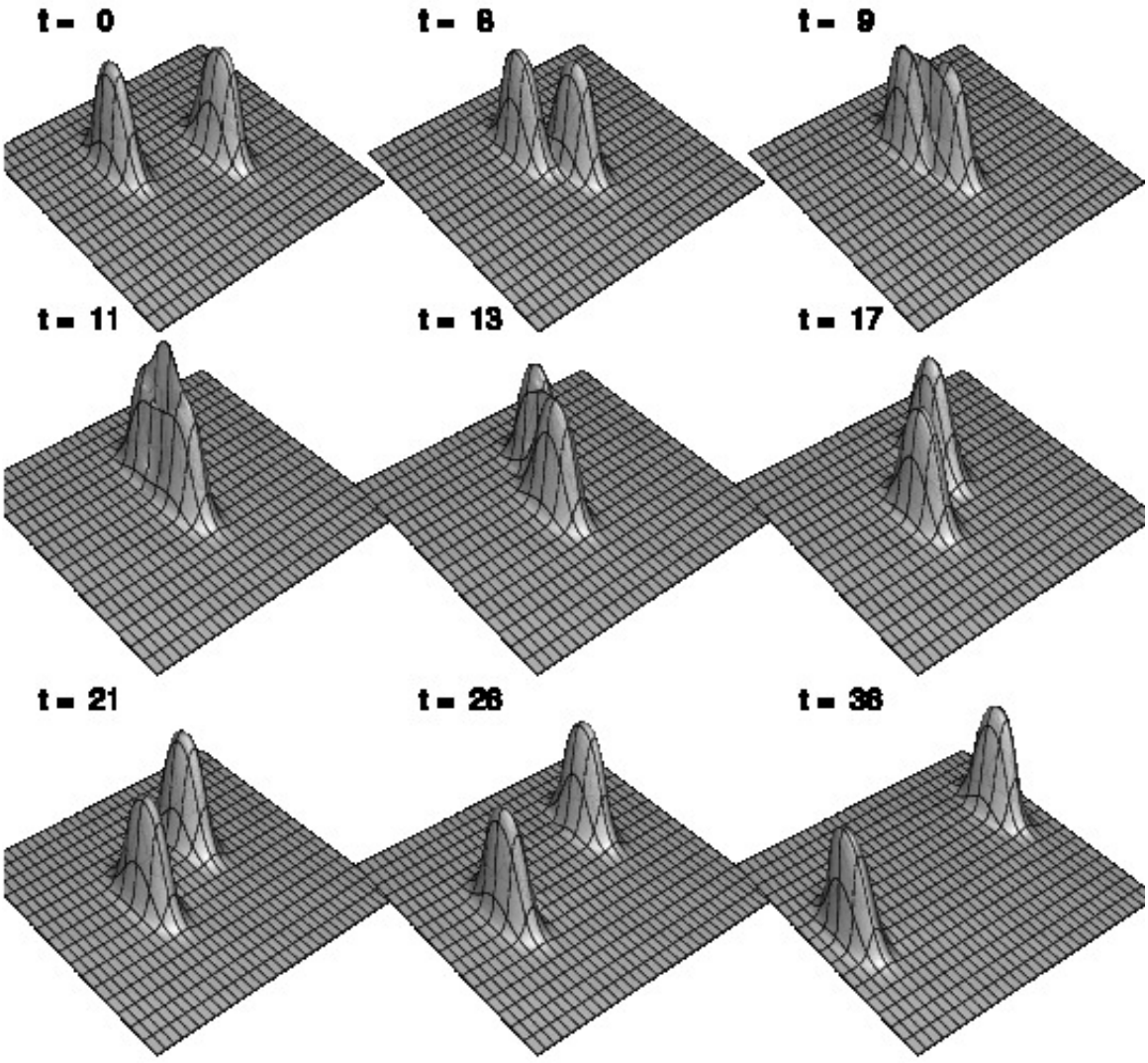

Figure 3.24: Evolution of the modulus $|\phi|$ for a grazing Q^+ Q^- collision at $\gamma = 2.4$, with impact parameter $b = 10$. The numerical parameters are the same as those listed in Fig. 3.21. It is evident that—at least at this velocity—the off-axis nature of the collision does not appreciably affect the dynamics of the Q-balls, which again emerge unscathed.

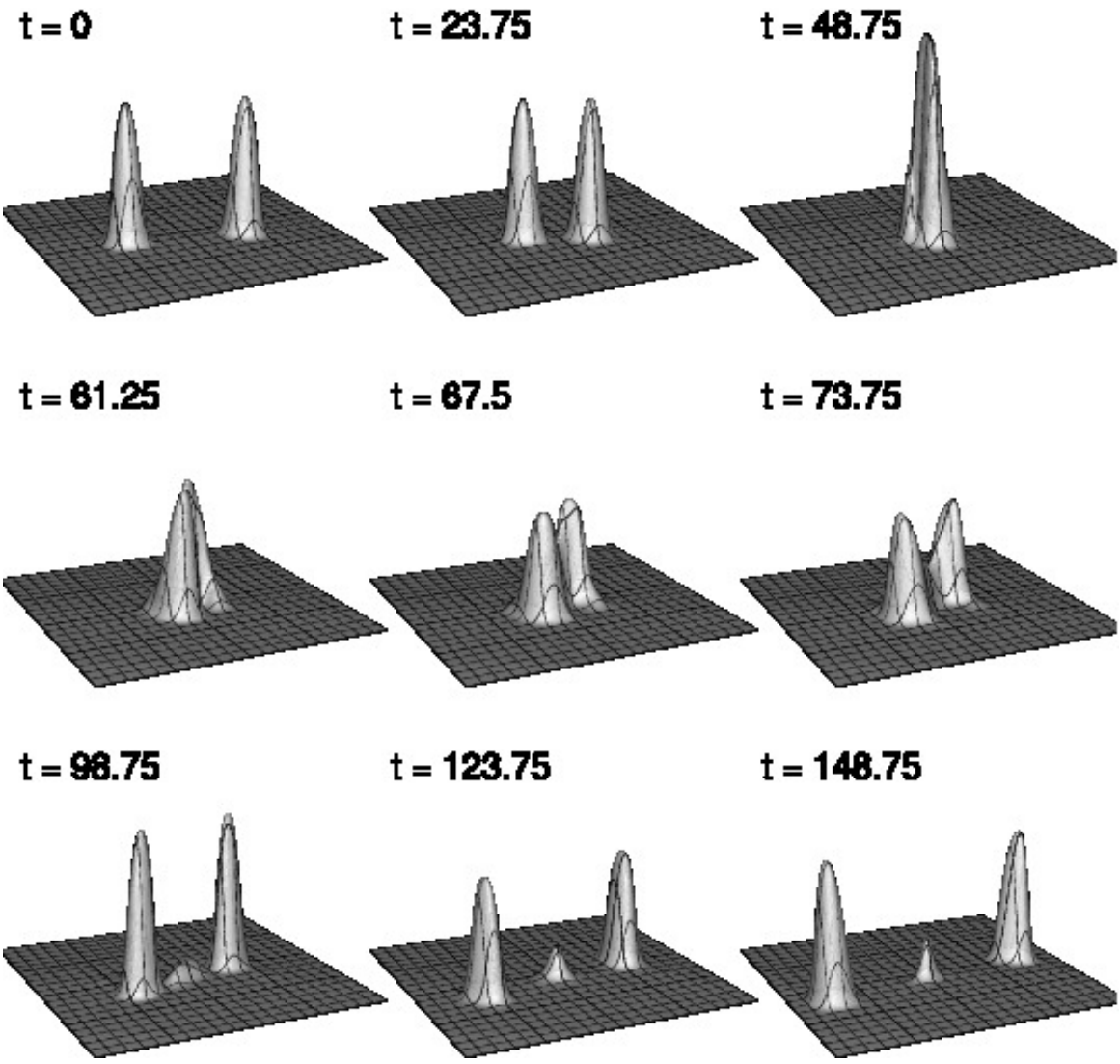

Figure 3.25: Evolution of the charge density, Q, for a grazing Q^+ Q^+ collision at $\gamma = 1.09$ ($v = 0.4$), and impact parameter $b = 8$. The numerical parameters are the same as those listed in Fig. 3.21. The Q-balls appear to lose some charge to a small "remnant" in the center, although the remnant is probably unstable. The same set-up with $b = 0$ leads to right-angle scattering. We note that each Q-ball has a diameter in the y direction ≈ 30. It is thus interesting that a small change in b seems to affect the outcome of the encounter dramatically. In particular, right-angle scattering appears to be largely a consequence of a very symmetric initial configuration.

are driven by the information in the script. The results from the three calculations can then be used to compute Q^h as usual.[21]

Following this prescription, we performed an AMR convergence test of our code using the Q^+ Q^- collision data described in the previous section (again, with $\gamma = 2.41$). The computations were carried out in a 40×40 box, with $\lambda = 0.3$, $\epsilon_{\rm KO} = 0.6$, and $\tau_{\rm max} = 5 \times 10^{-4}$. Following the notation introduced in Sec. 2.4, $L = 1$ had a resolution of 257×257, and the evolution reached $L_f = 4$ levels of refinement during the calculation. Results from the test are shown in Fig. 3.27, from which we see that convergence appears to be second order.

Fig. 3.27 compares the convergence factors for the AMR run with those from a set of unigrid calculations with comparable resolutions, namely 257×257, 513×513 and 1025×1025. Overall, the convergence behaviour is quite similar, although the fluctuations in Q^h during the time the Q-balls are interacting is somewhat smaller for the AMR calculations.

As mentioned in Sec. 2.4, AMRD/PAMR's implementation of the Berger and Oliger algorithm includes a number of key parameters that can be tuned in order to optimize code performance. Two of these which are related to one another are the regridding interval, $n_{\rm regrid}$, and the buffering width, $w_{\rm buffer}$. The first of these specifies the number of time steps to be taken on any level between regridding operations, while the second determines the width (in number of grid spacings) by which a region flagged as needing refinement is extended in each direction ($\pm x, \pm y$ in the 2D case). Assuming a maximum speed of signal propagation of 1 (which is true in our case), then provided that

$$\lambda\, n_{\rm regrid} < w_{\rm buffer} \tag{3.56}$$

where λ is the Courant factor, signals travelling out of the flagged region will remain within the (refined) buffered region until the next regrid operation. Adjustment of $n_{\rm regrid}$ and $w_{\rm buffer}$ amounts to an optimization process: increasing $n_{\rm regrid}$ reduces the regridding overhead, while increasing $w_{\rm buffer}$ adds to the overall computational cost of the calculation. For typical Q-ball collisions with $\gamma = 2.4$ or larger we found that $n_{\rm regrid}$ in the range 50 to 60 produced good results.

Another very important control parameter of the adaptive algorithm is the truncation error threshold, $\tau_{\rm max}$. In principle, this parameter, more than any other, controls the overall behaviour of the algorithm: in particular, decreasing $\tau_{\rm max}$ should result in better resolution of extreme solution

[21] However, due to limitations imposed by the utility we use to compute Q^h, we must first restrict the grid function values that are defined on the adaptive hierarchy to a (global) uniform grid.

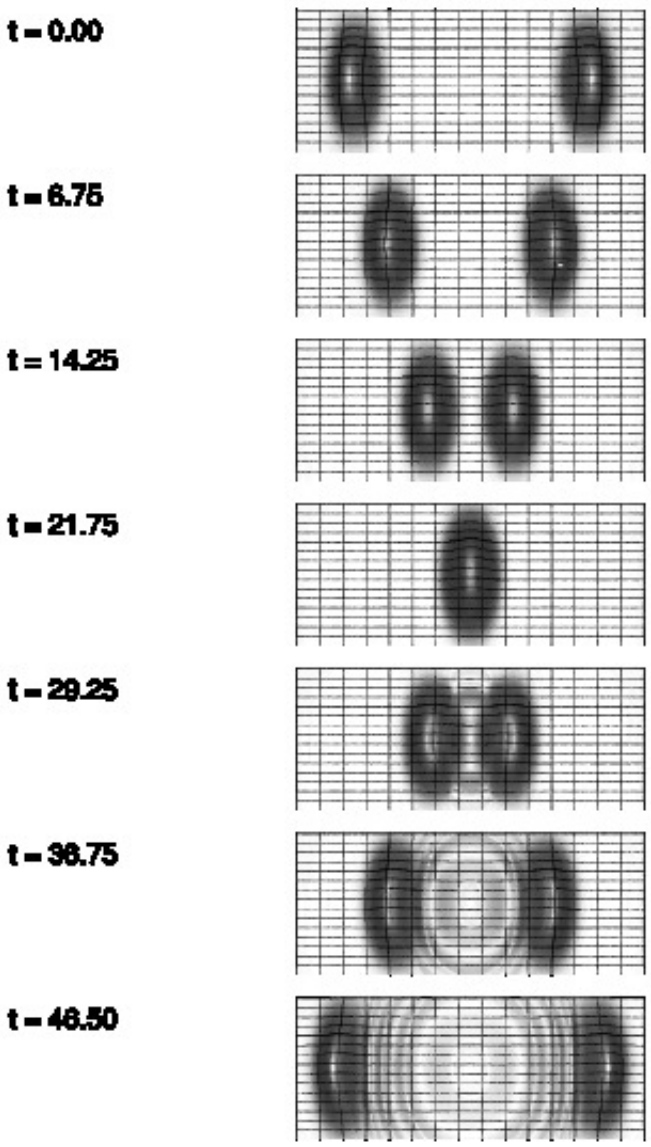

Figure 3.26: Top view of the evolution of the modulus, $|\phi|$, for a head-on Q^+ Q^- collision at $\gamma = 2.4$, and where AMR was used. The collision is almost elastic, except for the radiation released. The AMR parameters (see Sec. 2.4) were: 513×513 base level ($L = 1$), finest level $L_f = 4$ and truncation error threshold, $\tau_{\rm max} = 5 \times 10^{-4}$. The Courant number was $\lambda = 0.2$, the dissipation parameter was $\epsilon_{\rm KO} = 0.5$ and Dirichlet boundary conditions were used. Each snapshot has been clipped from the 60×60 complete domain to about 60×30 units.

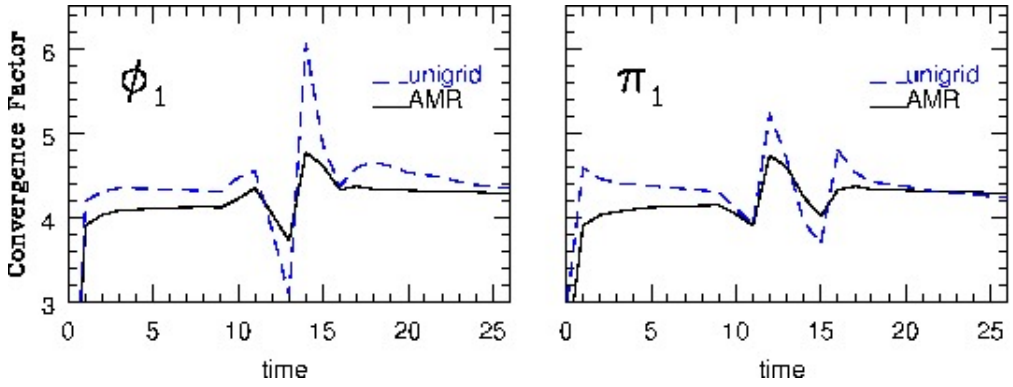

Figure 3.27: Comparison of the convergence factors from unigrid and AMR runs for a collision at $\gamma = 2.41$.

features, and in increased solution accuracy. However, we have not done much in the way of experimentation with $\tau_{\max}$ apart from determining a value for which good convergence was observed when evolving typical collision data.

3.6.1 Stability of Unigrid and AMR Calculations

Stability is a key issue in the solution of time-dependent PDEs using finite difference approximations, and the fact that the iterated Crank-Nicholson scheme has proven to be quite robustly stable in this context [115, 133, 119] was a prime motivating factor in our adopting it. In order to address the question of stability of our code, we performed experiments in which we varied the Courant factor for fixed initial data. We set the Kreiss-Oliger dissipation parameter to $\epsilon_{\rm KO} = 0.5$. For unigrid computations we observed that for $0.1 \leq \lambda \leq 0.6$, there was little, if any, variation in the stability or rate of convergence of the code. However, for adaptive calculations, we found that λ was restricted to significantly smaller values. For example, a typical AMR run for a $\gamma = 2.4$ collision that used 2 or 3 additional levels of refinement beyond a 513×513 base grid would become unstable for $\lambda \geq 0.4$. The instability would manifest itself as a nonconvergence of the overall pointwise Newton-Gauss-Seidel iteration that advances the difference solution from $t = t^n$ to $t = t^{n+1}$. Enabling additional levels of refinement exacerbated this problem: if a total of 5 levels were used, we found that we needed $\lambda \leq 0.2$. We were not able to definitively identify the source of this instability, although we suspect that it may be associated with the interpolation of values at fine grid boundaries (from coarse grids) that occurs in the Berger and Oliger algorithm.

3.6.2 Comparison of Equal-Charge and Opposite-Charge Collisions

We now compare collisions between Q-balls having opposite charge (a Q^+ Q^- collision, as considered thus far), and the same charge (a Q^+ Q^+ collision). Figs. 3.29 and 3.30 show edge-on snapshots of $|\phi(t,x,y)|$ for Q^+ Q^- and Q^+ Q^+ collisions, respectively, during intermediate times when the interaction of the Q-balls is most significant. The key qualitative difference that is evident from these plots is that the Q^+ Q^- case appears to exhibit purely constructive interference, while the Q^+ Q^+ collision shows signs of destructive interference.

Closer examination of the evolution of the field modulus $|\phi|$ reveals another interesting difference in the two types of collisions. Fig. 3.28 shows contour plots of $|\phi(t,x,y)|$ from the late stages of the two collisions (left panel, Q^+ Q^-; right panel, Q^+ Q^+). As was already seen in Fig. 3.26, the opposite-charge collision generates a small but significant amount of scalar radiation that seems largely absent in the Q^+ Q^+ case. Convergence testing strongly suggests that this is a genuine effect. We thus conclude that Q^+ Q^+ collisions are even more elastic than Q^+ Q^- ones.

Figs. 3.31–3.37 illustrate the most typical scattering patterns that Q^+ Q^+ and Q^+ Q^- collisions exhibit as a function of velocity The former were discussed in Sec. 3.5.1, and we reproduced these results using AMR runs, as shown in Figs. 3.31, 3.32 and 3.33. We note that there has been little reference to Q^+ Q^+ scattering in previously reported work [18, 72]. We investigated Q^+ Q^- scattering for the same dynamical regimes as for our earlier Q^+ Q^+ collisions and found that these produce significant residual outgoing scalar radiation, supporting the conclusion of the last paragraph about the elasticity of Q^+ Q^+ and Q^+ Q^- collisions. This is the case independently of the type of boundary condition used (Dirichlet or Sommerfeld). The evolution of the modulus $|\phi|$ for Q^+ Q^- interactions is illustrated in Figs. 3.34, 3.35 and 3.37. Below $\gamma = 1.09$ ($v = 0.4$), Q^+ Q^- initial data resulted in the formation of a bound state, with the Q-balls performing oscillations around the center of the collision. At $\gamma = 1.09$ ($v = 0.4$) the outcome of the interaction is quite complex, and it is difficult to determine a defined trend either towards forward or right-angle scattering. For larger boosts, forward scattering seems to be dominant, with little evidence of right-angle scattering. Nonetheless, the end state of the evolutions typically contains a significant amount of scalar radiation which complicates the identification of the actual Q-ball products. In order to shed some light on this issue, we looked at the evolution of the charge density for the collisions. Figures 3.36 and 3.38 show the time development of the charge density for Q^+ Q^- collisions at $\gamma = 1.09$ and $\gamma = 1.4$, respectively. These results provide a much clearer picture of

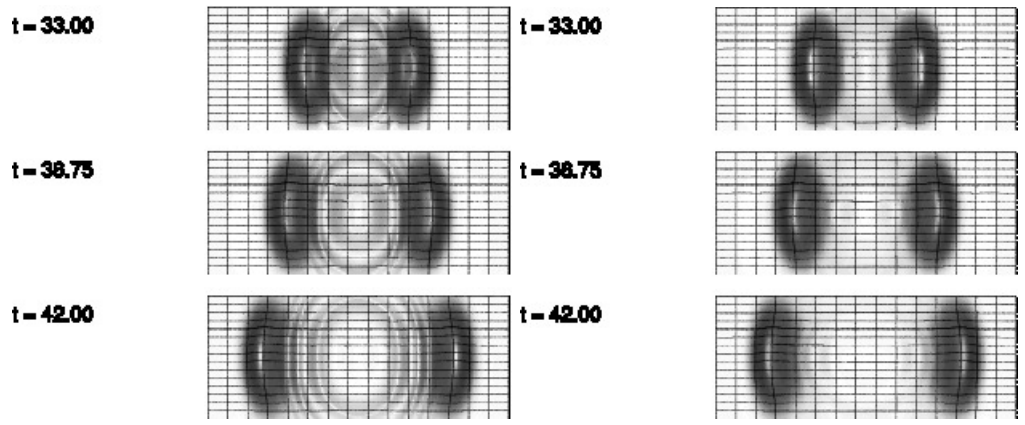

Figure 3.28: Late stages of AMR calculations for Q-ball collisions with $\gamma = 2.41$. At these times the Q-balls are receding from one another. The sequence on the left shows a $+Q - Q$ calculation (opposite charge), while the one on the right displays a $\pm Q \pm Q$ computation (same charge). Radiation is observed in the opposite-charge case, and we believe this a genuine physical effect since the pattern converges as the resolution is increased. Generally, collisions between Q-balls with the same charge are "cleaner", than those with opposite charges; again, the latter usually emit radiation, and are thus less elastic. Each snapshot of the collision has been clipped from the 60×60 computational domain, to about 60×15 units. The AMR parameters here are a 257×257 base grid, $L_f = 4$ and $\tau_{\max} = 10^{-4}$.

the interaction. In particular, since scalar radiation does not carry charge, effects from radiation do not appear in the plots of the charge density. From the plots of Q we unambiguously conclude that $Q^+\ Q^-$ collisions always exhibit forward scattering.

We have made a crude effort to assess the degree of elasticity of $Q^+\ Q^+$ collisions by estimating the post-interaction speeds of the Q-balls. For example, we simulated a $Q^+\ Q^+$ collision with $\gamma = 3.2$ ($v = v_0 = 0.95$) in a 50×50 box, and with the Q-balls initially centred at $(x_1, y_1) = (-20, 0)$ and $(x_2, y_2) = (20, 0)$.

By tracking relative maxima in $|\phi(t, x, y)|$, we estimate the time t_A at which one of the Q-balls reaches the center of the computational domain, as well as the time t_B when the Q-ball reaches the starting position of its counterpart. Estimates of the average velocities in the intervals $0 \le t \le t_A$ and $t_A \le t \le t_B$ are then given by $v_A = 20/t_A$ and $v_B = 20/(t_B - t_A)$ respectively. We found $t_A \approx 21.25$ and $t_B \approx 42.5$, yielding $v_A \approx 0.94$ and $v_B = 0.95$—which is to be compared with the initial velocity $v_0 = 0.95$. Another computation with $\gamma = 5.0$ ($v = v_0 = 0.98$) gave $t_A = 20.625$ and $t_B = 41.25 - 20.625 = 20.625$. The estimated velocities were $v_A = v_B \approx 20/20.625 = 0.97$. These estimates provide additional support for the claim that high energy head-on collisions of Q-balls are increasingly elastic for larger and larger relative velocities.

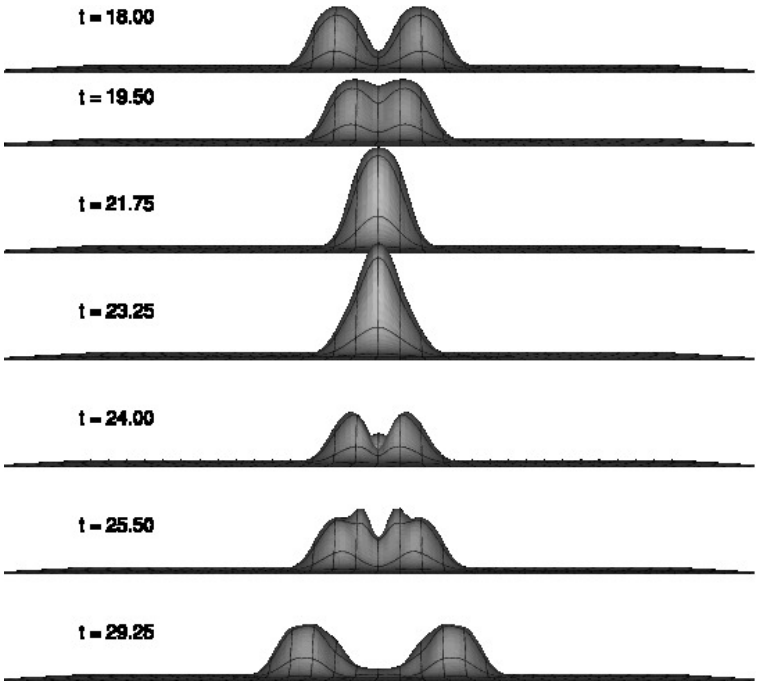

Figure 3.29: Central stages of a $\gamma = 2.41$ collision between two Q-balls with equal and opposite charges. During the interaction a transient state that looks like a larger Q-ball develops. The calculation used AMR with a 257×257 base grid, $L_f = 4$ and $\tau_{\max} = 8 \times 10^{-4}$.

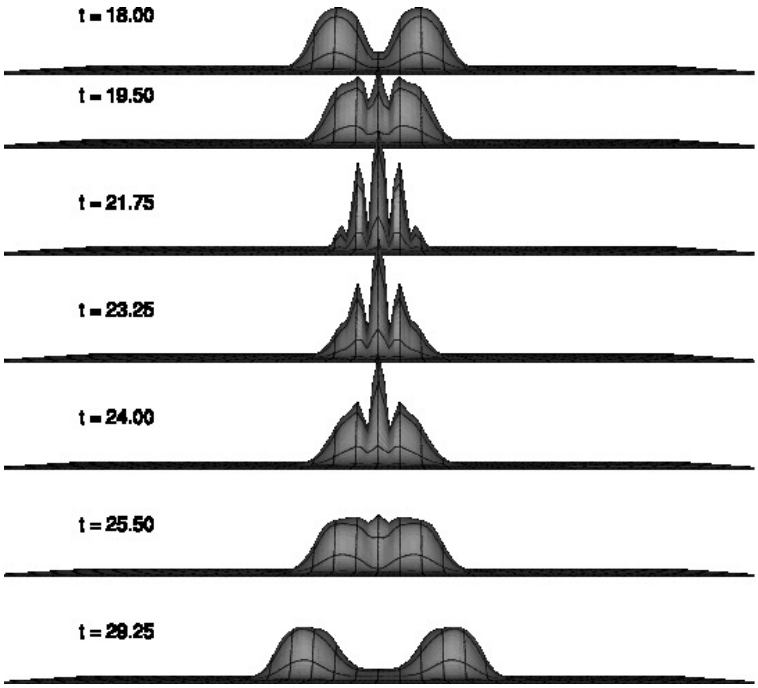

Figure 3.30: Central stages of a $\gamma = 2.41$ collision between two Q-balls with the same charge. In contrast to what is seen in Fig. 3.29 for oppositely-charged Q-balls, an interference pattern is observed during the interaction.

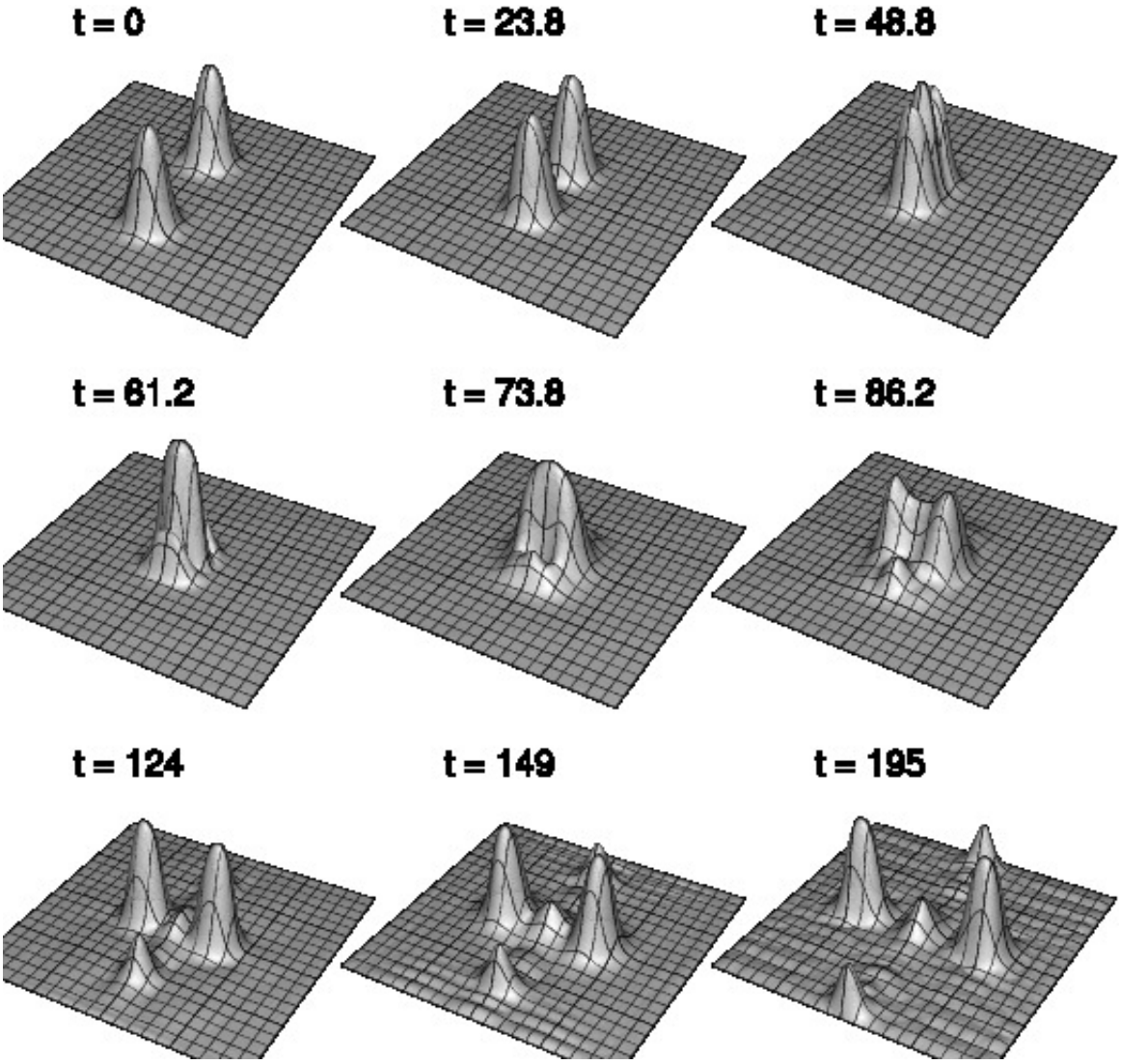

Figure 3.31: Scalar field modulus, $|\phi|$, for a Q^+ Q^+ collision at $\gamma = 1.04$ ($v = 0.3$). For the range of low velocities, $0 < v \leq 0.3$, we observe right-angle scattering as in the case illustrated here: this is similar to what is seen in the collision of topological solitons. The plots also show the development of a small "remnant" Q-ball—which is at rest at the centre of the computational domain—as well as an additional pair of small Q-balls that are forward-scattered. This phenomenology has previously been reported in [18, 72]. For this and the subsequent collision experiments described in this section and illustrated in Fig. 3.31 to Fig. 3.37 we used AMR with a fixed set of control parameters. Specifically, we used a base mesh with 257×257 points, $L_f = 4$ and $\tau_{\rm max} = 5 \times 10^{-5}$. In addition we imposed Dirichlet boundary conditions (unless otherwise stated) and set the Kreiss-Oliger dissipation parameter to $\epsilon_{\rm KO} = 0.5$ (we could also achieve stable evolution with $\epsilon_{\rm KO} = 0.0$). The computational domain was $[-25, 25] \times [-25, 25]$ and the Q-balls were initially centred at $(-20, 0)$ and $(20, 0)$. The domain and starting locations are also the same in the calculations described in the rest of this subsection.

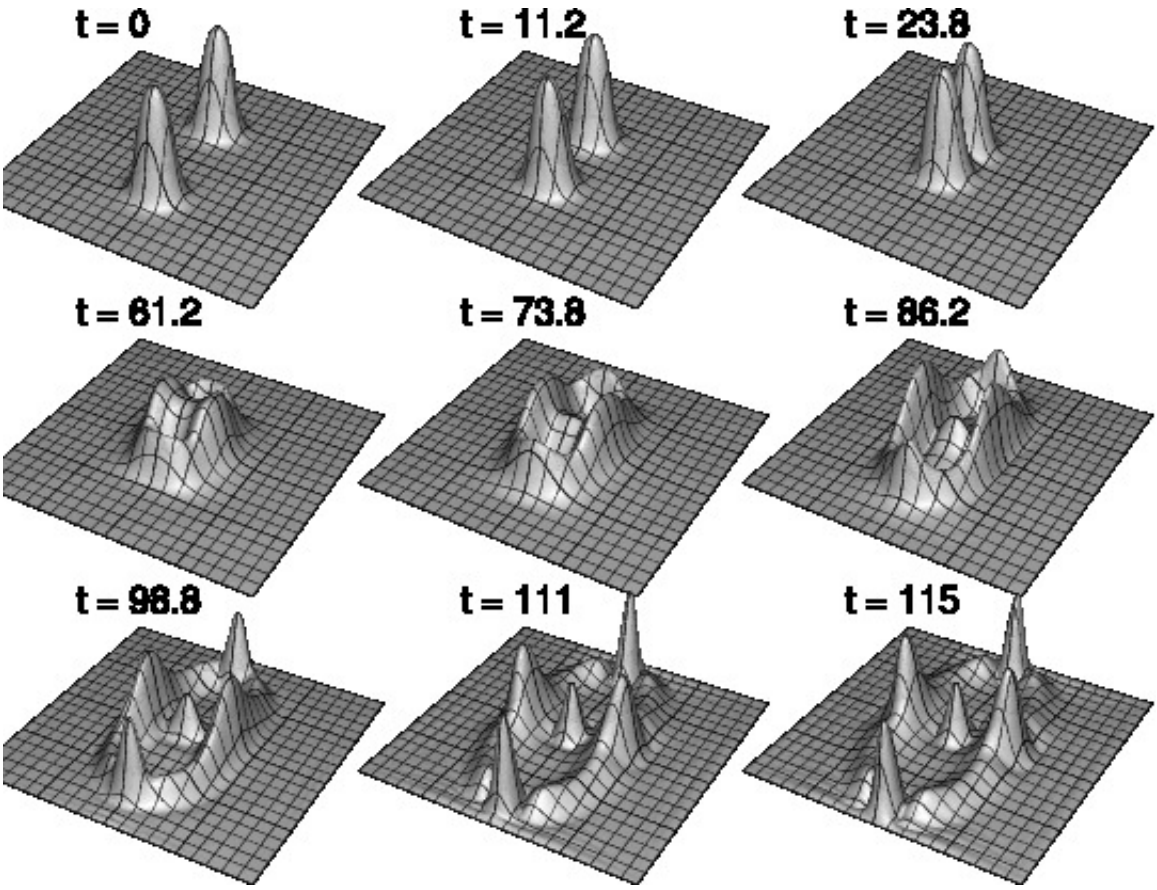

Figure 3.32: Scalar field modulus, $|\phi|$, for a Q^+ Q^+ collision at $\gamma = 1.15$ ($v = 0.5$). For an intermediate range of velocities $0.3 < v < 0.7$, Q^+ Q^+ scattering produces a mixed end state, with both forward and right angle scattering. On the time scales simulated, we find a small residual Q-ball remaining in the center of the computational domain, while the rest of the collision products eventually escape through the domain boundaries. We refer to this mixed scattering as *fragmentation*. Similar results were previously reported in [18]. The relative size of the Q-balls that are forward- or right-angle scattered depends on the initial velocity. At low velocities the right-angle products are larger than the forward ones, while the situation is reversed for higher velocities (close to $v = 0.7$). The field excitations that join the different Q-balls eventually dissipate.

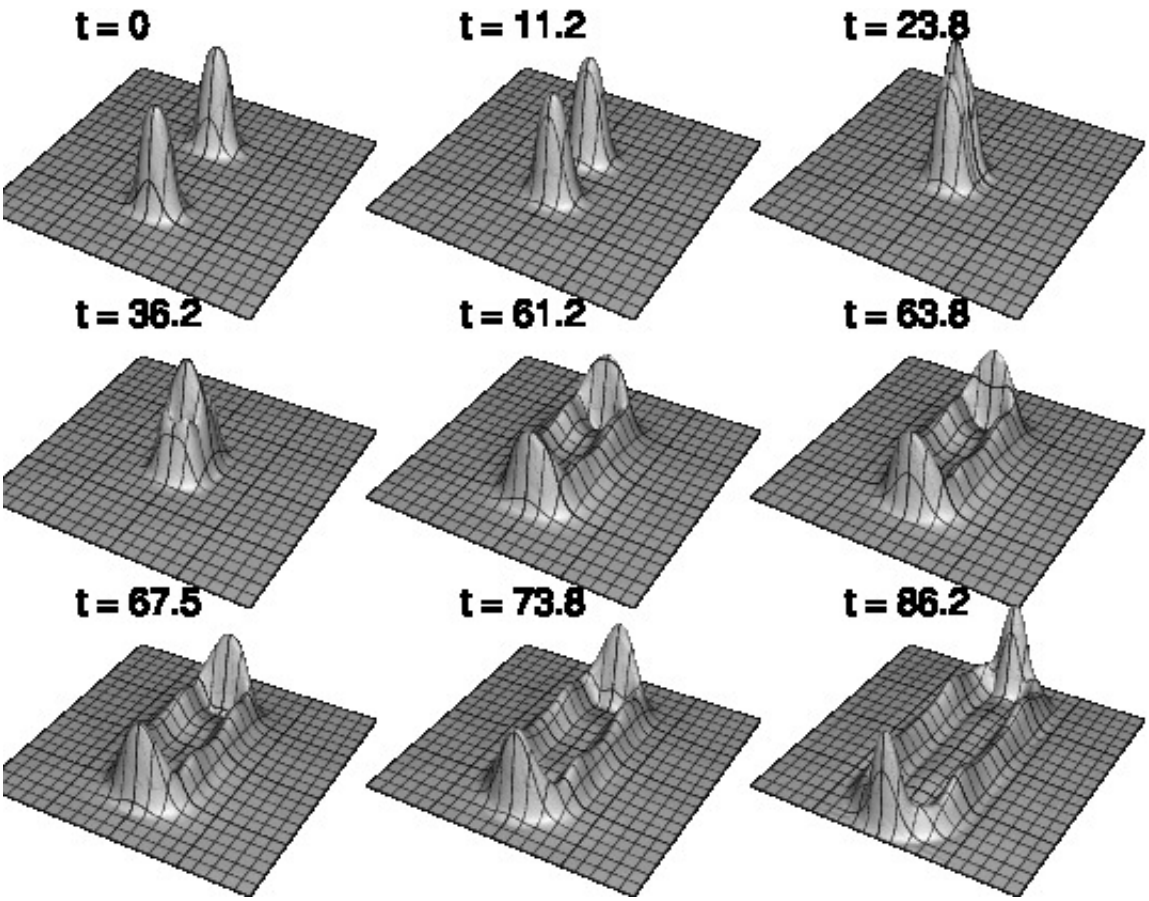

Figure 3.33: Scalar field modulus, $|\phi|$, for a Q^+ Q^+ collision at $\gamma = 1.4$ ($v = 0.7$). For velocities above $v = 0.7$ ($\gamma = 1.4$)—a Q^+ Q^+ collision exhibits almost purely forwarding scattering. The process is quite elastic, with the solitons emerging from the interaction mostly unscathed. This behaviour is to be expected since the soliton potential and rest mass energies are much smaller than the kinetic energy at high γ. Similarly to the mixed scattering case shown in Fig. 3.32, the waves between the Q-balls eventually dissipate.

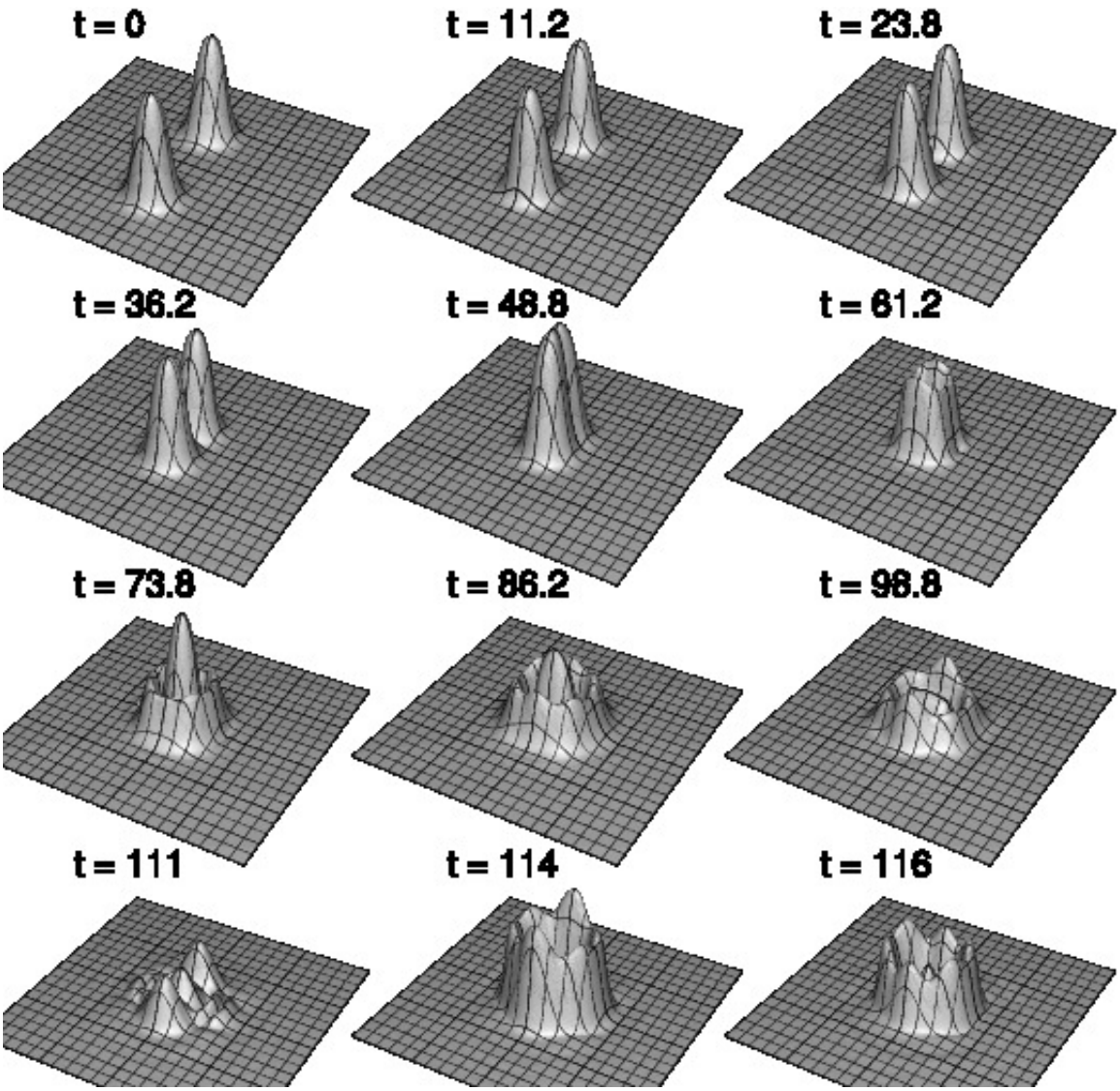

Figure 3.34: Scalar field modulus, $|\phi|$, for a Q^+ Q^- collision at $\gamma = 1.04$ ($v = 0.3$). In this instance—and, more generally, for initial velocities below $\approx v = 0.4$—the Q-balls fuse and form an oscillatory bound state. This can be understood in terms of an effective trapping potential that results from the attractive interaction between Q-balls with charges of opposite sign: here the kinetic energy initially imparted to the Q-balls is insufficient to allow them to escape the trap.

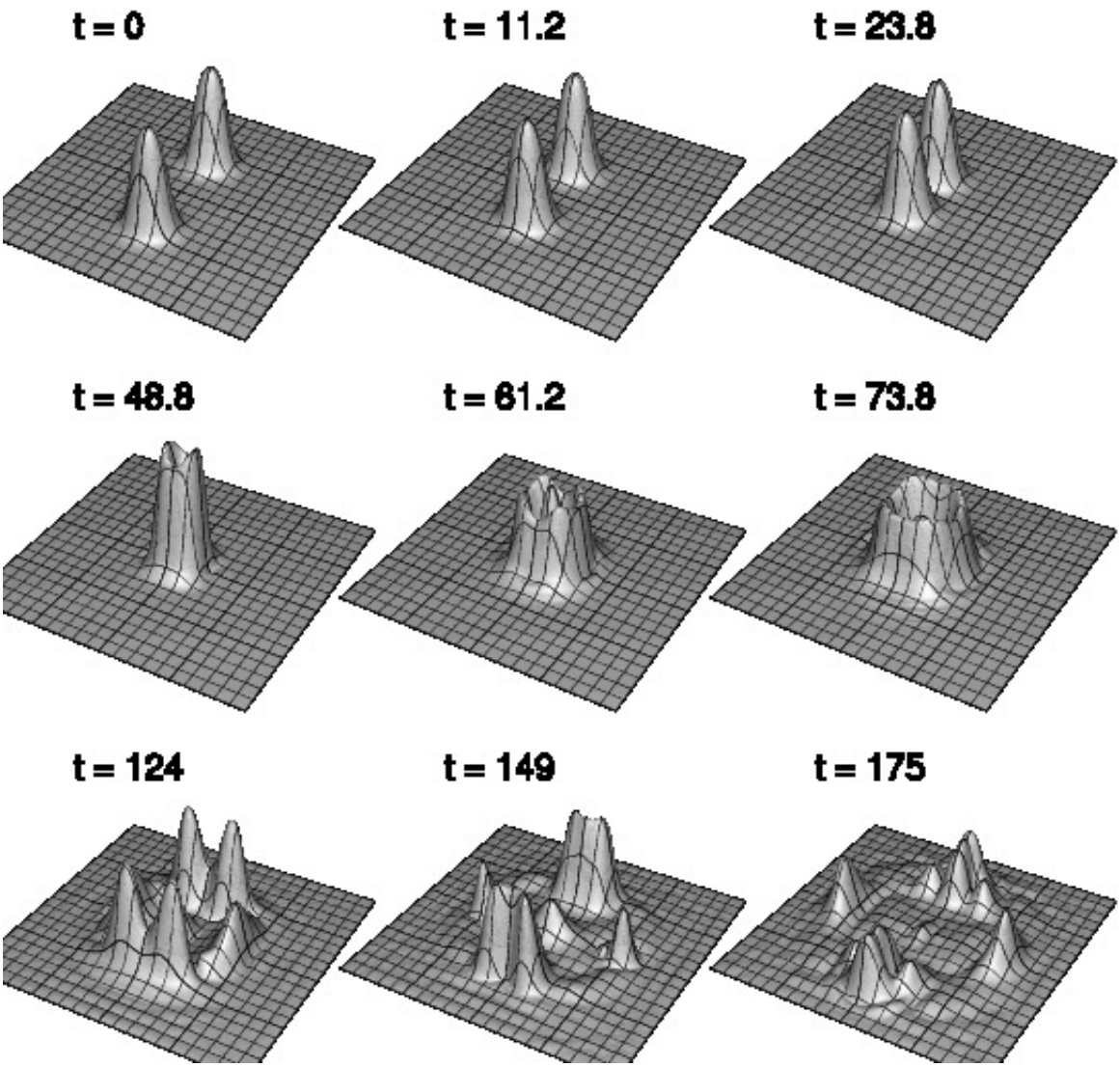

Figure 3.35: Scalar field modulus, $|\phi|$, for a Q^+ Q^- collision at $\gamma = 1.09$ ($v = 0.4$). The dynamics in this case is quite complex, and at late times it is difficult to distinguish between outgoing radiation, and scattered Q-balls (both right-angle and forward).

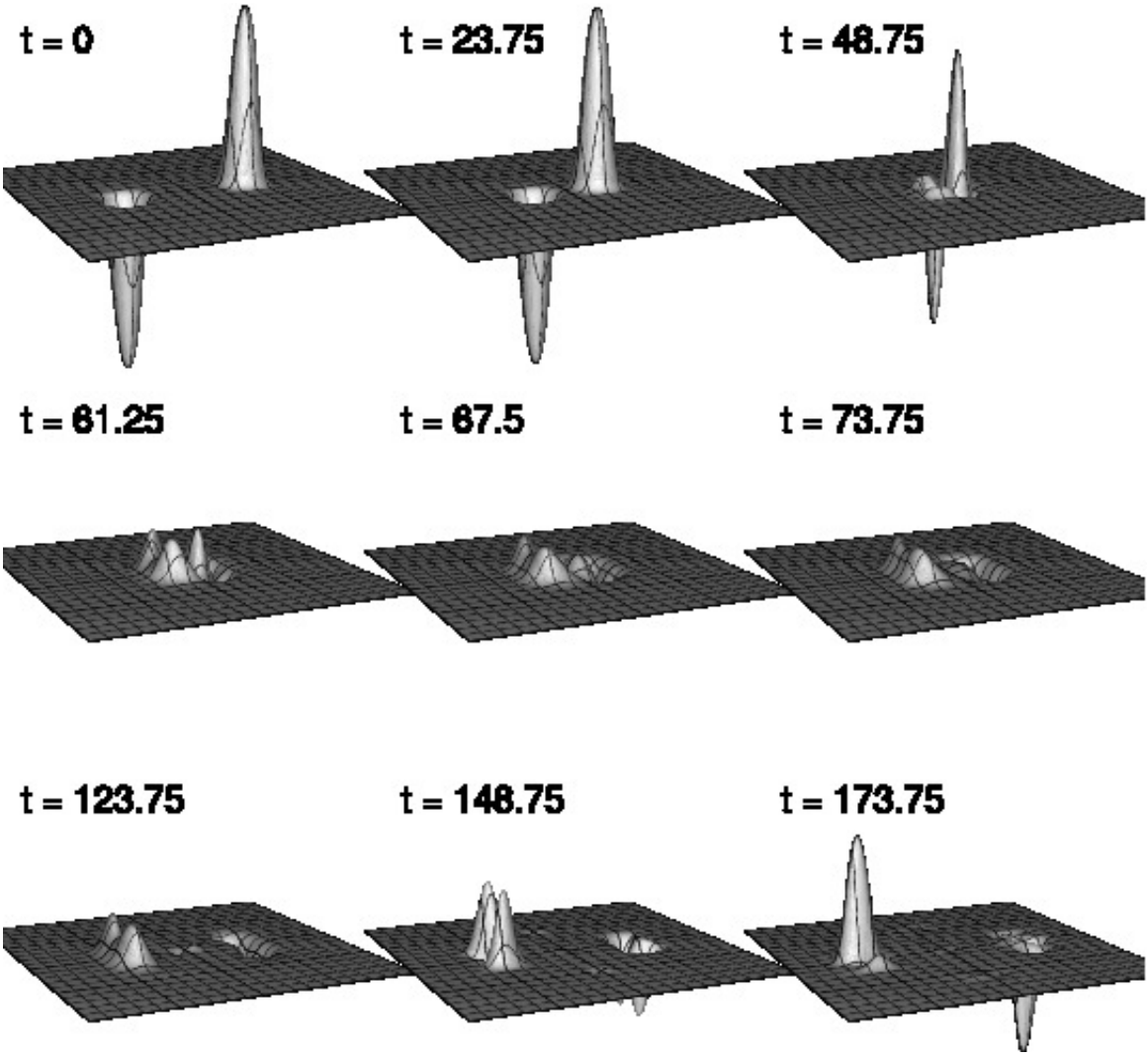

Figure 3.36: Charge density, Q, for a Q^+ Q^- collision at $\gamma = 1.09$ ($v = 0.4$). In contrast to the previous plot of $|\phi|$ from the same calculation (except that outgoing radiation conditions are used here) it is evident from this sequence that the collision describes a primarily forward-scattering process. The opposite signs of the Q-ball charges can also be clearly inferred. We note that many of the features appearing in the $|\phi|$ plot do not appear here, indicating that the corresponding excitations do not carry charge (this is also the case for the scalar radiation that is seen in some of the previous figures).

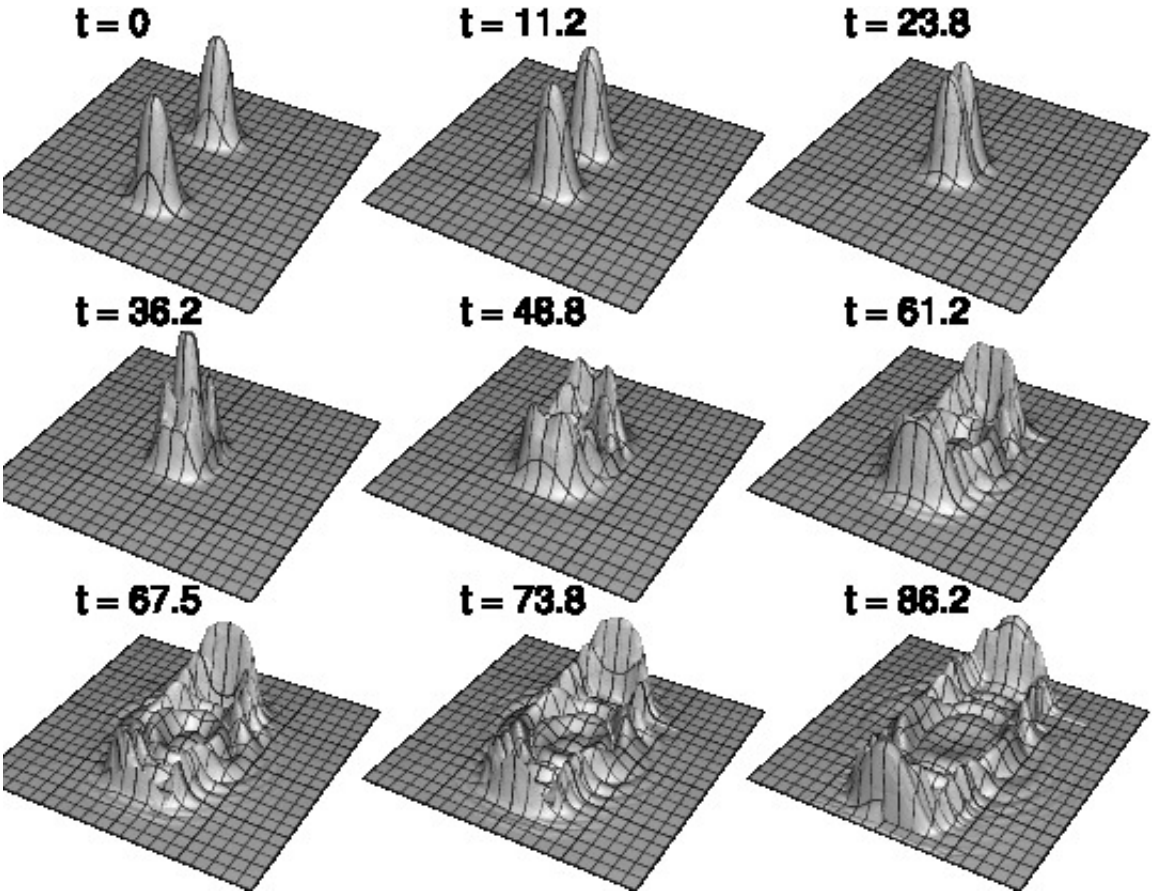

Figure 3.37: Scalar field modulus, $|\phi|$, for a Q^+ Q^- collision at $\gamma = 1.4$ ($v = 0.7$). For initial velocities $\gamma \geq 1.4$ ($v \geq 0.7$) the forward-scattering nature of the interaction becomes evident in the plot of the modulus. (this was also the case for Q^+ Q^+ collisions, where the velocity threshold was approximately the same). Again, this is an indication of kinetic-energy dominance of the process. Relative to the Q^+ Q^+ collisions, there seems to be more radiation emitted here, an effect that was previously seen in Fig 3.26. This provides additional support for the claim that Q^+ Q^+ collisions are more elastic than Q^+ Q^- ones.

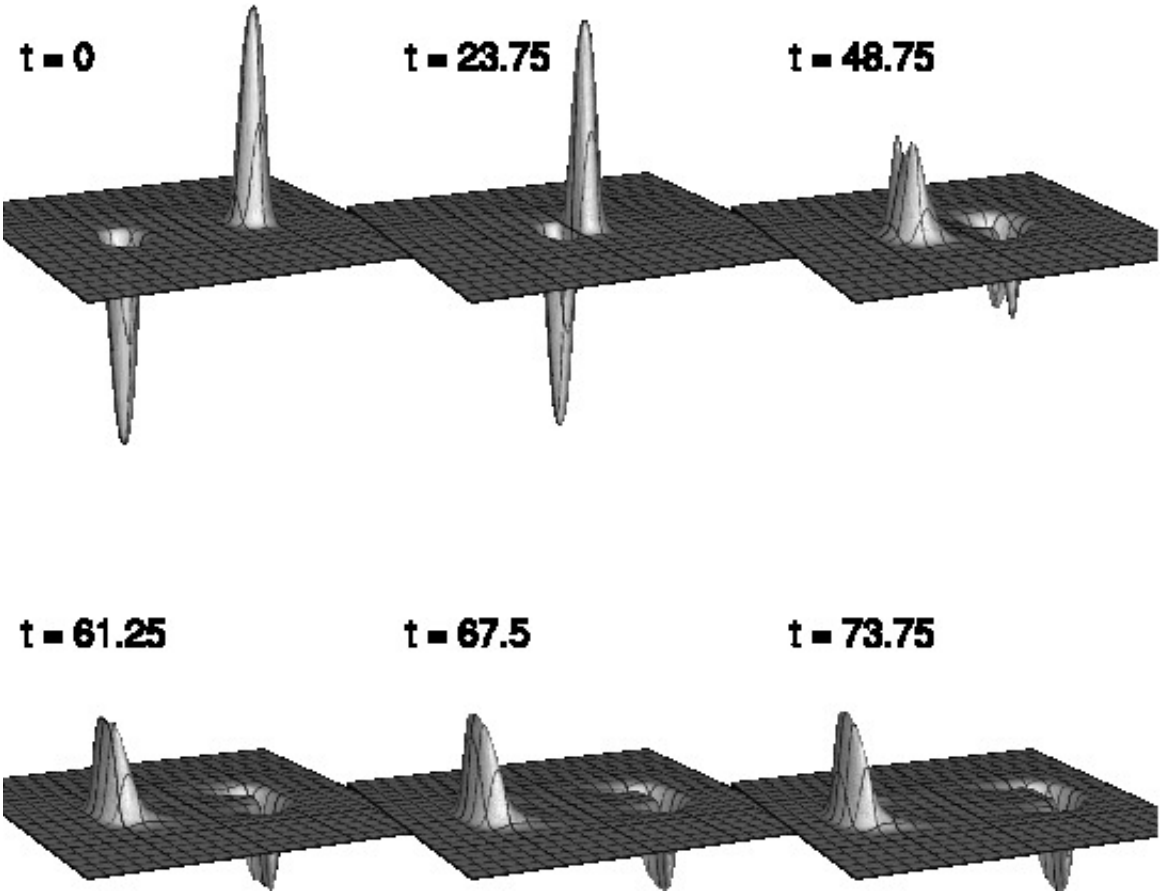

Figure 3.38: Charge density, Q, for the Q^+ Q^- collision at $\gamma = 1.4$ ($v = 0.7$) described in the previous figure. Again, examination of the evolution of Q gives a clear picture of the forward-scattering nature of the interaction. Outgoing radiation conditions were used in the computation.

3.6.3 Q-ball Collisions with Varying Q

So far our numerical experiments have used only a single static profile, namely the configuration with $\omega \approx 0.7739293$ as listed in Table 3.1 of Sec. 3.2.1. It is of interest to ask if evolutions involving other Q-ball solutions defined by that table result in similar dynamics. We thus performed a set of AMR experiments to investigate this issue. The $\sigma(r)$ profiles of the additional configurations that we considered are shown in Fig. 3.39, along with the corresponding values of ω and Q. Note that all of the configurations have about the same size (≈ 10) for a fairly wide range of charges ($Q = 2.8$–127).

The numerical experiments involved head-on Q^+ Q^+ and Q^+ Q^-, equal-Q collisions (i.e. both participants had the same value of Q) with Q varying from 2.8 to 127.3, and with γ in the range $1.005 \leq \gamma \leq 5$ ($0.1 \leq v \leq 0.98$). A very interesting feature emerged from the calculations. For charge values below $Q = 71.3$ ($Q = 2.8$, 8.2 and 26.6) and for both the Q^+ Q^+ and Q^+ Q^- cases, we saw neither right-angle scattering nor fragmentation, but only forward scattering. For values of $\gamma < 0.2$ the Q-balls form a bound, oscillatory state, while for larger velocities, we observe only forward scattering. We note that Multamäki and Vilja [97] have previously reported the absence of right angle scattering—even at low velocities—for a Q-ball model whose potential includes both polynomial and logarithmic terms. At first glance this seemed surprising, but our current results with low Q configurations seem consistent with their results. We will return to this issue in the context of the baby Skyrme model in Sec. 4.5.

3.7 Q-ball Scattering by a Potential Obstruction

One of the most interesting aspects of the dynamics of Q-balls is scattering by obstacles, which we will define here to be obstructions that are generated through *ad hoc*, position-dependent modifications of the scalar field's self-interaction potential. These obstacles can take the form of barriers, wells, etc. and which aspects of Q-ball phenomenology—such as wave/particle "duality"[22]—are seen will depend on the precise nature of the obstruction. Although there is substantial literature on the interaction of topological solitons with obstructions—in particular, see the extensive work due to Collins and Zakrzewski [98]—there has not been much research that uses Q-balls. A notable

[22]We emphasize that the notion of wave/particle duality that we use here is different from that encountered in quantum mechanics. In our case, the notion of "particle" corresponds to a "solitonic" solution of a nonlinear PDE, while the "wave" nomenclature appeals to the fact that the PDE generally describes wave-like behaviour (i.e. is of hyperbolic type).

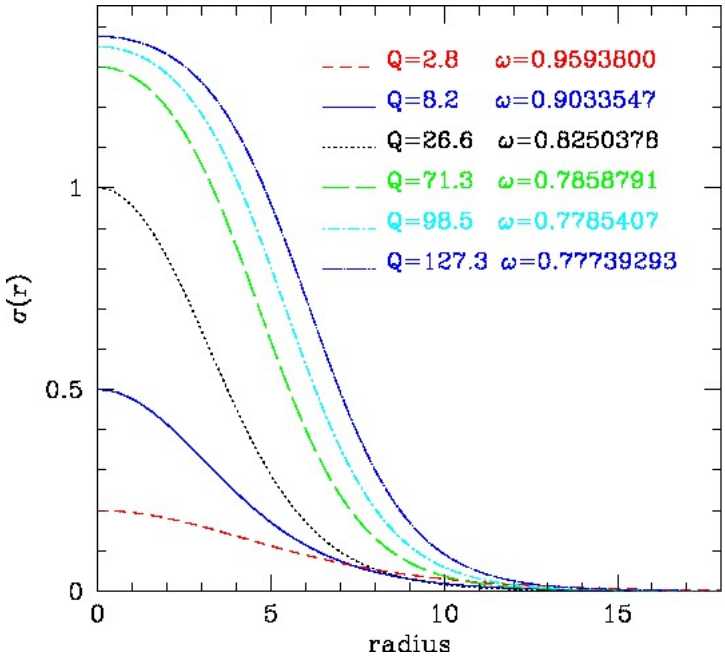

Figure 3.39: Profile functions of Q-ball solutions for different values of ω, previously listed in Table 3.1. The charge, Q, decreases as ω increases. We compared the dynamics of Q-balls of varying Q, and we found that right-angle scattering is completely absent from the dynamics of small Q-balls, specifically for $Q \lesssim 71.3$.

exception is the study by Al-Alawi and Zakrzewski [99] who considered the relativistic scattering of Q-balls in both $1+1$ and $2+1$ dimensions, for different values of the Q-ball internal phase ω. They found that the $1+1$ case was very similar to the topological one, provided that the Q-balls remained dynamically stable. They determined the critical velocity necessary to overcome a given barrier or hole, of a specified height or depth, respectively, and found that the critical velocity was also a function of the charge (ω) of the Q-ball. They also observed that some Q-balls became unstable and fragmented into smaller ones. This type of fragmentation is not possible in the topological case, where the solitons have specific (quantized) charges. On the other hand, their investigations in $2+1$ were limited to determination of the deflection angles for scattering of a Q-ball against a localized hole or barrier. The maximum γ they used was 1.02 ($v = 0.2$).

We note that the calculations reported in [99] used grid sizes of the order of 300×300, with a mesh spacing $h = 0.1$ and $\lambda = 0.2$. The Q-balls used had typical diameters ≈ 6. Further details on the numerics, such as the FDA scheme, were not discussed.

In this section we report results that extend the study of Al-Alawi and Zakrzewski to higher energies, using Q-balls boosted to γ of the order of 2 to 3. A main aim of this work is to see

whether high energy Q-balls still fragment into stable end-products following interaction with an obstacle. As usual we will provide evidence through convergence tests and monitoring of conserved quantities that our results are trustworthy.

Following [99] we implement a potential obstacle as follows. Consider the equations of motion (3.23). We modify the self-interaction potential of the complex field by introducing a position-dependent (but time-independent) multiplicative *obstacle function*, $\Sigma(x, y)$, yielding new evolution equations for the π_a variables:

$$\frac{\partial \pi_1}{\partial t} - \frac{\partial \phi_1}{\partial x} - \frac{\partial \phi_1}{\partial y} + \Sigma(x,y)\left(\phi_1 - |\phi|\phi_1 + B|\phi|^2\phi_1\right) = 0 \tag{3.57}$$

$$\frac{\partial \pi_2}{\partial t} - \frac{\partial \phi_2}{\partial x} - \frac{\partial \phi_2}{\partial y} + \Sigma(x,y)\left(\phi_2 - |\phi|\phi_2 + B|\phi|^2\phi_2\right) = 0 \tag{3.58}$$

The specific form of the obstacle function that we adopt is defined by three parameters, $X_{\min}$, $X_{\max}$ and H:

$$\Sigma\left(x, y; X_{\min}, X_{\max}, H\right) = \begin{cases} H & \text{If } X_{\min} \leq x \leq X_{\max} \\ 1 & \text{Otherwise} \end{cases} \tag{3.59}$$

Loosely speaking, we can view H as the "height" of the obstacle, and we note that in the region where $\Sigma\left(x, y; X_{\min}, X_{\max}, H\right) \neq 1$ (i.e. for $X_{\min} \leq x \leq X_{\max}$), which is the part of the domain occupied by the obstruction[23], the original Q-ball configurations are no longer stationary solutions of the (modified) equations of motion.

We now turn to the results and convergence properties of some numerical experiments involving the scattering of boosted Q-balls against obstacles of the form (3.59).

3.7.1 Unigrid Calculations for Potential Barriers

Potential barrier $H = 2$, $\gamma = 2.4$

Our first simulation used a potential barrier of unit width and height $H = 2$, located slightly to the right of the centre of a 50×50 computational box: the obstacle function was thus $\Sigma(x, y; 0.0, 1.0, 2)$. The initial data consisted of a single boosted Q-ball (once again with $\sigma_0 = 1.375$) centred at $(-20, 0)$. The boost parameter was $\gamma = 2.4$, the Courant number was $\lambda = 0.2$ and no Kreiss-Oliger dissipation was used, i.e. $\epsilon_{\rm KO} = 0.0$.

As can be seen from Fig.3.40, it appears that the initial Q-ball fragments into two stable

[23] In our coordinate system, the origin $(0, 0)$ is always located at the center of the domain

products after encountering the barrier at this velocity. Most of the original soliton penetrates the barrier, and a small Q-ball is reflected. No outgoing scalar radiation is observed. The convergence factors for the representative fields ϕ_1 and π_1 are shown in Fig. 3.42. We observe second order convergence in the Q^h for high enough resolution, and the independent residuals of both fields (Fig. 3.43) show first order convergence. The Q-ball collides with the barrier at $t \sim 21$, and convergence degrades somewhat during the collision.

Potential barrier $H = 10$, $\gamma = 2.4$

We increased the barrier parameter to $H = 10$ (so the obstacle function becomes $\Sigma(x, y; 0.0, 1.0, 10)$) and left the rest of the parameters as above. The exception is that we used $\epsilon_{\rm KO} = 0.6$ since a non-zero value of the dissipation parameter improved convergence, especially at high resolution. Repeating the scattering experiment, we found this time that—not surprisingly—most of the Q-ball reflected back from the barrier while only a small component penetrated to the other side (Fig. 3.44). The convergence properties of this experiment are shown in Figs. 3.46 and 3.47. We observe that the deviation from $O(h^2)$ convergence ($O(h)$ for the independent residuals) during the encounter is more pronounced than for the $H = 2$ case.

Potential barrier $H = 10$, $\gamma = 3.5$

For the next experiment we increased the boost of the Q-ball to $\gamma = 3.5$, keeping the same obstacle function, $\Sigma(x, y; 0.0, 1.0, 10)$. In this case we performed the computation in a 40×40 box, since the Q-ball length in the boost direction x is significantly more contracted than for the previous two experiments. The use of the smaller domain yields higher resolutions at fixed grid sizes (these are unigrid calculations and practical concerns limit us to a maximum grid size of 2049×2049) which aids in keeping the solution error reasonable.

With this setup we again find an end state describing one Q-ball that has penetrated the barrier, and another of smaller amplitude that has reflected from it (see Fig. 3.48). Both end products are stable, and no scalar radiation is observed. The calculation shows $O(h^2)$ convergence of the Q^h, as can be seen from Fig. 3.49, but the independent residual convergence is even more degraded in this case than previously. However, there is still evidence that the independent residuals will tend to 0 as $h \to 0$. Investigation of charge conservation in this case yields a graph similar to Fig. 3.45.

Further experimentation for the case of the obstacle function used in the previous two compu-

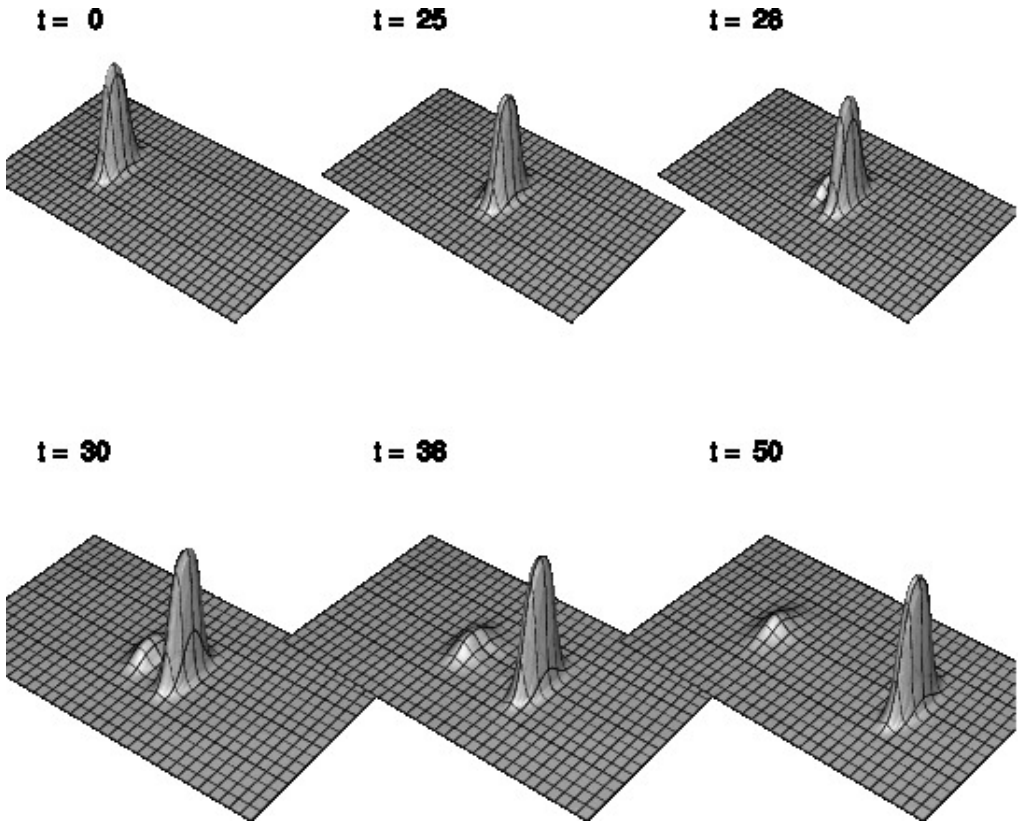

Figure 3.40: Plot of scalar field modulus $|\phi|$ for the scattering of a Q-ball by a barrier defined by an obstacle function $\Sigma(x; y, 0.0, 1.0, 2)$ (see (3.59) for the definition of Σ). The initial boost of the Q-ball is $\gamma = 2.4$ ($v = 0.91$). The barrier is located slightly to the right of the center of the domain and the Q-ball is initially centred 20 units from it. The interaction of the Q-ball with the barrier begins at $t \approx 21$. The end products are a small reflected Q-ball and a larger transmitted one. The computation was performed on a 50×50 box with $\lambda = 0.2$, $\epsilon_{\rm KO} = 0.0$, and with Dirichlet boundary conditions. The domain has been cropped in the y direction for illustrative purposes.

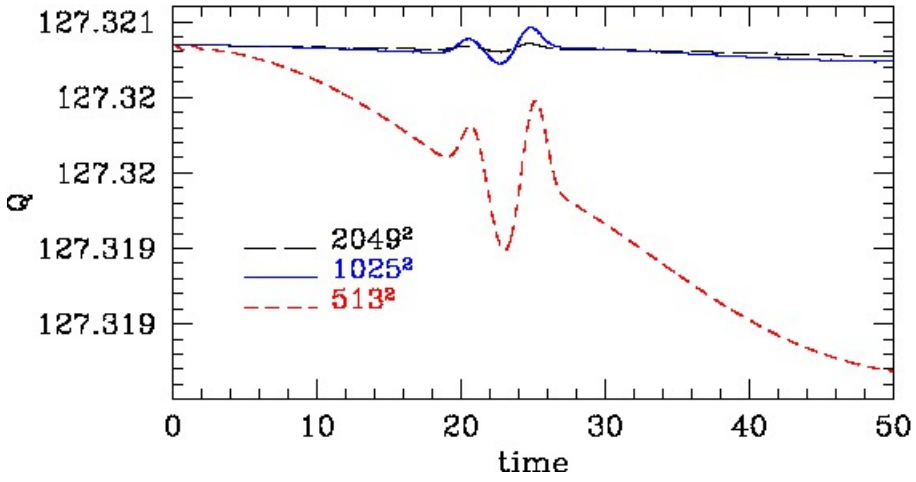

Figure 3.41: Resolution-dependence of the evolution of the computed total charge, Q, for the calculation described in Fig. 3.40.

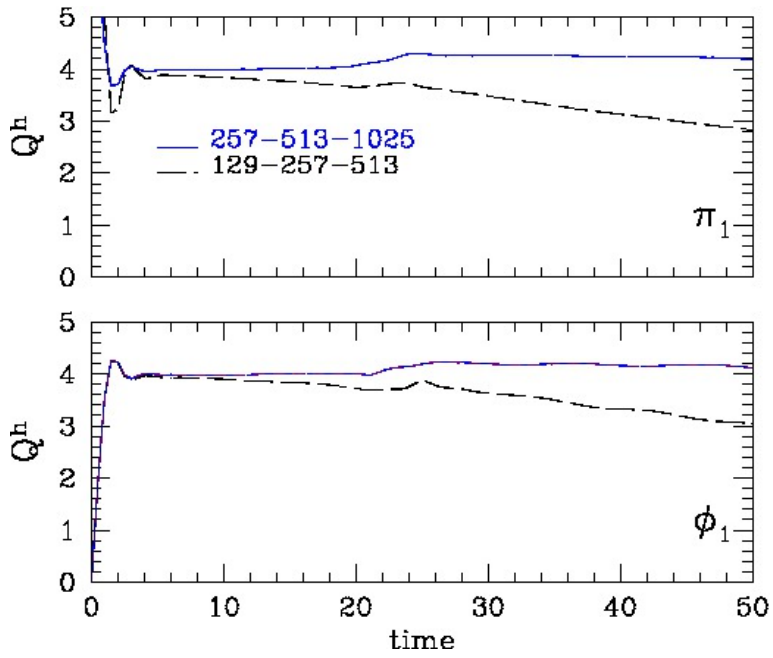

Figure 3.42: Convergence factors for the fields π_1 and ϕ_1 from the calculation described in Fig. 3.40. Evidence for second-order convergence is seen, although there is a degradation of convergence during and after the interaction of the Q-ball with the barrier.

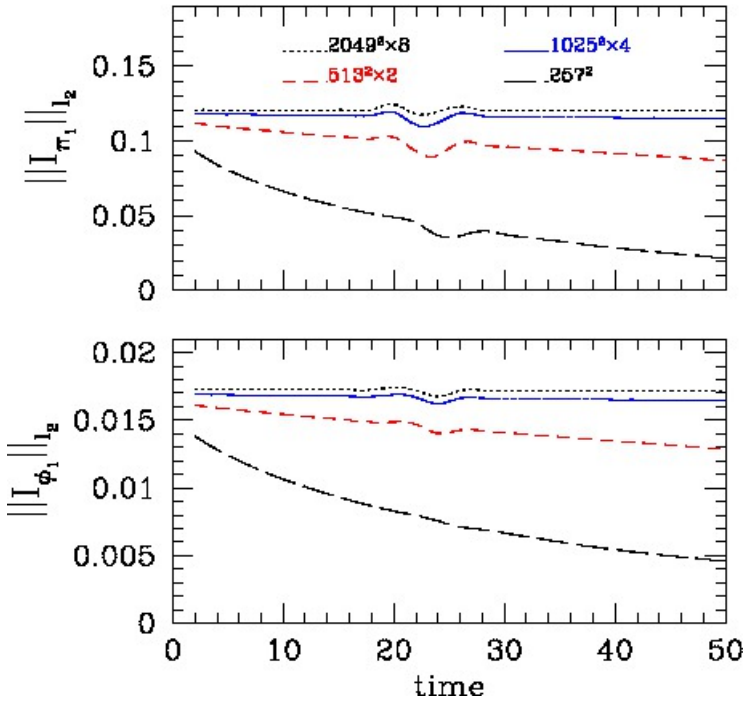

Figure 3.43: Rescaled l_2 norm of the independent residuals for the fields π_1 and ϕ_1 from the calculation described in Fig. 3.40. The expected linear convergence as $h \to 0$ is observed.

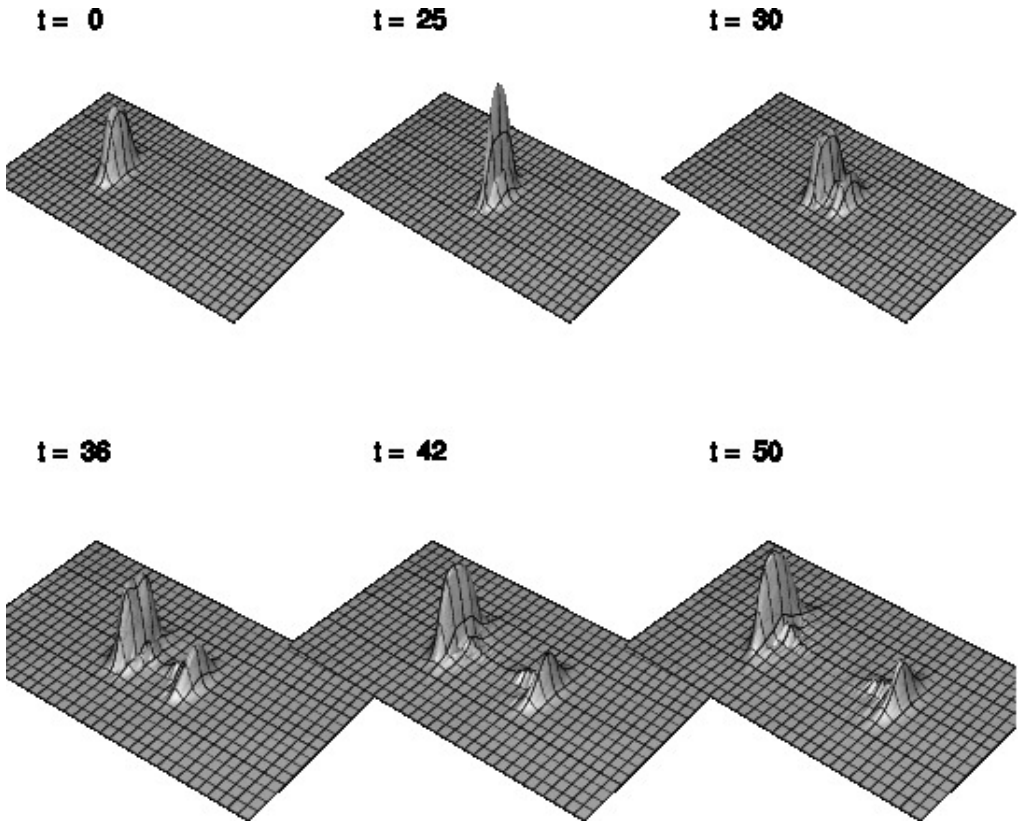

Figure 3.44: Plot of scalar field modulus $|\phi|$ for the scattering of a Q-ball by a barrier defined by an obstacle function $\Sigma(x; y, 0.0, 1.0, 10)$. As in the previously described computation, the initial boost of the Q-ball is $\gamma = 2.4$ ($v = 0.91$), the barrier is located slightly to the right of the center of the domain and the Q-ball is initially centred 20 units from it. In this case, most of the soliton reflects from the barrier with a small Q-ball penetrating it. Both end products are stable. Computational parameters are as listed in Fig. 3.40, except that $\epsilon_{\rm KO} = 0.6$.

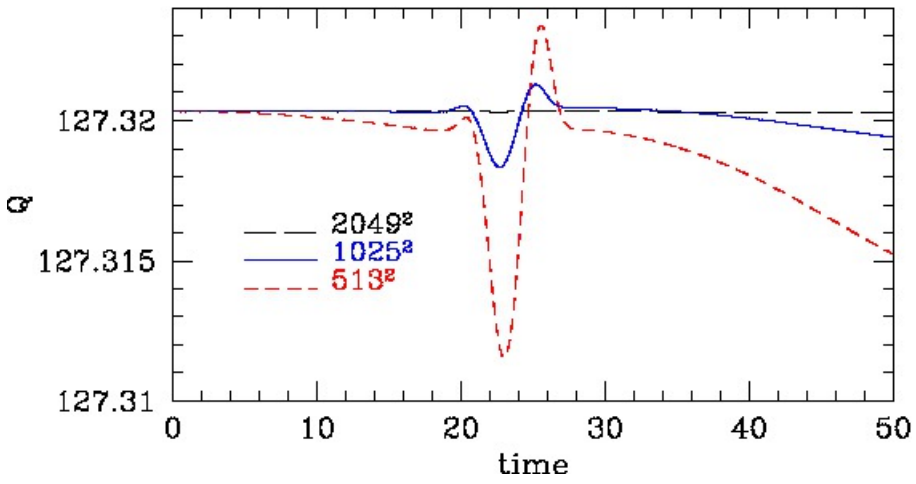

Figure 3.45: Resolution-dependence of the evolution of the computed total charge, Q, for the calculation described in Fig. 3.44.

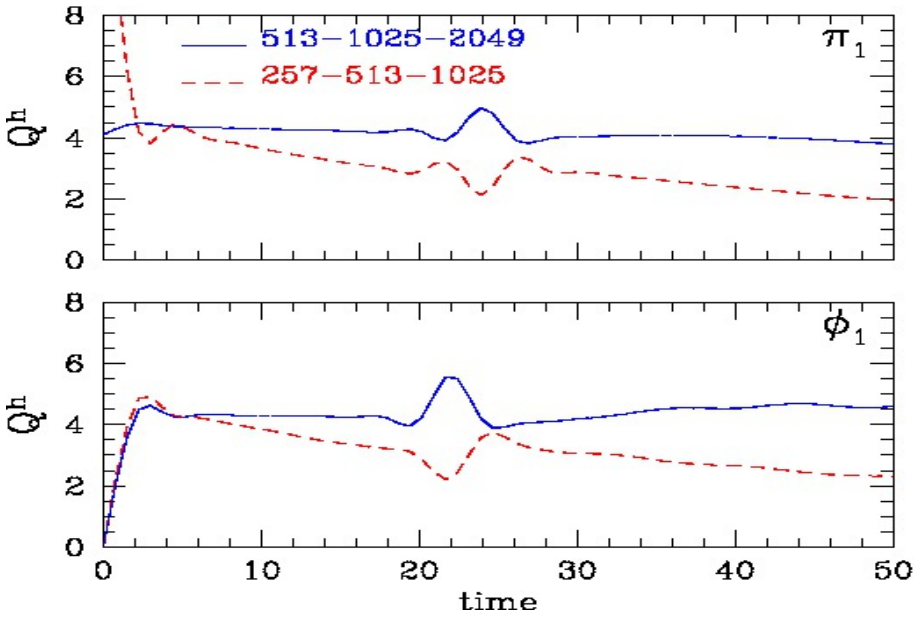

Figure 3.46: Convergence factors for the fields π_1 and ϕ_1 from the calculation described in Fig. 3.40. Again, a trend to second order convergence is observed. However the effect of the collision of the Q-ball with the obstruction is even more pronounced here than it is in Fig. 3.44.

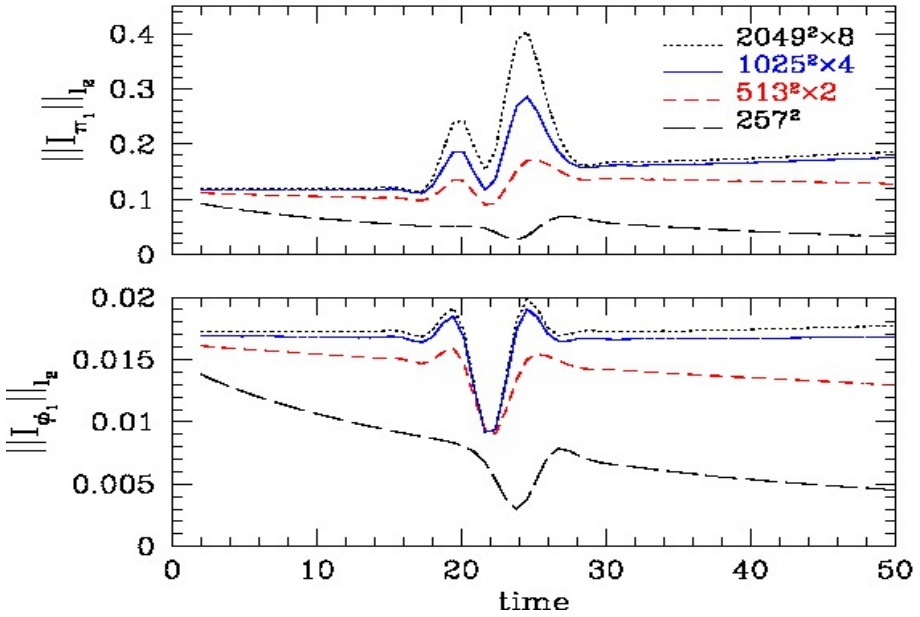

Figure 3.47: Rescaled l_2 norms of the independent residuals for the fields π_1 and ϕ_1 from the calculation described in Fig. 3.44. The graphs show a trend to linear convergence with high resolution, but the degradation of convergence due to the interaction is again apparent.

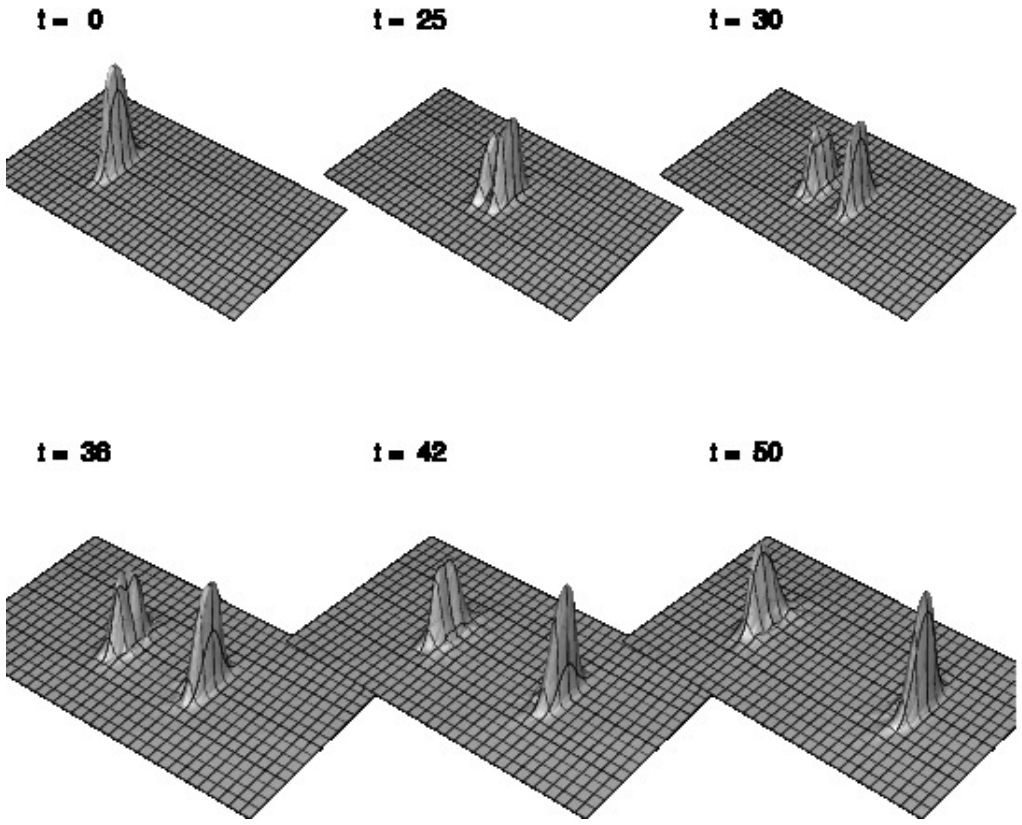

Figure 3.48: Plot of scalar field modulus $|\phi|$ for the scattering of a Q-ball by a barrier defined by an obstacle function $\Sigma(x; y, 0.0, 1.0, 10)$, and with $\gamma = 3.5$ ($v = 0.91$). Relative to the calculation described in Fig. 3.44 ($\gamma = 2.4$), the initial boost in this case is significantly higher. Otherwise the setup of the numerical experiment is the same. In this instance the end state also contains reflected and transmitted Q-balls, with the latter being slightly larger than the former. Both end products are stable, and minimal scalar radiation is seen.

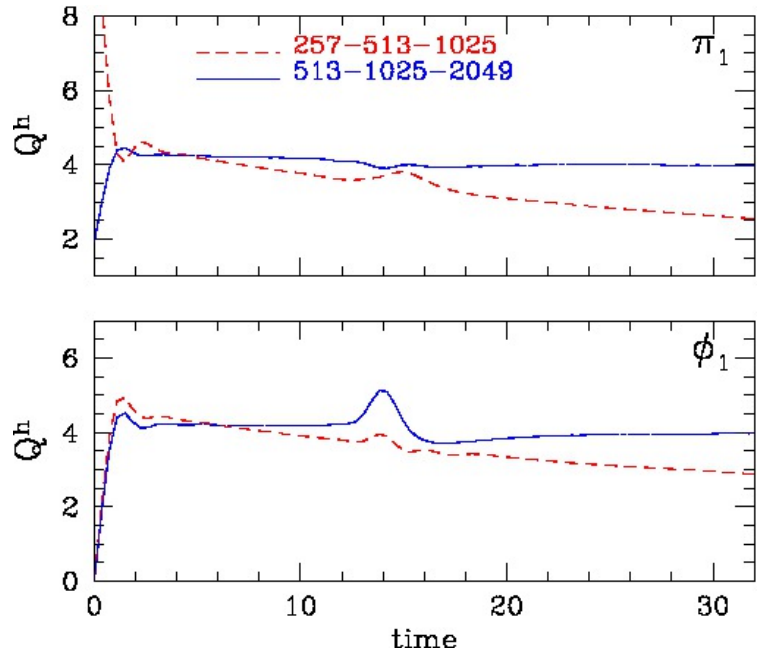

Figure 3.49: Convergence factors for the fields π_1 and ϕ_1 from the calculation described in Fig. 3.48. A trend to second order convergence is observed, but with fluctuations in the convergence factors during and after the collision.

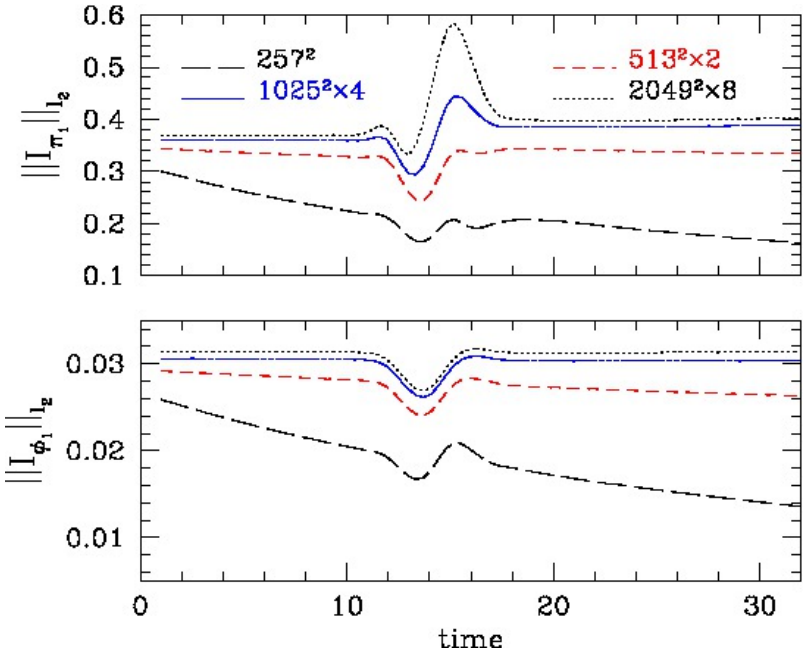

Figure 3.50: Rescaled l_2 norms of the independent residuals for the fields π_1 and ϕ_1 from the calculation described in Fig. 3.48. Again, although there is degradation of convergence during the interaction, the plots provide good evidence for the expected behaviour of the residuals.

tations, $\Sigma(x, y; 0.0, 1.0, 10)$, showed that the critical γ factor at which the two end-product Q-balls have the same size is somewhere in the range $3.2 \leq \gamma \leq 3.5$ ($0.95 \leq v \leq 0.96$).

In total, the experiments described above demonstrate that Q-balls behave as we might expect when scattered against a potential barrier. For fixed barrier height, if we increase the velocity of the Q-ball, we find that, as expected, a larger fraction of the field penetrates the barrier. In all cases we observe conservation of charge (see e.g. Fig. 3.45) for the combined reflected and transmitted components. It is perhaps most notable that the end-products of the interactions appear to be Q-balls (or at least approximate Q-balls) themselves. This is another indication that it is legitimate to view Q-balls as solitons.

3.7.2 AMR Calculations for Potential Barriers

In this section we will discuss further phenomenological results involving potential obstructions, but now exploiting the AMR capability of our code (as discussed in Sec. 3.6 and Sec. 2.4). In the computations described here we used, for the most part, a fixed set of parameters to control the AMR algorithm. In particular we used an $L = 1$ base grid having 257×257 mesh points, $L_f = 5$ and $\tau_{\max} = 0.01$. The computations were performed on a 50×50 box with $\lambda = 0.2$ and $\epsilon_{\rm KO} = 0.5$ (we could also get stable evolutions with $\epsilon_{\rm KO} = 0.0$).

We also used outgoing radiation (Sommerfeld) boundary conditions in order to minimize the effects of reflections on the dynamics.

Wide Barrier $H = 10$, $\gamma = 3.5$

The first experiment involved scattering of a boosted Q-ball with $\gamma = 3.5$ ($v = 0.96$) by a barrier with $H = 10$ but now with width 8 units, corresponding to an obstacle function $\Sigma(x, y; 0.0, 8.0, 10)$. This width of the barrier is comparable to the (contracted) diameter of the Q-ball for this value of γ, which is ≈ 8.5.

The resulting evolution of the modulus $|\phi|$ of the complex scalar field is shown in Fig. 3.51. As the Q-ball enters the barrier region it loses amplitude, while another Q-ball is ejected backwards—typical of what we have seen in previous experiments of this type. However, at late times there is now a small amount of field remaining in the barrier region, similar to those found in some of the Q^+ Q^+ and Q^+ Q^+ collisions described in Sec. 3.6. At the end of the computation the reflected Q-ball has a larger amplitude than the transmitted one. Considering that the adaptive algorithm reached a $L_f = 5$, and the fact that Sec. 3.7.1 provided evidence that the code is $O(h^2)$ convergent,

we feel that the observed features of the interaction are genuine. Additionally, computation of the charge density reveals that all three end products are charged. However, calculations carried out to later times (and perhaps the use of a more stringent truncation error threshold) would be needed to more definitively determine if the field in the barrier region is indeed a stable product of the scattering.

Shallow trench $H = -2$, $\gamma = 3.5$

Next we considered the following scenario: a $\gamma = 3.5$ boosted Q-ball is scattered by a potential obstruction describing a shallow trench having unit width and $H = -2$. The trench is centred in the same position as the barriers used above, and thus corresponds to an obstacle function $\Sigma(x, y; 0.0, 1.0, -2)$. Again, the x-diameter of the Q-ball at this velocity is ≈ 8.5. We note that we discovered by trial and error that for deeper trenches, i.e. for $H < -2$—and independently of the value of γ—the code becomes unstable, in the sense that the point-wise Newton iteration stops converging.

The Q-ball encounters the obstruction at $t \sim 21$, and the end-state seen in this instance is again quite rich. Specifically, we see a small reflected Q-ball, and a larger Q-ball that penetrates the trench. Perhaps the most interesting outcome of the scattering is that part of the field "falls" into the trench, and forms an oscillating wall that persists for the rest of the evolution. This is perhaps not surprising, since a region with negative potential is expected to give rise to bound-states, or trapped configurations. In order to further investigate the nature of the end product in the trench, we examined the charge density: interestingly, we found that the field trapped in the obstruction *contained no charge*. We suspect this is due to the boundary conditions on the trench at the edges of the computational domain. It appears that only field configurations that vanish at infinity carry charge, and the trench clearly does not satisfy this requirement.

Potential Barrier $H = 10$, $\gamma = 7$

The last configuration we considered was a boosted Q-ball with $\gamma = 7$, scattered by a a potential barrier having unit width and $H = 10$. The obstacle function is thus $\Sigma(x, y; 0.0, 1.0, 10)$. At this value of γ the Q-ball has an x-diameter of ≈ 4.2. In this case, as can be seen in Fig. 3.53 the Q-ball is largely unaffected by the barrier, emerging mostly unscathed from the encounter, with only a small lump of the field back-scattered. In other words, the kinetic energy of the soliton completely dominates the potential obstruction.

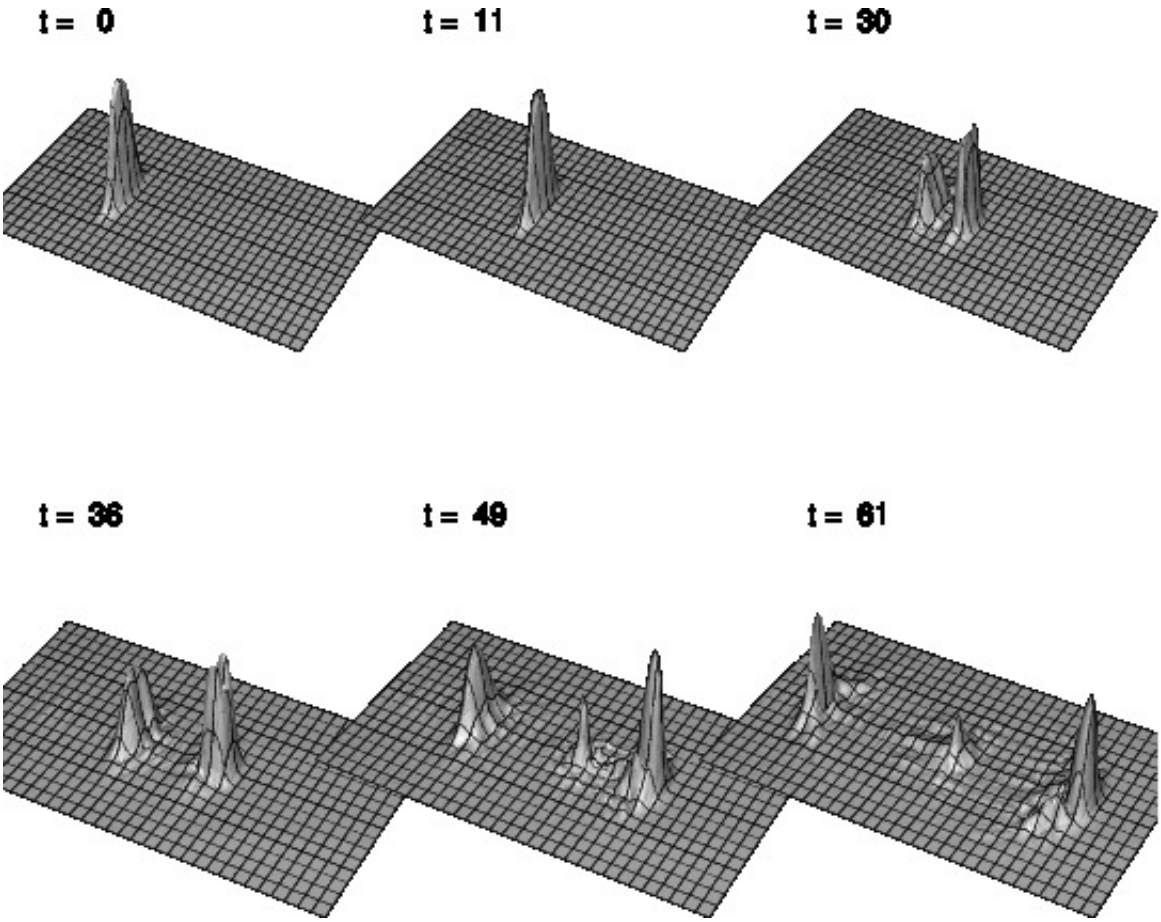

Figure 3.51: Plot of scalar field modulus $|\phi|$ for the scattering of a Q-ball by a barrier defined by an obstacle function $\Sigma(x; y, 0.0, 8.0, 10)$, and with $\gamma = 3.5$ ($v = 0.91$). The setup of this experiment is similar to that described in Fig. 3.48, except that the barrier is wider in this case (8 units vs 1). The boosted Q-ball is initially centred 20 units to the left of the obstruction. We again see both transmitted and reflected Q-balls, as well as some remnant field in the barrier: the latter probably decays away. The calculation was performed using AMR on a 50×50 computational domain, a base grid having 257×257 points, $L_f = 5$, $\tau_{\max} = 0.01$, $\lambda = 0.2$ and $\epsilon_{\rm KO} = 0.5$
.

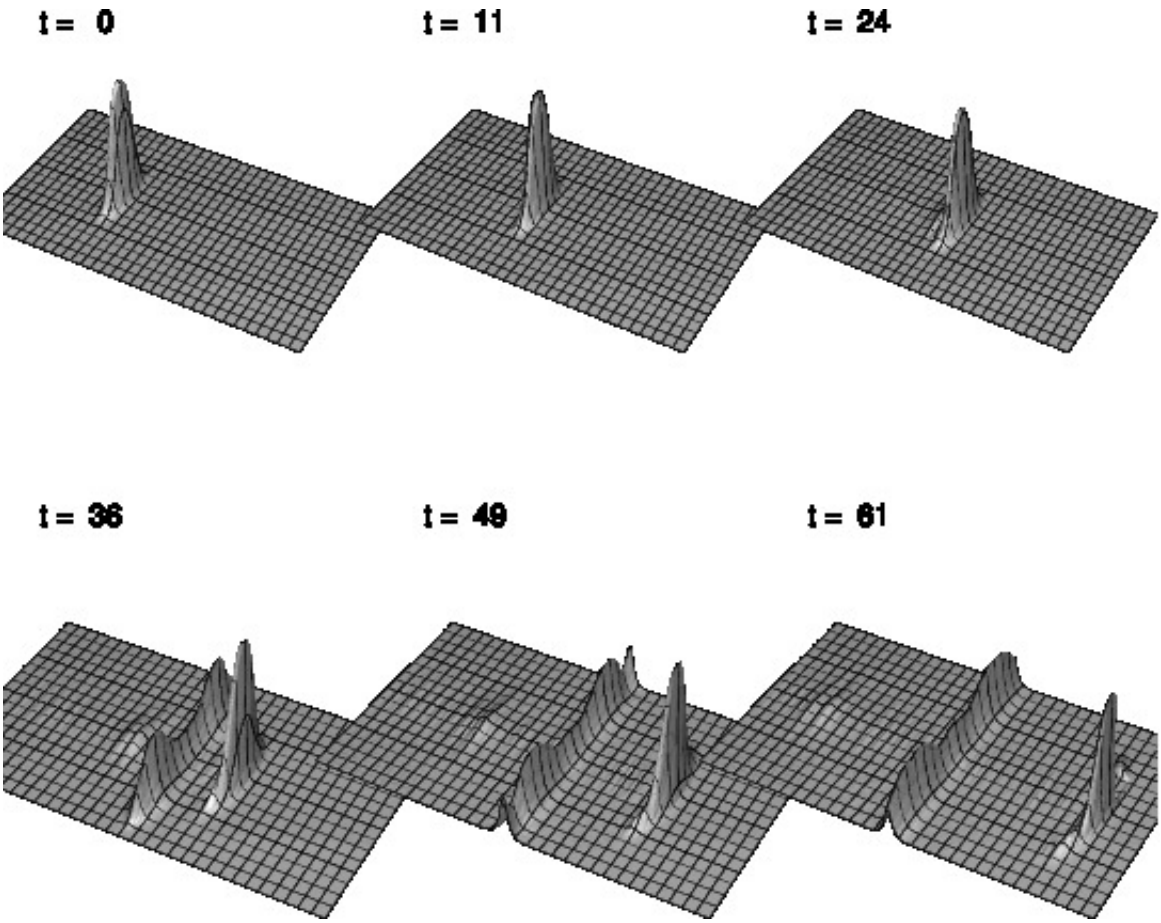

Figure 3.52: Plot of scalar field modulus $|\phi|$ for the scattering of a Q-ball by a trench obstruction defined by an obstacle function $\Sigma(x; y, 0.0, 1.0, -2)$, and with $\gamma = 3.5$ ($v = 0.91$). Other than the use of a different obstacle (in particular a well rather than a barrier) the numerical setup—including the AMR parameters—is the same here as in Fig. 3.51. The final configuration includes a large transmitted Q-ball, a small reflected one—both of which are stable—and little evidence of radiation. There is also some scalar field trapped in the well which carries no charge.

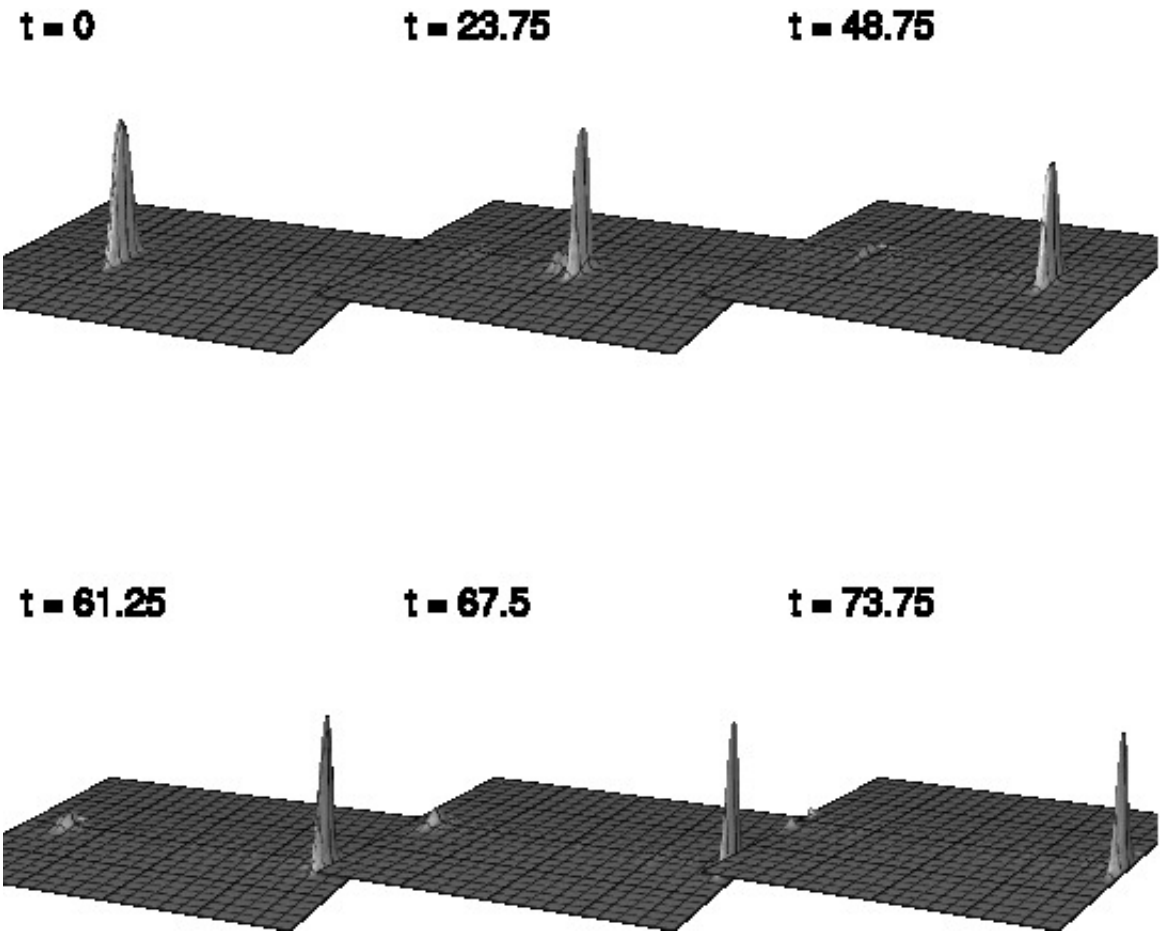

Figure 3.53: Plot of scalar field modulus $|\phi|$ for the scattering of a Q-ball by a barrier defined by an obstacle function $\Sigma(x; y, 0.0, 1.0, 10)$, and with $\gamma = 7.0$ ($v = 0.99$). This calculation is similar to that described in Fig. 3.44 except that the boost factor is significantly higher. Indeed, the extreme amount of Lorentz contraction is readily apparent. In this case, and as expected, the interaction is characterized by almost total transmission of the initial Q-ball. However, a small reflected Q-ball can also be seen. The numerical parameters here are the same as those listed in the caption of Fig. 3.51 apart from the truncation error threshold which is $\tau_{\max} = 0.001$.

3.8 Summary

We now conclude with a summary of this chapter.

- With the aid of symbolic manipulation techniques, we successfully developed a computational infrastructure that we could use to develop finite difference codes for the approximate solution of hyperbolic time dependent partial differential equations. As a model problem, we studied a theory describing the dynamics of a complex scalar field, and which possesses stable, localized (solitonic) solutions called Q-balls.

- For the temporal discretization of the equations of motion, and motivated by its stability properties observed in previous computations of this type [133, 119], we used an implicit two-level Crank-Nicholson scheme.

- We validated our code using different types of initial data, including smooth Gaussian profiles and single Q-balls, which were either at rest, or boosted to moderate values of γ. Our tests displayed the expected $O(h^2)$ convergence for the dynamical grid functions and $O(h)$ convergence for the independent residuals. Together these tests provide strong evidence that the results produced by our code tend to correct continuum solutions as $h \to 0$. The computed total charge Q displayed $O(h^3)$ convergence, possibly due to the fact that we combined a Crank-Nicholson scheme with a second order trapezoidal rule for the integration of the charge density.

- We studied some aspects of the dynamics of Q-balls. We concentrated on two main scenarios: collisions between Q-balls having opposite charges, $Q^+\ Q^-$, and those between configurations with the same charge, $Q^+\ Q^+$. The observed interactions during the collision were qualitatively different for the two scenarios. $Q^+\ Q^-$ interactions exhibited purely constructive interference, whereas $Q^+\ Q^+$ collisions showed destructive interference patterns. We investigated the convergence properties of our collision experiments, obtaining the same satisfactory results as before. We then used the AMR capabilities of our code to perform calculations that reproduced the previously reported phenomenology of $Q^+\ Q^+$ scattering that were carried out for $\gamma < 1.4$ [18]. Namely, we found that $Q^+\ Q^+$ scattering results in (1) bound states for $v < 0.3$, (2) fragmentation into a combination of right-angle and forward-scattering (with the trend depending on the velocity) for $0.3 < v < 0.7$, and (3) strictly forward-scattering for $v > 0.7$.

To our knowledge, Q^+ Q^- collisions have not been described in any previous work, and we thus performed experiments using AMR to explore their dynamics. We found that the collisions in this case resulted in bound states for $v \lesssim 0.4$, and exhibited forward scattering at any higher velocity. In contrast to the Q^+ Q^+ interactions, Q^+ Q^- collisions typically produced a significant amount of scalar radiation, and analysis of the properties of this radiation required the consideration not only of the modulus $|\phi|$ of the complex field, but also other quantities, such as the charge density.

- For the higher boosts we considered—$\gamma = 1.2$ to 7—and for both Q^+ Q^+ and Q^+ Q^- collisions, we observed almost exclusively forward scattering We believe that at such velocities the nonlinearities which would give rise to significant interaction of the solitons are effectively very weak. Not surprisingly, we also found that at high boosts, and due to effects such as Lorentz contraction, substantially more finite-difference resolution was required to maintain a roughly constant solution error.

- We found that unigrid (non-adaptive) calculations were typically stable for a wide range of values of the Courant factor: in particular we investigated the regime $0.1 \leq \lambda \leq 0.6$ and found no indications of instabilities. For the AMR computations we found a more restrictive condition on λ; typically we needed $\lambda \lesssim 0.3$. We suspect that the instability that set in for higher values of the Courant number was related to the interpolation of values from coarse grids to boundaries of fine grids, which is part of the adaptive Berger and Oliger algorithm.

- We investigated the dynamics of Q-balls for different values of ω (Fig. 3.39), noting that the charge decreases with increasing ω. We found that right-angle scattering was completely absent from the dynamics of sufficiently low-charge Q-balls.

- We performed numerical experiments of the scattering of Q-balls against potential obstructions, using boosts in the range $2.4 < \gamma < 7$. We validated the expected convergence properties of the results, but noted that convergence during the interaction of the Q-balls with the obstructions was significantly degraded. Scattering against barriers was characterized by a combination of transmission and reflection of the soliton. Scattering against a trench of a certain depth resulted in part of the field being trapped in the trench (along with transmitted and reflected Q-balls). The trapped field possessed no significant charge density.

CHAPTER 4

RELATIVISTIC SCATTERING OF BABY SKYRMIONS IN $2+1$ DIMENSIONS

4.1 Introduction

This chapter is devoted to a description of our numerical simulations performed within the context of the baby Skyrme model, with an emphasis on the collision of baby skyrmions. Before proceeding to the scattering work, we discuss the formalism underlying our specific calculations, and describe some basic computations that were performed principally to test our numerical implementation. To this end, we start in Sec. 4.2 with a detailed formulation of the model, and discuss the static solitonic solutions it admits. We then derive the dynamical equations of motion in Sec. 4.3, and detail the specific implementation of the numerical methods—previously described in Chap. 2—that we use to approximately solve these equations. Secs. 4.3.4, 4.3.5 and 4.3.6 then discuss the generation of suitable initial data for static and boosted baby skyrmions, respectively. Code validation strategies—including convergence testing, independent residual evaluation and monitoring of conserved quantities—are developed in Sec. 4.4. Once the reliability of our code has been established, we proceed to use it as a laboratory to study the dynamics of baby skyrmions by means of a series of unigrid and adaptive computations. Sec. 4.5 describes general features of baby skyrmion scattering, and presents a survey of previous work relevant to our calculations. Experiments with single boosted skyrmions are discussed next in Sec. 4.6, followed by Sec. 4.7, which details the core results of this work on head-on baby skyrmion collisions (BB). Our investigations of BB grazing collisions are discussed in Sec. 4.8, while baby skyrmion-baby anti-skyrmion ($B\bar{B}$) scattering is covered in Sec. 4.9. The performance of the different constraint enforcement methods is discussed in Sec. 4.10. We conclude the chapter with a summary of our findings, as well as suggestions for extensions of our code (Sec. 4.11).

As discussed in the introduction (Sec. 1.5.2), a chief motivation of this work is to study in

detail the nature of the hyperbolic-elliptic transition (loss of well-posedness) in the baby Skyrme model [1, 26, 95]. By observing the behavior of the total energy, as well as by direct examination of the numerical solution, we provide strong evidence for the loss of hyperbolicity in certain situations—most notably in collisions at sufficiently high energies. By means of detailed explorations of parameter space for the classes of skyrmion interactions summarized above, we find specific conditions for the loss of well-posedness, and thus the limits for physically meaningful dynamics in those cases.

4.2 The Model

The baby Skyrme model describes the dynamics of a nonlinear vector field in $D = 2$ space plus one time dimension, and which, modulo the appearance of a potential term, possesses an $O(3)$ rotational symmetry. Extensive reviews have been written on the subject [31, 35, 55, 56], and we refer the interested reader to these references for details beyond those provided here. The model has the Lagrangian

$$\mathcal{L} = F_\pi \left(\frac{1}{2}\partial_\mu \phi_a \partial^\mu \phi_a + \frac{\kappa^2}{4}(\partial_\mu \phi_a \times \partial_\nu \phi_a)(\partial^\mu \phi_b \times \partial^\nu \phi_b) + \frac{\mu^2}{2}(1 - [\phi_3]^2) \right) , \tag{4.1}$$

where Latin indices, such as a, label the 3 real components of the field i.e. $\phi_a = (\phi_1, \phi_2, \phi_3)$, Greek indices label the dimensions of space-time, $\mu, \nu = 0, 1, 2$, and summation conventions apply to both index types. In the above $\times$ denotes the usual vector cross product. The vector field is thus viewed as a triplet of real scalar fields, and due to the "bare" (i.e. without a potential) rotational symmetry, must satisfy the "chiral" constraint $\phi_a \phi_a = 1$. The first term in (4.1)—a quadratic kinetic energy—defines the ordinary $O(3)$ sigma model. The second term, which is fourth order in the derivatives, is the planar equivalent of the $3 + 1$ Skyrme term in [31, 32, 33], and allows the model to admit non-trivial static solutions. As we will discuss immediately, the last term, which is a potential (and which breaks the $O(3)$ symmetry), is needed to stabilize the solitonic solutions of the theory. The constants F_π, κ and μ are parameters that are analogous to their $3+1$ dimensional counterparts. F_π has dimensions of energy and κ and $1/\mu$ have dimensions of length. Here we will fix units so that $F_\pi = \kappa = 1$.

A consequence of Derrick's argument (Sec. D.1) is that for $D = 2$ we need to include a *potential term* (with no derivatives) in order for stable solitonic solutions to exist. The form of the potential

is largely arbitrary, and this freedom gives rise to a series of different baby Skyrme models [134]. Our specific choice of potential in (4.1) yields what is known as the old baby Skyrme model [35]. We have adopted this potential principally since it is the most widely studied in the literature, and as a consequence we can compare our results with previous work.

We note, however, that for collisions in the ultrarelativistic regime, intuition suggests that the particular choice of the potential is not expected to affect the dynamics in a significant way, since the kinetic energy will be much larger than the potential energy in this case. Thus, we expect that the phenomenology we observe at high boosts should be generic to most, if not all, baby Skyrme model variants.

It is convenient and conventional to rewrite the Skyrme term in (4.1) using *Lagrange's identity*:

$$(\partial_\mu \phi_a \times \partial_\nu \phi_a)(\partial^\mu \phi_b \times \partial^\nu \phi_b) = (\partial_\mu \phi_a \partial^\mu \phi_a)^2 - (\partial_\mu \phi_a \partial_\nu \phi_a)(\partial^\mu \phi_b \partial^\nu \phi_b)\,. \tag{4.2}$$

Then, with $F_\pi = \kappa = 1$, we have,

$$\mathcal{L} = \frac{1}{2}\partial_\mu \phi_a \partial^\mu \phi_a + \frac{1}{4}(\partial_\mu \phi_a \partial^\mu \phi_a)^2 - \frac{1}{4}(\partial_\mu \phi_a \partial_\nu \phi_a)(\partial^\mu \phi_b \partial^\nu \phi_b) + \frac{\mu^2}{2}(1 - [\phi_3]^2)\,. \tag{4.3}$$

We will work with μ^2 in the range $0.001 \leq \mu^2 \leq 0.4$ in order to determine the effect of the potential term on the dynamics. A typical value used in previous studies is $\mu^2 \sim 0.1$ [135, 35, 55, 56].

4.2.1 Topological Structure and Static Solutions

We are interested in studying baby skyrmions, which are minimum energy static solutions of the model defined above. We will briefly discuss the existence of these solutions as a consequence of the non-trivial topology of the theory, and then move on to a description of their concrete computation.

The fields ϕ_a can be visualized as orthogonal directions of an *Euclidean* internal space [31], as illustrated in (Fig. 4.1). It is easy to see that the constraint $\phi_a \phi_a = 1$ restricts the fields to "live" on a S^2 unit sphere, in the tridimensional space spanned by (ϕ_1, ϕ_2, ϕ_3). The fields themselves are functions of the space-time coordinates, $\phi_a = \phi_a(t, x, y)$, and this defines a correspondence, or a mapping, between physical space (in this case R^2) and the space of triplets, or states, S^2, i.e. $M : R^2 \to S^2$. The S^2 manifold is known as the *target* space of the theory [122].

The non-trivial topology of the maps we consider is provided by a specific choice of boundary conditions. In particular, we demand that $(\phi_1(x, y), \phi_2(x, y), \phi_3(x, y)) \to (0, 0, 1)$ at $x \to \infty$,

$y \to \infty$, and $(\phi_1(x,y), \phi_2(x,y), \phi_3(x,y)) \to (0,0,-1)$ at the origin, $x = y = 0$. The first condition identifies infinity in any direction on the xy plane as the same point, effectively compactifying space into a sphere, $R^2 \cup \infty \simeq S^2$. Hence our maps become $M : S^2 \to S^2$. One possible structure arising from these boundary conditions is illustrated in Fig. 4.1, from which we see that the map M defines one possible configuration of the vector field in the plane. In accord with the boundary conditions, the vector (ϕ_1, ϕ_2, ϕ_3) points downwards at the origin, and upwards at large distances—and in any direction—from $(0,0)$. At intermediate distances, and, again, in any radial direction, we find a *twist* in the field. This (extended) twist is known as a texture. The existence of a baby skyrmion is possible precisely due to the non-trivial topology of the mapping M, since a solution with a twist cannot deform continuously into a solution without it, unless we break the twist. Assuming that such breakages cannot occur, the number of twists is conserved.

In analogy to the classification of kinks and anti-kinks of the ϕ^4-theory into equivalence classes [24], we can group our mappings, M, of vector field configurations in the plane, according to the number of twists we encounter as we move outwards from the origin to spatial infinity. This conserved (integer) number of twists is known as the topological charge, B, and is the analog of the conserved baryon number in the $3+1$ Skyrme model. Technically, B is the spatial integral of the zero component, B_0, or baryon number density, associated with the current,

$$B_\mu = \epsilon^{abc} \epsilon_{\mu\nu\rho} \phi_a \partial_\nu \phi_b \partial_\rho \phi_c \,. \tag{4.4}$$

Specifically, we have [35],

$$B = \frac{1}{4\pi} \int d^2x \;\; B_0 = \frac{1}{4\pi} \int d^2x \;\; \epsilon^{abc} \epsilon_{\nu\rho} \phi_a \partial_\nu \phi_b \partial_\rho \phi_c = \frac{1}{4\pi} \int dx\, dy \;\; \epsilon^{abc} \phi_a (\partial_x \phi_b)(\partial_y \phi_c) \,. \tag{4.5}$$

It is interesting to mention that by writing the energy density derived from the Lagrangian (4.1) as a perfect square, and using the the triangle inequality, it is possible to show that, [24, 15],

$$E \geq 4\pi B \,. \tag{4.6}$$

This is known as the *Bogomol'nyi bound* [24], and can be shown to mean that as long as the topology of the map remains non trivial, minimal energy stable solutions for $B \neq 0$ will exist.

We will focus on the study of baby skyrmions with $B = 1$, although static solutions with

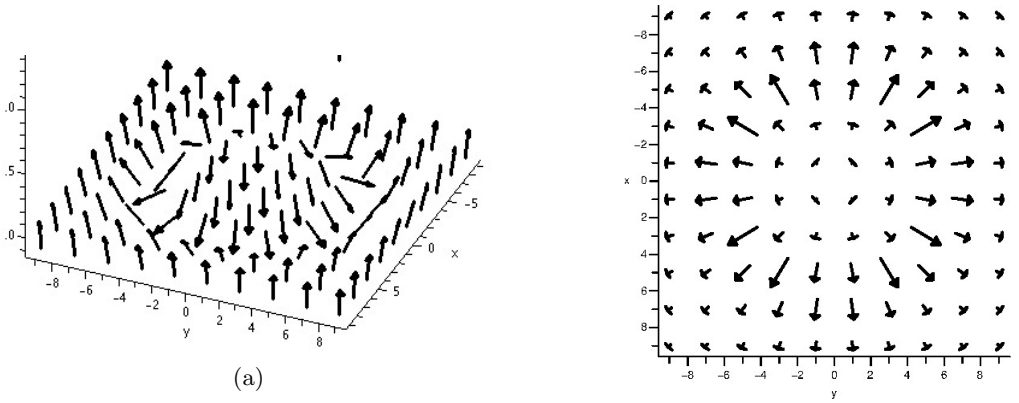

(a) (b)

Figure 4.1: We can think of a baby skyrmion as a topological structure (twist or texture, Fig. 4.1a) in a planar configuration of a 3 dimensional vector field, defined by an internal 3D space spanned by $(\phi_1(t,x,y), \phi_2(t,x,y), \phi_3(t,x,y))$. Due to the normalization condition, $\phi_a\phi_a = 1$, the value of the vector field at any point in the xy plane is equivalent to its direction there. Away from the origin, $x = y = 0$, the field approaches one vacuum state $(0,0,1)$ (pointing upwards), while at the origin, it attains the other vacuum state $(0,0,-1)$ (pointing downwards). Any radial trace of the field direction from the origin to large distances exhibits a topological twist (kink). Fig. 4.1b shows a view from above of the xy plane, making manifest the circularly-symmetric hedgehog configuration of outward-pointing radial vectors.

$B = 2$ and higher are well known [56, 20]. As already noted, the choice of potential in (4.1) breaks the target space invariance under $O(3)$ rotations. Specifically, the invariance becomes $O(2) \times Z_2$, where the discrete Z_2 symmetry corresponds to the two distinct vacua of the potential, namely $\phi_3 = \phi_\pm = \pm 1$. This in turn allows for domain wall solutions, which are an example of $B = 0$ configurations.

Clearly, the solution $\phi_a = (0,0,1)$, wherein the field is everywhere in the same vacuum state, is a minimal energy solution. However, it is topologically trivial; that is, it satisfies $B = 0$. A more interesting question is whether there are stable static configurations which are topologically nontrivial ($B \neq 0$), with localized energy density, and satisfying $\phi_a = (0,0,1)$ at infinity. Derrick's theorem (App. D.1) provides arguments for the existence of such solutions. More rigorous methods found that the answer is yes, and that the solutions could be determined via a specific rotationally symmetric ansatz, known as a hedgehog configuration

Introducing the usual polar coordinates (r, θ), the explicit form of this circularly symmetric

ansatz is

$$\phi_a = \begin{pmatrix} \sin f(r) \sin B\theta \\ \sin f(r) \cos B\theta \\ \cos f(r) \end{pmatrix} \tag{4.7}$$

where $f(r)$ is a radial profile function that must satisfy the boundary conditions $f(0) = B\pi$ and $f(\infty) = 0$ (localization). As mentioned earlier in this section, we will limit our attention to baby skyrmions with $B = 1$, so that central boundary condition is $f(0) = \pi$. Substitution of (4.7) in the Lagrangian (4.3) leads to a static energy density,

$$E = (4\pi)\frac{1}{2}\int_0^\infty r dr \left(f'^2 + n^2 \frac{\sin^2 f}{r^2}(1 + f'^2) + \mathrm{V}(f) \right) , \tag{4.8}$$

where $f' \equiv df/dr$. Minimization of (4.8) yields a second-order ordinary differential equation [56],

$$\left(r + \frac{\sin^2 f}{r} \right) f'' + \left(1 - \frac{\sin^2 f}{r^2} + \frac{\sin f \cos f f'}{r} \right) f' - \frac{\sin f \cos f}{r} - r\frac{1}{2}\frac{d\mathrm{V}(f)}{df} = 0 . \tag{4.9}$$

4.2.2 Solution of the Baby Skyrmion ODE

As for the Q-ball ODE described in Sec. 3.2.1, we numerically solve (4.9) using the LSODA routine from the ODEPACK package [125], which requires that we rewrite the ODE in first-order form. We thus introduce an auxiliary variable $u(r) \equiv df/dr$ and recast (4.9) as

$$\frac{df}{dr} = u \tag{4.10}$$

$$\frac{du}{dr} = \left(\frac{-ur\cos r \sin r - ur + u \sin r + r^3 \cos r \sin r \mu^2 + r \cos r \sin r}{r(1 + \sin r)} \right) . \tag{4.11}$$

The boundary conditions are

$$f(0) = \pi, \qquad \lim_{r\to\infty} f(r) = 0 . \tag{4.12}$$

The system (4.10–4.12) is solved using a shooting method, as previously described in Sec. 3.2.1, and adapted to this particular context. We first note that μ^2, the square of the potential constant, is a non-zero free parameter of the problem. We thus fix μ to some specific value, set the central value of $f(0)$ via (4.12), and then adjust the other initial value required by ODEPACK ,

$$\frac{df}{dr}(0) \equiv u(0) , \tag{4.13}$$

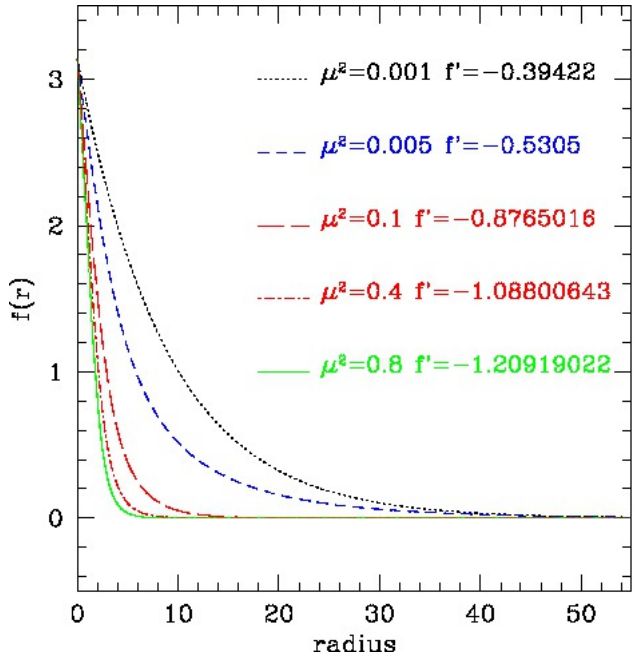

Figure 4.2: This figure displays baby skyrmion radial profile functions, $f(r)$, for various values of the squared potential parameter, μ^2. Also listed are the corresponding values of the shooting parameter, $f' = df/dr$ (We have fixed $f_0 = \pi$ as a boundary condition). The sizes of the baby skyrmions seem to be roughly inversely proportional to μ^2. We note that the plots show subsets of the full computations, which generally comprise discrete collections of points, r_p, $p = 1, \ldots, N$, where N is of the order of 1300, $r_1 = 0$ and $r_N \equiv r_{\rm max} \approx 300$ (i.e. only a small portion of the radial integration domain is shown here). The LSODA error tolerance is of the order of 1.0×10^{-9} which guarantees that the error in the profile function $f(r)$ is much smaller than the error of the evolved finite difference solutions that we subsequently generate. Note the rapid falloff of $f(r)$ once $r \gtrsim 40$. This is typical of a static localized baby skyrmion, and justifies the view of such configurations as "solitonic" (particle-like) entities.

by trial and error, until the solution satisfies the large-r boundary condition (4.12). As was the case for the Q-ball profiles of Sec. 3.2.1, we restrict attention to "ground state" profiles, $f(r)$, that are characterized by *no* crossings of the $f(r) = 0$ axis (no nodes). Fig 4.2 shows some profile functions, $f(r)$, for different values of μ^2, along with the corresponding values of the shooting parameter $f' = df/dr$. We notice that the size of the baby skyrmion is roughly inversely proportional to the value of μ^2.

4.3 Equations of Motion

The time-dependent equations of motion are derived from the Lagrangian (4.1), and details are provided in App. B. Special attention is required to impose the "chiral" constraint $\phi_a \phi_a = \phi_1^2 +$

$\phi_2^2+\phi_3^2=1$. The addition of a *Lagrange multiplier* is the traditional method to extremize functions, or functionals, subject to a constraint [31, 32, 25]. Accordingly, a constraint term is added to the Lagrangian (4.3)

$$\begin{aligned}\mathcal{L} = \frac{1}{2}\partial_\mu\phi_a\partial^\mu\phi_a \quad &+ \quad \frac{1}{4}(\partial_\mu\phi_a\partial_\nu\phi_a)^2 - \frac{1}{4}(\partial_\mu\phi_a\partial^a_\nu\phi_a)(\partial^\mu\phi_b\partial^\nu\phi_b) \\ &+ \quad \frac{\mu^2}{2}(1-[\phi_3]^2) + \lambda_{\rm LM}(\phi_a\phi_a - 1)\,, \end{aligned} \tag{4.14}$$

where $\lambda_{\rm LM}$ is the Lagrange multiplier. We again remind the reader that Latin indices $a, b, \ldots = 1, 2, 3$ label the components of the dynamical fields, while Greek indices label the dimensions of spacetime, $\mu, \nu \ldots = 0, 1, 2$. Again, relegating the details of the derivation to App. D.4, we find the following equations of motion:

$$\begin{aligned}(1 \quad &+ \quad \partial_\mu\phi_a\partial^\mu\phi_a)\Box\phi_a + \partial_\mu\partial_\nu\phi_b\partial^\mu\phi_b\partial^\nu\phi_a - \partial^\mu\phi_b\partial^\nu\phi_b\partial_\mu\partial_\nu\phi_a - \Box\phi_b\partial^\nu\phi_b\partial_\nu\phi_a \\ &+ \quad \lambda_{\rm LM}\phi_a + \mu^2\phi_3 = 0\,. \end{aligned} \tag{4.15}$$

We can further compute the exact form of the Lagrange multiplier term $\lambda_{\rm LM}$ (App. D.4) to obtain

$$\begin{aligned}&(1+\partial_\mu\phi_a\partial^\mu\phi_a)\Box\phi_a + \partial_\mu\partial_\nu\phi_b\partial^\mu\phi_b\partial^\nu\phi_a - \partial^\mu\phi_b\partial^\nu\phi_b\partial_\mu\partial_\nu\phi_a - \Box\phi_b\partial^\nu\phi_b\partial_\nu\phi_a \\ &+\Big[(1+\partial_\mu\phi_a\partial^\mu\phi_a)(\partial_\nu\phi_a\partial^\nu\phi_a) - (\partial_\mu\phi_a\partial_\nu\phi_a)(\partial^\mu\phi_b\partial^\nu\phi_b) - \mu^2\phi_3^2\Big]\phi_a + \mu^2\phi_3\,. \end{aligned} \tag{4.16}$$

As was the case for the Q-ball PDEs described in Sec. 3.3, we wish to rewrite (4.16) as a set of first-order-in-time equations, in order to employ a two time-level Crank-Nicholson finite-difference scheme. We thus eliminate the second order time derivatives (which would require a minimum of three discrete time levels) by introducing auxiliary fields π_1, π_2 and π_3, defined by

$$\pi_a(t,x,y) = \frac{\partial\phi_a(t,x,y)}{\partial t}\,. \tag{4.17}$$

4.3.1 Finite Difference Approach

The discretization of the equations of motion (4.16) follows the same methodology used for the Q-ball equations in Sec. 3.3.1. We again adopt a second order, Crank-Nicholson scheme, expressed on finite difference grids that are characterized by a single discrete scale, h. We thus have $\Delta x =$

$\Delta y = h$, and $\Delta t = \lambda h$, where λ is the Courant number.[24]

Due to the appearance of mixed derivatives, we have more extensive finite-difference expressions for the baby Skyrme model than for the Q-ball case. The finite-difference formulae used here are summarized in Tab. 4.1, where we continue to use the notation $\phi^n(i,j) \equiv \phi(t^n, x_i, y_j)$ for grid functions. Also following our previous procedure, we will express the difference approximations of (4.16) in residual form, and remind the reader that the process of computing a solution to the discrete equations of motion is equivalent to driving all of the residual quantities $\phi_1^{\rm res}, \phi_2^{\rm res}, \phi_3^{\rm res}, \pi_1^{\rm res}, \pi_2^{\rm res}, \pi_3^{\rm res}$ to 0.

For the ϕ fields the residual form of the difference approximations are simply

$$\begin{aligned}
\phi_1^{\rm res}(i,j) &= \frac{\pi_1^{n+1}(i,j) + \pi_1^n(i,j)}{2} - \frac{\phi_1^{n+1}(i,j) - \phi_1^n(i,j)}{\Delta t}\,, \\
\phi_2^{\rm res}(i,j) &= \frac{\pi_2^{n+1}(i,j) + \pi_2^n(i,j)}{2} - \frac{\phi_2^{n+1}(i,j) - \phi_2^n(i,j)}{\Delta t}\,, \\
\phi_3^{\rm res}(i,j) &= \frac{\pi_3^{n+1}(i,j) + \pi_3^n(i,j)}{2} - \frac{\phi_3^{n+1}(i,j) - \phi_3^n(i,j)}{\Delta t}\,.
\end{aligned} \tag{4.18}$$

The task of writing the residuals $\pi_1^{\rm res}, \pi_2^{\rm res}, \pi_3^{\rm res}$ fields explicitly is formidable, since equations (4.16) are long and complicated. Therefore, a Maple-based script was written to automate this task, substituting the finite difference stencils (4.1) into the continuum PDEs in order to construct the residual expressions.

The overall time-stepping methodology is also the same as that employed in Sec 3.3.1 for the Q-ball equations of motion. However, in contrast to the Q-ball case, where we had four fields, the baby Skyrme model has six independent dynamical fields. Correspondingly, at any grid point (i,j) the Crank-Nicholson discretization yields six nonlinear equations (defined by the three residual expressions (4.18) and $\pi_1^{\rm res}, \pi_2^{\rm res}, \pi_3^{\rm res}$) for the unknowns $\phi_a^{n+1}(i,j)$ and $\pi_a^{n+1}(i,j)$. The global system of equations is again solved using point-wise-Gauss-Seidel relaxation sweeps. During one sweep, each grid point is visited in turn, and the 6 unknowns defined at that point are simultaneously (collectively) updated by performing a single Newton-step. This step in turn

[24] As discussed in Chap.2, when we use adaptive mesh refinement (AMR), each of the component grids in the grid hierarchy satisfies these conditions for some h_L, where L labels the level of the grid in the hierarchy and $h_L = h_{L-1}/2$.

requires the construction of the 6×6 Jacobian matrix, $\mathcal{J}_{cd}$, with matrix elements defined by

$$\begin{aligned} \mathcal{R}_c &= \text{Residual Equations} = [\phi_1^{\text{res}}, \phi_2^{\text{res}}, \phi_3^{\text{res}}, \pi_1^{\text{res}}, \pi_2^{\text{res}}, \pi_3^{\text{res}}] \,, \\ \mathcal{V}_c &= \text{Variables} = [\phi_1, \phi_2, \phi_3, \pi_1, \pi_2, \pi_3] \,, \\ \mathcal{J}_{cd} &= \frac{\partial \mathcal{R}_c^{\text{res}}}{\partial \mathcal{V}_d} \,. \end{aligned} \tag{4.19}$$

Here the auxiliary Latin indices $c, d \ldots = 1 \ldots 6$ label the rows and columns for our 6×6 linear system. We have also suppressed the finite-differencing indexing for simplicity of expression, so the reader should note that we have, for example,

$$\frac{\partial \phi_1^{\text{res}}}{\partial \phi_1} \equiv \frac{\partial \phi_1^{\text{res}}(i,j)}{\partial \phi_1^{n+1}(i,j)} \,. \tag{4.20}$$

We then use the routine `DGESV` from the LAPACK package [126] to directly solve the following 6×6 linear system at every grid point (x_i, y_j)

$$\begin{pmatrix} \mathcal{J}_{11} & \mathcal{J}_{12} & \mathcal{J}_{13} & \mathcal{J}_{14} & \mathcal{J}_{15} & \mathcal{J}_{16} \\ \mathcal{J}_{21} & \mathcal{J}_{22} & \mathcal{J}_{23} & \mathcal{J}_{24} & \mathcal{J}_{25} & \mathcal{J}_{26} \\ \mathcal{J}_{31} & \mathcal{J}_{32} & \mathcal{J}_{33} & \mathcal{J}_{34} & \mathcal{J}_{35} & \mathcal{J}_{36} \\ \mathcal{J}_{41} & \mathcal{J}_{42} & \mathcal{J}_{43} & \mathcal{J}_{44} & \mathcal{J}_{45} & \mathcal{J}_{46} \\ \mathcal{J}_{51} & \mathcal{J}_{52} & \mathcal{J}_{53} & \mathcal{J}_{54} & \mathcal{J}_{55} & \mathcal{J}_{56} \\ \mathcal{J}_{61} & \mathcal{J}_{62} & \mathcal{J}_{63} & \mathcal{J}_{64} & \mathcal{J}_{65} & \mathcal{J}_{66} \end{pmatrix} \begin{pmatrix} \delta\phi_1(i,j) \\ \delta\phi_2(i,j) \\ \delta\phi_3(i,j) \\ \delta\pi_1(i,j) \\ \delta\pi_2(i,j) \\ \delta\pi_3(i,j) \end{pmatrix} = \begin{pmatrix} \phi_1^{\text{res}}(i,j) \\ \phi_2^{\text{res}}(i,j) \\ \phi_3^{\text{res}}(i,j) \\ \pi_1^{\text{res}}(i,j) \\ \pi_2^{\text{res}}(i,j) \\ \pi_3^{\text{res}}(i,j) \end{pmatrix} . \tag{4.21}$$

Once the corrections $\delta\phi$ and $\delta\pi$ have been obtained, the advanced-time unknowns are updated using

$$\begin{pmatrix} \phi_1^{n+1}(i,j) \\ \phi_2^{n+1}(i,j) \\ \phi_2^{n+1}(i,j) \\ \pi_1^{n+1}(i,j) \\ \pi_2^{n+1}(i,j) \\ \pi_3^{n+1}(i,j) \end{pmatrix} := \begin{pmatrix} \phi_1^{n+1}(i,j) \\ \phi_2^{n+1}(i,j) \\ \phi_3^{n+1}(i,j) \\ \pi_1^{n+1}(i,j) \\ \pi_2^{n+1}(i,j) \\ \pi_3^{n+1}(i,j) \end{pmatrix} - \begin{pmatrix} \delta\phi_1(i,j) \\ \delta\phi_2(i,j) \\ \delta\phi_3(i,j) \\ \delta\pi_1(i,j) \\ \delta\pi_2(i,j) \\ \delta\pi_3(i,j) \end{pmatrix} . \tag{4.22}$$

When the *global* l_2 norm of the corrections (see 2.31 and Sec. 3.3.1) is below a specified threshold, the solution is deemed converged, and we can advance from t^n to t^{n+1}; otherwise we execute

1: **for** $t^n = \Delta t, 2\Delta t, \ldots$ **do**
2: **for** $i = 1$ to Nx **do**
3: **for** $j = 1$ to Ny **do**
4: Set initial estimate for the solution vector $\boldsymbol{\phi_b^{(0)}} \equiv [\phi_1^{(0)}, \phi_2^{(0)}, \phi_3^{(0)}, \pi_1^{(0)}, \pi_2^{(0)}, \pi_3^{(0)}]^T$
5: Calculate the 6×6 Jacobian matrix $\boldsymbol{\mathcal{J}_{ab}}$ and the residual vector $\boldsymbol{B_a}$ at this point using nearest neighbour values, (some new, some old)
6: Solve $\boldsymbol{\mathcal{J}_{ab}\, \delta_b \phi = B_a}$ for the update $\boldsymbol{\delta_b \phi} = [\delta\phi_1^{(0)}, \delta\phi_2^{(0)}, \delta\phi_3^{(0)} \delta\pi_1^{(0)}, \delta\pi_2^{(0)}, \delta\pi_3^{(0)}]^T$ using `DGESV` and obtain a new estimate $\boldsymbol{\phi}_b^{\rm new} = \boldsymbol{\phi}_b^{(0)} - \boldsymbol{\delta_b \phi}$
7: **end for**
8: **end for**
9: Calculate the l_2 norm of the residuals using the new guess $\boldsymbol{\phi_b^{\rm new}}$ (This is a global norm for all subdomains used by the parallel infrastructure)
10: **if** l_2 norm of the residuals $<$ tolerance **then**
11: Convergence achieved
12: Goto 17
13: **else**
14: $\boldsymbol{\phi}_b^{(0)} = \boldsymbol{\phi}_b^{\rm new}$
15: Goto 2
16: **end if**
17: **end for**

Figure 4.3: Time stepping algorithm for the baby Skyrme evolution

another Newton-Gauss-Seidel sweep. A pseudo-code version of the full time-stepping algorithm is given in Fig. 4.3.

4.3.2 Implementation Strategy

The implementation of the algorithm described above closely followed that for the Q-ball code. In this case, however, we did not begin with a prototype serial unigrid (i.e. non-parallel, non-adaptive) version. Rather, we directly implemented our code using the AMRD (Adaptive Mesh Refinement Driver) / PAMR (Parallel Adaptive Mesh Refinement) infrastructure [120, 107, 108] (see Chap. 2 and Sec. 3.3.2 for more details).

The use of scripting and symbolic manipulation in the implementation process was significant. The derivation of the initial data equation, the continuum equations of motion, and their ensuing discretization, were all achieved using Maple [128] scripts and a Maple-based tensor-manipulation package [129].

The procedure to obtain the initial data ODE (4.9), described in Sec. 4.2.1, is managed by a Maple script. The script recasts the Lagrangian (4.3) in polar coordinates, substitutes the hedgehog

ansatz, and, following the Euler-Lagrange prescription, obtains and rewrites the resulting second order ODE as Fortran 77 code for subsequent solution using LSODA.

The discretization of the field equations, i.e. the replacement of the continuum differential operators by finite difference expressions, is divided into two steps.

Maple is used to algebraically perform a first partial discretization of the differential operators that involve values of the fields at (i, j), and the Jacobian matrix elements are then generated using symbolic differentiation. Finite difference versions of other operators, such as the mixed partial derivatives, do not reference (i, j) grid values, and can thus can be evaluated in a straightforward fashion directly in the final Fortran code.

The corresponding residuals for the ϕ and π fields are also generated symbolically with Maple. Both the residuals and the Jacobian matrix elements are then exported as Fortran 77 using Maple's code generation facility. This capability is essential for the baby Skyrme code since, as we noted in Sec. 4.3.1, the residuals for the π fields are too complicated to be written explicitly (not to mention by hand) in an error-free fashion.

Without the strategy of using symbolic computing, and script-based automation for code generation, it would be impractical to quickly implement any changes to the equations of motion or the discretization scheme, and the correctness of the residual and Jacobian elements would be very much in doubt. As stressed in Sec. 3.3.2, the flexibility of our infrastructure was successfully exhibited by the fact that once it had been developed in the context of the Q-ball study, it could be reused in a straightforward fashion to implement the baby Skyrme code.

4.3.3 Constraint Enforcement

In Sec. 4.3 we discussed a mechanism to impose the "chiral" constraint $\phi_a\phi_a = \phi_1^2 + \phi_2^2 + \phi_3^2 = 1$, which involved the introduction of a *Lagrange multiplier* λ_{LM}[25] [31, 32, 25] to the Lagrangian (4.3). However, we have found that, in practice, when numerical errors in the integration of the field equations lead to a violation of the constraint, the Lagrange-multiplier mechanism is not enough to confine the fields to the vicinity of the unit 2-sphere. Any small perturbations grow rapidly to the point that the whole evolution becomes unstable.

We thus have had to investigate and implement additional methods to enforce the constraint $\phi_a\phi_a = 1$ in numerical calculations. The simplest one involves the reprojection (normalization,

[25] λ_{LM} should not to be confused with the Courant number, λ, used elsewhere.

ϕ	$\frac{\phi^{n+1}_{ij}+\phi^{n}_{ij}}{2}$
ϕ_x	$\frac{1}{2}\left[\frac{\phi^{n+1}_{i+1,j}-\phi^{n+1}_{i-1,j}}{2\Delta x}+\frac{\phi^{n}_{i+1,j}-\phi^{n}_{i-1,j}}{2\Delta x}\right]$
ϕ_t	$\frac{\phi^{n+1}_{ij}-\phi^{n}_{ij}}{\Delta t}$
ϕ_{xx}	$\frac{1}{2}\left[\frac{\phi^{n+1}_{i+1,j}-2\phi^{n+1}_{i}j+\phi^{n+1}_{i-1,j}}{\Delta x^2}+\frac{\phi^{n}_{i+1,j}-2\phi^{n}_{i}j+\phi^{n}_{i-1,j}}{\Delta x^2}\right]+$
ϕ_{xy}	$\frac{1}{2}\left[\frac{\phi^{n+1}_{i+1,j+1}-\phi^{n+1}_{i-1,j+1}-\phi^{n+1}_{i+1,j-1}+\phi^{n+1}_{i-1,j-1}}{4\Delta x\Delta y}+\frac{\phi^{n}_{i+1,j+1}-\phi^{n}_{i-1,j+1}-\phi^{n}_{i+1,j-1}+\phi^{n}_{i-1,j-1}}{4\Delta x\Delta y}\right]$

Table 4.1: Crank-Nicholson (CN) two-(space) dimensional finite difference stencils used to convert the differential equations to difference equations, for any of the six dynamical variables ϕ_a or π_a Here we use the notation $\phi^n_{ij} \equiv \phi^n_{i,j} = \phi(t^n, x_i, y_j)$. We remind the reader that we use (component) finite difference grids that are characterized by a single discretization scale, h, so that $\Delta x = \Delta y = h$, and $\Delta t = \lambda h$, where λ is the Courant number. Each of the above expressions is a second order ($O(h^2)$) approximation to its continuum counterpart, and is centred at $(t^{n+1/2}, x_i, y_j)$.

rescaling) of the dynamical fields after one or more time steps [35, 136],

$$\phi_a \to \frac{\phi_a}{\sqrt{\phi_b\phi_b}} \qquad \pi_a \to \pi_a - \frac{\phi_b\partial_t\phi_b}{\phi_b\phi_b}\phi_a. \tag{4.23}$$

As we will see, this is a very effective method to reproject the field back into the S^2 sphere.

A more elaborate technique that parallels an approach that has been used very effectively in numerical relativity [137, 138] is known as *constraint damping*. One specific implementation of the technique involves the introduction of the constraints of the Einstein equations as independent fields, Z, followed by the addition of a damping (or frictional) term. Since the added terms do not contain higher derivatives, they do not affect the hyperbolicity (and thus the well-posedness) of the original equations of motion. The evolution equation for Z has the form,

$$\frac{\partial Z}{\partial t} = \text{Einstein constraints} + \text{damping terms...}, \tag{4.24}$$

In our case, the constraint $C(t,x,y) \equiv \phi_a\phi_a - 1$ is algebraic in the dynamical fields, ϕ. Thus, it is not necessary to promote $C(t,x,y)$ to an independent field. We simply add a damping term $-\xi_1 C = -\xi_1(\phi_a\phi_a - 1)$, where ξ is an adjustable positive parameter, to the evolution equations (4.17), yielding

$$\frac{\partial\phi_a(t,x,y)}{\partial t} = \pi_a(t,x,y) - \xi_1(\phi_a\phi_a - 1)\,. \tag{4.25}$$

Authors of previous implementations [137, 138] report that this modification is expected to exponentially damp violations from the constraint on a time scale $\approx \xi^{-1}$.

The constraint $C = \phi_a\phi_a - 1$ only involves the ϕ_a fields. However, we have evolution equations for both the ϕ and the time derivatives π. We have found that it is advantageous to include constraint damping for the π^a fields. We thus define

$$C' \equiv \frac{1}{2}\frac{\partial C}{\partial t} = \phi_1\pi_1 + \phi_2\pi_2 + \phi_3\pi_3 = 0\,, \tag{4.26}$$

and then modify the residual form of the equations for the π^a (4.16), via

$$\frac{\partial\pi_a(t,x,y)}{\partial t} = ... - \xi_2(\phi_b\pi_b)\,, \tag{4.27}$$

where ξ_2 is another adjustable positive parameter.

4.3.4 Initial Data

In order to investigate the dynamics in the baby Skyrme system we need to construct initial data $\phi_a^0(i,j)$ and $\pi_a^0(i,j)$, $a = 1,2,3$ (i.e. initial values defined on the finite difference grid (x_i, y_j). For a static baby skyrmion, this is achieved by first interpolating and translating the profile function $f(r)$ in exactly the same manner as was done for Q-ball initial data in Sec. 3.3.3. The procedure is summarized in Fig. 4.4.

```
1: for i = 1 to Nx do do
2:   for j = 1 to Ny do do
3:     Calculate interpolation radius r_ij = sqrt((x_i - x_c)^2 - (y_j - y_c)^2)
4:     Interpolation routine computes the value of f(r_ij) = f(i,j)
5:   end for
6: end for
```

Figure 4.4: Interpolation and translation of a baby skyrmion to (x_c, y_c).

Once the profile function has been transferred to the finite difference mesh, yielding values $f(i,j)$, the dynamical field values $\phi_a^0(i,j)$ are set via

$$\begin{aligned} \phi_1^0(i,j) &= \sin f(i,j)\cos\theta(i,j)\,, \\ \phi_2^0(i,j) &= \sin f(i,j)\sin\theta(i.j)\,, \\ \phi_3^0(i,j) &= \cos f(i,j) \end{aligned} \tag{4.28}$$

where

$$\theta(i,j) = \tan^{-1}\left(\frac{y_j - y_c}{x_i - x_c}\right). \tag{4.29}$$

Since we are considering a static initial configuration, the values for the π fields are simply given by

$$\pi_1^0(i,j) = \pi_2^0(i,j) = \pi_3^0(i,j) = 0\,. \tag{4.30}$$

We refer to the angle θ that appears in (4.28) as the *internal phase* of the skyrmion, and for single-skyrmion initial data it can be chosen arbitrarily with no impact on the subsequent evolution.

4.3.5 Boosted Initial Data

The procedure for determining initial data describing a boosted baby skyrmion is essentially the same as that used for generating boosted Q-ball initial conditions as described in Sec. 3.3.4. We again consider a boost with Lorentz factor γ in the $+x$ direction, and use primes to denote the coordinate system associated with the rest frame of the skyrmion. We thus have

$$t' = \gamma(t + vx) \quad x' = \gamma(x + vt) \quad y' = y\,, \tag{4.31}$$

and

$$t = \gamma(t' - vx') \quad x = \gamma(x' - vt') \quad y = y'\,. \tag{4.32}$$

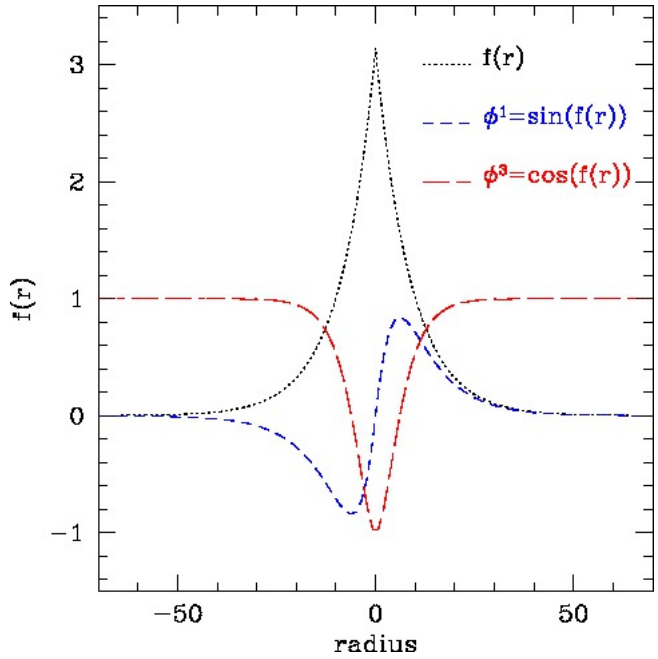

Figure 4.5: Initial data for the fields of a $B = 1$ baby skyrmion. This figure shows the profile function $f(r)$, along with the two non-vanishing field components, ϕ_1 and ϕ_2, which follow from the hedgehog ansatz (4.28) with $\theta = \pi/2$. A natural length scale is defined by the size of the baby skyrmion field, which appears to be around ≈ 50 units in radius (≈ 100 in diameter). We use this size to determine acceptable dimensions for our computational domains, noting that, as usual, the meaning of high (or low) resolution for a finite difference grid will always be relative to the natural scale.

From equations (3.39) the dynamical fields $\phi_a(t', x', y')$ have the following values in the boosted frame:

$$\begin{aligned}
\phi_1(t,x,y) &= \phi_1'(t',x',y') = \sin f(x',y')\cos\theta(x',y') = \sin f(\gamma[x+vt],y)\cos\theta([\gamma(x+vt),y])\,,\\
\phi_2(t,x,y) &= \phi_2'(t',x',y') = \sin f(x',y')\sin\theta(x',y') = \sin f(\gamma[x+vt],y)\sin\theta([\gamma(x+vt),y])\,,\\
\phi_3(t,x,y) &= \phi_3'(t',x',y') = \cos f(x',y') = \cos f([\gamma(x+vt)],y)\,,
\end{aligned} \tag{4.33}$$

where

$$\theta(x,y) = \tan^{-1}\left(\frac{y-y_c}{\gamma[(x-x_c)+vt]}\right)\,. \tag{4.34}$$

The time derivatives, $\pi_a(t,x,y)$, transform according to (3.40) and (3.41), yielding

$$\pi_1 = \frac{\partial\phi_1'}{\partial x'}\gamma v\,, \quad \pi_2 = \frac{\partial\phi_2'}{\partial x'}\gamma v\,, \quad \pi_3 = \frac{\partial\phi_3'}{\partial x'}\gamma v\,, \tag{4.35}$$

where we have used the fact that the rest-frame time derivatives, $\pi'_a(t', x', y')$, are identically 0.

At the initial time, $t = 0$, the coordinates in the rest frame are

$$t' = \gamma v x \qquad x' = x\gamma \qquad y' = y\,. \tag{4.36}$$

Again following the method described in Sec. 3.3.4, we interpolate in $f(x', y')$ to determine the values $f(\gamma x, y)$ in the lab frame, using $r' = \sqrt{x'^2 + y'^2}$, as well as the fact that in the rest frame $f(x', y')$ is a circularly symmetric function, i.e. $f(x', y') \equiv f(r')$. A complete set of initial values for a boosted baby skyrmion then follows by substituting $t = 0$ in (4.33). For the ϕ_a we have

$$\begin{aligned} \phi_1^0(x, y) &= \sin f(\gamma x, y) \cos\theta(\gamma x, y)\,, \\ \phi_2^0(x, y) &= \sin f(\gamma x, y) \sin\theta(\gamma x, y)\,, \\ \phi_3^0(x, y) &= \cos f(\gamma x, y)\,. \end{aligned} \tag{4.37}$$

while for the π_a we find

$$\pi_1^0(x, y) = \frac{\partial\phi_1^0}{\partial x'}\gamma v\,, \quad \pi_2^0(x, y) = \frac{\partial\phi_2^0}{\partial x'}\gamma v\,, \quad \pi_3^0(x, y) = \frac{\partial\phi_3^0}{\partial x'}\gamma v\,. \tag{4.38}$$

We note that the derivatives $\partial\phi_a^0/\partial x'$ in this last set of expressions are computed numerically.

4.3.6 Initial Data: Two Skyrmions

An important observation is that for the case of initial data describing two skyrmions we are free to choose separate internal phases to set the $t = 0$ values of the ϕ_a fields.

Specifically, let us consider two skyrmions, each defined by the hedgehog ansatz (4.7), but characterized by separate internal angles θ_1 and θ_2. Then denoting the fields for the two configurations by $\phi_a^{(1)}$ and $\phi_a^{(2)}$, respectively, we have from (4.28)

$$\phi_a^{(1)} = \begin{pmatrix} \sin f(r_1) \sin(\theta_1) \\ \sin f(r_1) \cos(\theta_1) \\ \cos f(r_1) \end{pmatrix}, \tag{4.39}$$

$$\phi_a^{(2)} = \begin{pmatrix} \sin f(r_2)\sin(\theta_2) \\ \sin f(r_2)\cos(\theta_2) \\ \cos f(r_2) \end{pmatrix}, \tag{4.40}$$

where r_1 and r_2 are the radial distances from the centres of the corresponding hedgehogs. We then refer to the parameter Ψ, defined by

$$\Psi \equiv \theta_2 - \theta_1 \,,$$

as the *relative phase* between the skyrmions. This quantity plays an important role in the dynamics of skyrmion collisions.

In particular, one of the well-known results from earlier studies is that a pair of skyrmions (or an skyrmion and antiskyrmion) separated by some distance, and at rest with respect to one another, will experience mutual forces ranging from maximally attractive to maximally repulsive, dependent on the value of Ψ [55, 139, 140]. Piette *et al* [55] define the *attractive channel* as a configuration of two hedgehogs with an initial $\Psi = \pm\pi$, while the *repulsive channel* corresponds to $\Psi = 0$ (i.e. no phase difference). We will adopt this terminology in the following.

4.4 Code Validation

In this section we describe the various tests that we have used to establish the correctness of our numerical implementation of the baby Skyrme model. These tests include 1) computation of convergence factors (eqn. (2.30)), and verification that the expected values are apparently achieved in the limit $h \to 0$; 2) a similar analysis of the convergence of independent residuals; and (3) where suitable, investigation of the conservation of the topological charge B and the the total energy E (defined below), again as function of the grid resolution. We note that the computation of B and E is limited to unigrid (non-adaptive) calculations, since the coding required for the adaptive case is beyond the scope of the current project.

We apply our tests to the following initial data sets: 1) smooth Gaussian data, 2) a static baby skyrmion, and 3) a boosted baby skyrmion. We will show the results of these tests for two of the six dynamical fields of our model, namely, ϕ_1 and π_1. Nevertheless, we emphasize that the other fields—ϕ_2, ϕ_3 and π_2, π_3—converge in the same manner. For all of the test calculations described here we used Dirichlet boundary conditions, (see App. E), and enforced the constraints using

the reprojection method given by (4.23). Additionally, all of the tests were run with a potential parameter $\mu^2 = 0.001$.

4.4.1 Computation of the Topological Charge B

We calculate the total topological charge (or baryon number), B, in the same fashion as the total charge, Q, was computed in Sec. 3.4.2. The baryon number density, B_0, is given by (4.5),

$$B_0 = \epsilon^{abc}\epsilon_{\nu\rho}\phi_a\partial_\nu\phi_b\partial_\rho\phi_c = \epsilon^{abc}\ \ \phi_a(\partial_x\phi_b)(\partial_y\phi_c)\,. \tag{4.41}$$

The total baryon number, B, is then given by the spatial integral

$$B = \frac{1}{4\pi}\int B_0\ \ dx\ \ dy\,. \tag{4.42}$$

When our computations are run in parallel the computational domain is divided into several subregions, and we thus perform the integration locally (i.e. one every subregion), using a second order trapezoidal rule. For the I-th subregion, we have a contribution, B_I, given by

$$B_I = \left(\frac{1}{4\pi}\right)\frac{\Delta x\ \Delta y}{4}\sum_{i,j}^{N_x-1,N_y-1}\left([B_0]_{i,j} + [B_0]_{i+1,j} + [B_0]_{i,j+1} + [B_0]_{i+1,j+1}\right)\,, \tag{4.43}$$

where Δx and Δy are the grid spacings of the two-dimensional mesh. We then sum the B_i to determine the final value of B, where care must again be taken to avoid "double counting" in overlapping regions introduced by the parallelization.

4.4.2 Computation of Energy Quantities

In the course of a calculation we compute the following locally defined energy densities: 1) total, T_{00}; 2) kinetic, T and 3) potential, P. We also evaluate the integrals of these quantities over the solution domain, yielding values denoted by E, K and U, respectively.

Computing the local energy density, T_{00}, is accomplished by first calculating the energy-momentum tensor, $\mathcal{T}_{\mu\nu}$, of the model. As usual, T_{00} describes the density and flow of the (local) 3-momentum. We have [32],

$$\mathcal{T}_{\mu\nu} = \frac{\partial\mathcal{L}}{\partial(\partial_\mu\phi_a)}\partial_\nu\phi_a - g_{\mu\nu}\mathcal{L}\,, \tag{4.44}$$

where $\mathcal{L}$ is given by (4.14). The local energy density, T_{00}, is then given by

$$T_{00} = \mathcal{T}_{\mu\nu} U^\mu U^\nu = \mathcal{T}_{00} \,, \tag{4.45}$$

where $U^\mu = (1, 0, 0)$ is the 3-velocity of a coordinate-stationary observer [141]. The calculation of the kinetic K and potential U energy densities follow from the decomposition of the Lagrangian density (4.1) as $\mathcal{L} = K - U$, yielding the expressions [55],

$$K = \int d^2x \;\; \frac{1}{2}\dot{\phi_a}\dot{\phi_a} + \frac{1}{2}(\dot{\phi_a} \times \partial_i \phi_a)(\dot{\phi_a} \times \partial_i \phi_a) \,, \tag{4.46}$$

and[26]

$$U = \int d^2x \;\; \frac{1}{2}\partial_i \phi_a \partial_i \phi_a + \frac{1}{4}(\partial_i \phi_a \times \partial_j \phi_a)(\partial_i \phi_a \times \partial_j \phi_a) - \frac{\mu^2}{2}(1 - \phi_3^2) \,. \tag{4.47}$$

The specific forms for T_{00}, K and U are calculated using symbolic manipulation, exported to Fortran 77, and then computed as separate grid functions in our code.

The total energy, E, is then calculated in complete analogy with the computation of B described above. Sub-integrals, E_I, are given by

$$E_I = \int d^2x \;\; E = \frac{\Delta x \; \Delta y}{4} \sum_{i,j}^{N_x - 1, N_y - 1} ([T_{00}]_{i,j} + [T_{00}]_{i+1,j} + [T_{00}]_{i,j+1} + [T_{00}]_{i+1,j+1}) \;, \tag{4.48}$$

and then the E_I are summed to yield the value of E. Correspondingly, the subintegrals for K and U are calculated via

$$K_I = \int d^2x \;\; T = \frac{\Delta x \; \Delta y}{4} \sum_{i,j}^{N_x - 1, N_y - 1} ([T]_{i,j} + [T]_{i+1,j} + [T]_{i,j+1} + [T]_{i+1,j+1}) \;, \tag{4.49}$$

$$U_I = \int d^2x \;\; P = \frac{\Delta x \; \Delta y}{4} \sum_{i,j}^{N_x - 1, N_y - 1} ([P_{00}]_{i,j} + [P_{00}]_{i+1,j} + [P_{00}]_{i,j+1} + [P_{00}]_{i+1,j+1}) \;. \tag{4.50}$$

Similarly to E_I, the K_I and U_I are summed to yield the values of K and U.

[26] The potential energy U is the sum of the spatial gradients and the potential function V.

4.4.3 Independent Residual Evaluators

As in Sec. 3.4.3 for the case of Q-ball evolution, we evaluate independent residuals for the field equations to provide strong evidence for the convergence of our finite difference approximations to the continuum solutions (see Chap. 2). Our specific independent residual evaluators are constructed using the same approach described in that section, although in this case we use a wider variety of finite difference operators due to the appearance of mixed spatial derivatives in the equations of motion. For the ϕ_a variables, we replace the Crank-Nicholson approximation with the following expression, which is first order accurate in time:

$$I_{\phi_a}(i,j) = \frac{\phi_a(i,j)^{n+1} - \phi_a(i,j)^n}{\Delta t} - \pi_a(i,j)^{n+1}\,. \tag{4.51}$$

As noted in Sec. 4.3.1, it is not practical to write the explicit expressions for the residuals of the π_a evolution equations, and for the independent residuals we are confronted with the same problem. Therefore we again use a Maple script to replace differential operations by finite difference approximations to generate the independent residual expressions $I_{\pi_a}(i,j)$. Here we use first order forward approximations for the first and second spatial derivatives of any of the ϕ_a or π_a, as well as a first order approximation for the time derivatives of the π_a:

$$\frac{\partial \pi_a}{\partial t} = \frac{\pi_a^{n+1}(i,j) - \pi_a^n(i,j)}{\Delta t} + O(\Delta t)\,. \tag{4.52}$$

The differential operators employed to construct the equations for $I_{\pi_a}(i,j)$ are summarized in Table (4.2).

If our finite difference solutions *are* converging to the appropriate continuum solutions, the independent residuals $I_{\phi_a}(i,j)$ and $I_{\pi_a}(i,j)$ should vanish in the limit $h \to 0$. As is the case for the Q-ball evolution, although we anticipate the finite difference solution itself to be $O(h^2)$ accurate, the independent residuals—which are constructed with first-order approximations—are only expected to be $O(h)$ as $h \to 0$. We also re-stress that since the independent residual operators are only *applied* to the fundamental difference solution—and not used in any evolutionary capacity—the stability of the FDAs used to construct them is not relevant.

In the following subsections we show results of independent residual tests for the functions ϕ_1 and π_1, and for the three different types of initial data we listed at the beginning of this section.

ϕ	ϕ_{ij}^{n+1}
ϕ_x	$\frac{-3\phi^{n+1}(i,j)+4\phi^{n+1}(i+1,j)-\phi^{n+1}(i+2,j)}{2\Delta x}$
ϕ_y	$\frac{-3\phi^{n+1}(i,j)+4\phi^{n+1}(i,j+1)-\phi^{n+1}(i,j+2)}{2\Delta y}$
ϕ_t	$\frac{\phi_{ij}^{n+1}-\phi_{ij}^{n}}{\Delta t}$
ϕ_{xx}	$\frac{\phi^{n+1}(i,j)-2\phi^{n+1}(i+1,j)+\phi^{n+1}(i+2,j)}{\Delta x^2}$
ϕ_{yy}	$\frac{\phi^{n+1}(i,j)-2\phi^{n+1}(i,j+1)+\phi^{n+1}(i,j+2)}{\Delta y^2}$
ϕ_{xy}	$\frac{-3\phi_x(i,j)+4\phi_x(i,j+1)-\phi_x(i,j+2)}{\Delta y}$

Table 4.2: Two-(space) dimensional forward finite difference stencils used to compute independent residuals for any of the six dynamical variables ϕ_a or π_a. The mixed derivative is nested, i.e. the ϕ_x terms are to be replaced by the corresponding forward approximation listed in the table. Here we use the notation $\phi_{ij}^n \equiv \phi_{i,j}^n = \phi(t^n, x_i, y_j)$. We remind the reader that we use (component) finite difference grids that are characterized by a single discretization scale, h, so that $\Delta x = \Delta y = h$, and $\Delta t = \lambda h$, where λ is the Courant number. Each of the above expressions is a first order ($O(h)$) approximation to its continuum counterpart at (t^n, x_i, y_j).

We use four distinct resolutions, h_L, $L = 1, 2, 3, 4$, where $h_L = h_{L-1}/2$. The residual norms have been rescaled by factors of 2^{L-1}, so that coincidence of the resulting plots indicates the expected first order convergence of the residuals.

4.4.4 Gaussian-smooth Data

We begin our tests with the evolution of "generic" initial data which, as was the case for the Q-ball test in Sec. 3.4.4, is based on a Gaussian form for the ϕ_a fields, and which is time-symmetric, so that the π_a identically vanish at $t = 0$. The initial data needs to satisfy the chiral constraint

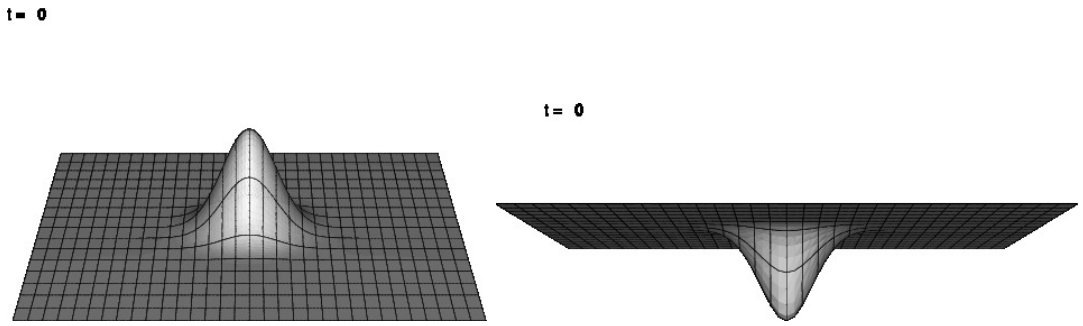

Figure 4.6: Field components for initial smooth data. The Gaussians ϕ_1 and ϕ_3 are concave down (left), whilst ϕ_2 is concave up (right). The three fields satisfy the chiral constraint $\phi_a\phi_a = 1$.

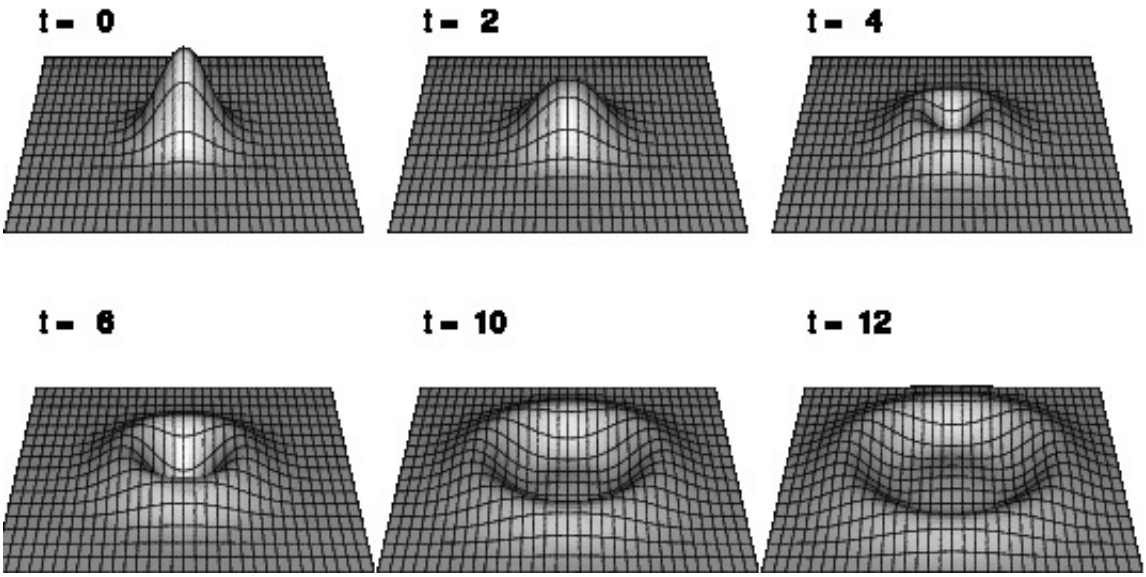

Figure 4.7: Evolution of ϕ_1 for a computation with Gaussian initial conditions. The three components of the field satisfy the chiral constraint $\phi_a\phi_a = 1$. This particular sequence corresponds to a unigrid resolution of 513×513 points, in a domain of dimensions 160×160 ($[-80, 80] \times [-80, 80]$), a Courant number of $\lambda = 0.2$, and a Gaussian pulse of width 20. The initial amplitude is $A = 1/\sqrt{2}$, which is the maximum value allowed given (4.55). No KO dissipation was used, i.e $\epsilon_{\rm KO} = 0.0$. Boundary conditions are reflecting (Dirichlet).

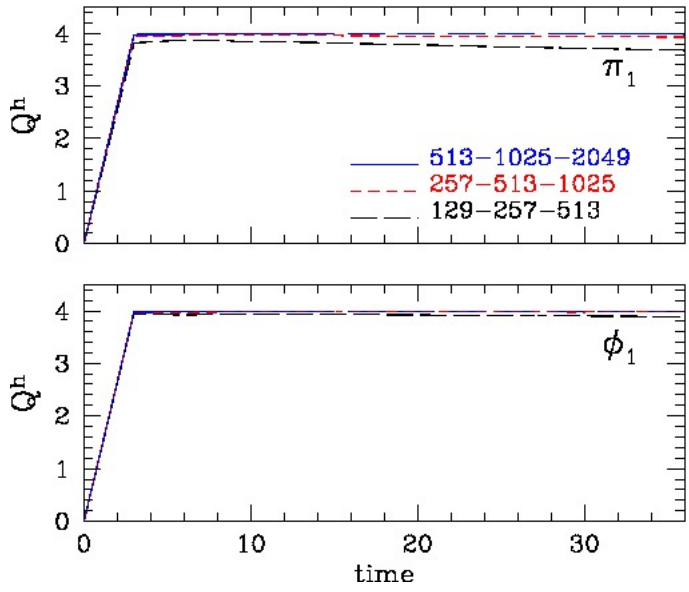

Figure 4.8: Q^h Convergence factors for the functions ϕ_1 and π_1, corresponding to the evolution of the smooth initial data in Fig. 4.7. Second order convergence is observed, since $Q^h \to 4$ as $h \to 0$.

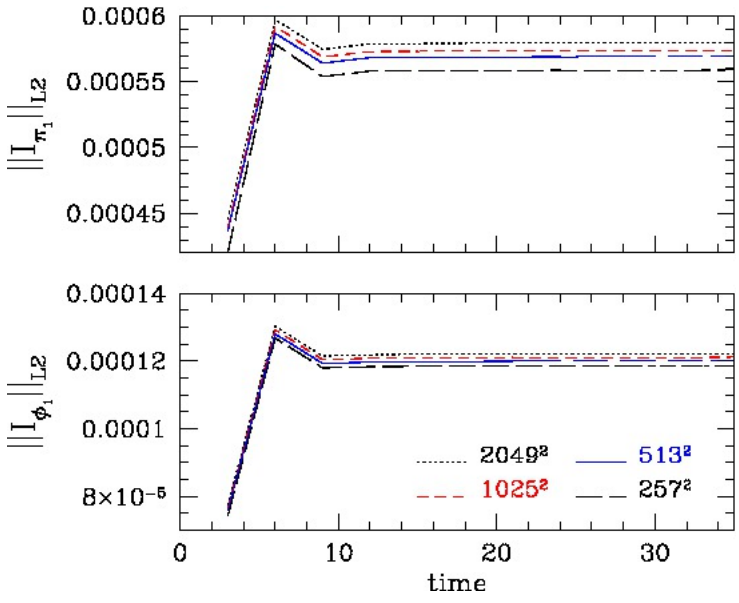

Figure 4.9: Rescaled l_2 norm of the independent residuals for the functions ϕ_1 and π_1, corresponding to the smooth initial data in Fig. 4.7. The near coincidence of the lines at different resolutions indicates first order convergence, as the mesh spacing $h \to 0$.

$\phi_a\phi_a = 1$, so we set

$$\phi_1(0, x_i, y_j) = A \exp\left[-\left(\frac{x_i - x_c}{w}\right)^2 - \left(\frac{y_j - y_c}{w}\right)^2 \right] \tag{4.53}$$

$$\phi_2(0, x_i, y_j) = A \exp\left[-\left(\frac{x_i - x_c}{w}\right)^2 - \left(\frac{y_j - y_c}{w}\right)^2 \right] \tag{4.54}$$

$$\phi_3(0, x_i, y_j) = \sqrt{1 - 2A^2 \exp\left[-2\left(\frac{x_i - x_c}{w}\right)^2 - 2\left(\frac{y_i - y_c}{w}\right)^2 \right]} \tag{4.55}$$

where w, A, x_c and y_c are parameters, and

$$\pi_1(0, x_i, y_j) = 0 \qquad \pi_2(0, x_i, y_j) = 0 \qquad \pi_3(0, x_i, y_j) = 0\,. \tag{4.56}$$

From (4.55), the maximum value of A that can be used is $1/\sqrt{2}$. An illustration of this type of initial data is given in Fig. 4.6. As shown in Fig. 4.7, the data evolves as an outgoing circularly-symmetric wavepacket (plots of ϕ_2 and ϕ_3 are very similar).

Results for the convergence factors and independent residuals for ϕ_1 and π_1 are shown in Figs. 4.8 and 4.9. Quadratic convergence of the finite difference solution is evident, since $Q^h \to 4$ as $h \to 0$, consistent with the $O(h^2)$ accuracy of the underlying difference scheme. Furthermore, the near-coincidence of the rescaled independent residuals indicates that, as expected, they converge linearly as $h \to 0$. We note that here—as well as in similar plots shown for the hedgehog evolutions described below—since the initial data is identical on all meshes, the $t = 0$ value of of Q^h is not defined (see 2.30) and has been arbitrarily set to 0.

The topological charge B for this type of initial data is effectively zero ($< 10^{-10}$) even for the coarsest resolution of our calculations (257×257 points). The computation of the conserved total energy, E, at various resolutions, is shown in Fig. 4.10. It converges quadratically to conservation as $h \to 0$, consistent with the $O(h^2)$ approximation of the finite difference scheme and the numerical integration technique (trapezoidal rule).

4.4.5 Static Hedgehog and Stability

We now turn our attention to the testing of our code using static initial data. Fig. 4.12 shows the numerical evolution of a single static hedgehog centred in the computational domain, with a potential parameter $\mu^2 = 0.001$ (Fig. 4.2). The numerical domain is 160×160 ($[-80, 80] \times$

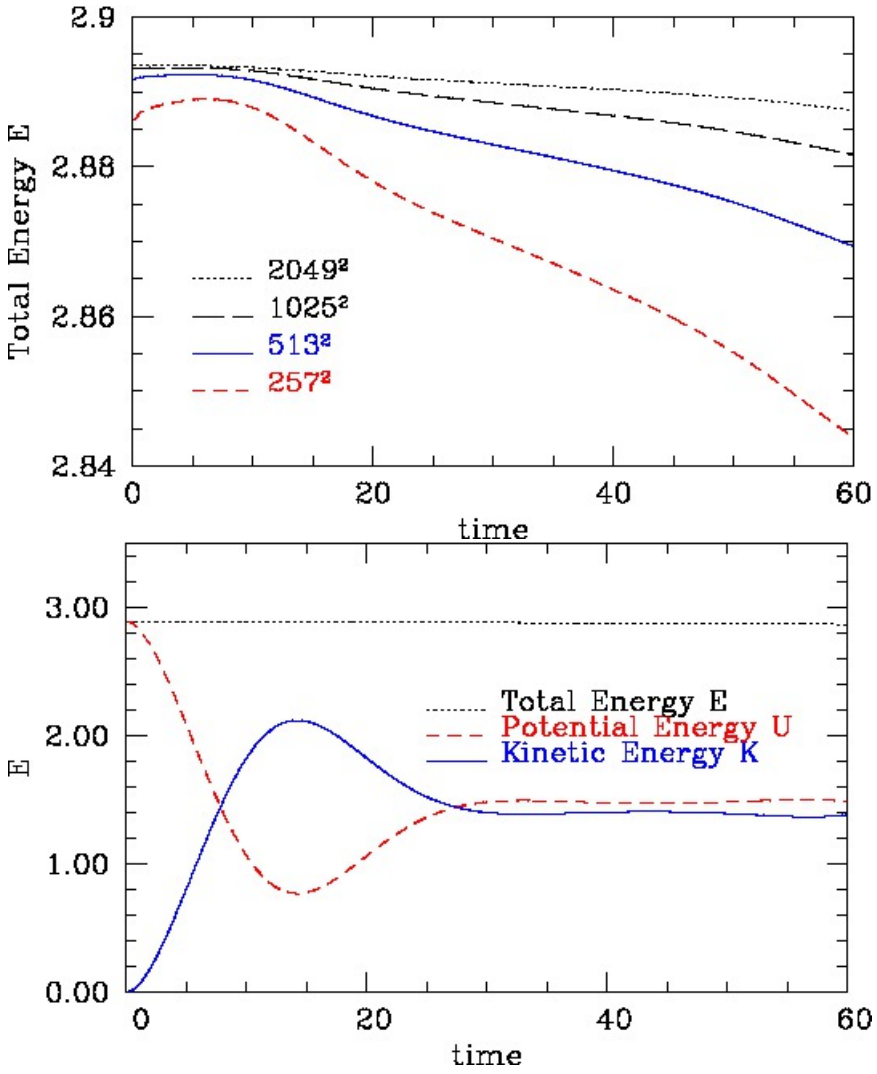

Figure 4.10: The top figure shows the evolution of the total energy E at different resolutions corresponding to the smooth initial data plotted in Fig. 4.7. Quadratic convergence to conservation is observed, as expected, since E is integrated using the second order trapezoidal rule on each subdomain as given by (4.48). The bottom plot shows the decomposition of E into kinetic energy K and potential energy U, for the same initial data at a resolution of 513×513 points. The kinetic energy increases from zero, while the potential energy proportionally decreases, and after some oscillations, K and U approach steady state values, corresponding to the circularly symmetric expanding wave front seen in Fig.4.7.

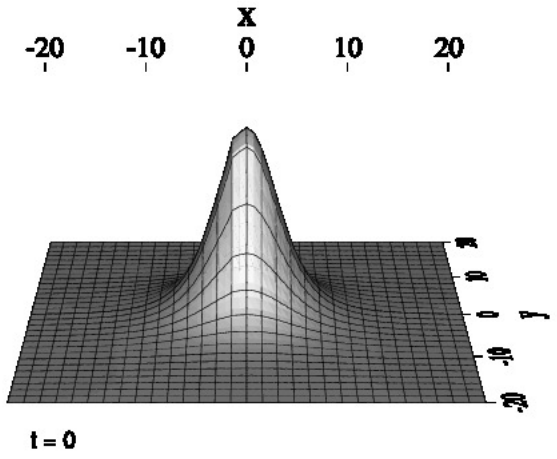

(a)

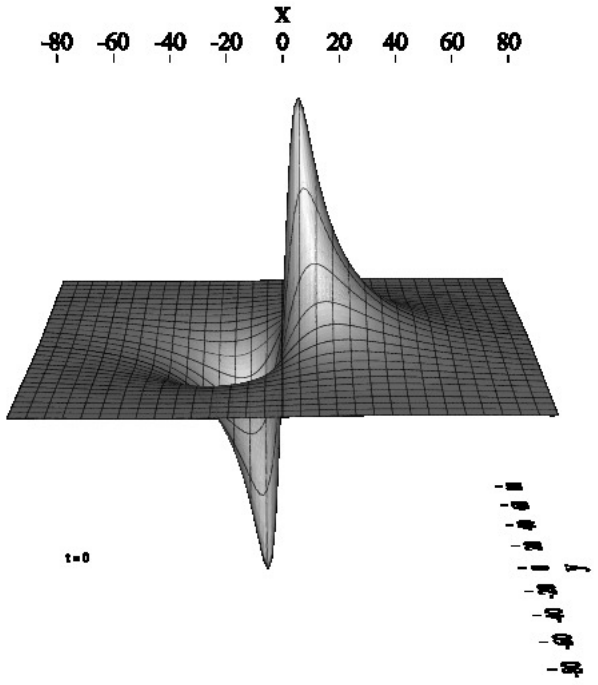

(b)

Figure 4.11: Comparison of the size of a skyrmion as defined by the baryon density, B_0, (top) and the field component, ϕ_1, (bottom). In both cases we define the approximate size via the distance from the center where the tail of the quantity is sufficiently small. Using B_0 this gives a diameter of ≈ 20 units, while using ϕ_1 we find a diameter of ≈ 100.

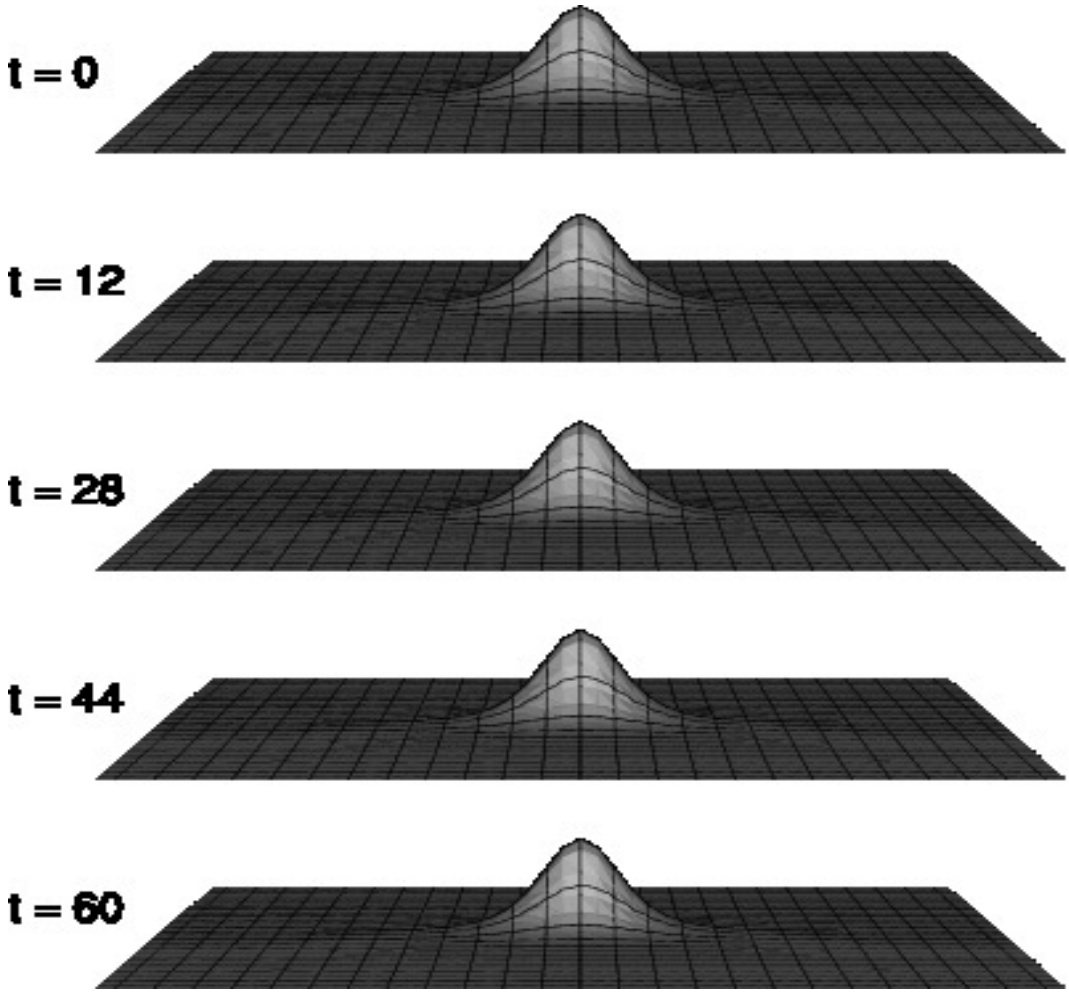

Figure 4.12: Evolution of the baryon density, B_0, for a static hedgehog sitting at the origin. The resolution is 513×513 points, on a domain of dimensions 160×160 ($[-80, 80] \times [-80, 80]$), but the figure has been cropped to $[-40, 40] \times [-40, 40]$ for illustrative purposes. The Courant number is $\lambda = 0.2$, and the potential parameter is $\mu^2 = 0.001$. The boundary conditions are Dirichlet (reflecting). No dissipation was used ($\epsilon_{\rm KO} = 0.0$). After a brief period of relaxation the hedgehog reaches a (visually) time-independent state.

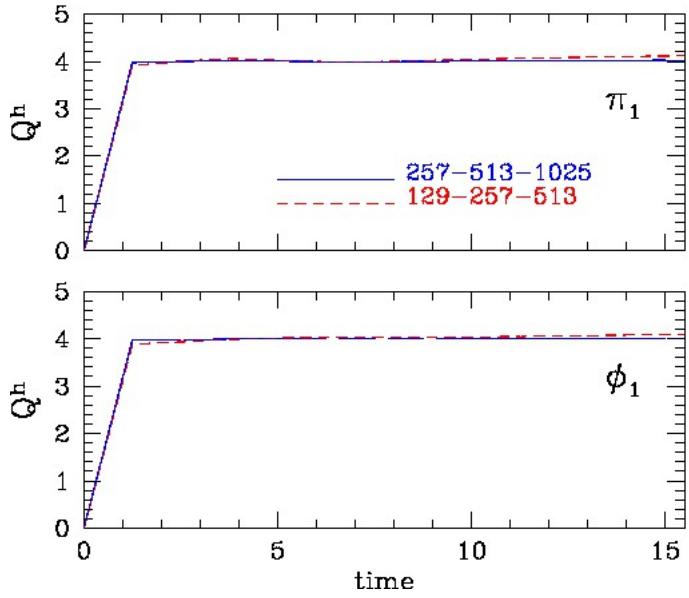

Figure 4.13: Convergence factors for the functions ϕ_1 and π_1, corresponding to the static baby skyrmion evolution in Fig. 4.12. Quadratic convergence is achieved, i.e. $Q^h \to 4$ as $h \to 0$, as expected from our finite difference approximation.

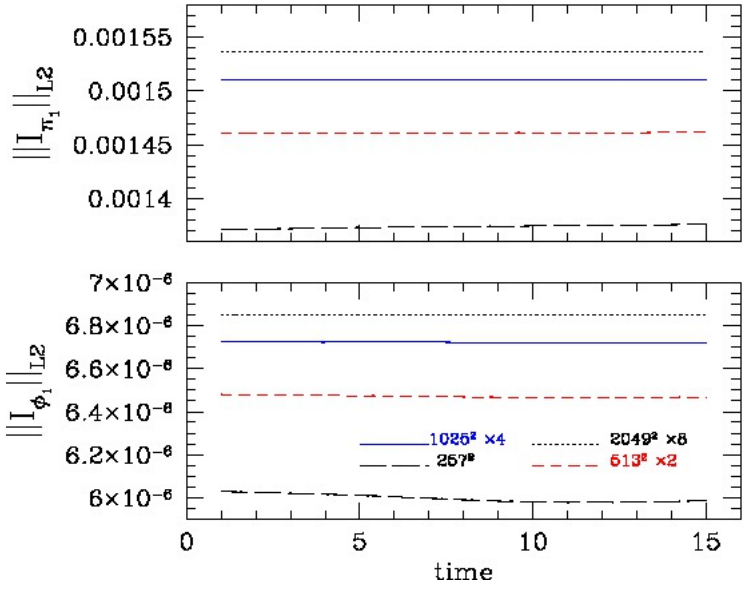

Figure 4.14: Rescaled l_2 norms of the independent residuals of ϕ_1 and π_1, at different resolutions, for the static baby skyrmion evolution shown in Fig. 4.12. Once again, the trend to coincidence of the lines as resolution is doubled signals the expected $O(h)$ convergence.

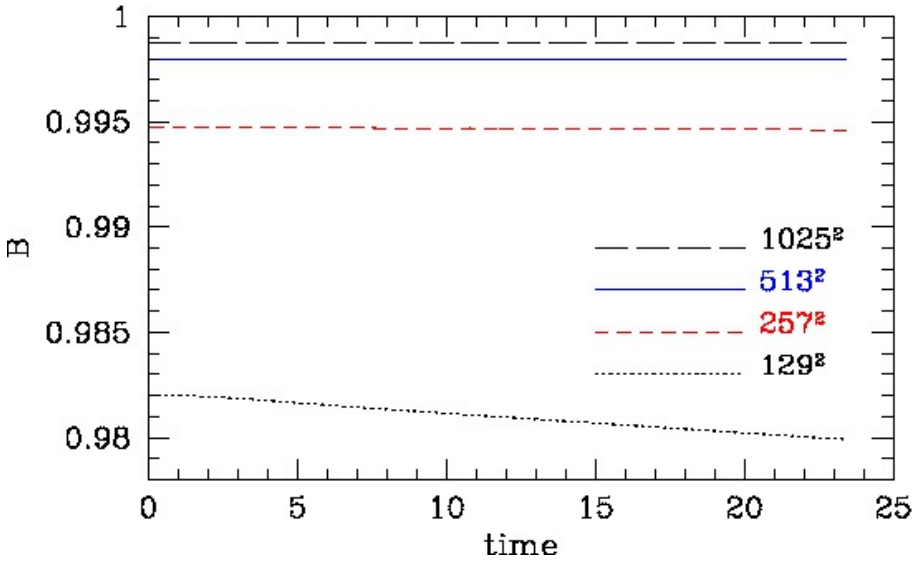

(a)

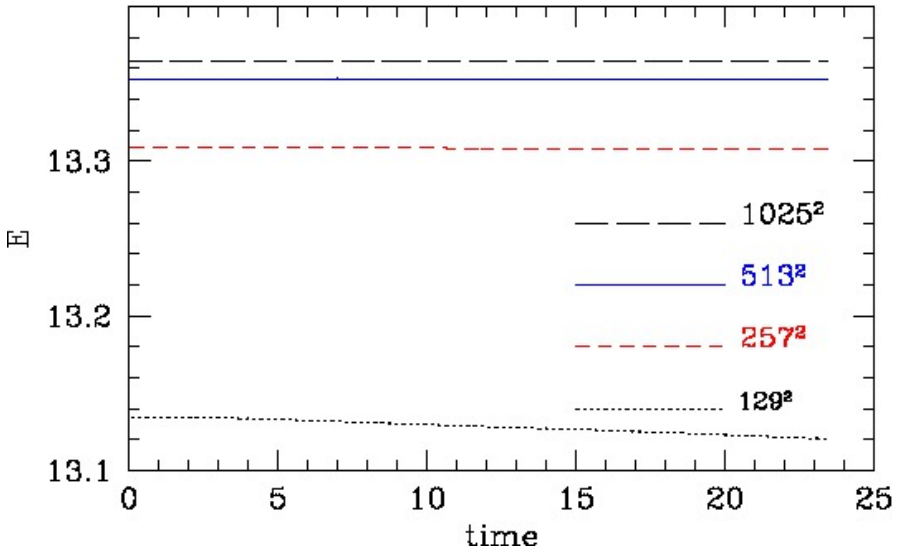

(b)

Figure 4.15: Evolution of the baryon number, B, (Fig. 4.15a) and total energy, E, (Fig. 4.15b) at different resolutions for the evolution of the static baby skyrmion initial data plotted in Fig. 4.12. The top plot shows the evolution of the baryon number B, while the bottom one shows the evolution of the total energy E. The kinetic energy K is of the order of 1×10^{-4}, thus for all practical purposes E is purely potential. Although at any fixed resolution there appears to a roughly linear "dissipation" of E and B with time, the expected quadratic convergence of both quantities is clearly observed. The use of a Dirichlet or Sommerfeld boundary condition did not produce any appreciable difference in the results of this test.

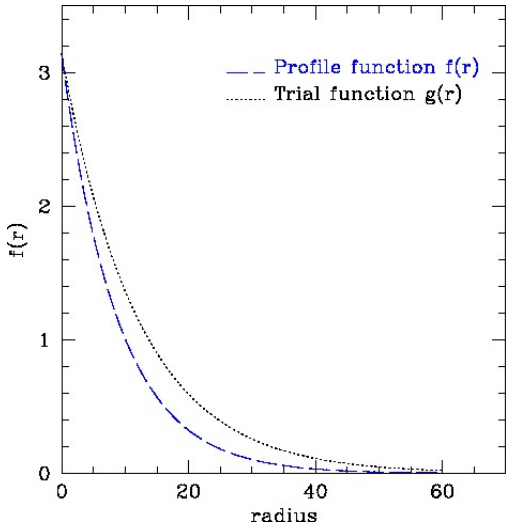

Figure 4.16: This figure displays a baby skyrmion radial profile function, $f(r)$, with $\mu^2 = 0.001$ and a trial profile function $g(r) = \pi \ \exp(-r/8.8)$.

$[-80, 80]$). [27] We note that this choice of domain ensures that the hedgehog, which has a diameter of about 100 units, is properly contained on the grid. The Courant number for this calculation is $\lambda = 0.1$, and Kreiss-Oliger dissipation is not used ($\epsilon_{\rm KO} = 0.0$) since the evolution is not affected (appreciably) by high frequency components in the solution. Again, the boundary conditions are Dirichlet (reflecting). After a brief period of relaxation, the skyrmion sets into a (visually) static state, inferred from the apparent time-independence of B_0.

Calculation of the convergence factors, Q^h, (Fig. 4.13) unambiguously reveals that they tend to four, which indicates second order ($O(h^2)$) convergence, consistent with our FDA scheme. The rescaled independent residuals for ϕ_1 and π_1 are shown in Fig. 4.14. As before, the trend to coincidence of the curves demonstrates that the residuals converge linearly ($O(h)$) with the mesh spacing h.

Fig. 4.15 shows the results of the computation of the conserved topological charge, B, and the total energy, E, at various resolutions. Both quantities converge quadratically to conservation as $h \to 0$. This is the expected rate of convergence since both the finite difference scheme and the approximate integration technique (second order trapezoidal rule) are $O(h^2)$.

We also devised a test to investigate simultaneously the dynamical stability and convergence of baby skyrmion data. The experiment involved trial-and-error approximation of the numerically

[27] We remind the reader that this notation, defined in Sec. 3.4.1, means that the computational domain has extent $[x_{\rm min}, x_{\rm max}] \times [y_{\rm min}, y_{\rm max}]$

computed profile, $f(r)$, with the closed form *trial* function, $g(r)$,

$$g(r) = \pi \, \exp\left(-r/8.8\right). \tag{4.57}$$

Fig. 4.16 shows plots of both functions. Heuristically, we can consider $g(r)$ a small perturbation of $f(r)$. Initializing the dynamical fields via (4.28), but with $f(r) \to g(r)$, the baryon density of the "perturbed" hedgehog oscillates slightly at early times, but then eventually settles into a stationary state, very close to that produced for the corresponding true baby skyrmion. This provides evidence that this particular soliton is indeed stable under small (but finite) perturbations. Furthermore, investigation of the conservation of B and E for the perturbed evolution yields the same rates of convergence as for the computations using $f(r)$.

4.4.6 Boosted Skyrmion

As for the previously described experiments with Q-balls, one of our principal objectives is to study collisions of baby skyrmions having large relative velocities. As a preliminary step towards this goal, we investigate our code's convergence properties using initial data for a single boosted baby skyrmion, prepared as described in Sec. 4.3.6. We consider a relatively small boost with $\gamma = 1.6$ (γ is the boost of the skyrmion relative to the lab frame). Evolutions of baby skyrmions with much larger boosts will be considered in Sec. 4.6. As an aside, and as stated in Sec. 3.4.6, it is important to keep in mind that at fixed resolution, and as a consequence of effects such as Lorentz contraction along the boost direction, the convergence of our code degrades with increasing γ. In order to perform computations with fixed accuracy as we increase the value of γ, we need an increase in grid resolution (increasingly fine mesh spacing), albeit not *globally*, i.e. not required throughout the whole computational domain. It is therefore evident that maintaining constant accuracy globally is computationally expensive and grossly inefficient. This constitutes the major motivating factor for the use of AMR in our calculations, as was the case for the evolution of highly boosted Q-balls.

We performed convergence and independent residual tests for a $\gamma = 1.6$ ($v = 0.8$) boosted baby skyrmion (Fig. 4.18), in a box with dimensions 120×120 ($[-60, 60] \times [-60, 60]$), with $\lambda = 0.1$, and $\epsilon_{\rm KO}$ in the range 0.4–0.6, (the precise choice of $\epsilon_{\rm KO}$ did not appreciably affect the results). We note that the decreased domain limits, with respect to the static baby skyrmion in Fig. 4.12,

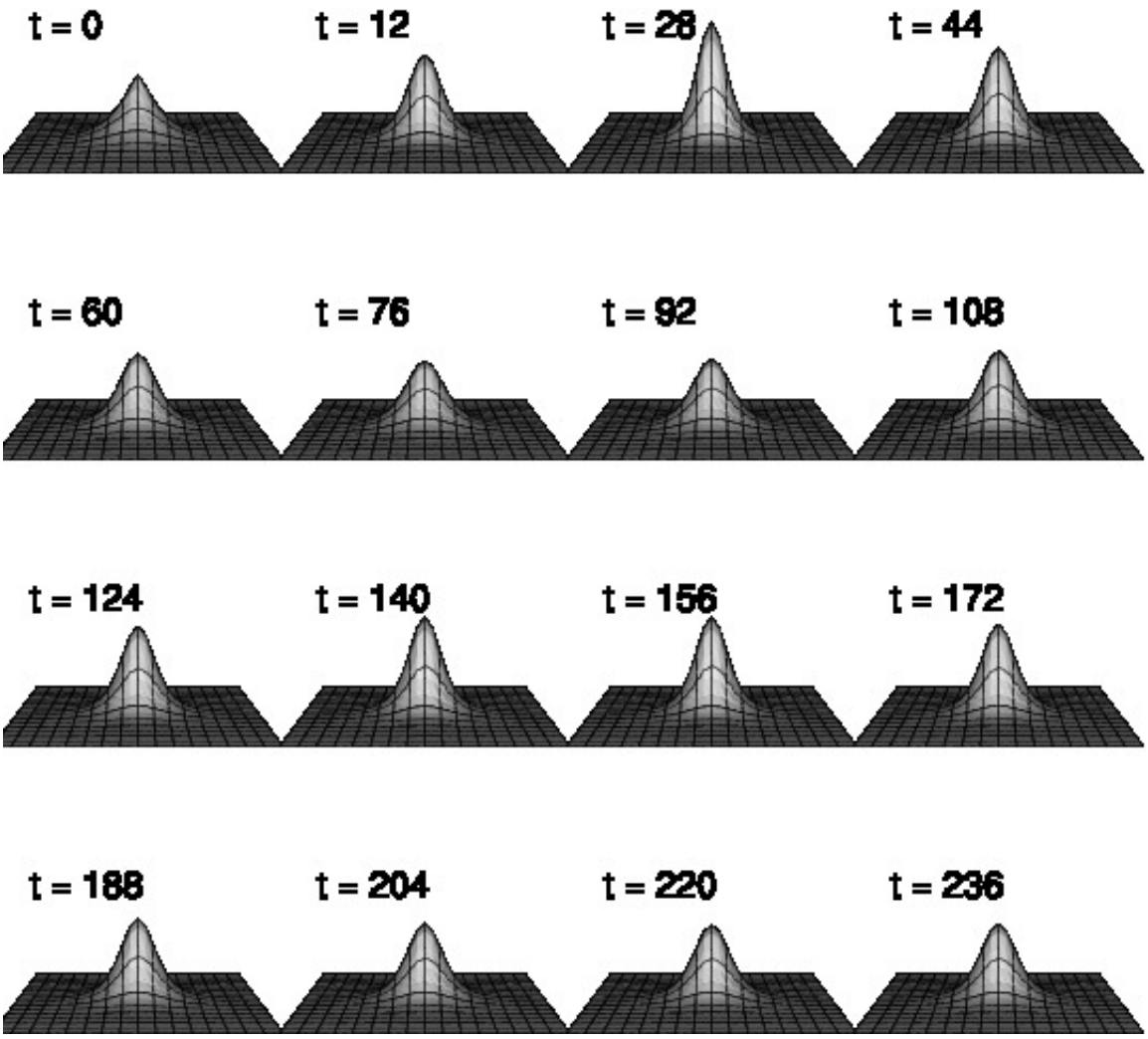

Figure 4.17: Evolution of the baryon density of a perturbed hedgehog, initialized using the trial function $g(r)$ in Fig. 4.16. The parameters of this run are identical to those in Fig. 4.12. However, each snapshot has been cropped to $[-25, 25] \times [-25, 25]$ for a better illustration. The soliton's maximum undergoes damped oscillations, and after some time it settles down around the value of the maximum of a hedgehog initialized with $f(r)$. Concentric outgoing waves are slightly visible: these waves carry the excess of energy released by the perturbed hedgehog while it relaxes into a static state, very close to that of the baby skyrmion initialized with $f(r)$. This behaviour shows that the hedgehog is indeed stable under small but finite perturbations. We note that the "jaggedness' apparent in some of the above plots, as well as those in Fig. 4.18, is an artifact of the plotting, which used a coarsening of the actual finite difference grid.

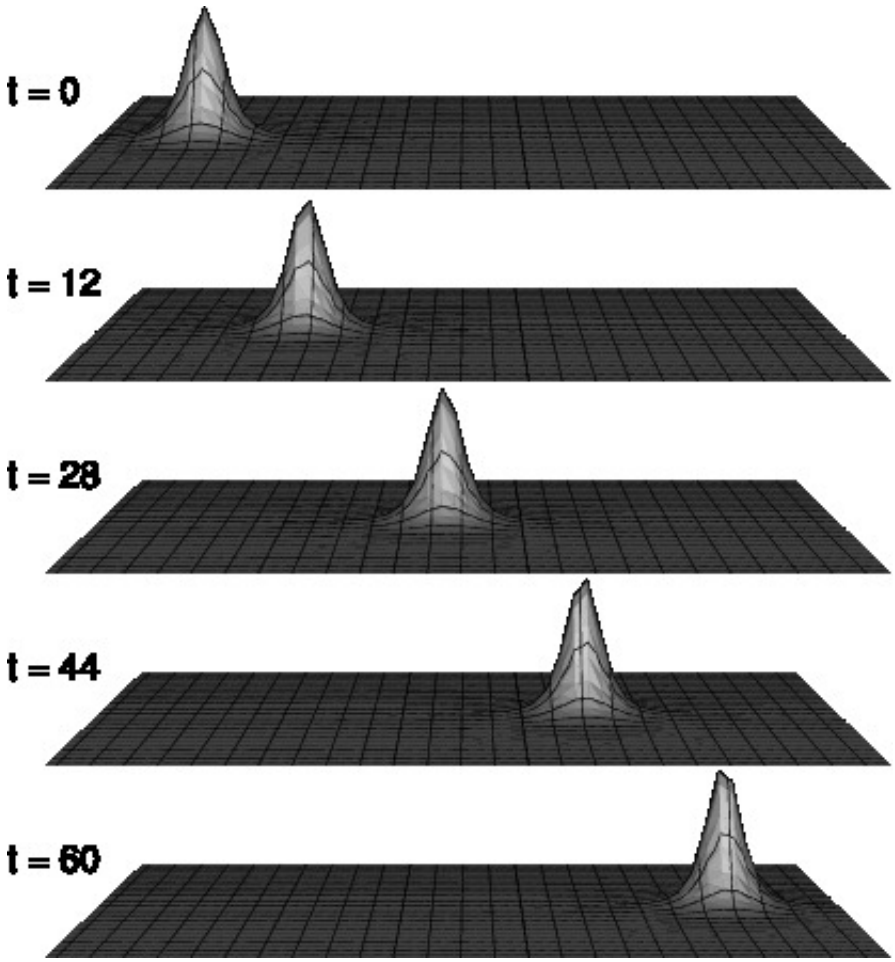

Figure 4.18: Evolution of the baryon number density B_0 of a boosted hedgehog at $\gamma = 1.6$ ($v = 0.8$). This data comes from a unigrid calculation with a numerical mesh of 513×513 points, on a domain of dimensions 120×120 ($[-60, 60] \times [-60, 60]$), but the figure has been cropped to $[-60, 60] \times [-30, 30]$ for clarity. The initial position of the soliton is $(x_0, y_0) = (-30, 0)$. The Courant number is $\lambda = 0.2$ and the dissipation parameter is $\epsilon_{\mathrm{KO}} = 0.5$. The diameter of the baby skyrmion (in the x-direction) for this value of γ contracts to $100/1.6 \approx 62.5$. The boundary conditions are Sommerfeld (outgoing radiation). We observe that the skyrmion evolves in an essentially unperturbed and stable fashion. We applied small changes to the value of γ and observed identical behaviour.

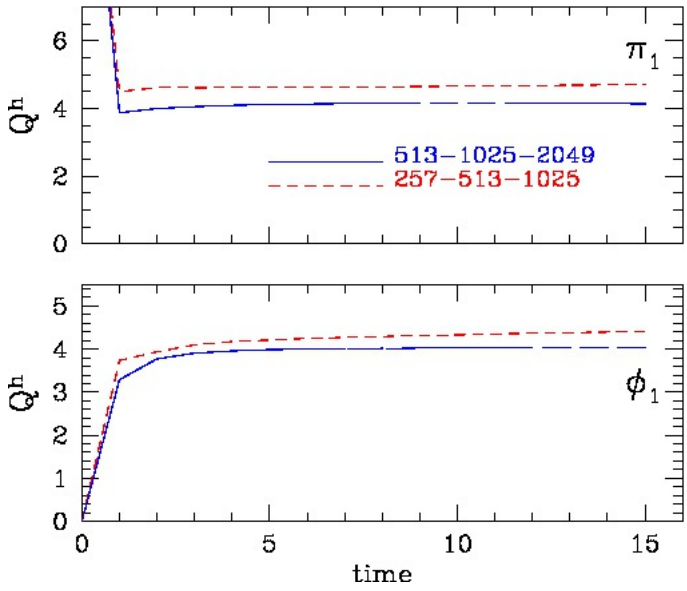

Figure 4.19: Convergence factors for the functions ϕ_1 and π_1, corresponding to the boosted baby skyrmion evolution in Fig. 4.18. $O(h^2)$ convergence is achieved, i.e. $Q^h \to 4$ as $h \to 0$, as expected from our finite difference approximation. As discussed in the text (Sec. 4.4.6), at fixed resolution the convergence of our code degrades with increasing γ, as a consequence of effects such as Lorentz contraction along the boost direction. Computations for larger γ require increased grid resolution (increasingly fine mesh spacing) for fixed accuracy.

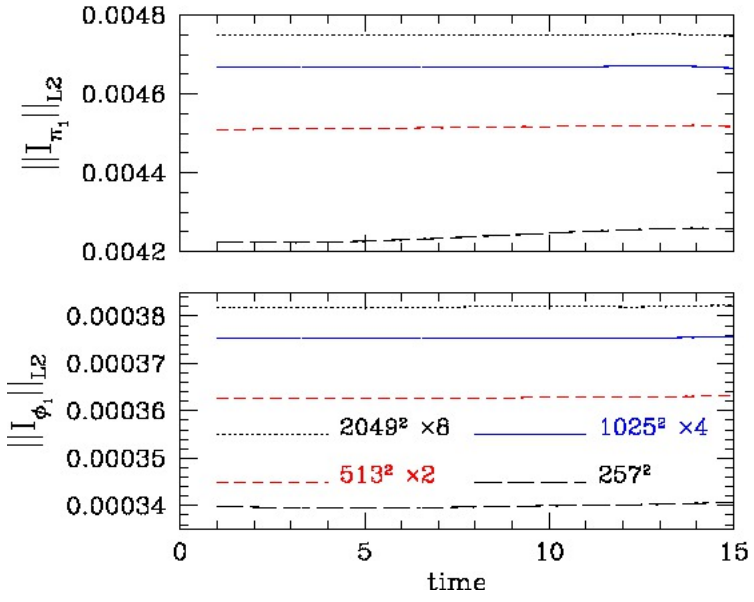

Figure 4.20: Rescaled l_2 norms of the independent residuals of ϕ_1 and π_1, at different resolutions, for the same boosted skyrmion evolution shown Fig. 4.18, with $\gamma = 1.6$ (v=0.8). The trend to overlap of the lines as $h \to 0$ signals linear convergence, as expected.

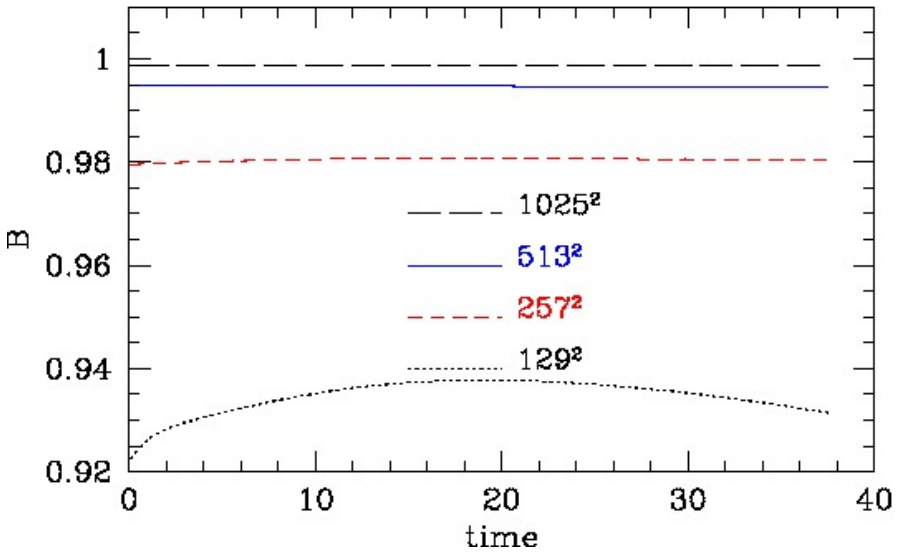

(a)

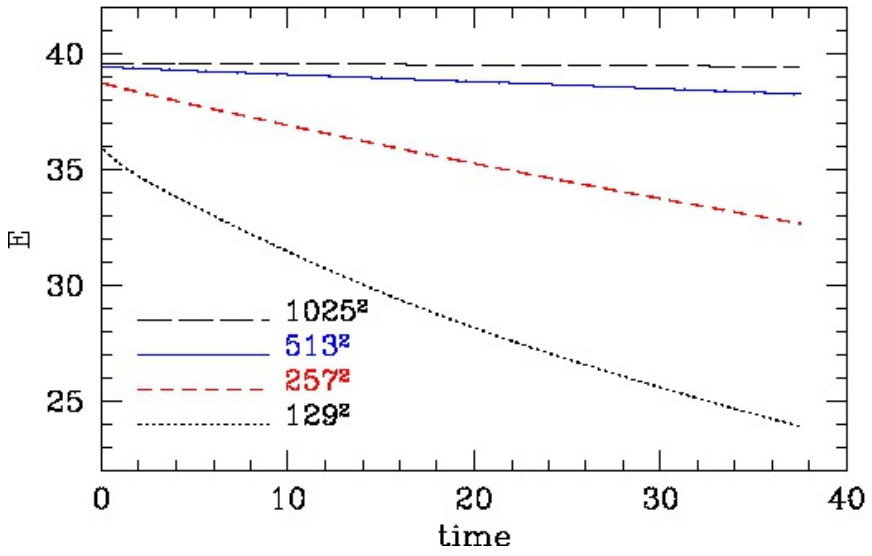

(b)

Figure 4.21: Evolution of of the baryon number B (Fig. 4.21a) and total energy E (Fig. 4.21b) at different resolutions for the $\gamma = 1.6$ boosted skyrmion evolution shown in Fig. 4.18. Quadratic convergence is observed for both quantities. At low resolution, there appears to be roughly linear "dissipation" of E with time, but there is clearly convergence to conservation as $h \to 0$. The use of a Dirichlet or Sommerfeld boundary condition did not produce any appreciable difference.

is motivated and justified by the severe Lorentz contraction of the highly-boosted configurations. This adjustment attempts to keep the soliton resolved with about the same number of points as for the static skyrmion. Fig. 4.19 shows the convergence factors for ϕ_1 and π_1, while Fig. 4.20 shows the evolution of the (rescaled) l_2 norms of the independent residuals for those fields. Once more we observe the expected second order convergence of the dynamical grid functions and first order convergence of the independent residuals. Finally, we computed the evolution of the baryon number, B, and the total energy, E, at different resolutions. At any resolution there appears to be roughly linear "dissipation" of E with time, but there is clearly convergence to conservation as $h \to 0$.

4.5 General Features of Baby Skyrmion Scattering: Previous Work

The classical scattering of two $B = 1$ baby skyrmions has been studied extensively: here we briefly review the work that is most relevant for this thesis.

First, we emphasize that although the original $3+1$ Skymre model is of most phenomenological interest, numerical simulations of the highly nonlinear full $3 + 1$ equations of motion are computationally expensive. This has provided much of the impetus for the focus on the baby Skyrme model, including the current work.

The earliest discussion of the possible presence of solitons in a sigma model in $2+1$ dimensions is due to Belavin and Polyakov (1975) [33, 57], who showed the existence of non-trivial static solutions in a $O(3)$ model describing the thermodynamics of ferromagnets, subject to the chiral constraint,

$$\mathcal{L} = \frac{1}{2}\partial_\mu \phi_a \partial^\mu \phi_a + \lambda_{LM}(1 - \phi_a \phi_a)\,, \tag{4.58}$$

(following the same notation as in (4.14)). They also suggested that the model be reformulated in terms of a complex field, W. This was motivated by their ability to then construct a two-dimensional analog of Euclidean Yang-Mills theories [58, 59], which are better suited for quantization using a path integral approach [142]. Since the boundary conditions at infinity are the same in any direction on the plane, the complex dynamical fields live on a Riemann sphere (that is, the complex plane plus the point at infinity, $\mathbb{C} \cup \{\infty\}$). The field W is therefore obtained by stereo-

graphic projection of the original fields ϕ in (4.58) [60]. The model (4.58) was thus referred to as the $\mathbb{CP}^1$ model, since the geometry and topology of the target space in this formalism correspond to the complex projective space $\mathbb{CP}^1$. A brief description of the W-formalism can be found in App. D.3.

The non-trivial solutions found in the $\mathbb{CP}^1$ model, although localized, turn out to be unstable under perturbation of their shape, leading to the solution either shrinking to a point (becoming an infinite spike in finite time), or expanding without bound [60, 143, 144]. Given that these solutions are not quite solitons (due to this instability), they were referred to as $\mathbb{CP}^1$ lumps [20]. The observed instability seems to arise from the conformal invariance of the model, i.e. for any fixed energy there is a continuously deformable family of lump shapes (and sizes).

It was found, however, that under certain conditions it was possible to study the head-on collision of two $\mathbb{CP}^1$ lumps before they collapsed to zero size, and Ward [60] used that fact to study such collisions using analytic methods to calculate geodesics in the internal space [20, 145, 146]. Using calculation of geodesic trajectories, Leese [61, 139] was the first to report the typical right-angle scattering seen in low velocity ($v \sim$0.2–0.3) head-on collisions of sigma-model-type solitons[28]. Indeed, using the fact that lumps follow geodesic paths, Manton showed that right-angle scattering can be understood in terms of the geometry of the internal space of the model [20, 147]. Manton also demonstrated that the scattering angle approaches zero as the impact parameter grows.

These results were verified and extended numerically by Zakrzewski [89] using initial data describing a two lump configuration. The lumps were specified using the W formalism, and each had a diameter ~ 1.0. The calculations were performed on computational domain $[-2,2]\times[-2,2]$, using a two dimensional mesh with 201×201 points, a mesh spacing of $\Delta x = \Delta y = 0.02$, and a Courant number $\Delta t/\Delta x = 0.5$. The time stepping was performed using a fourth order Runge-Kutta method, and the spatial derivatives were approximated with second order stencils. The chiral constraint was enforced by reprojection of the fields.

Zakrzewski found that head-on collisions always resulted in right angle scattering, and that a collision triggered shrinking of the lumps, which then became "spiky". The rate of lump shrinkage was observed to increase with increasing initial velocity. Furthermore, it was found that head-on scattering of two lumps of different initial sizes produced two lumps of the same size that had scattered at right angles. For initial data of this type, but with a non-zero impact parameter,

[28] Unless stated otherwise, velocities are always those of each soliton relative to the laboratory frame.

intermediate size lumps were produced (it is interesting to observe that the size of the extended object is also relevant to non-topological solitons, as discussed in the context of our results with small Q-balls in Sec. 3.6.3). Radiation from the collisions appeared negligible, except for the case of relatively large initial velocities ($v \sim 0.4$–0.5).

In order to stabilize W-lumps, thus promoting them to "true" solitons, Leese [61] introduced a term which took advantage of the invariance of the energy of the model under transformations of the form $W \to We^{i\alpha}$. The modification effectively adds internal angular momentum to the lump that prevents collapse. The resulting stable, static solutions are called Q-lumps, in analogy to Q-balls. Specifically, the nomenclature is motivated by the fact that besides a topological conserved number, N, a conserved Nöether charge, Q, arises from the $U(1)$ symmetry. In the same paper cited above, Zakrzewski [89] studied head-on collisions of Q-lumps, observing that the relative phase *did* prevent the shrinking of the soliton, and that it introduced repulsive forces that were important in determining scattering properties.

As discussed in Sec. 4.2, the stabilization of a lump can also be achieved by adding extra terms to the Lagrangian. Wilczek and Zee [58, 57] were the first to suggest that a $2+1$ sigma model could serve as a toy model for skyrmions. Specifically, they advocated the addition of a term that was fourth order in the field derivatives (a Skyrme term), as well as a mass or, more generally, a potential with no dependence on the field derivatives.

Within the context of this proposed model, Leese, Peyrard and Zakrzewski [90] then performed simulations of head-on scattering using the same basic numerical setup described in [89]. In this case the solitons had diameters of ~ 2 and velocities in the interval 0.2–0.6 were considered. The calculations confirmed that the solitons were indeed stable, and that they behaved as quasiparticles; i.e. their shapes were preserved after interaction. The force between the solitons was found to be repulsive, resulting in back-scattering until some critical velocity $v \sim 0.3$. Higher initial velocities led to right-angle scattering, and significant emission of radiation. These results were then corroborated by Sutcliffe [91], who calculated the critical velocity analytically, obtaining a value of ~ 0.21.

The term baby skyrmion actually first appears in a paper by Piette, Schroers and Zakrzewski [55]. As previously discussed, each specific potential term defines a particular baby skyrmion model. The one chosen in the studies just mentioned [90, 91] is $V = (1+\phi_3)^4$ and results in the so-called holomorphic model [35, 91]. The static solutions in this model may describe either a single solition,

or a multi-skyrmion. The latter is a minimal energy solution describing a bound state of multiple skyrmions, with each constituent having the same specified topological charge, B [93, 148].

However, the most well-studied members within the baby Skyrme model taxonomy are arguably 1) the old baby Skyrme model [93, 55, 56], with a potential function $V = 1 - \phi_3$, and 2) the new model, $V = 1 - \phi_3^2$, which we have adopted in this thesis. The old model gives rise to multi-skyrmions with complex structures and is the basis for the so called *skyrmion crystal* [35]. It is also of interest since it possesses multi-skyrmion ring-like solutions. The skyrmions appearing in the new and old models are expected to differ primarily at small distances (as measured from their respective centres), since they tend to the same vacuum state $\phi_a = (0, 0, 1)$ as $r \to \infty$.

Again, we have restricted attention to the new model in the studies described here. However, we are particularly interested in high-boost phenomenology and expect that the generic features we observe in that case will be largely independent of the details of the potential. We have also used the hedgehog ansatz (4.7) rather that the W-formalism in the calculation of our static initial configurations. This choice was largely made on the basis that the former is used in most of the more recent studies (see below), while the latter was motivated by arguments related to the quantization of the model, and which are thus not relevant for our classical computations.

We now summarize previous studies of baby skyrmion collisions that are most pertinent to our work. These include the following:

- One of the studies that is most relevant to this thesis is due to Crutchfield and Bell [1], whose work was in large part motivated by the observation of instabilities in earlier numerical investigations of the full $3+1$ Skyrme model [85, 84]. Two main possible sources of instability were posited: 1) a problem with the implementation of the chiral constraint in conjunction with leap-frog schemes and 2) a conjectured, configuration-dependent change in character of the dynamical equations from pure hyperbolic to mixed hyperbolic-elliptic. This second claim is of special interest to us. Crutchfield and Bell provided a non-rigorous argument for the loss of hyperbolicity based on the linearization of the equations of motion, and an analysis of the conditions under which some of the characteristics of the system could become complex (this issue is discussed in somewhat more detail in App. C.2). The argument applies to both the $3+1$ and $2+1$ versions of the Skyrme model, and has apparently become widely accepted in the field [25]. The authors also heuristically equate the loss of hyperbolicity to regions in solution space where "kinetic energy" is larger than "potential energy", although it

is not entirely clear how the two forms of energy were defined in their paper. In our work we have been especially concerned with the question of whether or not hyperbolicity loss (loss of well-posedness) is genuinely an issue in Skymre models.

The specific numerical calculations in [1] involved both the $2+1$ baby Skyrme model (which was referred to as the pseudo-Skyrme model)—but with no potential term—as well as the $3+1$ model. For the $2+1$ case the authors may have been unaware that the addition of a potential enables the existence of static solutions, since they noted that there are no localized solitons in the model and then focused their investigations on the evolution of generic, smooth Gaussian initial data.

Two separate $O(h^2)$ numerical schemes were considered. The first used "leap-frog" time stepping as employed in [85, 84], but with an improved implementation of the constraint enforcement relative to previous work (and which is quite similar to ours). The second was a predictor-corrector type scheme apparently largely motivated by the savings in memory it afforded relative to the "leap-frog" method, and which was a considerably more important consideration in the early 1990's than it is now. The results that are presented are notable in that convergence tests were performed, with the expected $O(h^2)$ convergence being observed for both $2+1$ and $3+1$ computations. The $3+1$ code was also used in a subsequent study [83].

Typical mesh sizes used were 32×32 to 256×256 in the 2D case, and $8\times8\times8$ to $32\times32\times32$ for the 3D computations. For both the leap-frog and predictor-corrector schemes, Courant factors of 0.5 were used without the appearance of numerical instability: in the 3D case this represented an order of magnitude improvement relative to the first numerical efforts [85, 84].

- Peyrad *et al*, [92], considered head-on BB collisions using the holomorphic potential. The rational ansatz W-formalism (App. D.3) was adopted, and in addition to the potential parameter θ_2 (corresponding to our μ^2), an adjustable coupling constant θ_1 was introduced to the Skyrme term. For a given initial velocity, scattering exit angles as a function of 1) the Skyrme term parameter θ_1, and 2) the relative phase of the skyrmion were computed for a range of velocities, $0.1 < v < 0.95$. An effective repulsive force between the solitons was found and, at low velocities, very little emitted radiation from the collisions was seen. The authors further demonstrated that the critical velocity separating back- and right-angle scattering depended on the parameters θ_1 and θ_2. In addition, for the case of right-angle scattering

close to the critical velocity they observed a quasi-bound ring-like intermediate state.

The boosted skyrmions in this study were generated using a Galilean transformation and there is mention that skyrmions with large initial velocities radiate strongly at the beginning of the simulation. It is possible that this may be a resolution-dependent phenomenon that should disappear as $h \to 0$. We note that apart from plots of scattering trajectories (which show the time evolution of the centres of the skyrmions in the xy plane) there were no results displayed for high-velocity computations. Additionally, there is no mention of the appearance of any instabilities.

Calculations were performed on a domain of approximate dimensions $[-5, 5] \times [-5, 5]$, using 512×512 grids and a mesh spacing $\Delta x = \Delta y = 0.02$. The skyrmions had diameters ≈ 2. The spatial discretization technique was the same as that adopted in [90], and a fourth order Runge-Kutta method was used for time stepping. The chiral constraint was implemented using reprojection.

- Piette *et al* [55] studied BB collisions—both head-on and grazing—using the old model and the hedgehog ansatz (4.7), with $\mu^2 = 0.1$. Initial velocities in the range $0.1 < v < 0.6$ were considered The authors demonstrated that variation of the relative phase would produce either attraction or repulsion between the skyrmions. They identified a *maximum attractive channel* when the relative phase is $\pm\pi$, and a *maximum repulsive channel* when the value is zero. It was reported that during head-on collisions a large amount of energy was lost through radiation. In fact, it was found that the skyrmions could only re-emerge from the interaction if the initial velocity was ≥ 0.46. At lower velocities, an intermediate "toroidal" bound state was formed (which was also observed by Peyrad *et al* [92] and Kudryavtsev *et al* [56]), and radiation continued to be emitted until the configuration relaxed to a static $B = 2$ ring soliton. They also reported that the relative phase of the skyrmions was relevant not only for the exit angle of the scattering, but for the post-collision velocity as well. They noted that the outcome of grazing collisions is particularly rich, since it depends on the initial velocity, the impact parameter b and the relative phase of the skyrmions: depending on the values of these parameters they could form bound orbits or scatter away from each other. For the particular case where the initial velocity was fixed to 0.4 and with the solitons prepared in the maximum attractive channel, they identified a critical impact parameter of $b = 1.5$ beyond which the skyrmions had essentially no effect on one another, with both escaping to

infinity.

The choice $\mu^2 = 0.1$ fixed the diameter of their solitons to ≈ 28 (see Fig. 4.2). The computational domain had dimensions $[-25, 25] \times [-25, 25]$, and a fixed resolution of 250×250 grid points was used. However, the description of the rest of their computational methodology is somewhat sparse.

- Dwyer and Rajagopal [94] studied head-on and grazing BB collisions in the range of velocities $0.1 < v < 0.8$, adopting a slightly modified baby Skyrme Lagrangian which they used as a toy model for electroweak (metastable) solitons. They used a potential $V = \lambda(\phi_a\phi_a - v^2)^2$ and treated λ as a parameter. For each value of λ they found a critical velocity above which a collision always ended in the annihilation of the skyrmions, i.e. the observed destruction of the solitons was independent of the details of the initial configuration.

  The authors were more explicit about their numerical setup than some of the other works mentioned thus far. They used a fourth order Runge-Kutta time integrator, with second order FDAs for the spatial derivatives. Static solutions were obtained by relaxation of an initial closed form profile function. They worked on a uniform two dimensional mesh with 125×125 points, $\Delta x = 0.2$, and Courant numbers in the range $0.05 < \lambda < 0.25$. Their solitons had a diameter of ≈ 20. Boosted initial conditions were generated by means of simple Galilean transformations, and they did not impose any constraint during time evolution. The lack of such a corrective mechanism, along with the coarseness of their mesh, suggests that the numerical errors might have been substantial. It thus would have been informative to have had information on the convergence properties of their code, but this was not provided.

- Soliton-antisoliton ($B\bar{B}$) configurations of baby skyrmions were studied in [149]. A generic characteristic of $B\bar{B}$ collisions mentioned in that work is that the $B\bar{B}$ pair interacts rather strongly, with mutual annihilation and the production of large amounts of radiation. It is notable that the peaks of the outgoing waves exit at 90° from the axis of approach of the solitons, i.e. in the transverse direction of motion. Kudryavtsev *et al* [56] studied excited skyrmion states with $B = 1$, observing decays into a baby skyrmion plus a baby skyrmion-antiskyrmion pair, which eventually decayed into pure waves.

- The dynamics of hedgehog baby skyrmions $B = 1$ has also been studied in the presence of various potential obstructions, such as barriers and holes. The obstructions are modelled

with the same technique employed in Sec. 3.7 for Q-balls, in which one introduces a localized spatial inhomogeneity in the coefficient of the potential term. As we mentioned in Sec. 1.2.2, some condensed matter developments have motivated a surge in activity in this area. One specific example is the study of magnetic bubbles [150] which are created by exposing a ferromagnetic material to a pulsed magnetic field. Such bubbles were once considered as the basis for computer memory storage due to the high spatial densities that could be achieved. We have not, however, considered any potential obstruction scattering of skyrmions in this thesis; interested readers can consult references [151, 152, 153, 98, 99].

4.6 Single-boosted Skyrmions

We now briefly describe our simulations of single boosted skyrmions. The chief aim is to understand the general numerical characteristics of the solutions, with numerical stability being of central interest. Our main conclusion is that the low-boost behaviour discussed in Sec. 4.4.6 is quite generic: in particular, baby skyrmion evolution at high values of γ remains stable and convergent. (We again note that γ is the boost of the skyrmion relative to the lab frame.) In addition, these results hold for both unigrid and adaptive calculations.

In Sec. 4.4.6 we tested the convergence properties of our code for a boosted baby skyrmion with $\gamma = 1.6$ ($v = 0.8$). We systematically increased this value of γ, and as we did so we monitored convergence and the conservation of the total energy E.

We performed two AMR calculations, one with $\gamma = 3.2$ ($v = 0.95$, Fig. 4.22a) and another with $\gamma = 5.79$ ($v = 0.985$, Fig. 4.22b). The numerical setup is detailed in the figure caption. We applied outgoing radiation (Sommerfeld) conditions at the outer boundaries (App. E). As usual, this choice of boundary condition is motivated by a desire to minimize the amount of radiation that reflects from the boundaries, and which would subsequently "contaminate" the interior solution. We used reprojection, as defined by (4.23), for constraint enforcement here and, unless otherwise stated, for all the numerical experiments described in this chapter.

As can be seen in Figs. 4.22a and 4.22b, evolutions at large γ using the resolution parameters given above display radiation "leaking" from the solition, particularly at early times. We can interpret this as a relaxation of the skyrmion from its initial configuration (presumably to a slightly lower energy state) and it is almost certainly a resolution-dependent phenomenon that should

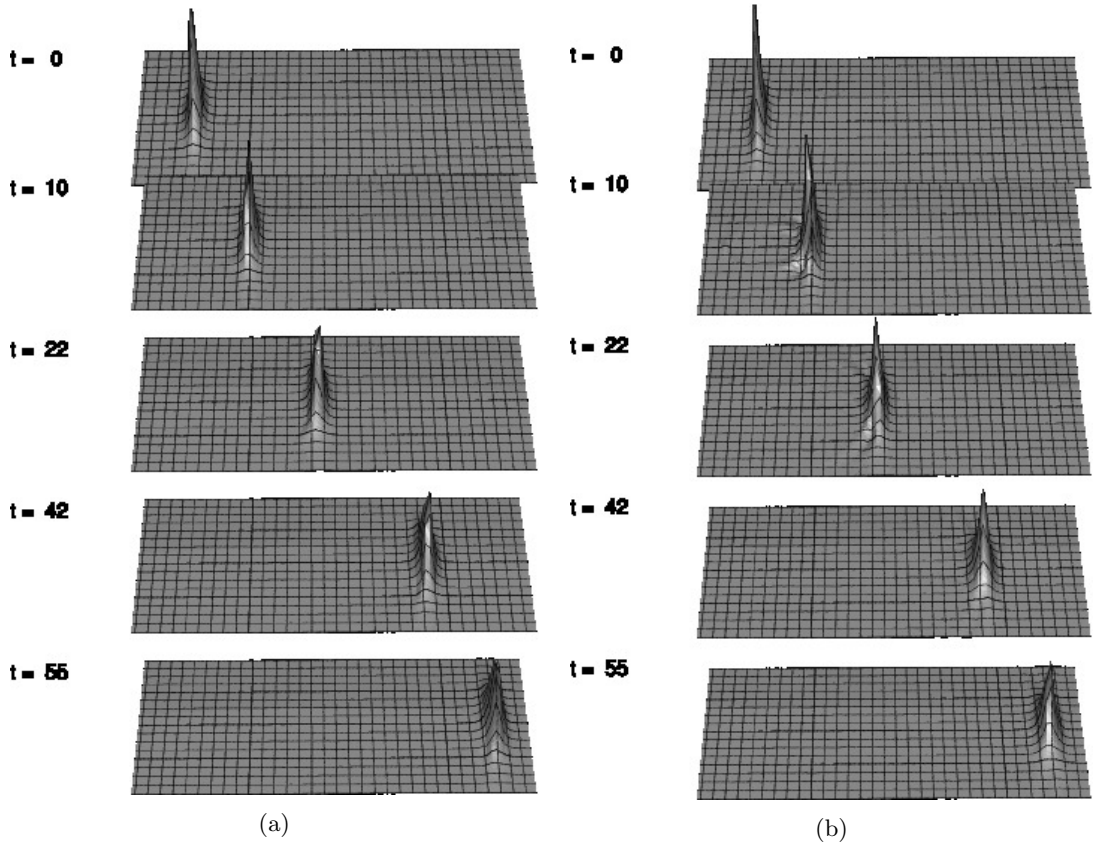

(a) (b)

Figure 4.22: This figure shows the evolution of the baryon number density B_0 of two boosted baby skyrmions, one at $\gamma = 3.2$ (v=0.95, Fig. 4.22a), and another at $\gamma = 5.79$ (v=0.985, Fig. 4.22b). Evolutions at the latter values of large γ, using the resolution parameters given below, display radiation "leaking" from the solition, particularly at early times. We can interpret this as a relaxation of the skyrmion from its initial configuration (presumably to a slightly lower energy state) and is almost certainly a resolution-dependent phenomenon that should disappear as $h \to 0$. In addition, although the overall shape of a very rapidly propagating skyrmion stays the same, the height of the central "spike" decreases slightly, indicating that the gradients of the fields have decreased too. Note that the skyrmion in (4.22a) has contracted to $100/3.2 = 31.2$ in the x direction, while the x-extent of the fastest skyrmion (4.22b) is $100/5.79 = 17.2$. These are AMR calculations with $\tau_{\max} = 5 \times 10^{-3}$, an $L = 1$ mesh having 257×257 points, and $L_f = 5$ (according to the notation established in Sec. 2.4). We set the Kreiss-Oliger dissipation parameter to $\epsilon_{\rm KO} = 0.5$, and the Courant number to $\lambda = 0.2$. The boundary conditions are Sommerfeld outgoing radiation (App. E), and the domain has dimensions 120×120 ($[-60, 60] \times [-60, 60]$). Given the fact that the baryon density is less extended than the Skyrme fields (see Fig. 4.11), and in order to better visualize the solitons, the domain has been cropped to $[-60, 60] \times [-20, 20]$. The starting location of the center of each boosted baby skyrmion is $(x_0, y_0) = (-30, 0)$. The constraint enforcement method was reprojection (4.23).

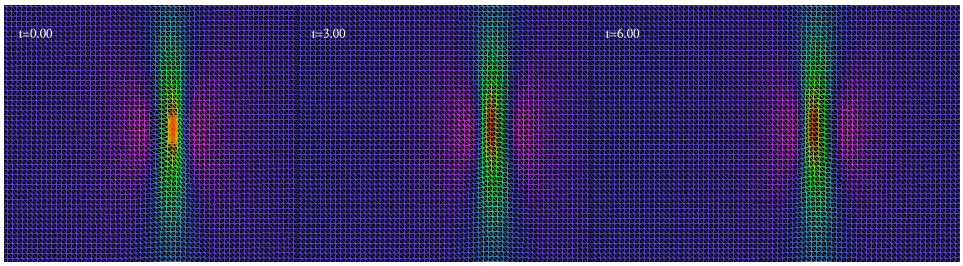

(a) t=0.0 (b) t=3.0 (c) t=6.0

Figure 4.23: Surface plot of the the evolution of the π_1 field corresponding to the AMR calculation of a single boosted baby skyrmion in Fig. 4.22a. We observe that the field for the soliton remains smooth as it propagates.

disappear as $h \to 0$. In addition, although the overall shape of a very rapidly propagating skyrmion stays the same, the height of the central "spike" decreases slightly, indicating that the gradients of the fields have decreased too. Use of a more stringent value of $\tau_{\max}$, which leads to larger parts of the computational domain being covered by finer meshes, reduces these effects, providing evidence for the claim that they will vanish in the limit of infinitesimal grid spacing. Fig. 4.23 illustrates the grid function, π_1, from the $\gamma = 3.2$ calculation. We observe that π_1 remains smooth and stable as the skyrmion propagates.

We also computed the evolution of the total energy, E, at different resolutions (non-adaptive mode) for the $\gamma = 5.79$ boosted skyrmion and this is shown in Fig. 4.24a. The decomposition of E into kinetic, K, and potential, U, contributions from a 2049×2049 unigrid calculation is shown in Fig. 4.24b. The expected trend towards conservation of E at an $O(h^2)$ rate is observed (higher resolution computations would be useful to make this statement more definitive, but are too costly). In particular, as the skyrmion travels to the right (Fig. 4.23), we do not observe the development of any discontinuity in E. As we will describe below, this behaviour is seen in some of our collision simulations where it is viewed as signalling a loss of hyperbolicity. We also note that at this value of γ the potential energy barely exceeds the kinetic energy.

We conclude that our numerical evolutions of single boosted baby skyrmions are stable—with the configurations remaining localized as expected—even at large values of γ.

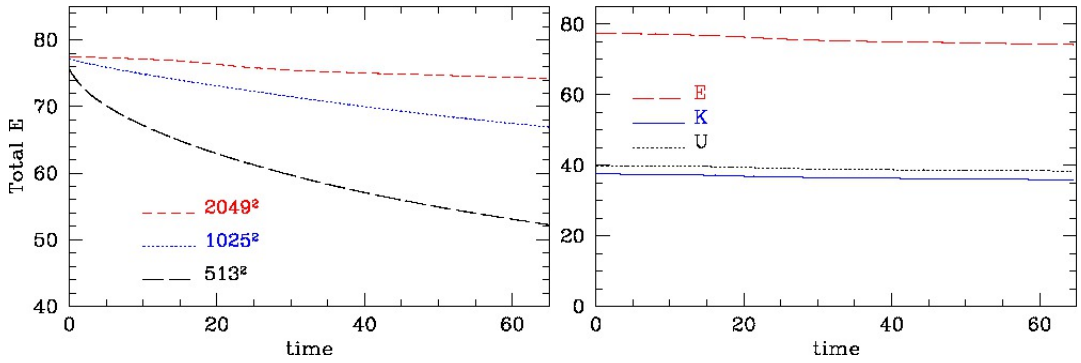

(a) (b)

Figure 4.24: Evolution of energy quantities from unigrid calculations of a boosted baby skyrmion with $\gamma = 5.79$ (Fig. 4.22b). We show the time development of the total energy, E, at different resolutions (Fig. 4.24a), and the decomposition of E into kinetic and potential components (K and U, respectively) using a 2049×2049 grid (Fig. 4.24b). Although higher-resolution calculations—which are too costly—would allow us to make a more definitive statement, there is evidence that E is trending towards conservation at the expected $O(h^2)$ rate. This bolsters the claim that our simulations of propagating skyrmions remain stable even at high boosts; i.e. that the evolutions are well-posed. Note that for this value of γ the potential energy is only marginally greater than the kinetic energy. Finally, we observe that there was no appreciable difference between calculations that used Dirichlet instead of Sommerfeld boundary conditions.

4.7 Baby Skyrmion Head-on Collisions

In this section we analyze head-on collisions of two baby skyrmions defined by the same hedgehog profile function, $f(r)$, used previously and, unless stated otherwise, with a potential parameter $\mu^2 = 0.001$. As discussed in Sec. 4.3.6, the interaction of initially separated skyrmions is characterized by the relative phase, Ψ. One important feature of skyrmion collisions is that the end state exhibits strong Ψ-dependence.

In the subsections below we present the results from our simulations of various head-on collision processes using both unigrid and AMR calculations. Our central result is the confirmation of the existence of mixed hyperbolic-elliptic dynamical regions (loss of hyperbolicity and well-posedness), and for the various experiments performed we approximately identify values of the critical velocity in the lab frame (denoted by $\gamma^\star$) where the transition takes place. To this end, we primarily rely on the monitoring of the conservation of the total energy, E.

We first note that if a baby skyrmion has a baryon charge, B, we define a baby anti-skyrmion as a configuration with a conjugate topological charge, $-B$. Specifically, the anti-skyrmion is

obtained by charge-conjugation of a hedgehog $(\phi_1, \phi_2, \phi_3) \to (-\phi_1, -\phi_2, \phi_3)$ followed by a reflection $(-\phi_1, -\phi_2, \phi_3) \to (\phi_1, -\phi_2, \phi_3)$ [88]. This results in a hedgehog with charge $-B$.

We will adopt the following notation to refer to the most common type of scattering that we consider here and in subsequent sections. BB denotes the collision of two baby skyrmions, each with topological charge B, while $B\bar{B}$ refers to the scattering of a baby skyrmion with charge B and an baby anti-skyrmion with charge $-B$. The latter case will be discussed in detail in Sec. 4.9.

We begin by describing the initial configuration for a typical BB collision. Given that the equations of motion are nonlinear, we cannot rely on a general superposition principle to produce an initial state that genuinely describes two distinct solitons. However, provided that we prepare hedgehogs that are sufficiently well-separated that there is essentially no overlap between them, then it is straightforward to argue that data given by

$$\phi_a = \begin{pmatrix} \sin f(r_1)\sin(\theta_1) + \sin f(r_2)\sin(\theta_2) \\ \sin f(r_1)\cos(\theta_1) + \sin f(r_2)\cos(\theta_2) \\ \cos f(r_1) + \cos f(r_2) - 1 \end{pmatrix} \tag{4.59}$$

will closely approximate a two-soliton initial configuration.[29] In the last expression the subtraction of 1 in the third component is necessary to ensure that the fields tend to the vacuum state $(0, 0, 1)$ as $r \to \infty$. The key physical parameters characterizing the collisions we consider here include the Lorentz boost factor, γ, the potential parameter, μ^2, the internal phase, Ψ, and, for the grazing (off-axis) collisions studied later, (see e.g. Sec. 4.8) the impact parameter, b. Computational limitations preclude an exhaustive exploration of parameter space so we focus attention on specific families of initial data that produce dynamics that we hope to be representative of the overall phenomenology of the model.

As well as the physical parameters there are variables that control the numerical scheme itself. AMR-pertinent values used here include: a regridding interval of $n_{\text{regrid}} = 20$–25, a buffering width of $w_{\text{buffer}} = 6$, and a Courant number in the range $\lambda = 0.1$–0.2. These values are consistent with the restriction (3.56), which reads

$$\lambda\, n_{\text{regrid}} < w_{\text{buffer}}\,. \tag{4.60}$$

The truncation error threshold values used are in the interval $\tau_{\max} = 1 \times 10^{-5}$ to 1×10^{-2},

[29] We note, however, that we always perform a projection of the $t = 0$ data to ensure that the constraint is precisely satisfied.

but a trial and error search led us to choose $\tau_{\rm max} = 6 \times 10^{-4}$ as a default. The Kreiss-Oliger dissipation parameter was set to $\epsilon_{\rm KO} = 0.4$, and, in order to minimize any interference from radiation reflection, Sommerfeld boundary conditions were adopted. Our default computational domain was $[-60, 60] \times [-60, 60]$, with the boosted baby skyrmions centred at $(-30, 0)$ and $(30, 0)$. For the AMR calculations, the base grid (level $L = 1$) had 257×257 points, and we typically set the maximum refinement level to $L_f = 5$ or 6.

Finally we point out that given that the computation of the convergence factor Q^h for AMR calculation is more complicated than for a unigrid one (see Sec. 3.6), and given that our code in unigrid mode is apparently convergent for generic initial data (convergence tests are shown in Sec. 4.4 and Sec. 4.7.1), we do not perform convergence testing in AMR mode.

4.7.1 Baby Skyrmion Head-on Collisions with the Same Internal Phase

We begin by focusing our attention on one specific computation with the primary goal of investigating convergence, and thereby estimating typical resolutions that are required for reasonably accurate results.

We thus consider a $\gamma = 1.6$ ($v = 0.8$), head-on BB collision with an internal phase difference $\Psi = 0$ (repulsive channel). Fig. 4.25 shows the evolution of the baryon number density for this configuration. (We note that here and in the following we will typically list the numerical parameters used in the figure captions and will not repeat the enumeration in the main text.) This event, which exhibits forward scattering, is typical of what we observe for high velocity interactions in the repulsive channel. For this initial data setup we observe back scattering for velocities lower than $\gamma \sim 1.02$ ($v \sim 0.2$). In such cases the skyrmions do not have enough kinetic energy to overcome their mutual repulsion; they thus slow down, stop, and then go back along the axis of approach. However, for γ in excess of this critical value ~ 1.02, we always observe forward scattering in the repulsive channel.

Following the same methodology used for single boosted baby skyrmions in Sec. 4.6, we performed similar collisions to the one we just described (Fig. 4.25) for larger values of γ, and we observe the same generic forward scattering behaviour. Not surprisingly, the baby skyrmions contract even more, and they emerge from the encounter more perturbed from their original shapes, a possible effect of the increase in the overall error caused by the more pronounced Lorentz contraction.

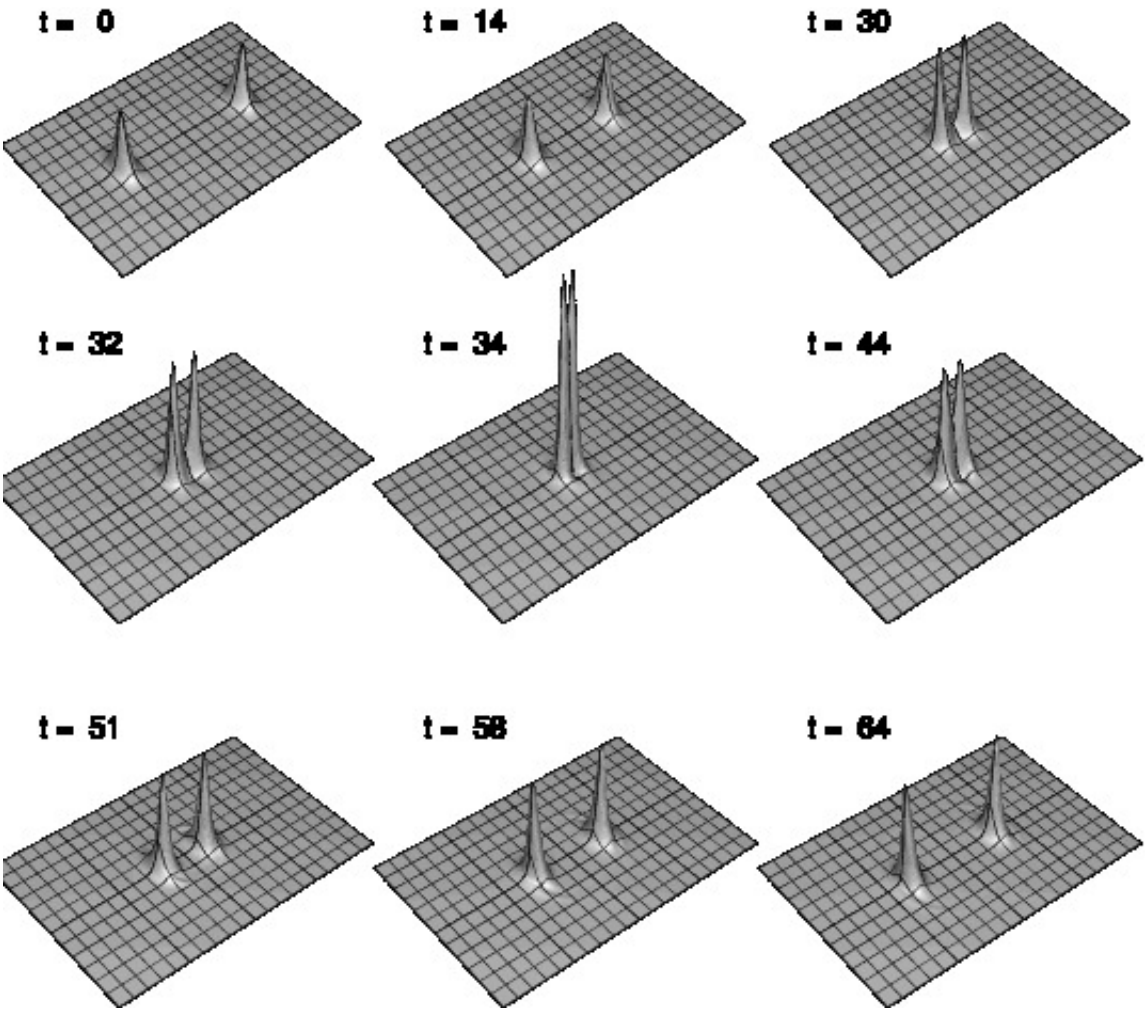

Figure 4.25: Evolution of the baryon number density, B_0, for a $\gamma = 1.6$ ($v = 0.8$) head-on BB collision in the repulsive channel—i.e. the relative phase of the baby skyrmions is $\Psi = 0$. This interaction exhibits forward scattering. The baryon density grows significantly during the collision (forming spikes), a consequence of the large gradients in the spatial derivatives of the fundamental fields. This data comes from a unigrid (non-adaptive) calculation with a 1025×1025 mesh and a domain $[-60, 60] \times [-60, 60]$. For illustrative purposes the region displayed has been cropped to $[-60, 60] \times [-40, 40]$. The starting locations of the centres of the boosted baby skyrmions are $(-30, 0)$ and $(30, 0)$, the Courant number is $\lambda = 0.2$, and the KO dissipation parameter is $\epsilon_{\text{KO}} = 0.5$. The diameter of the baby skyrmions in the x direction for this value of γ is $\approx 100/1.6 \approx 62.5$. The boundary condition is outgoing Sommerfeld, which resulted in better convergence properties than a Dirichlet (reflecting) condition.

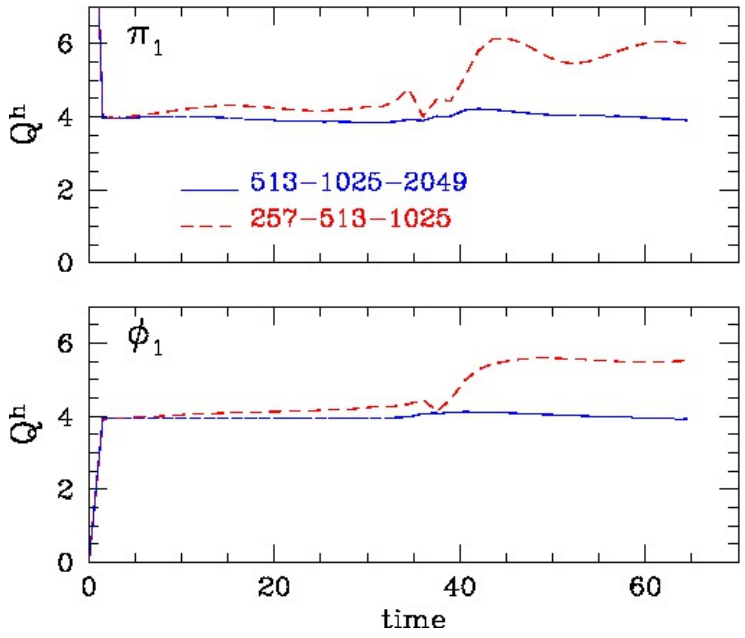

Figure 4.26: Convergence factors for the functions ϕ_1 and π_1 corresponding to the head-on BB collision summarized in Fig. 4.25. $O(h^2)$ convergence is observed; i.e. $Q^h \to 4$ as $h \to 0$. The degradation of convergence after the collision for the the 257–513–1025 plot is an indication of the substantial error in the 257×257 run.

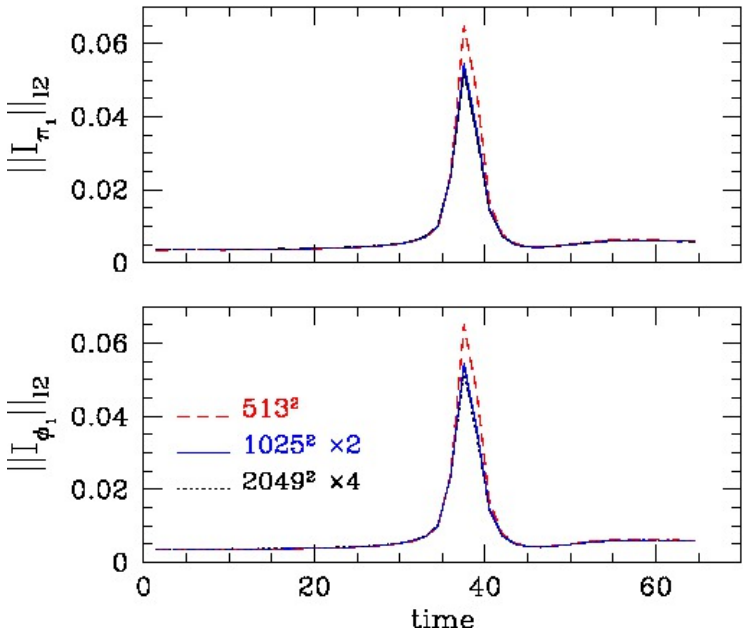

Figure 4.27: Evolution of the l_2 norm of the independent residuals of ϕ_1 and π_1, at different resolutions, for the head-on BB collision shown in Fig. 4.25. The trend to overlap of the lines as $h \to 0$ signals linear convergence, consistent with the FDA of the independent residual evaluator. Observe that even during and after the collision this overlap is maintained, at least for sufficiently high resolution.

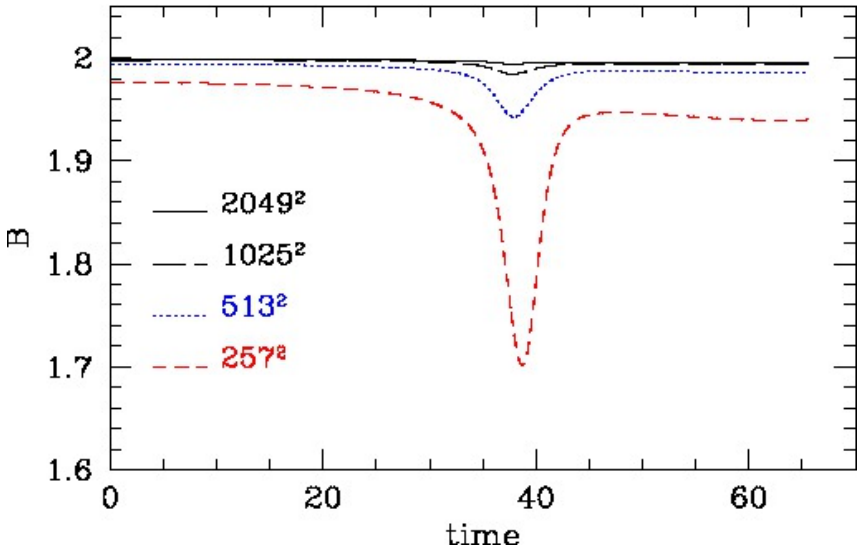

(a)

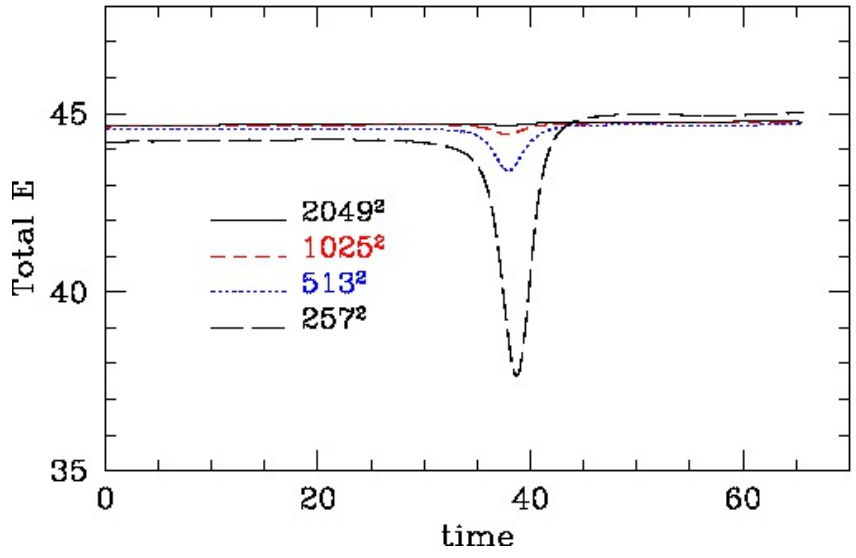

(b)

Figure 4.28: Resolution dependence of the computed baryon number B (Fig. 4.28a) and total energy E (Fig. 4.28b) for the $\gamma = 1.6$ head-on BB collision shown in Fig. 4.25. Overall, the expected quadratic convergence to conservation of both quantities is observed. However, the convergence is clearly affected during the collision ($t \approx 30$–45), due to the large gradients in the grid functions during that time interval. In spite of this, B and E still appear to converge to conservation during the interaction as $h \to 0$. The observed jump in both quantities—most visible at low resolution—pre- and post-collision is probably correlated with the degradation of convergence of the π fields shown in Fig. 4.26. The boundary condition is outgoing Sommerfeld, which resulted in better convergence properties than a Dirichlet (reflecting) condition.

Fig. 4.29 shows the total energy, E, of various head-on BB collisions, in the repulsive channel ($\Psi = 0$), with the same numerical setup, except for the value of γ. We also display the decomposition of the total energy E into kinetic (K) and potential (U) components.

One key effect of the presumed departure from pure hyperbolic dynamics is a loss of conservation of energy that begins to appear around $\gamma \geq \gamma^\star \sim 2.1$, although this is not clearly evident in the plots of Fig. 4.29 until values of $\gamma \approx 3.2$ (we remind the reader that, throughout this Chapter, $\gamma^\star$ and $v^\star$ denote the critical velocity in the lab frame where the transition takes place). We note that conservation of E is always affected during a collision, irrespective of the value of γ. For $\gamma < \gamma^\star$ the fluctuations in E decrease as $h \to 0$, i.e. E converges to conservation, as in the data shown Fig. 4.28b. However, for $\gamma \geq \gamma^\star$ the post-collision values of E show a gap relative to the pre-collision values, which is most clearly visible in the $\gamma = 5$ plot. For $\gamma > 5$ the gap becomes even more pronounced. Moreover, the magnitude of the jumps *increase* as $h \to 0$ (see Fig. 4.38a), a clear sign that the anomalous behaviour is not due to a lack of resolution. We also note that increasing the value of KO dissipation parameter did not improve the convergence behaviour.

Fig. 4.30 illustrates the features of this type of head-on collision (with $\Psi = 0$) for a value of $\gamma = 2.1 \sim \gamma^\star$, i.e. very near the upper limit for a boost before the claimed transition to a mixed hyperbolic-elliptic regime occurs—but still in the purely hyperbolic (physical) regime. As in Fig. 4.25 we observe forward scattering, and although the baryon density spikes significantly during the collision, it remains bounded. In comparison to Fig. 4.25 more radiation is seen, particularly upon closer examination of the data. Overall, the interaction has the same generic features seen in the repulsive channel calculations.

We also performed an AMR calculation with the near-threshold boost $\gamma = 2.1$ and the resulting time evolution of B_0 is shown in Fig. 4.31. Although the results are generally consistent with the unigrid calculation plotted in Fig. 4.30, some differences are evident: in particular, for the AMR case the heights of the peaks in B_0 during the collision phase are reduced, and post-collision there is more distortion of the skyrmions, as well as more radiation. However, use of more stringent values of $\tau_{\rm max}$, which leads to a greater portion of the computational domain being covered by finer meshes, reduces these differences, providing evidence that the unigrid and AMR calculations will coincide in the $h \to 0$ limit. In other words, we suspect that the observed deviations between the two types of computations are largely attributable to the AMR algorithm—most likely the interpolation needed to update boundary values on child grids from the corresponding parental

values.

4.7.2 Baby Skyrmion Head-on Collisions with Different Internal Phase

In this subsection we summarize a series of calculations of BB collisions, showing typical results computed with different non-zero values of the internal phase shift, Ψ.

We begin with the case of maximal attraction, that is, when the internal phase shift $\Psi = \pm\pi$. Fig. 4.33 shows a head-on BB collision at $\gamma = 1.6$, with the rest of the parameters as in Fig. 4.25. The outcome is clearly the right-angle scattering typically seen for topological solitons, particularly at low velocities (see Sec. 4.5). At $t \approx 32$ we see a short-lived intermediate $B = 2$ bound state previously reported by some authors (Peyrad [92] and Kudryavtsev [56]). Here the kinetic energy is large enough to allow the baby skyrmions to easily escape from their mutual attraction, and the late-time configuration of outwardly-propagating solitons is stable. We also observe that although maximal values of the baryon density grow significantly during the collision—a consequence of the enhancement in the spatial gradients of the fundamental fields—B_0 remains bounded at all times. Fig. 4.34 shows convergence tests of the baryon number B and total energy E for the calculation. Comments concerning the observed convergence to conservation are essentially the same as those made in Fig. 4.26 for the repulsive-channel computation.

Fig. 4.35 shows the decomposition of the total energy E into kinetic (K) and potential (U) components for head-on BB collisions in the attractive channel ($\Psi = \pi$), and for different values of γ. In contrast to the repulsive-channel calculations (Fig. 4.29), the values of K and U tend to approach each other as the evolutions proceed, leading to $K > U$ during the interaction for larger values of γ. Loss of hyperbolicity appears to set in for $\gamma^\star \sim 1.96$ ($v^\star \sim 0.86$), when the values of K at a few grid points near the centre of the computational domain begin to exceed the corresponding values of U. As for the repulsive-channel evolutions, conservation of energy is no longer observed during the interaction period for boosts above $\gamma^\star$. Instead, an apparent discontinuity in E forms; this is most clearly visible in the bottom two plots of Fig. 4.35. Again, the magnitudes of these discontinuities increase as $h \to 0$. We note that the loss of hyperbolicity for the attractive channel evolutions occurs at slightly lower velocities than for the repulsive channel ones (for which $\gamma^\star \sim 2.19$, $v^\star \sim 0.89$). This seems plausible since the attractive nature of the force in this case makes it easier for kinetic energy to exceed potential, as can be deduced by comparing Fig. 4.35 with Fig. 4.29.

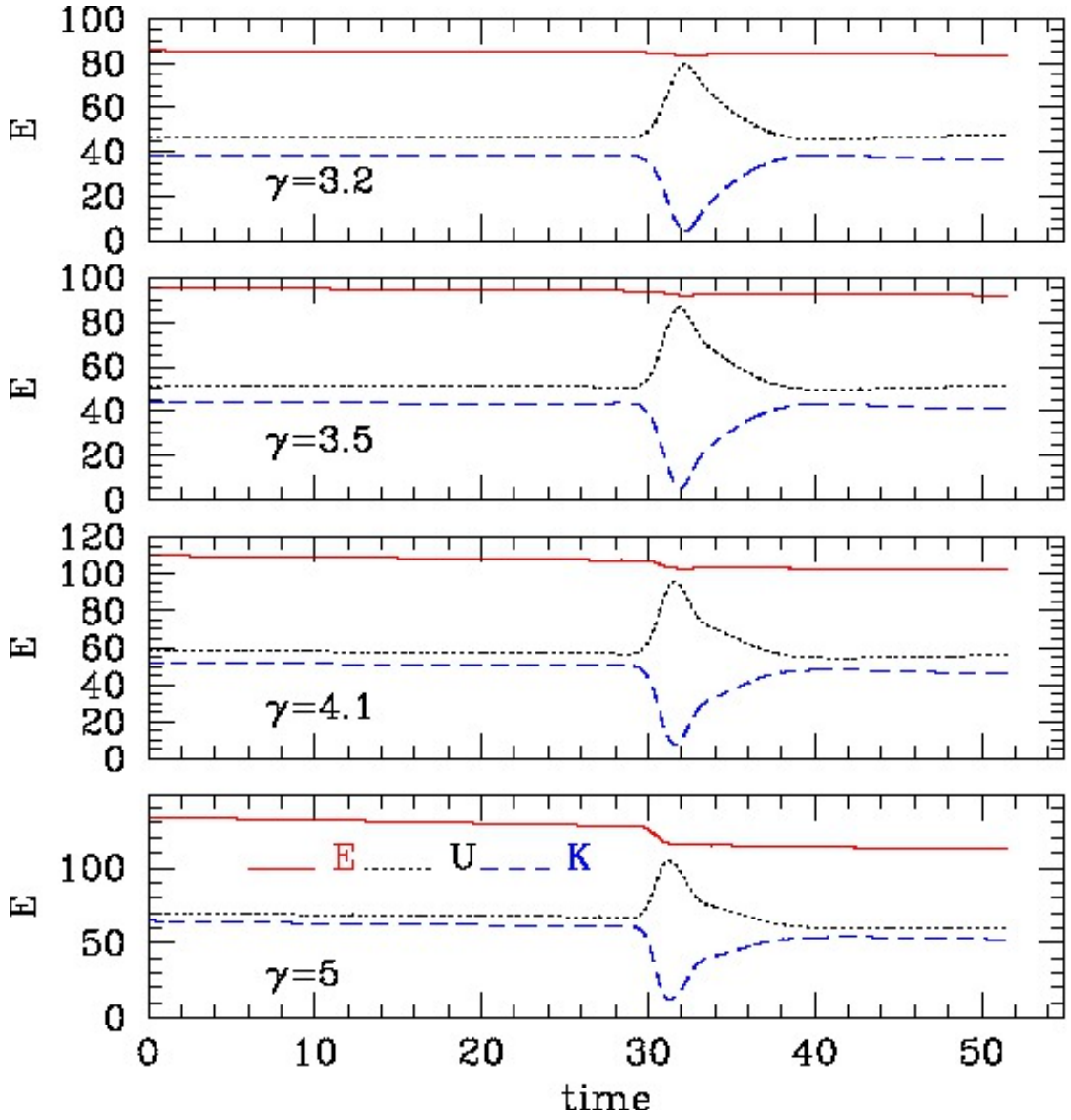

Figure 4.29: Decomposition of the total energy E into kinetic (K) and potential (U) components for head-on BB collisions in the repulsive channel ($\Psi = 0$), and for different values of γ. One key effect of the presumed departure from pure hyperbolic dynamics for $\gamma \geq \gamma^\star$ is a loss of conservation of energy, although this is not clearly evident in plots such as the above until values of $\gamma \sim 3.2$. We note that conservation of E is always affected during a collision, irrespective of the value of γ. For $\gamma < \gamma^\star$ the fluctuations in E decrease as $h \to 0$, i.e. E converges to conservation, as in the data shown Fig. 4.28b. However, for $\gamma \geq \gamma^\star$ the post-collision values of E show a gap relative to the pre-collision values, which is most clearly visible in the $\gamma = 5$ plot. For $\gamma > 5$ the gap becomes even more pronounced. Moreover, the magnitude of the jumps *increase* as $h \to 0$ (see Fig. 4.38a), a clear sign that the anomalous behaviour is not due to a lack of resolution. We also note that increasing the value of KO dissipation parameter did not improve the convergence behaviour. The calculations were performed on a unigrid mesh of 1025×1025, with the rest of the numerical parameters identical to those listed in Fig. 4.25.

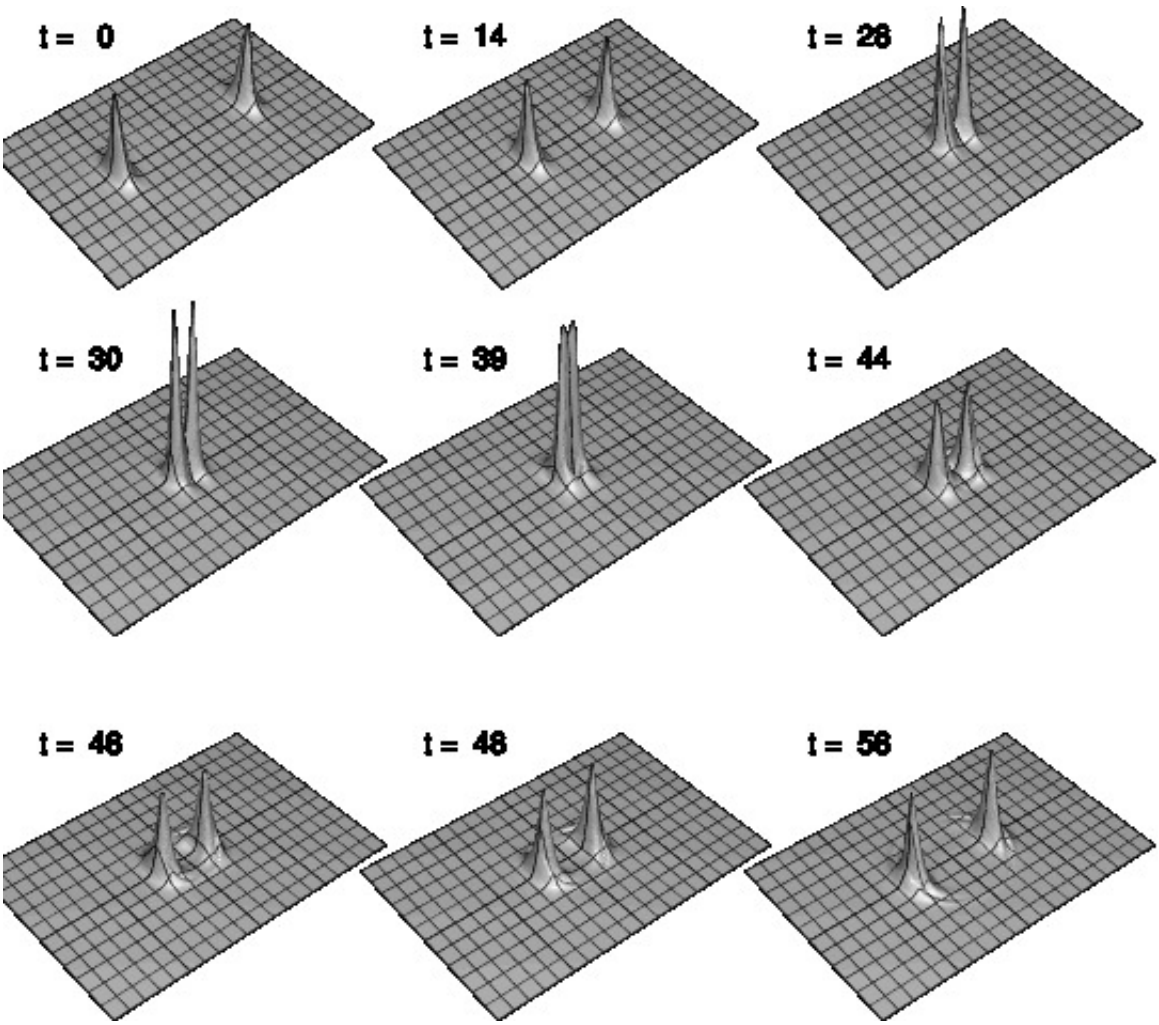

Figure 4.30: Evolution of the baryon number density B_0 for a head-on BB collision in the repulsive channel at $\gamma = 2.1$ ($v = 0.88$). This value of γ is very near the upper limit, $\gamma^\star$, at which the claimed transition to a mixed hyperbolic-elliptic regime occurs. As in Fig. 4.25 we observe forward scattering and although the baryon density spikes significantly during the collision, it remains bounded. In comparison to Fig. 4.25 more radiation is seen, particularly upon closer examination of the data. Overall, the interaction has the same generic features seen in the repulsive channel calculations. Numerical parameters, including the domain-cropping for the plots, are identical to those listed in Fig. 4.25. The diameter of the baby skyrmions for this value of γ is $\sim 100/2.1 \sim 47$.

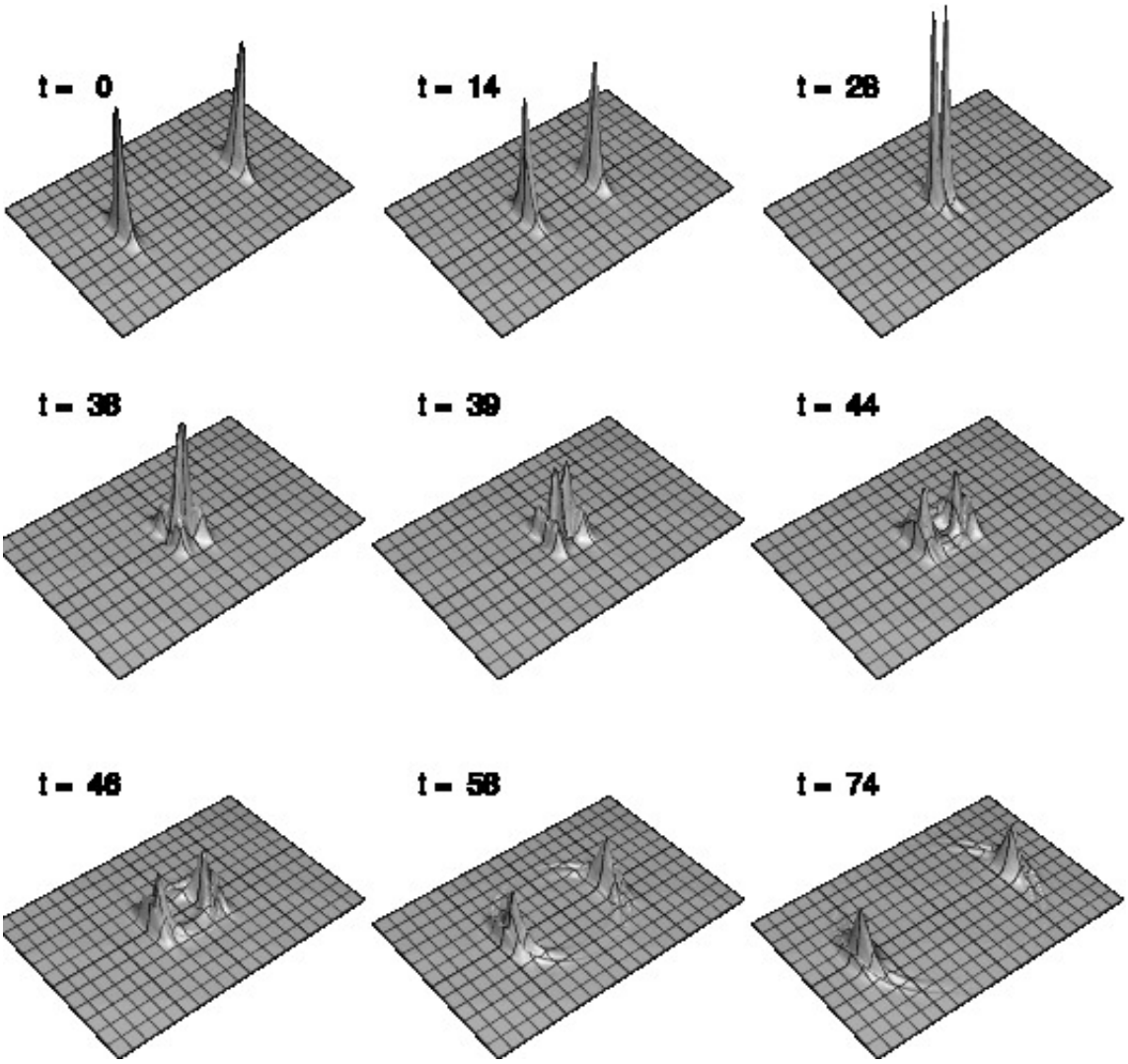

Figure 4.31: This figure shows the time development of the baryon number density B_0 from an AMR calculation that used the same initial configuration described in Fig. 4.30. Although the AMR results are generally consistent with the unigrid calculation, some differences are evident: in particular, for the AMR case the heights of the peaks in B_0 during the collision phase are reduced, and post-collision there is more distortion of the skyrmions, as well as more radiation. However, use of more stringent values of $\tau_{\max}$, which leads to a greater portion of the computational domain being covered by finer meshes, reduces these differences, providing evidence that the unigrid and AMR calculations will coincide in the $h \to 0$ limit. In other words, we suspect that the observed deviations between the two types of computations are largely attributable to the AMR algorithm—most likely the interpolation needed to update boundary values on child grids from the corresponding parental values. This particular run was performed with a truncation error threshold $\tau_{\max} = 6 \times 10^{-4}$, a coarse level ($L = 1$) having 257×257 points and a finest level $L_f = 5$ (again, see Sec. 2.4 for a definition of this notation). The finest resolution is equivalent to a 4097×4097 mesh. Numerical and plotting parameters are identical to those listed in Fig. 4.25. A colour-contour representation of this data is shown in the next figure (Fig. 4.32).

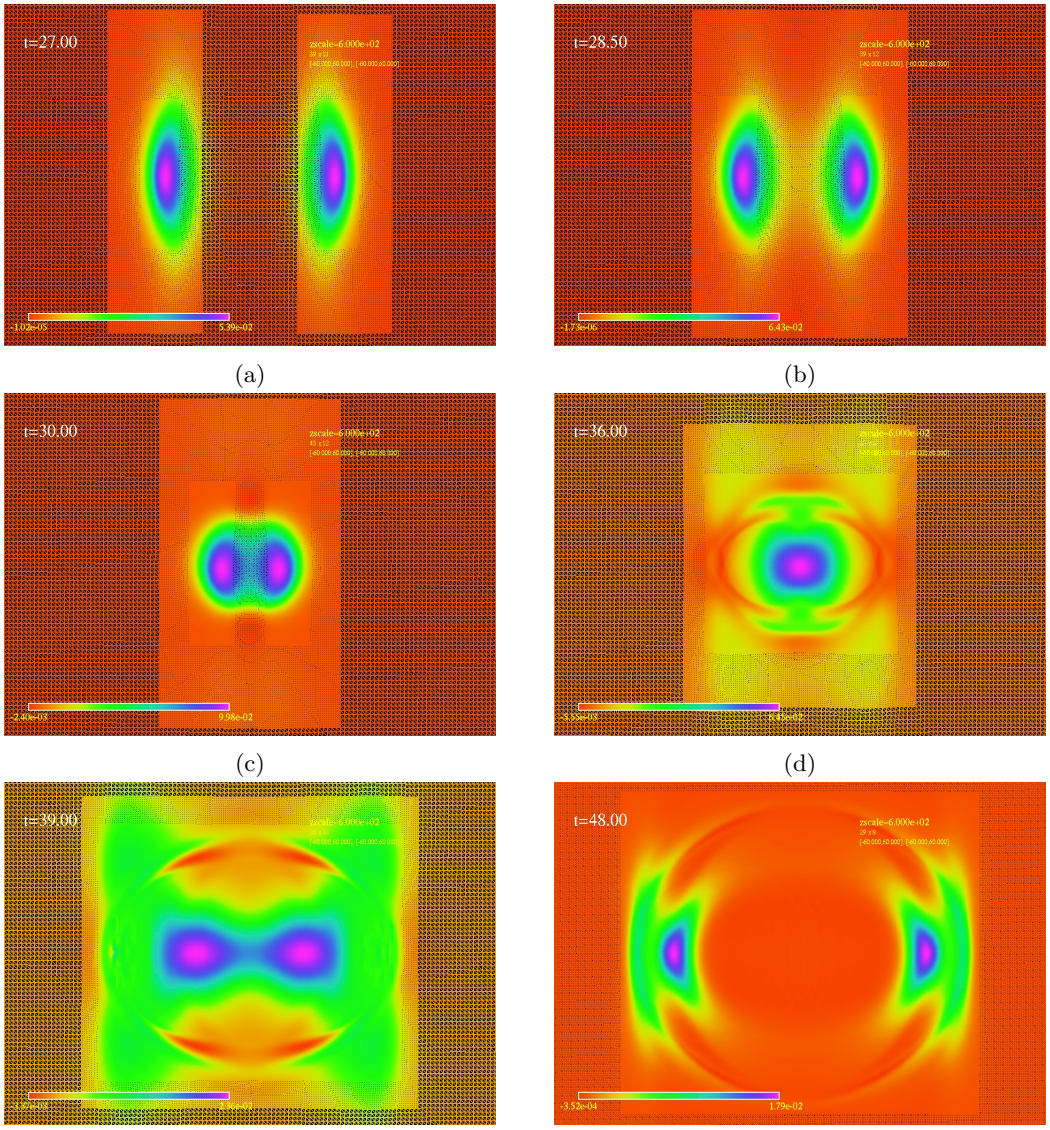

(a) (b) (c) (d) (e) (f)

Figure 4.32: Wire-mesh contour plot of the evolution of the baryon density B_0 as previously shown in Fig. 4.31. The figure shows the time-development of a typical adaptive mesh refinement hierarchy. Finer level grids are difficult to distinguish due to resolution limitations of the figure, as well as the fact that finer grids generally have small extent. For instance, we can identify 3 different levels in image 4.32d, while there are actually 5 levels at that time.

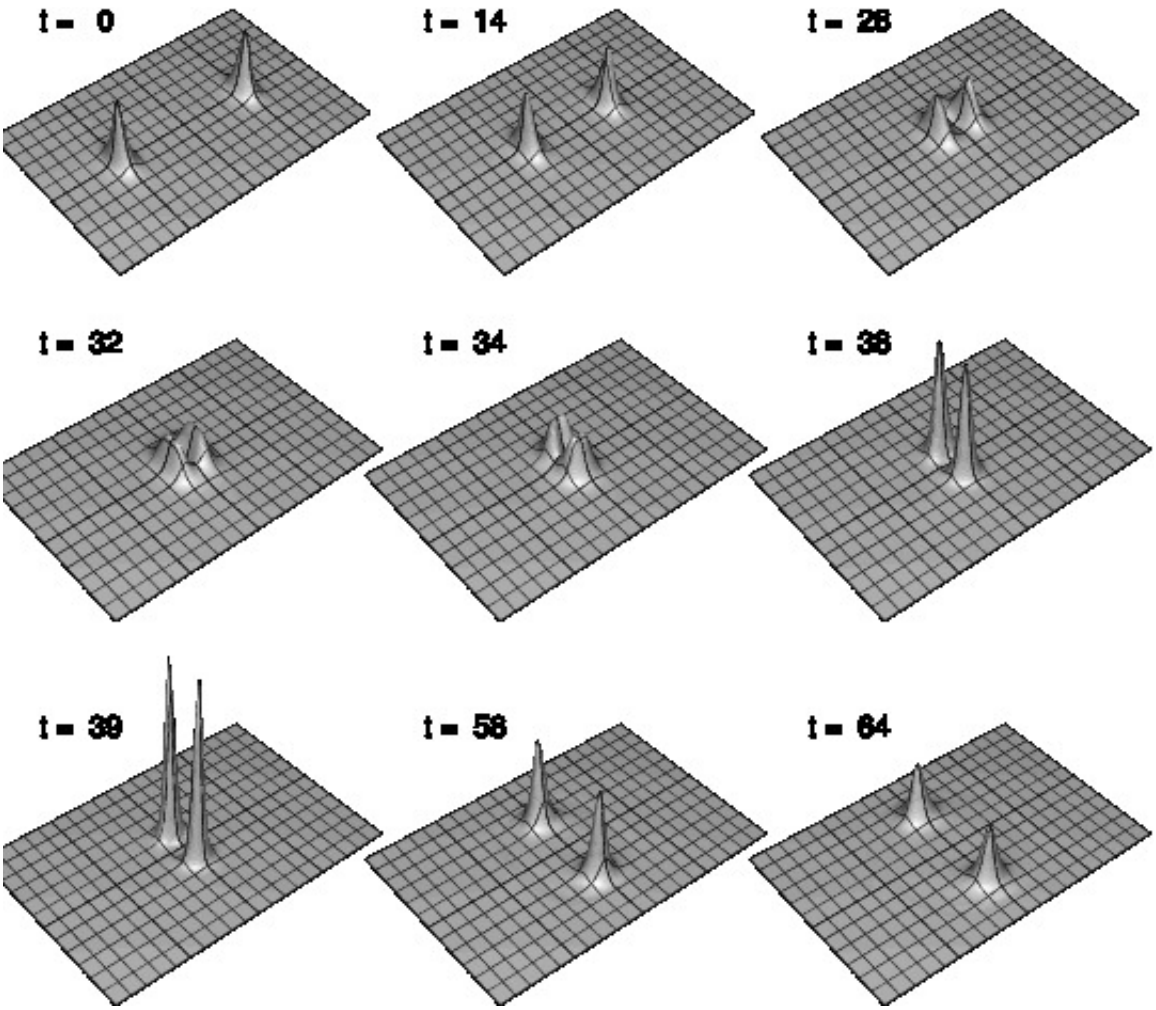

Figure 4.33: Evolution of the baryon number density for a $\gamma = 1.6$ ($v = 0.8$) head-on BB collision in the attractive channel—i.e. $\Psi = \pi$. This encounter exhibits the right-angle scattering that is typically seen for topological solitons, particularly at low velocities. At $t \approx 32$ we see a short-lived intermediate $B = 2$ bound state previously reported by some authors (Peyrad [92] and Kudryavtsev [56]). Here the kinetic energy is large enough to allow the baby skyrmions to easily escape from their mutual attraction, and the late-time configuration of outwardly-propagating solitons is stable. Numerical and plotting parameters are identical to those listed in Fig. 4.25, and the computation is unigrid.

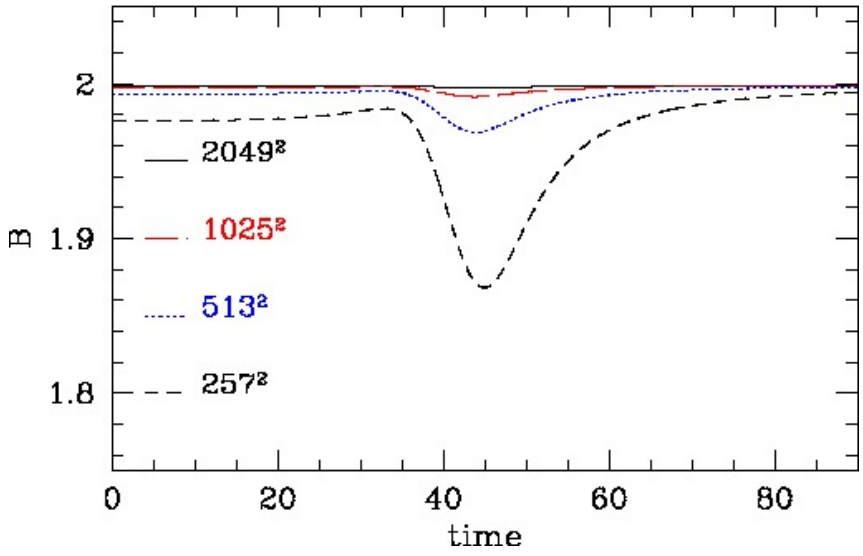

(a)

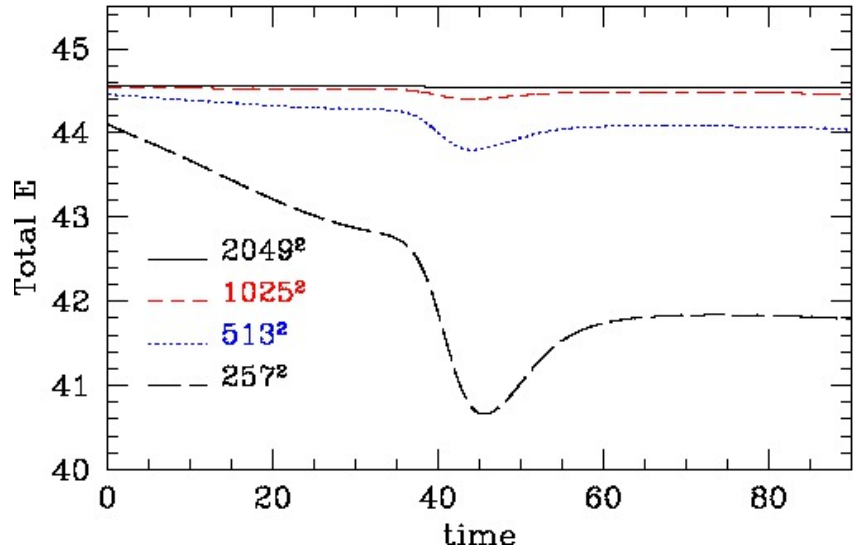

(b)

Figure 4.34: Convergence tests of the baryon number B and total energy E for the attractive-channel calculation described in Fig. 4.33. Comments concerning the observed convergence to conservation are essentially the same as those made in Fig. 4.26 for the repulsive-channel computation.

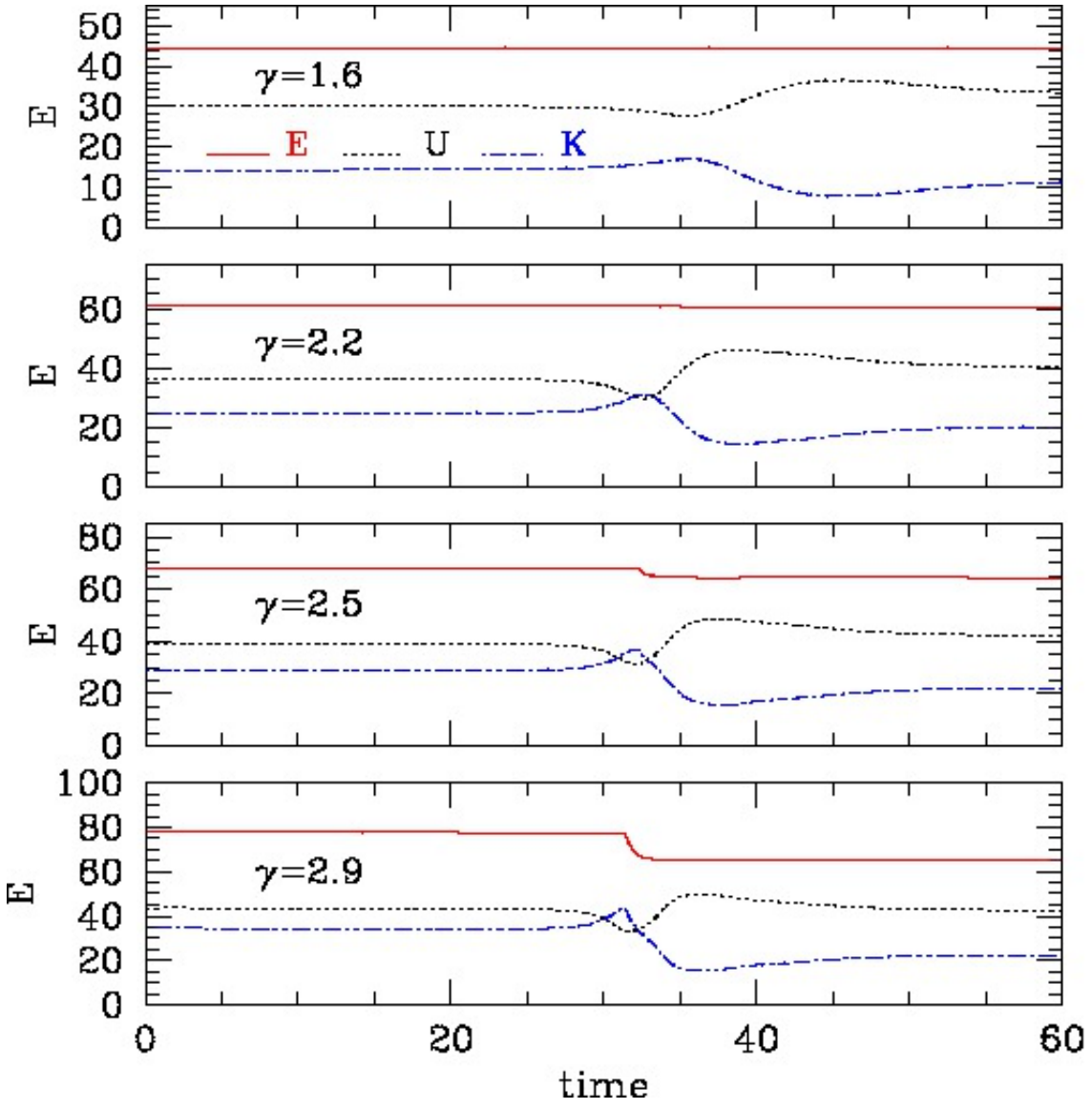

Figure 4.35: Decomposition of the total energy, E, into kinetic (K) and potential (U) components for head-on BB collisions in the attractive channel ($\Psi = \pi$), and for different values of γ. In contrast to the repulsive-channel calculations (Fig. 4.29), the values of K and U tend to approach each other as the evolutions proceed, leading to $K > U$ during the interaction for larger values of γ. Loss of hyperbolicity appears to set in for $\gamma^\star \sim 1.96$ ($v^\star \sim 0.86$), when the values of K at a few grid points near the centre of the computational domain begin to exceed the corresponding values of U. As for the repulsive-channel evolutions, conservation of energy is no longer observed during the interaction period for boosts above the critical value. Instead, an apparent discontinuity in E forms; this is most clearly visible in the bottom two plots Again, the magnitudes of these discontinuities increase as $h \to 0$. We note that the loss of hyperbolicity for the attractive channel evolutions occurs at slightly lower velocities than for the repulsive channel ones (for which $\gamma^\star \sim 2.19$, $v^\star \sim 0.89$). This seems plausible since the attractive nature of the force in the current case makes it easier for kinetic energy to exceed potential, as can be deduced from the plots shown above and in Fig. 4.29. Numerical parameters are identical to those listed in Fig. 4.33, except for the KO dissipation value, which is $\epsilon_{\rm KO} = 0.4$

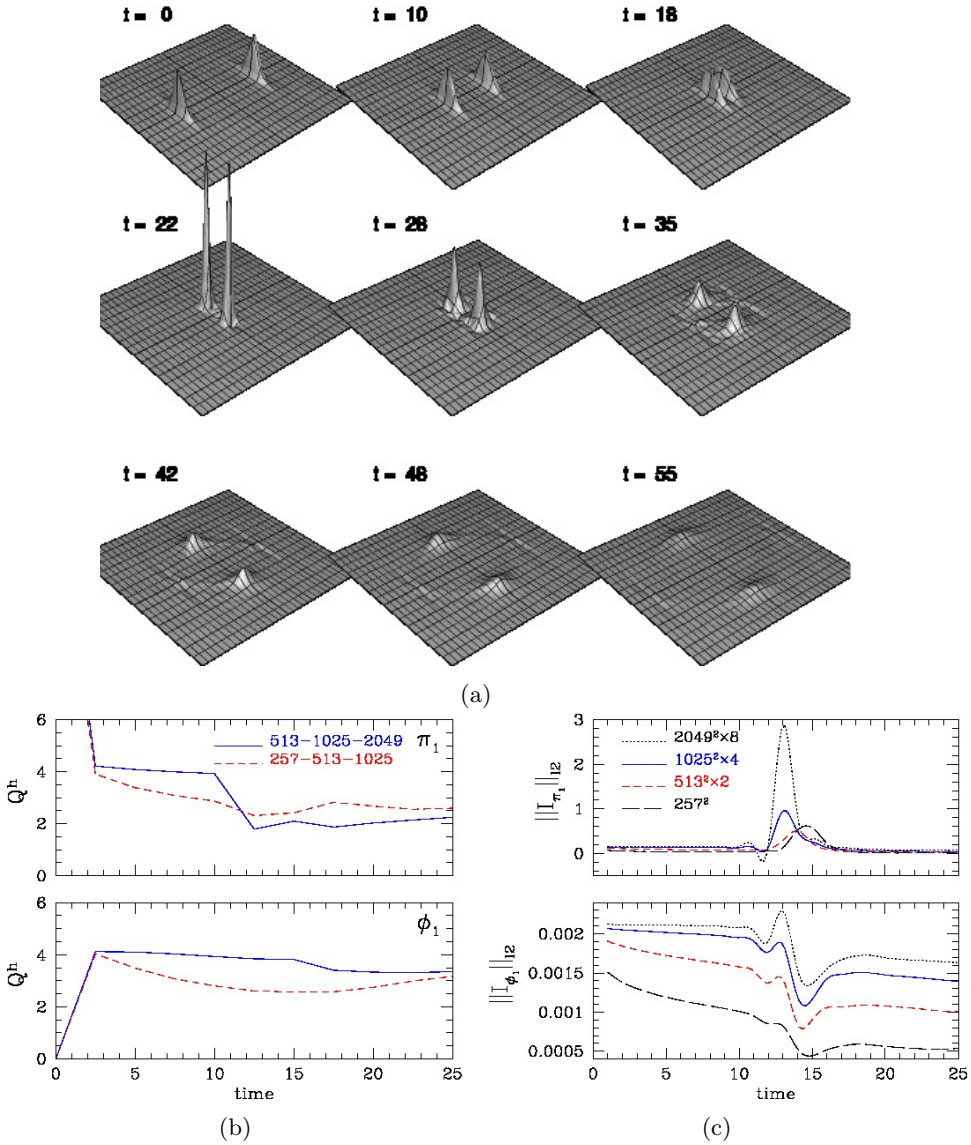

Figure 4.36: Unigrid calculation of a BB collision with $\Psi = \pi$ and $\gamma = 5$ which illustrates a transition into the mixed hyperbolic-elliptic regime. The top plot shows the evolution of the baryon density B_0. Figs. 4.36b and 4.36c show the resolution dependence of the convergence factors Q^h and the rescaled l_2-norms of the independent residuals, respectively, for ϕ_1 and π_1. Despite the fact that the baby skyrmions scatter at right angles, as might be expected from the value of Ψ, at the end they each disperse, and we interpret this as the solution failing to be physically meaningful at those times. We observe that the Q^h plots seem to indicate a change in convergence behaviour from $O(h^2)$ to $O(h)$ once the interaction begins. However, it is very clear from the behaviour of the independent residuals that the numerical solution is *not* converging to a bona fide continuum solution during and after the collision. This is especially evident from the π_1 independent residual where the rescaled values display less and less overlap as $h \to 0$. The calculation shown in the top plot was performed on the computational domain $[-30, 30] \times [-60, 60]$, using a 1025×1025 mesh and Sommerfeld boundary conditions. The baby skyrmions were initially centred at $(-20, 0)$ and $(20, 0)$, and the B_0 plots have been cropped to $[-30, 30] \times [-30, 30]$. The rest of the parameters are as given in Fig. 4.25.

Fig. 4.36 shows a unigrid calculation of a BB collision with $\Psi = \pi$ and $\gamma = 5$ and which illustrates a transition into the mixed hyperbolic-elliptic regime. The top plot shows the evolution of the baryon density B_0. Fig. 4.36b and 4.36c show the resolution dependence of the convergence factors, Q^h, and the rescaled l_2-norms of the independent residuals, respectively, for ϕ_1 and π_1. Despite the fact that the baby skyrmions scatter at right angles, as might be expected from the value of Ψ, at the end they each disperse, and we interpret this as the solution failing to be physically meaningful at those times. We observe that the Q^h plots seem to indicate a change in convergence behaviour from $O(h^2)$ to $O(h)$ once the interaction begins. However, it is very clear from the behaviour of the independent residuals that the numerical solution is *not* converging to a bona fide continuum solution during and after the collision. This is especially evident from the π_1 independent residual where the rescaled values display less and less overlap as $h \to 0$.

Direct visual inspection of grid functions from calculations with $\gamma > \gamma^\star$ provides additional evidence for the breakdown of well-posedness. Fig. 4.37 shows the evolution of π_1 during the central stages of a head-on BB collision in the attractive channel ($\Psi = \pi$) with $\gamma = 3.2$, which is well above the estimated threshold, $\gamma^\star \sim 1.96$, for a transition to non-hyperbolicity. Adaptive mesh refinement with the same parameters listed in Fig. 4.31 was used (except that $\epsilon_{\rm KO} = 0.4$ here), and the evolving structure of the mesh hierarchy is evident. The central region of Fig. 4.37d clearly illustrates a loss of smoothness of π_1. Indeed the solution there seems to be dominated by high frequency "noise"—which is what one would expect from the time evolution of a problem lacking a well posed initial value formulation—and this feature only worsens with an increase in resolution. Fig. 4.38 displays and discusses the expected development of an energy gap for this initial data set.

We now investigate solution features for a collision with $\gamma = 1.95$, which is slightly less than the estimated value ($\gamma^\star \sim 1.96$) at which the onset to non-hyperbolic behaviour occurs. Fig. 4.39 shows the baryon number density, B_0, from an AMR calculation for this case. The results are qualitatively consistent with the $\gamma = 1.6$ unigrid calculation shown in Fig. 4.33, in the sense that we also observe right-angle scattering in this instance. However, due to the increase in initial kinetic energy, the spikes in B_0 are larger here. A small amount of radiation is visible in the last few frames.

In the remainder of this subsection we will further explore head-on BB collisions for values of Ψ in the interval $[0, \pi]$, using the adaptive capabilities of our code. Fig. 4.40 shows the baryon

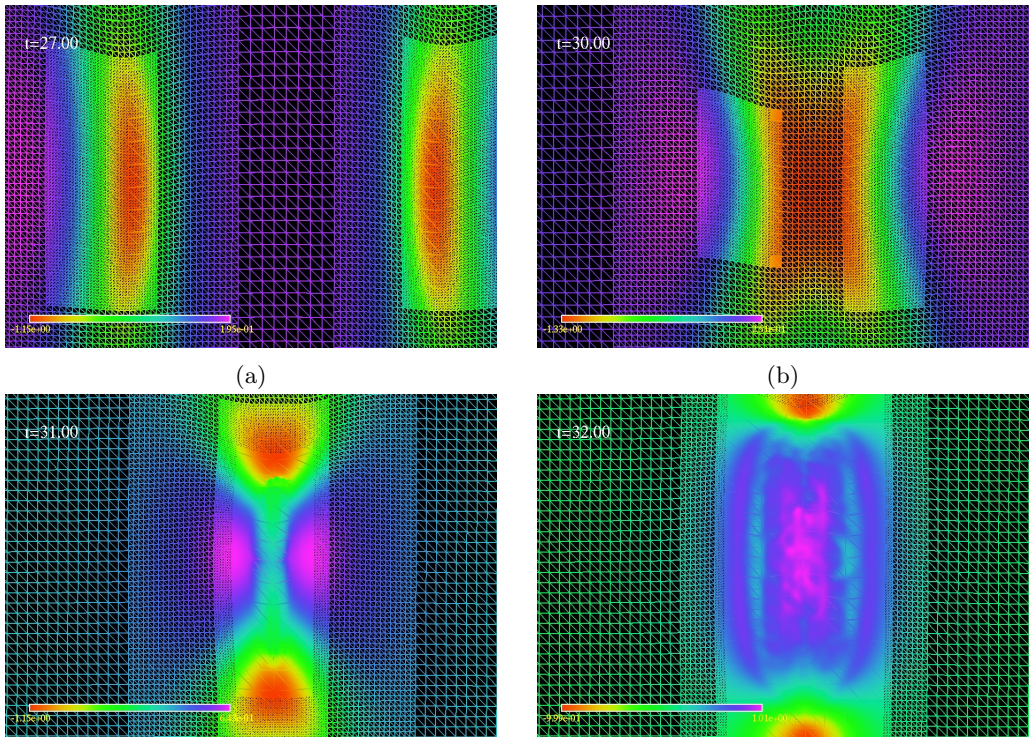

(a) (b) (c) (d)

Figure 4.37: This figure shows the evolution of π_1 during the central stages of a head-on BB collision in the attractive channel ($\Psi = \pi$) with $\gamma = 3.2$. The value of γ used is above the estimated threshold, $\gamma^\star$, for a transition to non-hyperbolicity. Adaptive mesh refinement with the same parameters listed in Fig. 4.31 was used (except that $\epsilon_{\rm KO} = 0.4$ here), and the evolving structure of the mesh hierarchy is evident. The central region of Fig. 4.37d clearly illustrates a loss of smoothness of π_1. Indeed the solution there seems to be dominated by high frequency "noise"—which is what one would expect from the time evolution of a problem lacking a well posed initial value formation—and this feature only worsens with an increase in resolution.

number density, B_0, from an an AMR calculation of a head-on BB collision with a relative phase of $\Psi = \pi/2$ and $\gamma = 1.6$ ($v = 0.8$). The baby skyrmions form large B_0 density spikes at the collision point, and then scatter at right angles. However, the baby skyrmions that emerge from the interaction are of different sizes: the large skyrmion scatters at an angle of $\pi/2$, while the small one scatters in the opposite direction; i.e at an angle $3\pi/2$. If we change the relative phase to $\Psi = -\pi/2$, the scattering angles are exchanged.

Fig. 4.41 illustrates the decomposition of the total energy E into its kinetic (K) and potential (U) components for head-on BB collisions using $\Psi = \pi/2$ and varying values of γ. By monitoring the conservation of E, we estimate that there is a transition to a mixed hyperbolic-elliptic regime for $\gamma^\star \sim 2$.

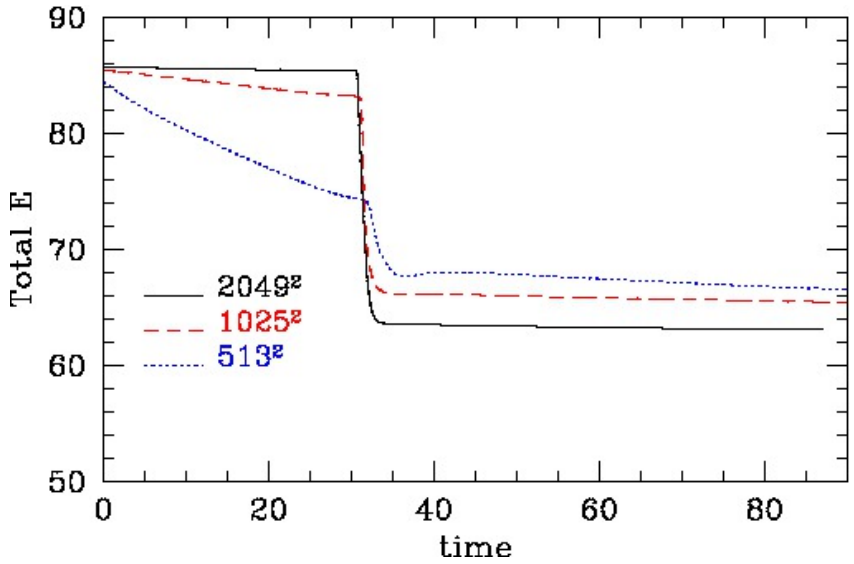

(a)

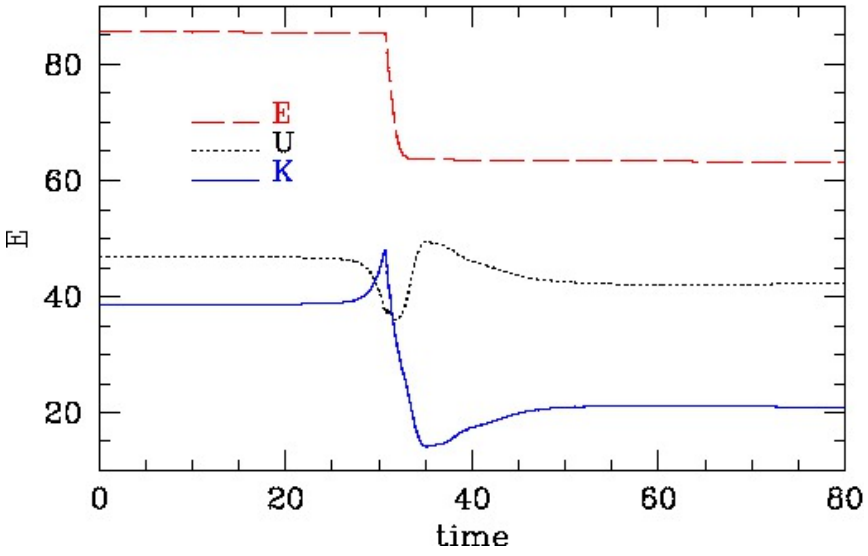

(b)

Figure 4.38: Development of energy gap for a head-on BB collision with $\gamma = 3.2$ and $\Psi = \pi$. Fig. 4.38a shows the evolution of the total energy E at different resolutions. The observed jump in E occurs during the period when the colliding skyrmions are most strongly interacting. Furthermore, as the mesh spacing decreases the jump becomes sharper, and actually increases in magnitude. We interpret these features as signs of a transition into a mixed hyperbolic-elliptic regime during the interaction. Although the jump appears to be tending towards a discontinuity for increasing resolution, we do not yet understand why this might be so. Fig. 4.38b displays the decomposition of E into kinetic (K) and potential (U) components for the highest resolution computation (2049×2049). We observe that the variation of total energy pre- and post-collision can primarily be attributed to a loss of kinetic energy. The choice of Dirichlet or Sommerfeld boundary conditions did not produce any appreciable difference in the results, nor did the use of different values of the KO dissipation parameter in the range 0.2–0.6.

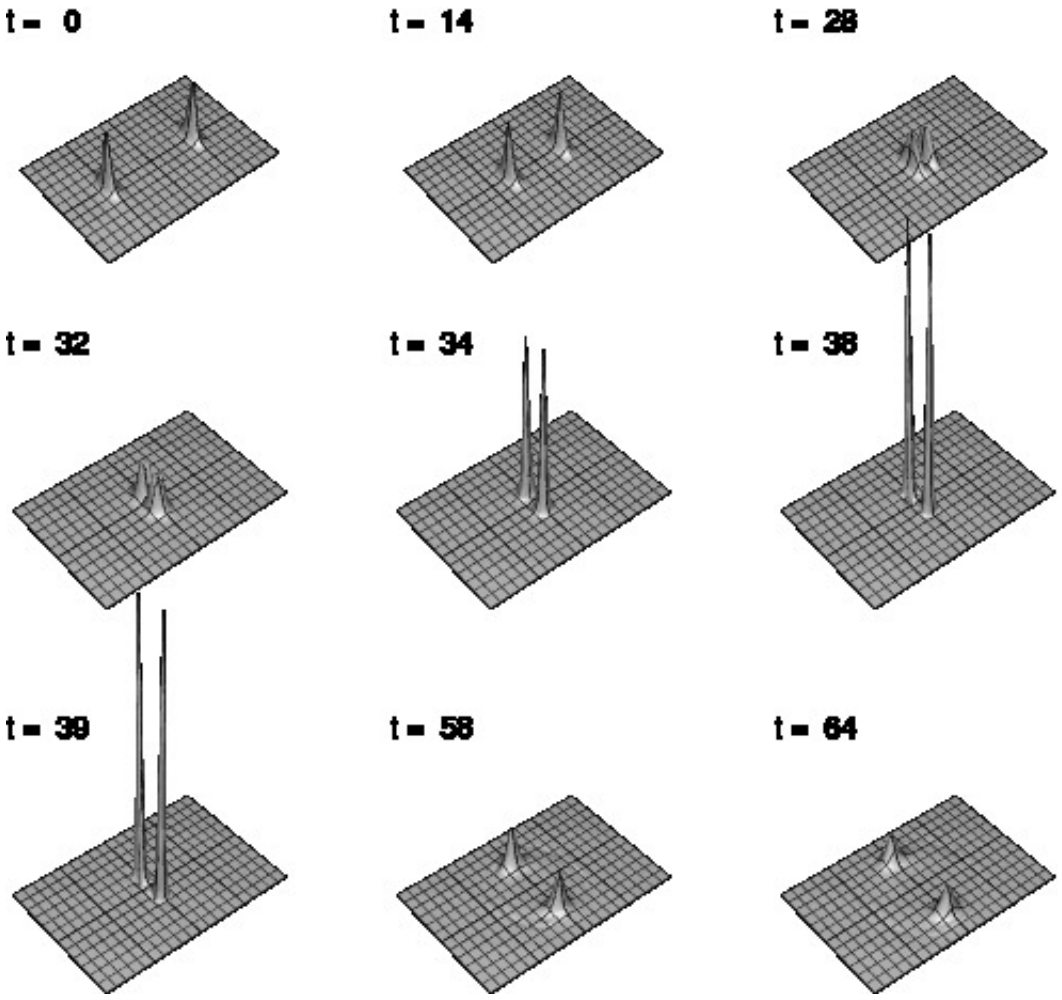

Figure 4.39: This figure shows the baryon number density B_0 from an AMR calculation of a head-on BB collision with a relative phase $\Psi = \pi$ and $\gamma \approx 1.95$ ($v \sim 0.858$); this initial boost is just below the estimated value, $\gamma^\star$, for loss of hyperbolicity. The results are qualitatively consistent with the $\gamma = 1.6$ unigrid calculation shown in Fig. 4.33, in the sense that we also observe right-angle scattering in this case. However, due to the increase in initial kinetic energy, the spikes in B_0 are larger here. A small amount of radiation is visible in the last few frames. The computational parameters, including those controlling the AMR algorithm, are identical to those listed in Fig. 4.37. except that we used $\epsilon_{\rm KO} = 0.4$. The initial skyrmion diameters in the x direction are $\approx 100/1.95 \approx 51.2$ units.

Fig. 4.42 displays the baryon number density, B_0, at late times (end states) from AMR calculations of head-on collisions with $\gamma = 1.6$, and using values of the relative phase Ψ in the interval $[\pi/8, \pi]$. For small values of Ψ we observe that the baryon density, B_0, is concentrated along one of the right-angle exit directions, $+\pi/2$. In these cases radiation is emitted in the other direction in accord with momentum conservation. As Ψ increases, more and more baryon density is ejected in the $3\pi/2$ direction, culminating with symmetric right-angle scattering for $\Psi = \pi$. We observe that the end state of the collision with $\Psi = \pi/4$ (Fig. 4.42b) is somewhat toroidally shaped. If we vary Ψ from $-\pi/8$ to $-\pi$, we obtain end states that are reflected with respect to the axis of approach. These results clearly show that the outcome of head-on BB collisions strongly depends on the initial value of Ψ.

4.8 Grazing Baby Skyrmion Collisions

We now consider calculations of more general off-axis BB collisions (grazing) for different values of the impact parameter b. Fig. 4.43 shows an AMR calculation of a BB grazing collision with $\gamma = 1.6$, $\Psi = 0$ (repulsive channel) and impact parameter $b = 5$. The baby skyrmions propagate unscathed until they meet. Surprisingly, when the skyrmions collide they appear to attract one another, despite the fact that the configuration corresponds to the repulsive channel (at least in the head-on limit). In fact they seem to fuse into a single skyrmion for a short length of time. The attractive force seems to act in an orthogonal direction (y) with respect to the axis of approach (x). After their brief interaction, the skyrmions acquire velocity components in the y direction, and then exit at nonzero angles with respect to the axis of approach. Conversely, Fig. 4.44 displays the results of an AMR calculation of a BB grazing collision with $\gamma = 1.6$, $\Psi = \pi$ (attractive channel) and impact parameter $b = 5$. The change of the value of Ψ with respect to the calculation shown in Fig. 4.43 results in the skyrmions exerting a repulsive force on one another in the y direction, i.e. orthogonal to the axis of approach, x. In contrast to the $\Psi = 0$ case, the solitons never merge, but are deflected at larger angles and suffer larger deformations as a result of the interaction. The initial kinetic energy is enough to preclude the formation of a bound state.

We also experimented with small initial velocities, such as $\gamma = 1.1$, in an attempt to form a bound configuration. However, even this amount of kinetic energy is still enough to prevent the mutual capture of the baby skyrmions. For sufficiently large impact parameters the baby skyrmions

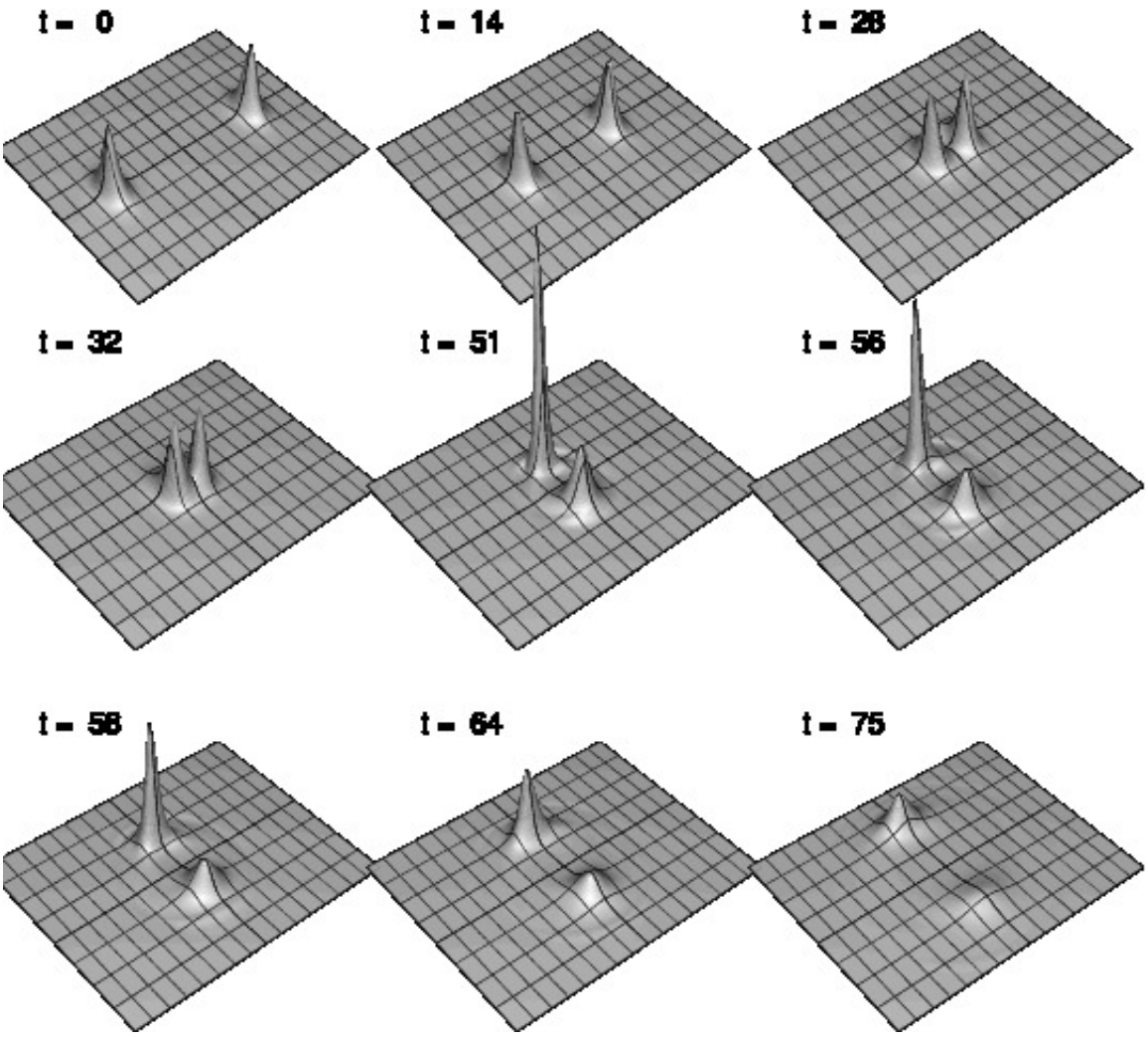

Figure 4.40: This figure shows the baryon number density, B_0, from an AMR calculation of a head-on BB collision with a relative phase of $\Psi = \pi/2$ and $\gamma = 1.6$ ($v = 0.8$). The baby skyrmions form large B_0 density spikes at the collision point, and then scatter at right angles. However, the baby skyrmions that emerge from the interaction are of different sizes: the large skyrmion scatters at an angle of $\pi/2$, while the small one scatters in the opposite direction, i.e at an angle $3\pi/2$. If we change the relative phase to $\Psi = -\pi/2$, the scattering angles are exchanged. This run was performed with the same parameters listed in Fig. 4.31, but this time the domain has been cropped to $[-50, 50] \times [-40, 40]$ in order to better see the small skyrmion. The boosted baby skyrmions are again centred at $(-30, 0)$ and $(30, 0)$, and their diameters in the x direction are $\approx 100/1.6 \approx 62$ units.

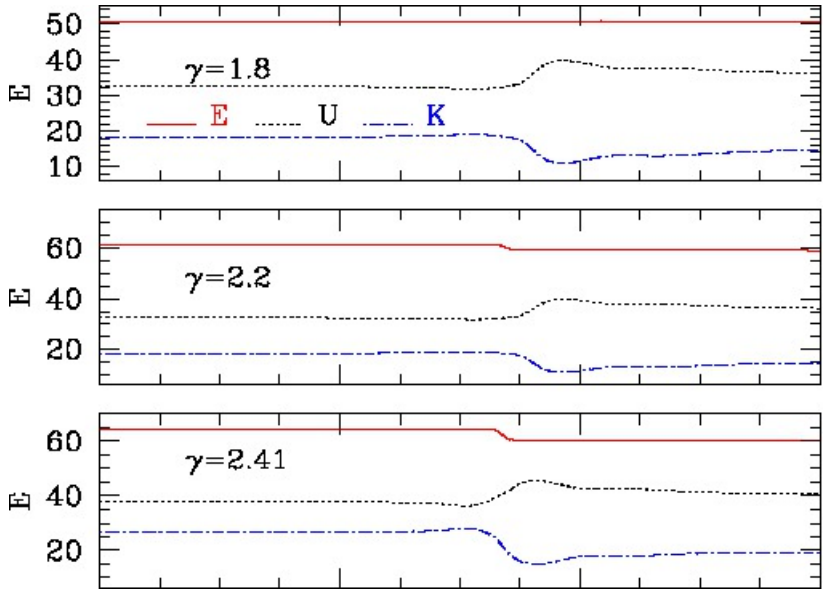

Figure 4.41: This graph shows the decomposition of the total energy E into its kinetic (K) and potential (U) components for head-on BB collisions using $\Psi = \pi/2$ and varying values of γ. By monitoring the conservation of E, we estimate that there is a transition to a mixed hyperbolic-elliptic regime for $\gamma \approx 2$. The parameters for these calculations are identical to those listed in Fig. 4.25 except that $\epsilon_{\rm KO} = 0.4$.

become essentially non-interacting, as is to be expected.

4.9 Baby Skyrmion–Baby Anti-skyrmion Collisions

Soliton–anti-soliton scattering is one of the most violent processes in skyrmion dynamics: it is characterized by rapid and extreme growth of gradients of the field variables, as well as the emission of large amounts of radiation. In this subsection we study the dynamics of this type of interaction for values of γ similar to those used thus far in this chapter. As before, a key aim of the calculations is to identify transitions to ill-posed (mixed hyperbolic-elliptic) behaviour.

We first remind the reader that, as discussed at the beginning of Sec. 4.7, a baby anti-skyrmion is a skyrmion with a conjugate topological charge $-B$, and is obtained by charge-conjugation of a hedgehog $(\phi_1, \phi_2, \phi_3) \rightarrow (-\phi_1, -\phi_2, \phi_3)$, followed by a reflection $(-\phi_1, -\phi_2, \phi_3) \rightarrow (\phi_1, -\phi_2, \phi_3)$ [88].

In the calculations we now discuss, the values of the numerical parameters are similar to those adopted in the preceding subsection. Specifically, unless otherwise stated they are: $\tau_{\rm max} = 6 \times 10^{-4}$,

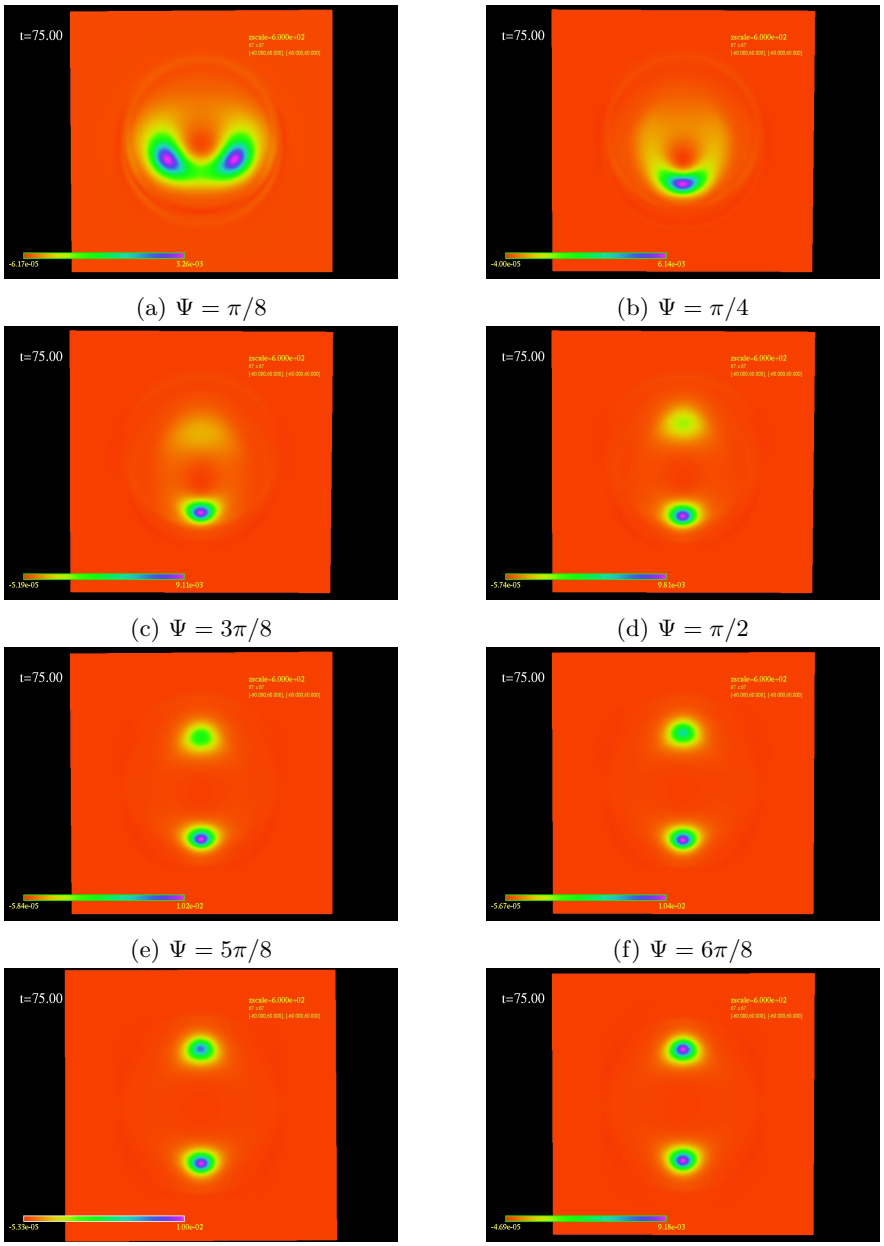

(a) $\Psi = \pi/8$ (b) $\Psi = \pi/4$

(c) $\Psi = 3\pi/8$ (d) $\Psi = \pi/2$

(e) $\Psi = 5\pi/8$ (f) $\Psi = 6\pi/8$

(g) $\Psi = 7\pi/8$ (h) $\Psi = \pi$

Figure 4.42: This figure shows the the baryon number density, B_0, at late times (end states) from head-on BB collisions with $\gamma = 1.6$ and using values of the relative phase Ψ between $\pi/8$ and π. For small values of Ψ we observe that the B_0 density is concentrated along one of the right-angle exit directions, $+\pi/2$. In these cases radiation is emitted in the other direction in accord with momentum conservation. As Ψ increases, more and more baryon density is ejected in the $3\pi/2$ direction, culminating with the symmetric right-angle scattering for $\Psi = \pi$. We observe that the end state of the collision with $\Psi = \pi/4$ (Fig. 4.42b) is somewhat toroidally shaped. If we vary Ψ from $-\pi/8$ to $-\pi$, we obtain end states that are reflected with respect to the axis of approach. The calculations were performed using AMR with the same parameters given in Fig. 4.31, except with $\epsilon_{\rm KO} = 0.4$.

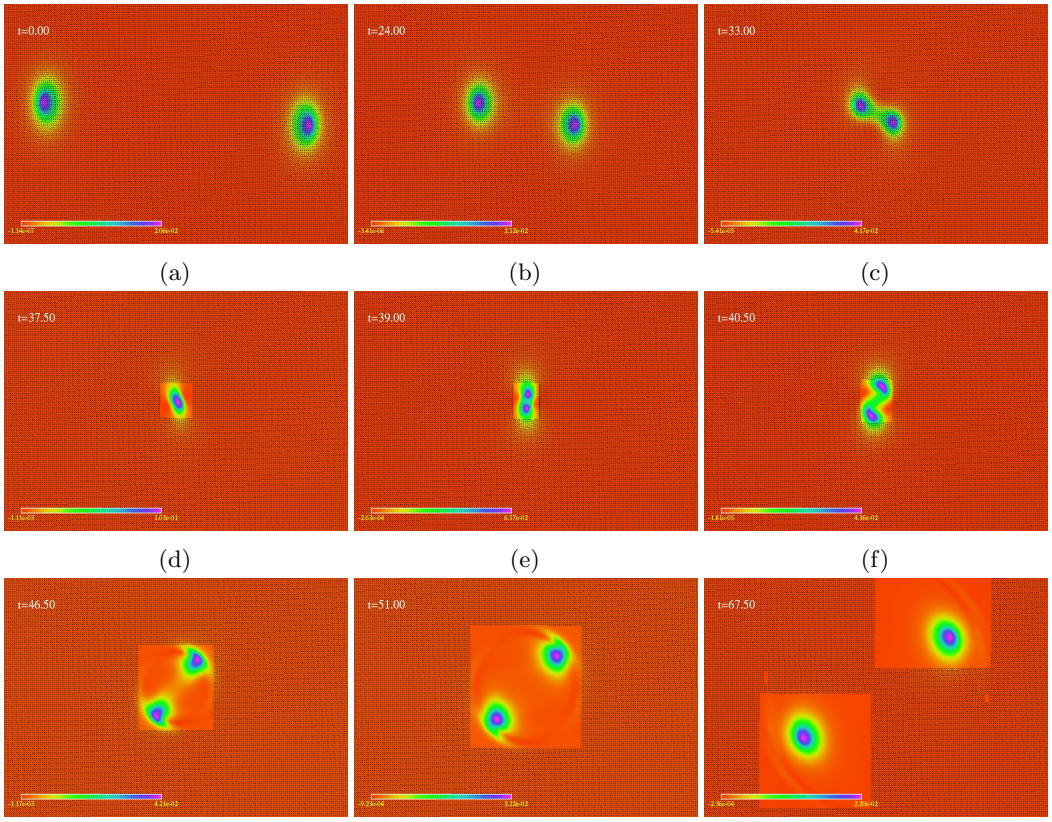

Figure 4.43: AMR Calculation of a BB grazing collision with $\gamma = 1.6$, $\Psi = 0$ (repulsive channel) and impact parameter $b = 5$. The baby skyrmions propagate unscathed until they meet. Surprisingly, when the skyrmions collide they appear to attract one another, despite the fact that the configuration corresponds to the repulsive channel (at least in the head-on limit). In fact they seem to fuse into a single skyrmion for a short length of time. The attractive force seems to act in an orthogonal direction (y) with respect to the axis of approach (x). After their brief interaction, the skyrmions acquire velocity components in the y direction, and then exit at nonzero angles with respect to the axis of approach. The skyrmions are initially centred at $(-30, 5)$ and $(30, 0)$. Numerical parameters are the same as those listed in Fig. 4.31, and the maximum level of grid refinement achieved was $L_f = 5$.

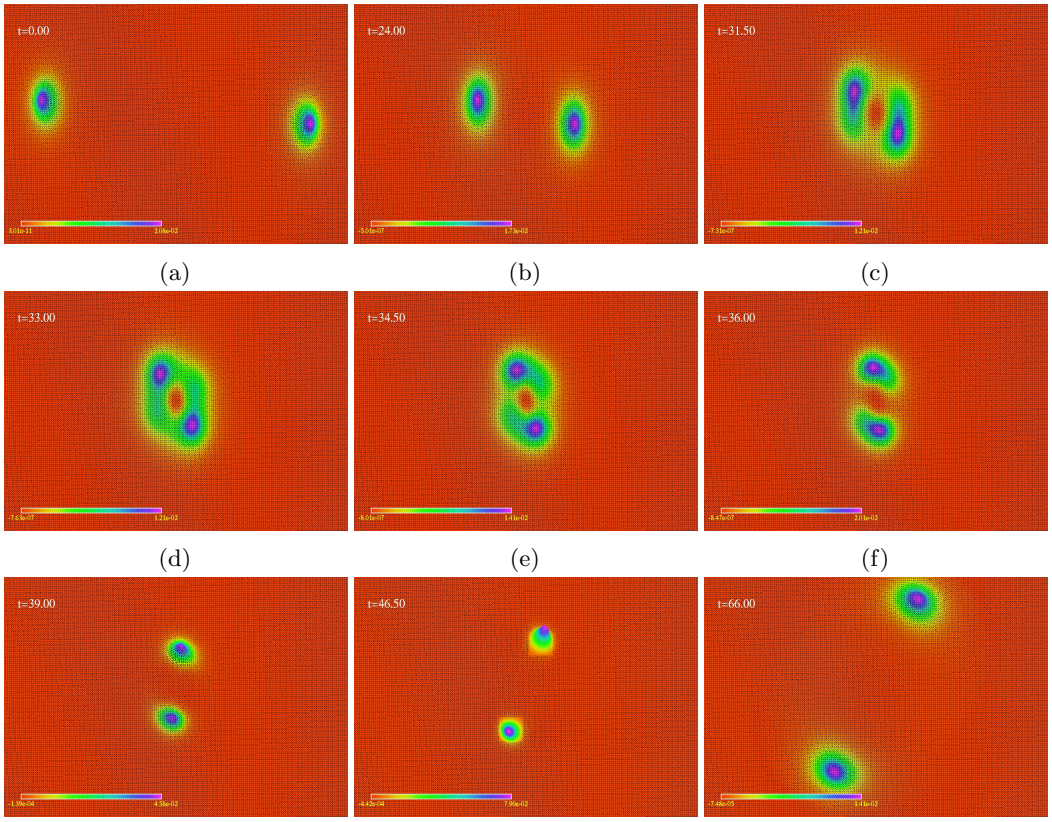

Figure 4.44: AMR calculation of a BB grazing collision with $\gamma = 1.6$, $\Psi = \pi$ (attractive channel) and impact parameter $b = 5$. The change of the value of Ψ with respect to the calculation shown in Fig. 4.43 results in the skyrmions exerting a repulsive force on one another in the y direction, i.e. orthogonal to the axis of approach, x. In comparison to the $\Psi = 0$ case the solitons never merge, but are deflected at larger angles and suffer larger deformations as a result of the interaction. The initial kinetic energy is enough to preclude the formation of a bound state. The starting locations of the centres of the boosted baby skyrmions are $(-30, 5)$ and $(30, 0)$. Numerical parameters are the same as those listed in Fig. 4.31.

$\epsilon_{\rm KO} = 0.5$ and $\lambda = 0.2$. Again, in order to eliminate any interference from radiation reflected from the boundaries, we use Sommerfeld conditions. The domain is a box with dimensions 120×120 ($[-60, 60] \times [-60, 60]$), and the starting locations of the centres of the boosted baby skyrmions are $(-30, 0)$ and $(30, 0)$. We continue to use the notation BB and $B\bar{B}$ to refer to a baby skyrmion–baby skyrmion collision, and a baby skyrmion–baby anti-skyrmion collision respectively.

Our first set of computations simulate $B\bar{B}$ scattering in the attractive channel ($\Psi = \pi$) for different values of γ. We begin with a typical $B\bar{B}$ annihilation with $\gamma = 1.6$ ($v = 0.8$); a plot of the time evolution of B_0 is shown in Fig. 4.45. We see that the two lumps of baryon density—which have opposite sign—merge and annihilate one another, leaving an outgoing circular wave whose amplitude quickly decreases to negligible levels, i.e. the baryon density vanishes. By this we infer that the outgoing wave is not a topological object, but scalar radiation. During the evolution the total baryon number, B, (which, in the limit $h \to 0$ should vanish at all times) is conserved to one part in 10^5. For this type of interaction it very is instructive to consider the evolution of the energy density, T_{00} (defined by (4.45)), as shown in Fig. 4.46. Since T_{00} is a strictly positive quantity (unlike B_0), "annihilation" is not seen in the time sequence. Rather, after the merger the energy is radiated away from the center of the collision as an outgoing circular wave pulse, similar to what was observed when we evolved a Gaussian pulse (Fig. 4.7).

We now turn to a head-on $B\bar{B}$ collision in the repulsive channel. Here we choose $\gamma = 2.1$ ($v = 0.88$) which is marginally below the critical value, $\gamma^\star \sim 2.15$, at which the evolutions appear to become ill-posed (see below). Figs. 4.47a and Fig. 4.47b display the time development of the baryon number density, B_0, and energy density, T_{00}. In contrast to the attractive channel computation illustrated in Fig. 4.45, the soliton anti-soliton pair does not annihilate in this case. Rather, after briefly merging and forming the characteristic spikes of baby skyrmion interactions, the solitons back scatter, emitting a significant amount of radiation that is most visible in the energy density plot.

Figs. 4.48a and 4.48c shows the evolution of the total energy E (at different resolutions) for the attractive and repulsive channel collisions, respectively, and provide evidence that in both cases the total energy converges as $h \to 0$. Not surprisingly the fluctuations in E are most significant (again, in both instances) while the skyrmions are interacting. Plots of the time evolution of E, K and U for the 1024×1024 for the attractive and repulsive channels are shown in Figs. 4.48b and 4.48d, respectively.

As we have already intimated, $B\bar{B}$ collisions also appear to become ill-posed for sufficiently large γ. The development of gaps in the computed total energy E for attractive-channel computations with different values of γ is shown in Fig. 4.49a. For the chosen values of γ we observe the same generic features in the graphs $E(t)$ that are seen for BB collisions (see Fig 4.35 for the attractive channel BB case). Again, we interpret the appearance of the gap as an indication of a transition into a hyperbolic-elliptic regime during the interaction of the solitons.

Similarly, the development of the gap in E for the repulsive channel is shown in Fig. 4.49b. Note that the transition occurs at a higher velocity for the repulsive channel than the attractive one.

We performed further experiments using the adaptive capabilities of the code. Our adaptive calculations of head-on $B\bar{B}$ annihilation in both the attractive and repulsive channels showed the same generic phenomenology in plots of B_0 and T_{00} that are described in the captions of their unigrid counterparts, Figs. 4.45, 4.46 and 4.47. We complemented these studies via an AMR calculation of the evolution of of a grazing $B\bar{B}$ collision with $\gamma = 1.6$, $\Psi = \pi$ and impact parameter $b = 5$. The time development of the energy density, T_{00}, for this case is shown in Fig. 4.50. We observe that after a brief merger of the soliton-antisoliton pair, the end state is a combination of scattering—with an exit angle $\approx \pi/4$—and emission of radiation that resembles the outgoing waves that follow the head-on $B\bar{B}$ annihilation shown in Fig. 4.45. We conclude that grazing baby skyrmion-antiskyrmion collisions lead to a mixture of annihilation and scattering. The initial kinetic energy here is large enough to preclude the formation of a bound state.

Some authors [149, 88] report a continuous emission of radiation after a baby $B\bar{B}$ annihilation, rather than the single outgoing pulse that we observe (see Fig. 4.46). Suspecting that this discrepancy was due to model-dependence (or parameter-dependence) of the annihilation phenomenon, we explored the outcome of a baby skyrmion $B\bar{B}$ interaction using a different value for potential parameter than that adopted in all of the calculations described above. Specifically we took $\mu^2 = 0.1$ (all of the other computations had $\mu^2 = 0.001$), but initialized the solitons with the same profile function, $f(r)$, used previously. Fig. 4.51 shows the time evolution of the energy density T_{00} from a unigrid computation of a $B\bar{B}$ collision in the attractive channel with $\gamma = 1.1$ ($v = 0.5$), and using $\mu^2 = 0.1$. This boost factor was chosen to ensure that the evolution remained well-posed (i.e. so that there was no transition to a mixed hyperbolic-elliptic state); our experiments indicate that $\gamma^\star$ decreases as μ^2 increases. In contrast to the $\mu^2 = 0.001$ skyrmion-antiskyrmion annihilation

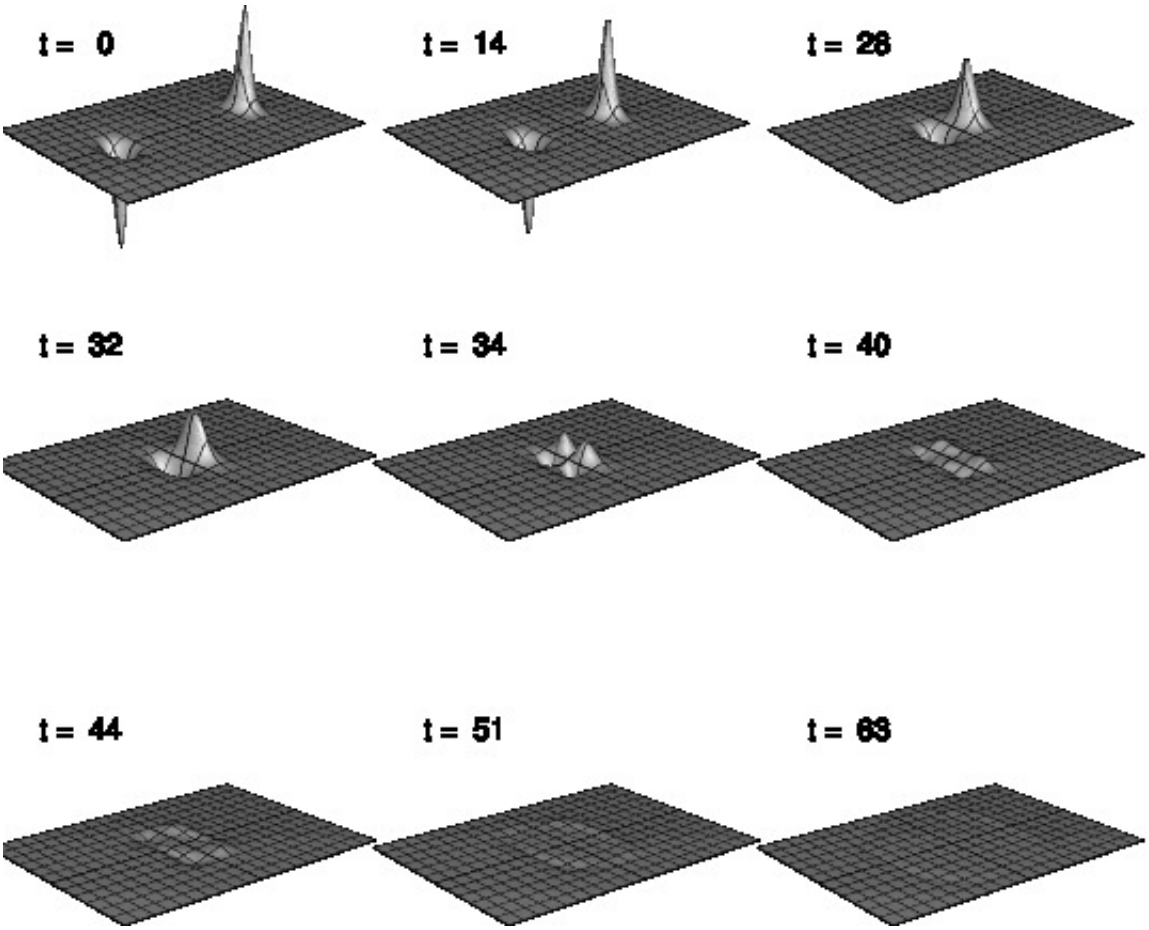

Figure 4.45: Evolution of the baryon number density, B_0, for $B\bar{B}$ annihilation in the attractive channel ($\Psi = \pi$) with $\gamma = 1.6$ ($v = 0.8$). The end state consists of outgoing circular waves with very small amplitude. The calculation was unigrid, using a computational domain $[-60, 60] \times [-60, 60]$ and a 1025×1025 mesh. The Courant number was $\lambda = 0.2$, the KO dissipation parameter was $\epsilon_{\rm KO} = 0.4$ and Sommerfeld boundary conditions were used. For illustrative purposes the domain has been cropped to $[-60, 60] \times [-40, 40]$. The boosted baby skyrmions are initially centred at $(-30, 0)$ and $(30, 0)$ and have initial diameters in the x direction of $\approx 100/1.6 \approx 62.5$.

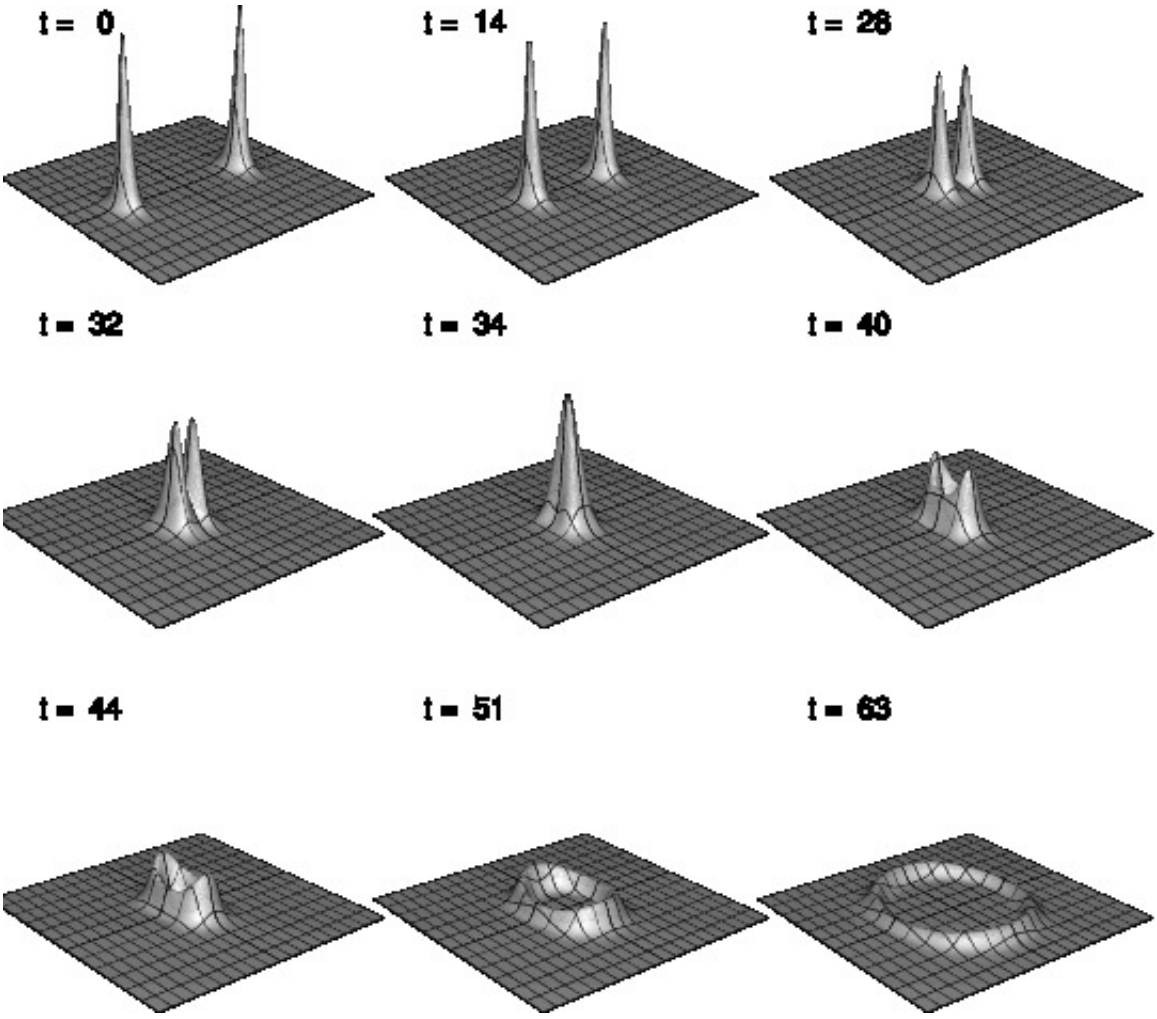

Figure 4.46: Evolution of the energy density, T_{00}, from the calculation described in Fig. 4.45. Since T_{00} is a strictly positive quantity (unlike B_0), "annihilation" is not seen in this sequence. Rather, after the merger, the energy is radiated away from the center of the collision as an outgoing circular wave pulse.

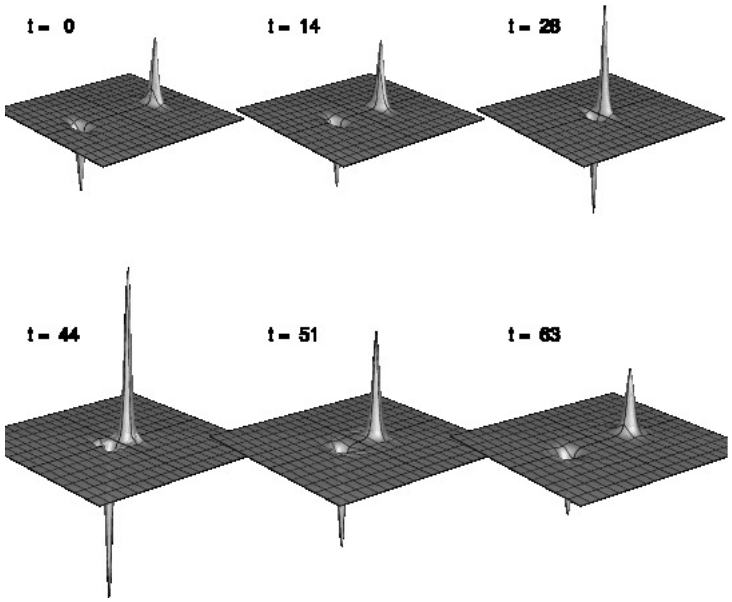

(a)

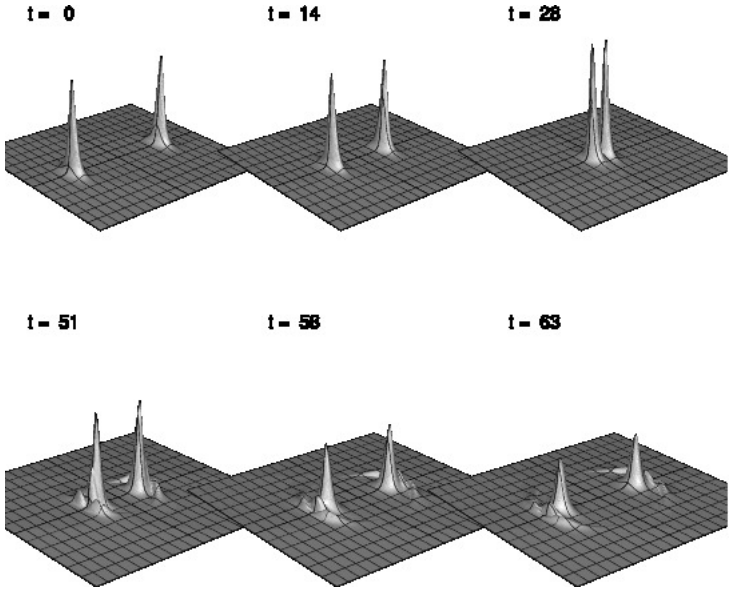

(b)

Figure 4.47: Evolution of the baryon number density, B_0, (Fig (a)) and total energy, E, (Fig (b)) for a $B\bar{B}$ collision in the repulsive channel ($\Psi = 0$) with $\gamma = 2.1$ ($v = 0.88$). In contrast to the attractive channel computation illustrated in Fig. 4.45, the soliton anti-soliton pair does not annihilate. After briefly merging and forming the characteristic spikes of baby skyrmion interactions, the solitons backscatter, emitting a significant amount of radiation that is most visible in the energy density plots. The parameters for this unigrid computation are identical to those listed in Fig. 4.45, except that the plotted domain has been cropped to $[-55, 55] \times [-55, 55]$. The initial diameters of the skyrmions in the x direction are $\approx 100/1.6 \approx 62.5$.

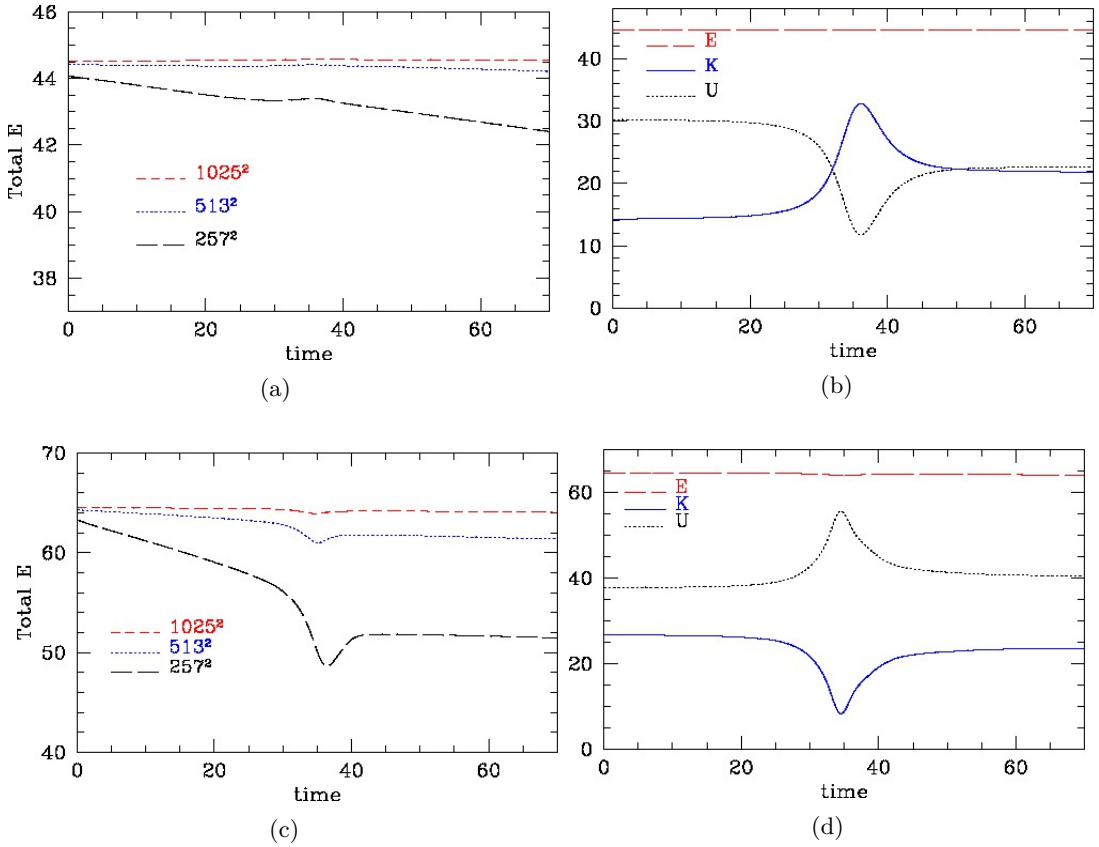

Figure 4.48: Convergence of computed energy quantities for the head-on $B\bar{B}$ collisions described in the previous figures. Plots (4.48a) and (4.48b) correspond to the $\gamma = 1.6$ attractive-channel collision detailed in the caption of Fig. 4.45, while (4.48c) and (4.48d) come from the $\gamma = 2.1$ repulsive-channel computation discussed in Fig. 4.47. Plots (4.48a) and (4.48c) provide evidence that the total energy converges as $h \to 0$ in both cases. Not surprisingly the fluctuations in E are most significant (again, in both instances) while the skyrmions are interacting.

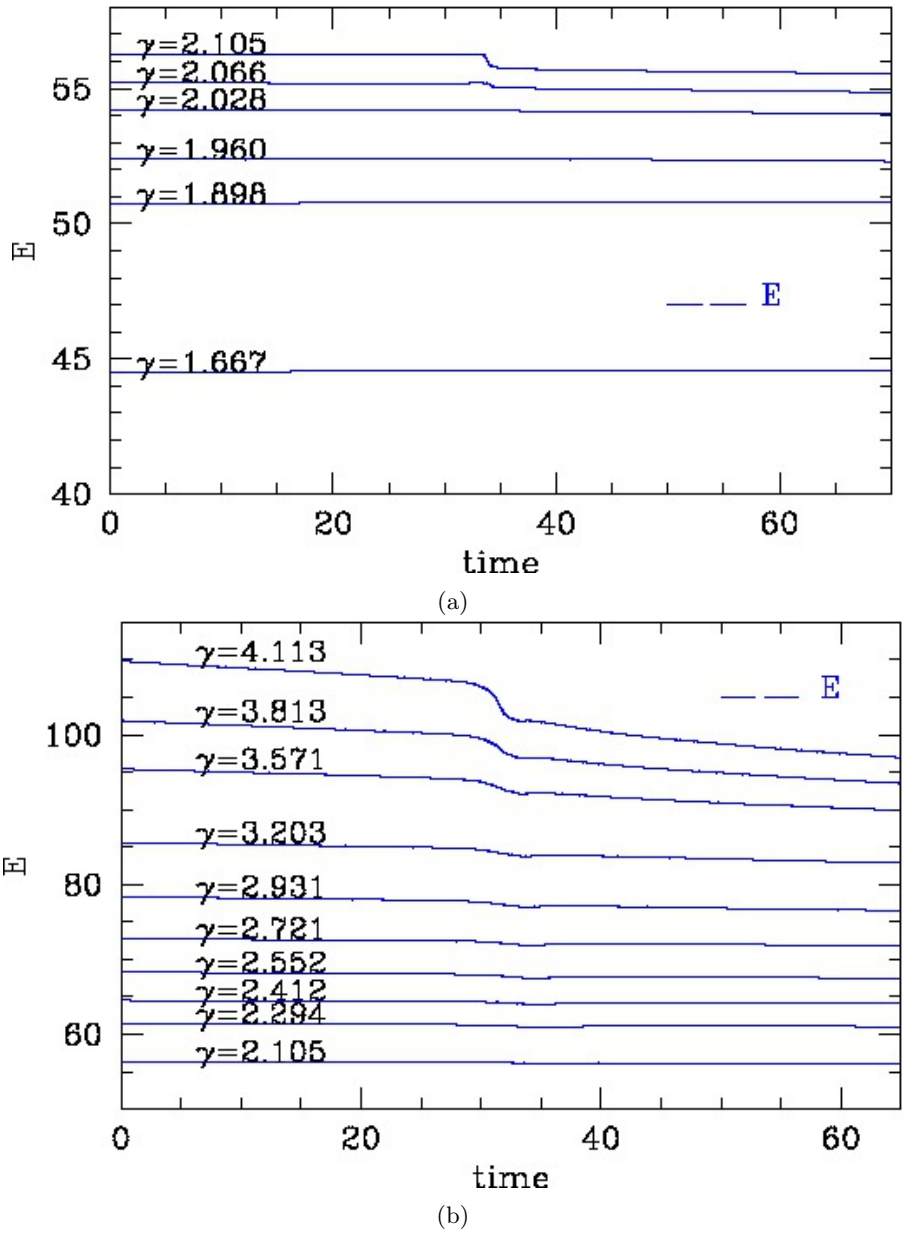

Figure 4.49: Development of the gap in the computed total energy E for head-on $B\bar{B}$ collisions with different values of γ, and for both the attractive (top) and repulsive (bottom) channels. For these values of γ we observed the same generic features in plots of B_0 and E that are described in the captions of Figs. 4.45, 4.46 and 4.47. However, the above graphs demonstrate the same effect observed in the case of BB collisions and shown—for the attractive channel case—in Fig 4.35. We again interpret the development of the gap as an indication of a transition into a hyperbolic-elliptic regime during the interaction of the solitons. The discontinuity can be detected visually for $\gamma^\star \approx 2$ (Fig. 4.49a). For the repulsive channel we have a similar situation, with an estimate of $\gamma^\star \sim 2.15$ ($v^\star \sim 0.886$) for the onset of loss of hyperbolicity, and the transition becoming noticeable in a plot at $\gamma \approx 2.9$ (Fig. 4.49b). Note that the transition occurs at a higher velocity for the repulsive channel than the attractive one. Numerical parameters for the computations were identical to those listed in Fig. 4.45.

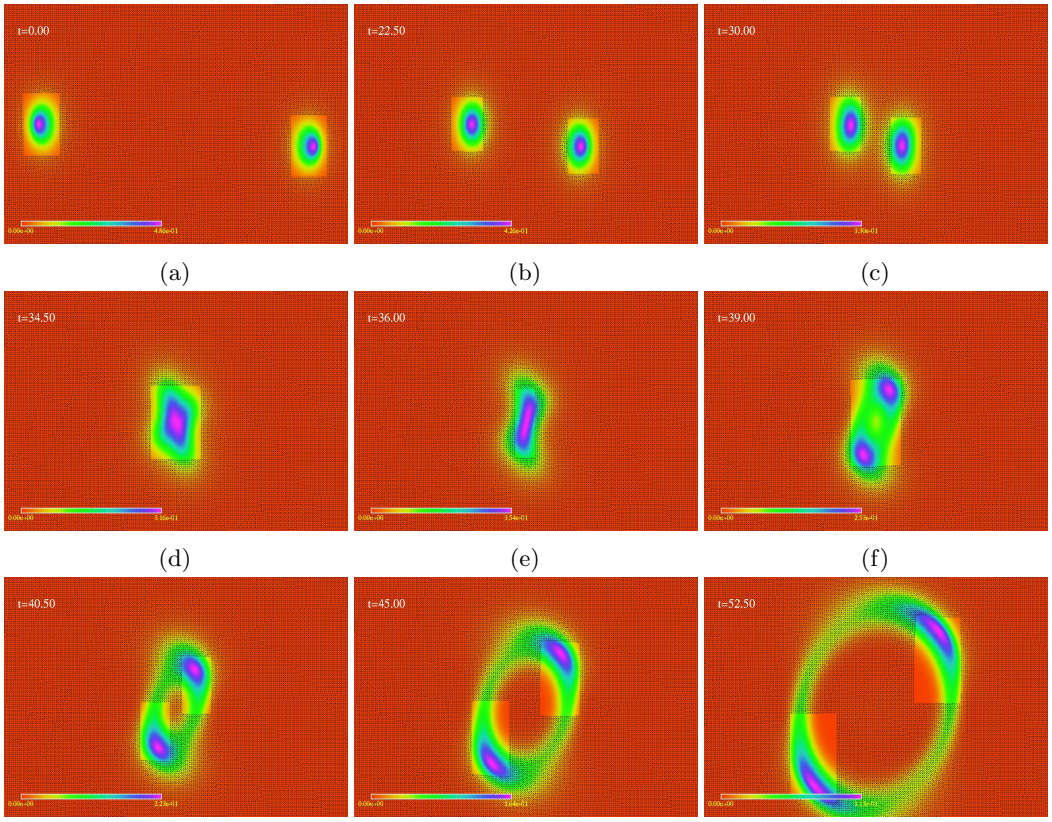

Figure 4.50: Evolution of the energy density, T_{00}, from an AMR calculation of a $B\bar{B}$ grazing collision with $\gamma = 1.6$, $\Psi = \pi$ and impact parameter $b = 5$. We observe that after a brief merger of the soliton-antisoliton pair, the end state is a combination of scattering—with an exit angle $\approx \pi/4$—and emission of radiation that resembles the outgoing waves that follow the head-on $B\bar{B}$ annihilation shown in Fig. 4.45. We conclude that grazing baby skyrmion-antiskyrmion collisions lead to a mixture of annihilation and scattering. The initial kinetic energy here is large enough to preclude the formation of a bound state. Numerical parameters for this calculation were the same as those given in Fig. 4.43, except that the truncation error threshold was set to $\tau_{\rm max} = 5 \times 10^{-5}$.

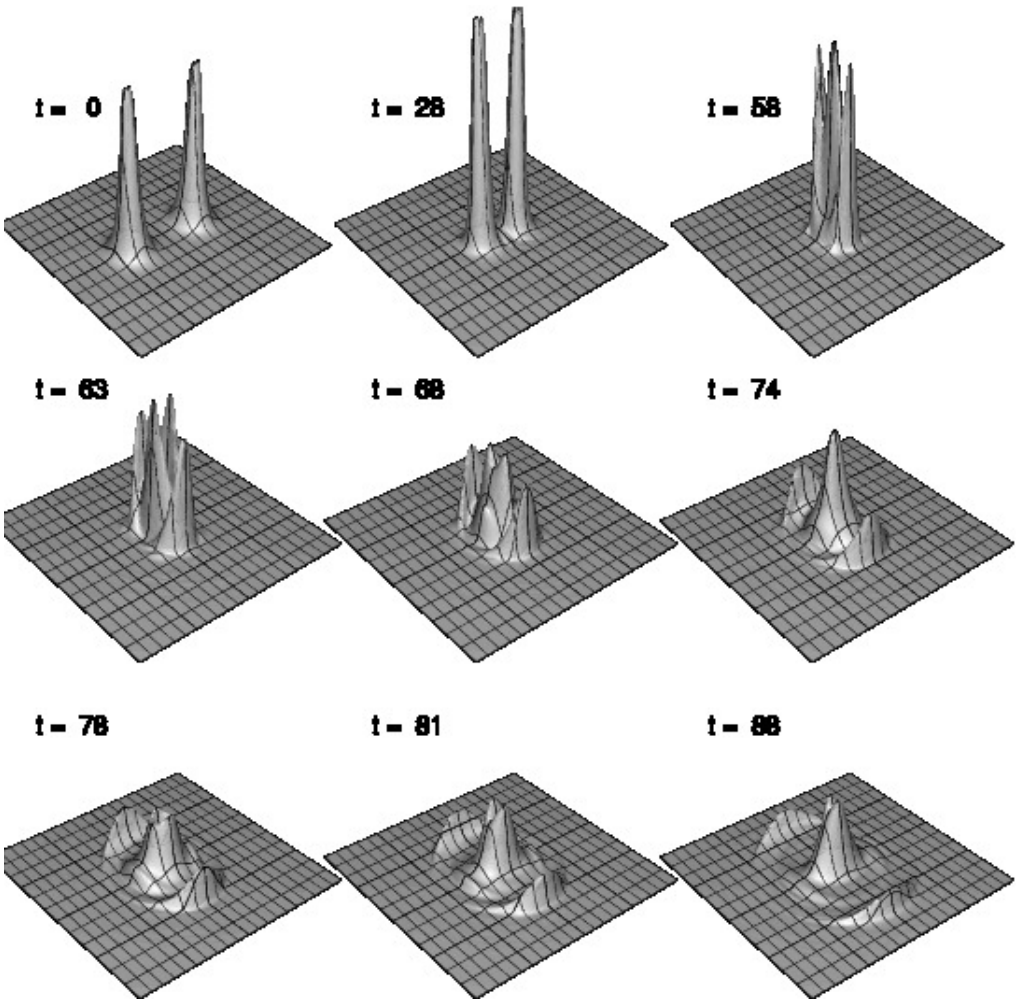

Figure 4.51: Time evolution of the energy density, T_{00}, for an attractive channel $B\bar{B}$ collision with $\gamma = 1.15$ ($v = 0.5$). The potential parameter here is $\mu^2 = 0.1$ whereas in all previous calculations discussed in this chapter we set $\mu^2 = 0.001$. In contrast to the $\mu^2 = 0.001$ skyrmion-antiskyrmion annihilation shown in Fig. 4.46, the soliton-antisoliton pair now merges into a circularly symmetric bound state centred at the origin, then emits a large pulse of radiation followed by a train of similar waves of smaller amplitude. The emission pattern appears to be largely dipole in nature (see Fig. 4.52). The central bound state is stable in the sense that it persisted for as long as the calculation was run. The computation was unigrid with a domain 160×160—this is larger than that used in previous calculations since at this boost the solitons are only slightly Lorentz contracted in the x direction to $\approx /1.15 \approx 87$. A 1025×1025 grid was used and the rest of the parameters were as listed in Fig. 4.45.

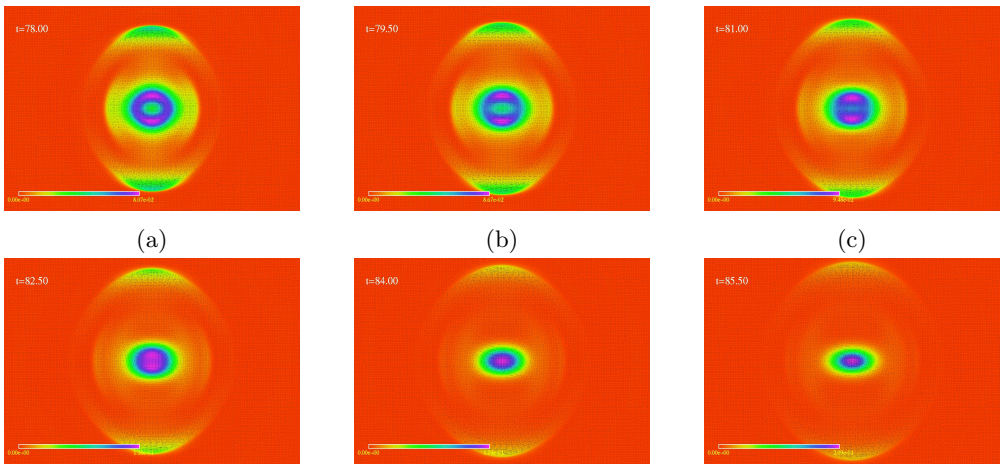

(a) (b) (c)

(d) (e) (f)

Figure 4.52: Late-time evolution of T_{00} from the $B\bar{B}$ computation with $\mu^2 = 0.1$ described in Fig. 4.51. The dipole nature of the radiation emitted from the final bound state is apparent.

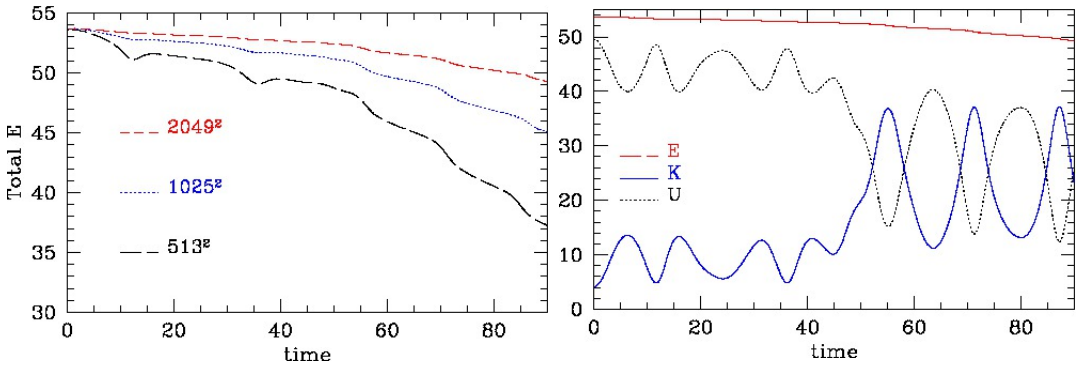

(a) (b)

Figure 4.53: Conservation of energy and evolution of energy components for the $B\bar{B}$ collision described in Fig. 4.51 ($\gamma = 1.6$, $\Psi = \pi$, and $\mu^2 = 0.1$). Figure 4.53a shows the evolution of the total energy E at different resolutions while Fig. 4.53b shows the kinetic (K) and potential energy (U) components from the 2049×2049 calculation. There is evidence for convergence to conservation of E although the rate of convergence is not definitive for the resolutions used here.

shown in Fig. 4.46, the soliton-antisoliton pair now merges into a circularly symmetric bound state centred at the origin, then emits a large pulse of radiation followed by a train of similar waves of smaller amplitude. The emission pattern appears to be largely dipole in nature (see Fig. 4.52). The observed behaviour is thus at least qualitatively consistent with what has been previously reported. We also note that the central bound state is stable in the sense that it persists for as long as the calculation is run. Convergence tests for this setup are shown in Fig. 4.53.

4.9.1 Other Indications of Non-hyperbolicity

We performed additional experiments involving smooth initial data, similar to the Gaussian pulses evolved in Sec. 4.4.4, but with the time derivatives set to very large values at $t = 0$. Hence, at the initial time the kinetic energy was already significantly greater than the potential energy. Not surprisingly these calculations exhibited a breakdown in the conservation of energy such as we have reported above and which we again interpret as a loss of hyperbolicity.

4.10 Comparison of Constraint Enforcement Methods

In this subsection we compare the different methods presented in Sec. 4.3.3 that are used to enforce the chiral constraint $\phi_a\phi_a = 1$ in the evolution of the grid functions of our baby Skyrme model. In all of the calculations described thus far we have imposed the constraint by means of the reprojection technique, (4.23), which keeps the l_2 norm of the violations ($C = \phi_a\phi_a - 1$) everywhere in the computational domain at the level of machine epsilon ($\sim 1 \times 10^{-16}$) for all the types of initial data, and the typical values of γ presented in this chapter. This technique is equally effective for adaptive and non-adaptive calculations.

As also discussed in Sec. 4.3.3, constraint damping is a dynamical alternative for enforcing the constraint. We experimented with calculations of a head-on BB collision in the attractive channel ($\Psi = \pi$) with $\gamma = 1.6$ ($v = 0.8$), employing constraint damping exclusively (i.e. with the Lagrange multiplier and reprojection disabled). We remind the reader that the constraint damping procedure is characterized by two adjustable parameters, ξ_1 and ξ_2. These control the amount of friction, or damping, introduced via the "constraint-violating" terms, (4.25) and (4.27), that are added to the fundamental dynamical equations.

We first consider the search for a suitable value of the parameter ξ_2, which controls the constraint

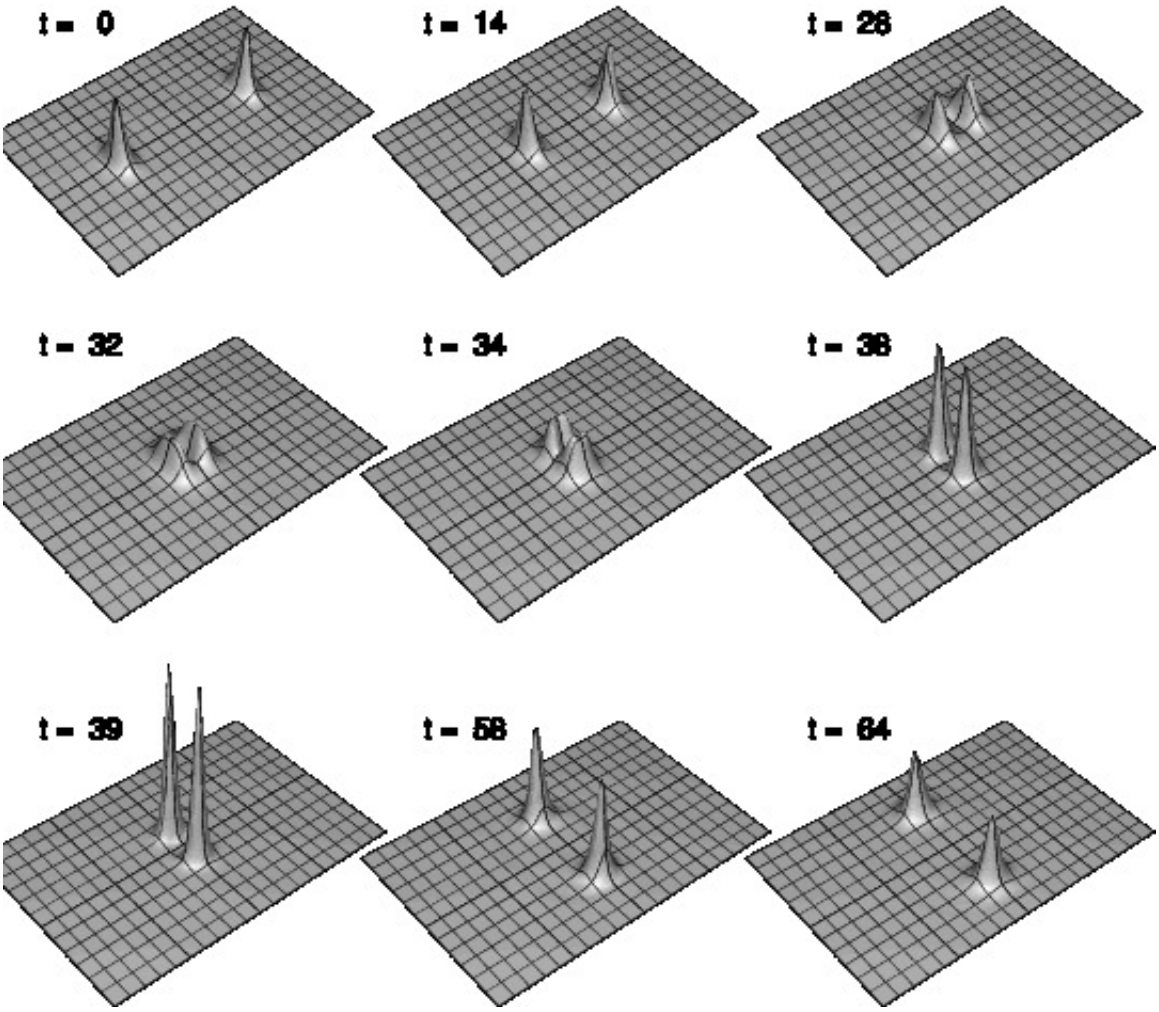

Figure 4.54: Evolution of the baryon density B_0 for an attractive channel head-on BB collision with $\gamma = 1.6$, using constraint damping. The values of the damping constants are $\xi_1 = -900$ and $\xi_2 = 80$. The results are consistent with a similar experiment that used reprojection and that is shown in Fig. 4.33. The unigrid calculation was performed on the domain $[-60, 60]\times[-60, 60]$ with a 1025×1025 mesh, and, for clarity, the displayed domain has been cropped to $[-60, 60] \times [-40, 40]$. The baby skyrmions were initially centred at $(-30, 0)$ and $(30, 0)$ and had diameters in the x direction of $\approx 100/1.6 = 62.5$. The boundary conditions were Dirichlet (reflecting).

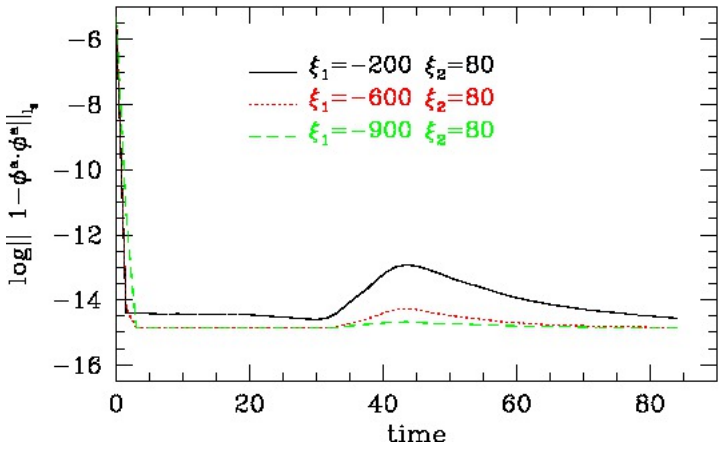

Figure 4.55: Natural logarithm of the l_2 norm of the constraint violation, $C \equiv \phi_a\phi_a - 1$, for a BB collision with $\gamma = 1.6$, $\Psi = \pi$, and where constraint damping is used. We show results for three values of ξ_1 ($-200, -600$ and -900) with ξ_2 fixed to 80. In all three cases C is quickly damped and remains small until the collision—at $t \sim 30$—when the violations grow (presumably caused by the strong fluctuation of the gradients) but then are damped once more at a rate which increases with increasing ξ_1. These plots illustrate the difference between reprojection and damping: while the former imposes the constraint immediately after the solution is updated at each time step, the latter is a corrective process that takes place over a period of time that is roughly inversely proportional to the damping parameters. The numerical parameters for these calculations are described in the caption of Fig. 4.54.

term (4.26) and which involves the field time derivatives (i.e. π^a). Too large a value of ξ_2 dissipates kinetic energy in excess, thus leading to the non-conservation of the total energy E (and, in fact, stopping the propagation of the solitons). Conversely, very small values lead to large violations of the constraint during collisions, which, naturally, is undesirable. Trial and error led us to a value of $\xi_2 = 80$. Energy conservation with this choice of ξ_2 is similar to that shown in Fig. 4.35 (where reprojection was employed) for the $\gamma = 1.6$ calculation. On the other hand, energy conservation does not seem to be very sensitive to the value of ξ_1. Having found a good setting for ξ_2 we found that, overall, constraint violations were damped exponentially, with the rate of decay controlled by ξ_1: the larger its value, the faster the decay.

Fig. 4.54 shows the evolution of the baryon density, B_0, for a unigrid constraint damping run with the values of the damping constants set to $\xi_1 = -900$ and $\xi_2 = 80$. The observed phenomenology is consistent with results obtained using reprojection (Fig. 4.33). Adaptive calculations of this type are equally consistent with the reprojection technique.

In order to demonstrate the effect of varying ξ_1, Fig. 4.55 shows the evolution of the natural logarithm of the l_2 norm of the constraint violations, $C = \phi_a\phi_a - 1$, for $\xi_1 = 80$ and three values

of ξ_1: -200,-600 and -900. For all three cases C is quickly damped to values of the order of machine epsilon. At the time of the collision, $t \sim 30$, the violations grow (presumably due to the strong fluctuation of the field gradients) but are damped again following the interaction. In this last phase one can clearly see the variation of the damping rate as a function of ξ_1. The plot also illustrates the contrast between reprojection and damping: while the former imposes the constraint immediately after the solution is updated at each time step, the latter is a corrective process that takes place over a period of time that decreases with increasing ξ_1.

In conclusion, we have found that constraint damping is an effective means for constraint enforcement in the numerical treatment of the baby Skyrme model. However, we emphasize that the simple reprojection method is at least as effective, easier to implement, and less costly computationally than the damping approach. It is for these reasons that we have exclusively used reprojection for the computations described in previous sections.

4.11 Conclusions and Future Developments

In this chapter we have performed adaptive and non-adaptive convergent numerical evolutions of single-boosted baby skyrmions, head-on BB collisions, grazing BB interactions, head-on and grazing $B\bar{B}$ collisions.

We developed a second order accurate ($O(h^2)$) code with adaptive mesh refinement capabilities, which were essential for optimal use of computational resources. (Sec. 4.4.6). Of central interest was the study of the loss of well-posedness (hyperbolic-elliptic transition) [1, 26, 95] for certain initial configurations in the model. By observing the behavior of the total energy (as well as direct examination of the behaviour of the dynamical variables) we confirmed the loss of hyperbolicity for specific types of evolutions, including baby skyrmion–baby skyrmion or baby skyrmion–baby anti-skyrmion collisions at high enough energies. Using detailed parameter space surveys we were able to define specific conditions for the loss of well-posedness, thus establishing some limits beyond which the model ceases to describe physically meaningful dynamics.

Our unigrid calculations are stable for Courant numbers as large as $\lambda = 0.5$, despite the fact that the numerical scheme is effectively explicit (since we update the grid functions using point-wise Newton-Gauss-Seidel iteration). This represents progress with respect to earlier numerical work on both the baby and the full $3+1$ Skyrme models [85, 84, 88, 86], where the Courant number

was frequently restricted to excessively small values. This improved stability likely results from our use of a Crank-Nicholson update scheme, as well as our constraint enforcement technique. AMR calculations required a somewhat smaller Courant factor—typically $\lambda \sim 0.1$–0.2—and this may be related to the interpolation at parent-child grid boundaries in the AMR hierarchy that is part of the Berger and Oliger algorithm. For both adaptive and unigrid calculations, and as long as the evolution remains well-posed (purely hyperbolic), the baryon number B and total energy E converge to conservation in the limit $h \to 0$.

The results of our extensive study of baby skyrmion phenomenology in this chapter can be summarized as follows:

- Adaptive and non-adaptive numerical evolutions of single boosted baby skyrmions (Sec. 4.6) remain stable and localized, even at large values of γ. Given the fundamental Lorentz invariance of the theory, this is to be expected.

- In contrast to the reported existence of a critical velocity separating right-angle from forward-scattering (for the same value of Ψ) [92], and given our specific model, our experiments of head-on BB collisions for the attractive channel *always* produce right-angle scattering, and for the repulsive channel *always* exhibit forward scattering, regardless of the initial velocity (see Sec. 4.7). The baryon density B_0 grows significantly during all collisions (forming spikes), a consequence of the enhancement of the gradients in the spatial derivatives during the interactions. Sommerfeld outgoing radiation boundary conditions resulted in better convergence properties than did Dirichlet (reflecting) conditions.

- BB collisions in the repulsive channel ($\Psi = 0$, Sec. 4.7.1): These collisions generically exhibit forward scattering. One key effect of the presumed departure from pure hyperbolic dynamics for $\gamma \geq \gamma^\star$ is a loss of conservation of energy. When γ exceeds $\gamma^\star$, post-collision values of E show a gap relative to the pre-collision values. Moreover, the magnitude of the jumps *increase* as $h \to 0$, a clear sign that the anomalous behaviour is not due to a lack of resolution.

- BB collisions in the attractive channel ($\Psi = \pm\pi$, Sec. 4.7.2): Particularly at low velocities, these interactions display the right-angle scattering typically seen for topological solitons. During the collisions, we observe the toroidal, short-lived intermediate $B = 2$ bound state previously reported by some authors (Peyrad [92] and Kudryavtsev [56]). However, with our choice of potential parameter the initial kinetic kinetic energy imparted to the baby skyrmions

was typically large enough to allow them to easily escape from their mutual attraction, leading to late-time configurations of stable outwardly-propagating solitons. As for the repulsive-channel evolutions, conservation of energy is no longer observed during the interaction period for boosts above $\gamma^\star$. Instead, an apparent discontinuity in E forms, and the magnitude of the jump increases as $h \to 0$. The loss of hyperbolicity in the attractive channel evolutions occurs at slightly lower velocities than for the repulsive channel ones.

- BB collisions with intermediate values of the internal phase ($0 < \Psi < \pi$, Sec. 4.7.2): Here the baby skyrmions form large B_0 density spikes at the collision point, and then scatter at right angles. However, the baby skyrmions that emerge from the interaction are of different sizes: the large skyrmion scatters at an angle of $\pi/2$, while the small one scatters in the opposite direction, i.e at an angle $3\pi/2$. If we change the relative phase to $\Psi = -\pi/2$, the scattering angles are exchanged. For sufficiently large γ we again observe a loss of hyperbolicity.

- BB grazing collisions (Sec. 4.8): In the repulsive channel ($\Psi = 0$), and with moderate impact parameter, the skyrmions appear to attract one another, fuse for a short time, then exit at nonzero angles with respect to the axis of approach. In the attractive channel ($\Psi = \pi$) the skyrmions experience a mutually repulsive force and scatter without a merger period. The solitons are deflected at larger angles and emerge more deformed relative to the $\Psi = 0$ case.

  With the values of γ that we used no loss of well-posedness was detected in either type of grazing collision.

- Head-on $B\bar{B}$ collisions: In the attractive channel ($\Psi = \pi$), and in terms of the baryon density, these result in annihilation, with the total energy of the configuration being released as a pulse of radiation that propagates outwards as a circularly-symmetric wave. In the repulsive channel case, the $B\bar{B}$ pair does not annihilate. Rather, there is a brief merger, followed by backscattering of the solitons and the emission of a significant amount of radiation.

- $B\bar{B}$ grazing collision with $\Psi = \pi$: This interaction is characterized by a brief merger of the $B\bar{B}$ pair, followed by evolution to an end state that is a combination of scattering and emission of radiation.

- By increasing the value of the potential parameter from $\mu^2 = 0.001$ to $\mu^2 = 0.1$ we were able to qualitatively reproduce some previous results wherein a $B\bar{B}$ collision results in a stable

circularly-symmetric bound state, accompanied by a train of primarily dipolar outgoing waves (in the baryon density). Furthermore, loss of hyperbolicity for $\mu^2 = 0.1$ set in at a smaller value of γ than for $\mu^2 = 0.001$.

- We found that reprojection (Sec. 4.3.3) is a very robust and reliable method for enforcing the constraint $\phi_a\phi_a = 1$. We also experimented with constraint damping (Sec. 4.10) and found that provided the adjustable parameters, ξ_1, and, more importantly, ξ_2, were chosen judiciously the approach was quite effective in preserving the constraint.

Finally, we make the following observation. Crutchfield and Bell [1] have conjectured that a loss of hyperbolicity should arise when the kinetic energy of a configuration significantly exceeds the potential energy. Although our findings are in accord with this, we have found that there are some subtleties in correlating $K > U$—i.e. not necessarily $K \gg U$—with a loss of well-posedness. For instance, the correlation appears to hold for head-on BB collisions in the attractive channel (Fig. 4.35), but not for $B\bar{B}$ collisions in the same channel (Fig. 4.49). The correlation also appears to fail for $B\bar{B}$ collisions with $\mu^2 = 0.1$ (Fig. 4.53), where $K > U$ but the evolution appears to be perfectly well posed. We also note that for head-on BB collisions in the repulsive channel (Fig. 4.29) and head-on BB collisions with $\Psi = \pi/2$, hyperbolicity is apparently lost even in cases where $K < U$. Our experience thus suggests that the loss of well-posedness is not connected in a *simple* manner to the relative magnitudes of the potential and kinetic contributions to the total energy (considered either globally or locally).

It is quite possible that there are quantities other than the total energy, E, that are computable from the field variables, and that could serve as additional indicators of the breakdown of hyperbolicity. In particular, following Crutchfield and Bell [1], we performed a linear normal-mode analysis of the characteristic structure of the baby Skyrme model: this is described in App. C.2. Numerical calculations based on this specific linearization confirmed the presence of unstable modes (complex eigenvalues) for values of $\gamma > \gamma^\star$; i.e. the appearance of the unphysical modes was correlated with the observation of loss of conservation of E in the full nonlinear evolution of the field equations. Further investigation of this issue is an important way in which our code could be extended.

Other possible extensions of this work include a study of the scattering of a wider set of solutions of the baby Skyrme model. In Sec.4.5 we mentioned that Kudryavtsev *et al* [56] considered excited skyrmion highly exited skyrmion-like states with $B = 1$, observing decays into a skyrmion and a skyrmion-anti-skyrmion pair, and sometimes nonlinear waves (pseudo-breathers), and other

interesting non-topological quasi-stable objects such as breathers. Clearly the baby Skyrme model admits a very rich phenomenology and has dynamics that warrant further investigation. An investigation of the μ^2 dependence of scattering experiments is one such topic that immediately comes to mind. Additionally, we are especially interested in extending the capabilities of our code to provide an improved and fuller understanding of the hyperbolicity (well-posedness) properties of the baby Skyrme model.

CHAPTER 5

RELATIVISTIC SCATTERING OF SKYRMIONS IN $3+1$ DIMENSIONS

5.1 Introduction

This chapter of the thesis presents preliminary results of the phenomenology of head-on skyrmion collisions in three spatial dimensions. Limitations in computer resources have prevented us from establishing definitive convergence behaviour for unigrid computations. Nevertheless, by using AMR we have been able to perform evolution of the dynamics of the full Skyrme model with some confidence in our results. The development in this chapter closely parallels that of the previous one in which we discussed our work with baby skyrmions[30]. Sec. 5.2 begins with a description of the model and the dynamical equations of motion. In Sec. 5.2.1 and 5.2.2 we discuss the specific implementation of the numerical methods that we use to approximately solve these equations. Sec. 5.2.4 then discusses the generation of suitable initial data for boosted skyrmions. Monitoring of conserved quantities is described in Sec. 5.2.5. Sec. 5.3 describes general features of skyrmion scattering, and presents a survey of previous work relevant to our calculations. We then make a brief study of the phenomenology of head-on skyrmion collisions (SS) by means of a series of adaptive computations—these are summarized in Sec. 5.4. Sec. 5.5 concludes the chapter with a summary of our findings, as well as suggestions for extensions of our code.

5.2 The Model

The model is described in terms of the right $SU(2)$ valued-current, R_μ, with a Lagrangian density [25, 26, 20, 27]

$$\mathcal{L} = \frac{F_\pi^2}{16}\mathrm{Tr}(R_\mu R^\mu) + \frac{1}{32e^2}\mathrm{Tr}[R_\mu, R_\nu]^2\,, \tag{5.1}$$

[30] In fact, the reader will note that some of the text describing the modelling procedure has been recycled with little or no change.

where $\mu, \nu = 0, 1, 2, 3$. F_π is the pion weak decay constant—the energy scale of chiral symmetry breaking [28]—and e is a dimensionless real parameter. The first term is the σ-model, and the second term is added to stabilize soliton solutions. In contrast to the baby Skyrme model we studied in Chap. 4, the presence of a potential term V (sometimes referred as a mass term) in the full 3D Skyrme model is optional, since static solutions exist for $V = 0$. Though elegant, the Lagrangian density (5.1) is not suited for numerical treatment. We use the relation[31]

$$R_\mu = (\partial_\mu U)U^{-1} = -U\partial_\mu U^{-1}\,, \tag{5.2}$$

to express (5.1) in sigma-model form in terms of the $SU(2)$-valued scalar (the Skyrme field), U,

$$\mathcal{L} = \frac{F_\pi^2}{16}\mathrm{Tr}(\partial_\mu U \partial_\mu U^\dagger) + \frac{1}{32e^2}\mathrm{Tr}[(\partial_\mu U)U^\dagger, (\partial_\mu U)U^\dagger]^2\,. \tag{5.3}$$

The parameters F_π and e can be scaled away by choosing suitable units of energy ($F_\pi/4e$) and length ($2/eF_\pi$) [20], yielding

$$\mathcal{L} = \frac{1}{2}\mathrm{Tr}(\partial_\mu U \partial_\mu U^\dagger) + \frac{1}{4}\mathrm{Tr}[(\partial_\mu U)U^\dagger, (\partial_\mu U)U^\dagger]^2\,. \tag{5.4}$$

We now construct a four component vector representation of $SU(2)$ [25, 26, 20, 27], by defining $\phi_a \equiv (\phi_1, \phi_2, \phi_3, \phi_4)$, which satisfies the constraint $\phi_a\phi_a = 1$. We then have

$$U = \phi_1\mathbb{I} + i(\phi_2\sigma_1 + \phi_3\sigma_2 + \phi_4\sigma_3) = \begin{pmatrix} \phi_1 + i\phi_4 & \phi_3 + i\phi_2 \\ -\phi_3 + i\phi_2 & \phi_1 - i\phi_4 \end{pmatrix}, \tag{5.5}$$

where $\sigma_1, \sigma_2, \sigma_3$ are the Pauli matrices, and $\mathbb{I}$ is a suitable identity matrix. We note that $U^\dagger = U^{-1}$, and $\phi_a = \phi_a(x^\mu)$, with x^μ the spacetime coordinates. Writing U and U^{-1} in terms of its components, one finds after lengthy manipulation [154, 25, 26] that

$$\mathcal{L} = \frac{1}{2}\partial_\mu\phi_a\partial^\mu\phi_a + \frac{1}{4}(\partial_\mu\phi_a\partial^\mu\phi_a)^2 - \frac{1}{4}(\partial_\mu\phi_a\partial_\nu\phi_a)(\partial^\mu\phi_b\partial^\nu\phi_b) + \lambda_{\mathrm{LM}}(\phi_a\phi_a - 1)\,. \tag{5.6}$$

Here Latin indices $a, b, \ldots = 1, 2, 3, 4$ label the components of the dynamical fields, while, as usual, Greek indices label the dimensions of spacetime, $\mu, \nu \ldots = 0, 1, 2, 3$. The last term in (5.6) has

[31] This relation follows from the Hermiticity of U, i.e. $U^\dagger U = \mathcal{I} \to \partial_\mu(UU^{-1}) = 0$

been added to enforce the constraint $\phi_a\phi_a = \phi_1^2 + \phi_2^2 + \phi_3^2 + \phi_4^2 = 1$, analogously to the case of the baby Skyrme model (4.1). Thus, by varying the Lagrangian constraint with respect to $\lambda_{\rm LM}$ we will again generate equations of motion which preserve the constraint [31, 32, 25]. The time-dependent equations of motion derived from the Lagrangian (5.6) are (See App. D.4),

$$\begin{aligned}(1 \quad &+ \quad \partial_\mu\phi_a\partial^\mu\phi_a)\Box\phi_a + \partial_\mu\partial_\nu\phi_b\partial^\mu\phi_b\partial^\nu\phi_a - \partial^\mu\phi_b\partial^\nu\phi_b\partial_\mu\partial_\nu\phi_a - \Box\phi_b\partial^\nu\phi_b\partial_\nu\phi_a \\ &+ \quad \Big[(1+\partial_\mu\phi_a\partial^\mu\phi_a)(\partial_\nu\phi_a\partial^\nu\phi_a) - (\partial_\mu\phi_a\partial_\nu\phi_a)(\partial^\mu\phi_b\partial^\nu\phi_b)\Big]\phi_a\,, \end{aligned} \tag{5.7}$$

where the exact form of the Lagrange multiplier term $\lambda_{\rm LM}$ has been computed (App. B) and included. Note that these equations are identical to those describing the dynamics of the baby Skyrme model (4.16) except that we now have four dynamical fields, $\phi_a(x^\mu)$ $a = 1, 2, 3, 4$, that depend on all 3 space dimensions plus time.

As was the case for the Q-ball PDEs described in Sec. 3.3 and the baby Skyrme model in Sec. 4.3, we wish to rewrite (5.7) as a set of first-order-in-time equations, in order to employ a two time-level Crank-Nicholson finite-difference scheme. We thus eliminate the second order time derivatives by introducing auxiliary fields, π_1, π_2, π_3 and π_4, defined by

$$\pi_a(t,x,y,z) = \frac{\partial\phi_a(t,x,y,z)}{\partial t}\,. \tag{5.8}$$

Our central interest is to study the scattering of head-on collisions of skyrmions which, again, are solitonic solutions of the model sketched above (see Sec. 4.2.1). As with the baby skyrmion case—which we discussed in some detail in Sec. 4.2.1—skyrmions display non-trivial topological properties. Here, the dynamical field ϕ_a represents a mapping from the compactified space-time $R^3 \cup \infty \simeq S^3$ into the internal space $SU(2)$ with the condition that $U(t,x,y,z) \to \mathbb{I}$ when $\sqrt{x^2+y^2+z^2} \to \infty$. We recall that maps are topologically equivalent [16, 24, 15] if they can be deformed into one another continuously, and we say that such maps belong to the same class. These classes are labeled by an integer, known as the topological charge, B, which is a conserved quantity that is interpreted as the baryon number [16, 24, 15]. B can be defined by first noting that the model admits a conserved current, B_μ, given by [48, 53],

$$B_\mu = \epsilon_{\alpha\beta\gamma\delta}\epsilon_{\mu\nu\rho\sigma}\phi_a\partial^\nu\phi_\beta\partial^\rho\phi_\gamma\partial^\sigma\phi_\delta\,. \tag{5.9}$$

B is then given by the spatial integral over the first component of (5.9). We will consider the explicit calculation of this quantity in Sec. 5.2.5.

5.2.1 Finite Difference Approach

The discretization of the equations of motion (5.7) is simply a generalization to three spatial dimensions of the methodology used for the baby Skyrme model equations in Sec. 4.3.1. We follow the same strategy of adopting a second order, Crank-Nicholson scheme, expressed on finite difference grids that are characterized by a single discrete scale, h. We thus have $\Delta x = \Delta y = \Delta z = h$, and $\Delta t = \lambda h$, where λ is the Courant number.[32]

Naturally, with the inclusion of an extra spatial dimension, namely z, we have additional finite-difference expressions for the full Skyrme model relative to the baby Skyrme model. These are summarized in Tab. 5.1, where we continue to use the notation $\phi^n(i,j,k) \equiv \phi(t^n, x_i, y_j, z_k)$ for grid functions. Also following our previous procedure, we will express the difference approximations of (5.7) in residual form, and remind the reader that the process of computing a solution to the discrete equations of motion is equivalent to driving all of the residual quantities, $\phi_1^{\rm res}, \phi_2^{\rm res}, \phi_3^{\rm res}, \phi_4^{\rm res}, \pi_1^{\rm res}, \pi_2^{\rm res}, \pi_3^{\rm res}, \pi_4^{\rm res}$, to 0.

For any of the the ϕ_a fields the residual form of the difference approximations are simply

$$\phi_a^{\rm res}(i,j) = \frac{\pi_a^{n+1}(i,j) + \pi_a^n(i,j)}{2} - \frac{\phi_a^{n+1}(i,j) - \phi_a^n(i,j)}{\Delta t}\,, \tag{5.10}$$

where the Latin index $a\ldots = 1,2,3,4$ labels the dynamical field. We again stress that here and below—and due to our use of superscripts for other purposes—we will often adopt a notation whereby ϕ_1, ϕ_2 , ϕ_3 and ϕ_4 (and similarly π_1, π_2, π_3 and π_4), rather than ϕ^1, ϕ^2, ϕ^3 and ϕ^4, denote field components.

As in the case of the baby Skyrme model, the task of writing the residuals $\pi_1^{\rm res}, \pi_2^{\rm res}, \pi_3^{\rm res}, \pi_4^{\rm res}$ fields explicitly is formidable, since the equations (5.7) in three spatial dimensions are quite complicated. Therefore, a Maple-based script was again written to automate this task: the script substitutes the finite difference stencils (5.1) into the continuum PDEs, thereby constructing the residual expressions.

[32]Once more we stress that, as discussed in Chap.2, when we use adaptive mesh refinement (AMR), each of the component grids in the grid hierarchy satisfies these conditions for some h_L, where L labels the level of the grid in the hierarchy and $h_L = h_{L-1}/2$.

The overall time-stepping methodology is also the same as that employed in Sec 4.3.1 for the baby Skyrme model. In the current case we have eight dynamical fields so, at any grid point (i, j, k), the Crank-Nicholson discretization yields eight nonlinear equations (defined by the four residual expressions (5.10) and $\pi_1^{\rm res}, \pi_2^{\rm res}, \pi_3^{\rm res}, \pi_4^{\rm res}$) for the unknowns $\phi_a^{n+1}(i, j, k)$ and $\pi_a^{n+1}(i, j, k)$. The global system of equations is again solved using point-wise-Gauss-Seidel relaxation sweeps. During one sweep, each grid point is visited in turn, and the 8 unknowns defined at that point are simultaneously (collectively) updated by performing a single Newton-step. This step in turn requires the construction of the 8×8 Jacobian matrix $\mathcal{J}_{cd}$, with matrix elements defined by

$$\mathcal{J}_{cd} \equiv \frac{\partial \mathcal{R}_c}{\partial \mathcal{V}_d}\,, \tag{5.11}$$

where

$$\begin{aligned} \mathcal{R} &\equiv \text{Residual Equations} = [\phi_1^{\rm res}, \phi_2^{\rm res}, \phi_3^{\rm res}, \phi_4^{\rm res}, \pi_1^{\rm res}, \pi_2^{\rm res}, \pi_3^{\rm res}, \pi_4^{\rm res}]\,, \\ \mathcal{V} &\equiv \text{Variables} = [\phi_1, \phi_2, \phi_3, \phi_4, \pi_1, \pi_2, \pi_3\, \pi_4]\,. \end{aligned} \tag{5.12}$$

In (5.11) the Latin indices $c, d \ldots = 1 \ldots 8$ label the rows and columns of the 8×8 linear system. We also note that we have suppressed the finite-differencing indexing for simplicity of expression, so that we have, for example,

$$\frac{\partial \phi_1^{\rm res}}{\partial \phi_1} \equiv \frac{\partial \phi_1^{\rm res}(i, j, k)}{\partial \phi_1^{n+1}(i, j, k)}\,. \tag{5.13}$$

We then use the routine `DGESV` from the LAPACK package [126] to directly solve the linear system at every grid point (x_i, y_j, z_k):

$$\mathcal{J}_{cd}\delta\mathcal{V}_d(i, j, k) = \mathcal{V}_c(i, j, k)\,. \tag{5.14}$$

Once the corrections $\delta\mathcal{V}_d = [\delta\phi,\delta\pi]$ have been obtained, the advanced-time unknowns are updated using

$$\begin{aligned} \phi_a^{n+1}(i, j, k) &= \phi_a^{n+1}(i, j, k) - \delta\phi_a(i, j, k)\,, \\ \pi_a^{n+1}(i, j, k) &= \pi_a^{n+1}(i, j, k) - \delta\pi_a(i, j, k)\,. \end{aligned} \tag{5.15}$$

When the global l_2 norm of the corrections (see 2.31 and Sec. 3.3.1) is below a specified threshold,

1: **for** $t^n = \Delta t, 2\Delta t, \ldots$ **do**
2: **for** $i = 1$ to Nx **do**
3: **for** $j = 1$ to Ny **do**
4: **for** $k = 1$ to Nz **do**
5: Set initial estimate for the solution vector $\boldsymbol{\phi_b^{(0)}} \equiv [\phi_1^{(0)}, \phi_2^{(0)}, \phi_3^{(0)}, \phi_4^{(0)}, \pi_1^{(0)}, \pi_2^{(0)}, \pi_3^{(0)}, \pi_4^{(0)}]^T$
6: Calculate the 8×8 Jacobian matrix $\boldsymbol{\mathcal{J}_{ab}}$ and the residual vector $\boldsymbol{B_a}$ at this point using nearest neighbour values, (some new, some old)
7: Solve $\boldsymbol{\mathcal{J}_{ab}\, \delta_b \phi = B_a}$ for the update $\boldsymbol{\delta_b \phi} = [\delta\phi_1^{(0)}, \delta\phi_2^{(0)}, \delta\phi_3^{(0)}, \delta\phi_4^{(0)}, \delta\pi_1^{(0)}, \delta\pi_2^{(0)}, \delta\pi_3^{(0)}, \delta\pi_4^{(0)}]^T$ using `DGESV` and obtain a new estimate $\boldsymbol{\phi}_b^{\rm new} = \boldsymbol{\phi}_b^{(0)} - \boldsymbol{\delta_b \phi}$
8: **end for**
9: **end for**
10: **end for**
11: Calculate the l_2 norm of the residuals using the new guess $\boldsymbol{\phi_b^{\rm new}}$ (This is a global norm for all subdomains used by the parallel infrastructure)
12: **if** l_2 norm of the residuals $<$ tolerance **then**
13: Convergence achieved
14: Goto 17
15: **else**
16: $\boldsymbol{\phi}_b^{(0)} = \boldsymbol{\phi}_b^{\rm new}$
17: Goto 2
18: **end if**
19: **end for**

Figure 5.1: Time stepping algorithm for the full Skyrme model evolution

the solution is deemed converged, and we can advance from t^n to t^{n+1}; otherwise we execute another Newton-Gauss-Seidel sweep. A pseudo-code version of the full time-stepping algorithm is given in Fig. 5.1.

5.2.2 Implementation Strategy

The implementation of the algorithm described above closely followed that of the code for the baby Skyrme model, including the use of the AMRD (Adaptive Mesh Refinement Driver) / PAMR (Parallel Adaptive Mesh Refinement) infrastructure [120, 107, 108] (see Chap. 2 and Sec. 3.3.2 for more details).

As described in Sec. 4.3.2 (and briefly above), the use of scripting and symbolic manipulation in the implementation process was crucial, particularly given the additional complexity introduced by the addition of a third spatial dimension, z. The derivation of the continuum equations of motion, and their ensuing discretization, were all achieved using Maple [128] scripts and a Maple-based tensor-manipulation package [129]. Once again, the discretization of the field equations, i.e. the

ϕ	$\frac{\phi^{n+1}_{ijk}+\phi^{n}_{ijk}}{2}$
ϕ_x	$\frac{1}{2}\left[\frac{\phi^{n+1}_{i+1,j,k}-\phi^{n+1}_{i-1,j,k}}{2\Delta x}+\frac{\phi^{n}_{i+1,j,k}-\phi^{n}_{i-1,j,k}}{2\Delta x}\right]$
ϕ_t	$\frac{\phi^{n+1}_{ijk}-\phi^{n}_{ijk}}{\Delta t}$
ϕ_{xx}	$\frac{1}{2}\left[\frac{\phi^{n+1}_{i+1,j,k}-2\phi^{n+1}_{i}jk+\phi^{n+1}_{i-1,j,k}}{\Delta x^2}+\frac{\phi^{n}_{i+1,j,k}-2\phi^{n}_{i}jk+\phi^{n}_{i-1,j,k}}{\Delta x^2}\right]$
ϕ_{xy}	$\frac{1}{2}\Big[\frac{\phi^{n+1}_{i+1,j+1,k}-\phi^{n+1}_{i-1,j+1,k}-\phi^{n+1}_{i+1,j-1,k}+\phi^{n+1}_{i-1,j-1,k}}{4\Delta x\Delta y}$ $+\frac{\phi^{n}_{i+1,j+1,k}-\phi^{n}_{i-1,j+1,k}-\phi^{n}_{i+1,j-1,k}+\phi^{n}_{i-1,j-1,k}}{4\Delta x\Delta y}\Big]$
ϕ_{xz}	$\frac{1}{2}\Big[\frac{\phi^{n+1}_{i+1,j,k+1}-\phi^{n+1}_{i-1,j,k+1}-\phi^{n+1}_{i+1,j,k-1}+\phi^{n+1}_{i-1,j,k-1}}{4\Delta x\Delta z}$ $+\frac{\phi^{n}_{i+1,j,k+1}-\phi^{n}_{i-1,j,k+1}-\phi^{n}_{i+1,j,k-1}+\phi^{n}_{i-1,j,k-1}}{4\Delta x\Delta z}\Big]$
ϕ_{yz}	$\frac{1}{2}\Big[\frac{\phi^{n+1}_{i,j+1,k+1}-\phi^{n+1}_{i,j-1,k+1}-\phi^{n+1}_{i,j+1,k-1}+\phi^{n+1}_{i,j-1,k-1}}{4\Delta y\Delta z}$ $+\frac{\phi^{n}_{i,j+1,k+1}-\phi^{n}_{i,j-1,k+1}-\phi^{n}_{i,j+1,k-1}+\phi^{n}_{i,j-1,k-1}}{4\Delta y\Delta z}\Big]$

Table 5.1: Crank-Nicholson (CN) three-(space) dimensional finite difference stencils used to convert the differential equations to difference equations, for any of the eight dynamical variables ϕ_a or π_a Here we use the notation $\phi^n_{ijk} \equiv \phi^n_{i,j,k} = \phi(t^n, x_i, y_j, z_k)$. We remind the reader that we use (component) finite difference grids that are characterized by a single discretization scale, h, so that $\Delta x = \Delta y = \Delta z = h$, and $\Delta t = \lambda h$, where λ is the Courant number. Each of the above expressions is a second order ($O(h^2)$) approximation to its continuum counterpart, and is centred at $(t^{n+1/2}, x_i, y_j, z_k)$.

replacement of the continuum differential operators by finite difference expressions, was done in the same way as for the baby Skyrme model (see Sec. 4.3.2 for further details).

5.2.3 Constraint Enforcement

We investigated two constraint enforcement mechanisms. The first was based on the addition of the Lagrange multiplier, $\lambda_{\rm LM}$, to the Lagrangian. However, as was the case for the baby Skyrme model, we found that this approach did not give satisfactory results. We thus opted for simple reprojection of the fields (see Sec. 4.3.3 for details), and this worked well.

5.2.4 Initial Data: Two Skyrmions

We wish to evolve minimum energy, topologically non-trivial, static solutions of the full Skyrme model, i.e. skyrmions. In order to construct a skyrmion, we adopt a generalization of the hedgehog ansatz employed in the baby Skyrme model (4.7). This ansatz also assumes spherical symmetry, and the configuration can again be described in terms of a radial profile function, $f(r)$. Specifically, adopting the usual spherical coordinates the ansatz is

$$\phi_a = \begin{pmatrix} \sin f(r)\ \sin\theta\ \cos(\varphi) \\ \sin f(r)\ \sin\theta\ \sin(\varphi) \\ \sin f(r)\ \cos\theta \\ \cos f(r) \end{pmatrix} . \tag{5.16}$$

Here

$$\varphi = \tan^{-1}\left(\frac{y}{x}\right) , \quad \theta = \tan^{-1}\left(\frac{\sqrt{x^2+y^2+z^2}}{z}\right) , \tag{5.17}$$

are referred to as the *internal phases* of the skyrmion. Substitution of (5.16) in (5.7) leads to a a nonlinear second order ordinary differential equation,

$$\left(r + \frac{n^2 \sin^2 f}{r}\right) f'' + \left(1 - \frac{n^2 \sin^2 f}{r^2} + \frac{n^2\, f' \sin f \cos f}{r}\right) f' - \frac{n^2 \sin f \cos f}{r} = 0 , \tag{5.18}$$

where $f' \equiv df/dr$. The radial function $f(r)$ must satisfy the boundary conditions $f(0) = B\pi$ and $f(\infty) = 0$ (localization), where B is the topological charge (see Sec. 5.2). As in the case of the baby Skyrme model, we will limit our attention to skyrmions with $B = 1$, so that the condition at

the center is $f(0) = \pi$. We numerically solved (5.18) using the same shooting technique described in Sec. 3.2.1 and Sec. 4.2.2. However, in the case of (5.18) there is also approximate closed form solution (suggested by Battye and Sutcliffe [25]),

$$f(r) = 4\tan^{-1}\exp(-r)\,. \tag{5.19}$$

Both numerical (which we now denote $g(r)$) and closed form (5.19) profile functions are shown in Fig. 5.2. Skyrmion scattering using either the numerical solution or the approximation (5.19) shows no appreciable difference for the type of calculations performed in this chapter. Additionally, the closed form approximation simplifies the generation of initial data, since the interpolation of the solution (see 4.3.4) onto our three dimensional domain is easier. We thus adopted (5.19) in our calculations. Note that although (5.19) is not regular at the origin of an (x, y, z) coordinate system, the components of (5.16) in those coordinates are (See App. D.5).

Let us consider two skyrmions, each defined by a hedgehog ansatz (5.16). In contrast to the baby Skyrme model, we now have *two phases*, θ and φ. Therefore we can characterize each skyrmion by two separate internal angles: θ_1, φ_1 for the first, and θ_2, φ_2 for the second. Then denoting the fields for the two configurations by $\phi_a^{(1)}$ and $\phi_a^{(2)}$ respectively, and using (5.16), we can write:

$$\phi_a^{(1)} = \begin{pmatrix} \sin f(r_1)\sin(\theta_1)\cos(\varphi_1) \\ \sin f(r_1)\sin(\theta_1)\sin(\varphi_1) \\ \sin f(r_1)\cos(\theta_1) \\ \cos f(r_1) \end{pmatrix}, \quad \phi_a^{(2)} = \begin{pmatrix} \sin f(r_1)\sin(\theta_2)\cos(\varphi_2) \\ \sin f(r_1)\sin(\theta_2)\sin(\varphi_2) \\ \sin f(r_1)\cos(\theta_2) \\ \cos f(r_1) \end{pmatrix}, \tag{5.20}$$

where r_1 and r_2 are the radial distances from the centres of the corresponding hedgehogs. We then refer to the parameters Ψ_1 and Ψ_2, defined by

$$\Psi_1 \equiv \theta_2 - \theta_1\,, \qquad \Psi_2 \equiv \varphi_2 - \varphi_1\,,$$

as the *relative phases* between the skyrmions. In $3+1$ dimensions it is common to refer to these phases as the *internal isospin orientation* [25] of the skyrmions. As in the case of the baby Skyrme model, these quantities play an important role in the dynamics of skyrmion collisions.

As for baby skyrmions, a pair of skyrmions (or skyrmion and antiskyrmion) separated by some distance, and at rest with respect to one another, will experience mutual forces ranging

from maximally attractive to maximally repulsive, dependent on the value of the phase Ψ_1. We will use the nomenclature defined in Sec. 4.3.6 wherein the *attractive channel* is a configuration of two hedgehogs with an initial $\Psi_1 = \pm\pi$, while the *repulsive channel* corresponds to $\Psi_1 = 0$ (i.e. no phase difference). Furthermore, we note that a configuration with $\Psi_2 = \pm\pi$ produces two skyrmions with opposite signs of the baryon number, i.e. a skyrmion-skyrmion pair in transformed to a skyrmion-antiskyrmion pair.

We can now define initial data $\phi_a^0(i,j,k)$ and $\pi_a^0(i,j,k)$, $a = 1,2,3,4$ (i.e. initial values defined on the finite difference grid (x_i, y_j, z_k)). This is achieved by first interpolating and translating the profile functions, $f(r_1)$ and $f(r_2)$, for the two skyrmions, in exactly the manner as was done for baby skyrmion initial data in Sec. 4.3.4.

Once the profile functions have been transferred to the finite difference mesh, yielding values $f_1(i,j,k)$ and $f_2(i,j,k)$, the dynamical field values $\phi_a^0(i,j)$ are set by

$$\begin{aligned}
\phi_1^0(i,j,k) &= \sin f_1(i,j,k)\sin\theta_1(i,j,k)\cos\varphi_1(i,j,k) + \sin f_2(i,j,k)\sin\theta_2(i,j,k)\cos\varphi_2(i,j,k)\,,\\
\phi_2^0(i,j,k) &= \sin f_1(i,j,k)\sin\theta_1(i,j,k)\sin\varphi_1(i,j,k) + \sin f_2(i,j,k)\sin\theta_1(i,j,k)\sin\varphi_1(i,j,k)\,,\\
\phi_3^0(i,j,k) &= \sin f_1(i,j,k)\cos\theta_1(i,j,k) + \sin f_2(i,j,k)\cos\theta_1(i,j,k)\,,\\
\phi_4^0(i,j,k) &= \cos f_1(i,j,k) + \cos f_2(i,j,k) - 1\,,
\end{aligned} \tag{5.21}$$

where the internal phases of the skyrmion are given by

$$\begin{aligned}
\varphi(i,j,k) &= \tan^{-1}\left(\frac{y_j - y_c}{x_i - x_c}\right),\\
\theta(i,j,k) &= \tan^{-1}\left(\frac{\sqrt{(x_i-x_c)^2 + (y_j-y_c)^2 + (z_k-z_c)^2}}{(z_k - z_c)}\right).
\end{aligned} \tag{5.22}$$

Since we are interested in colliding skyrmions with non-zero initial velocities, boosted initial data is obtained by an analogous procedure to the one described in Sec. 4.3.5. We briefly outline the procedure for a single boosted skyrmion. Once more we consider a boost with Lorentz factor, γ, in the $+x$ direction, and use primes to denote the coordinate system associated with the rest frame of the skyrmion. We thus have

$$t' = \gamma(t + vx) \quad x' = \gamma(x + vt) \quad y' = y \quad z' = z\,, \tag{5.23}$$

and

$$t = \gamma(t' - vx') \quad x = \gamma(x' - vt') \quad y = y' \quad z' = z\,. \tag{5.24}$$

From equations (3.39) the dynamical fields, $\phi_a(t', x', y', z')$, have the following values in the boosted frame:

$$\begin{aligned}
\phi_1(t,x,y,z) &= \phi_1'(t',x',y',z') = \sin f(x',y',z') \sin\theta(x',y',z') \cos\varphi(x',y',z')\,,\\
\phi_2(t,x,y,z) &= \phi_2'(t',x',y',z') = \sin f(x',y',z') \sin\theta(x',y',z') \sin\varphi(x',y',z')\,,\\
\phi_3(t,x,y,z) &= \phi_3'(t',x',y',z') = \sin f(x',y'.z') \cos\theta(x',y',z')\,,\\
.\phi_4(t,x,y,z) &= \phi_4'(t',x',y',z') = \cos f(x',y'.z')\,,
\end{aligned} \tag{5.25}$$

where

$$\begin{aligned}
\varphi(x,y,z) &= \tan^{-1}\left(\frac{y_j - y_c}{[\gamma[(x-x_c)+vt]}\right)\,,\\
\theta(z,y,z) &= \tan^{-1}\left(\frac{\sqrt{[\gamma[(x-x_c)+vt]^2 + (y_j-y_c)^2 + (z_k-z_c)^2}}{(z_k - z_c)}\right)\,.
\end{aligned} \tag{5.26}$$

The time derivatives, $\pi_a(t,x,y,z)$, transform according to (3.40) and (3.41), yielding

$$\pi_1 = \frac{\partial\phi_1'}{\partial x'}\gamma v\,, \quad \pi_2 = \frac{\partial\phi_2'}{\partial x'}\gamma v\,, \quad \pi_3 = \frac{\partial\phi_3'}{\partial x'}\gamma v\,, \quad \pi_4 = \frac{\partial\phi_4'}{\partial x'}\gamma v\,, \tag{5.27}$$

where we have used the fact that the rest-frame time derivatives, $\pi_a'(t', x', y', z')$, are identically 0.

At the initial time, $t = 0$, the coordinates in the rest frame are

$$t' = \gamma v x \qquad x' = x\gamma \qquad y' = y \qquad z' = z\,. \tag{5.28}$$

Again following the method described in Sec. 3.3.4, we interpolate in $f(x', y', z')$ to determine the values $f(\gamma x, y, z)$ in the lab frame, using $r' = \sqrt{x'^2 + y'^2 + z'^2}$, as well as the fact that in the rest frame $f(x', y', z')$ is a circularly symmetric function, i.e. $f(x', y', z') \equiv f(r')$. A complete set of initial values for a boosted baby skyrmion then follows by substituting $t = 0$ in (5.25). For the ϕ_a

we have

$$\begin{aligned}
\phi_1^0(x,y,z) &= \sin f(\gamma x,y,z)\sin\theta(\gamma x,y,z)\cos\varphi(\gamma x,y.z)\,,\\
\phi_2^0(x,y,z) &= \sin f(\gamma x,y,z)\sin\theta(\gamma x,y,z)\sin\varphi(\gamma x,y,z)\,,\\
\phi_3^0(x,y,z) &= \sin f(\gamma x,y,z)\cos\theta(\gamma x,y,z)\,,\\
\phi_4^0(x,y,z) &= \cos f(\gamma x,y,z)\,.
\end{aligned} \tag{5.29}$$

while for the π_a we find

$$\pi_1^0(x,y,z)=\frac{\partial\phi_1^0}{\partial x'}\gamma v\,,\quad \pi_2^0(x,y,z)=\frac{\partial\phi_2^0}{\partial x'}\gamma v\,,\quad \pi_3^0(x,y,z)=\frac{\partial\phi_3^0}{\partial x'}\gamma v\,,\quad \pi_4^0(x,y,z)=\frac{\partial\phi_4^0}{\partial x'}\gamma v\,. \tag{5.30}$$

We note that the derivatives $\partial\phi_a^0/\partial x'$ in this last set of expressions are computed numerically.

5.2.5 Computation of Conserved Quantities

In this subsection we will describe the computation of the total topological charge, B, the total energy, E, and the kinetic (K) and potential (U) components of E. Once more, the procedure is essentially the same as that implemented for the baby Skyrme model in Sec. 4.4.

The total baryon number, B, is given by the spatial integral [27, 15],

$$B=\frac{1}{2\pi^2}\int B_0\;\; d^3x=\frac{1}{2\pi^2}\int \epsilon_{\alpha\beta\gamma\delta}\epsilon_{\nu\rho\sigma}\phi_a\partial^\nu\phi_\beta\partial^\rho\phi_\gamma\partial^\sigma\phi_\delta\;\; d^3x\,, \tag{5.31}$$

where B_0 is the baryon number density.

We approximate this integral using a second-order trapezoidal rule, as described in Sec. 4.4.1. For the I-th subregion, we have a contribution, B_I, given by (see Sec. 4.4.1 for details),

$$\begin{aligned}
B_I &= \left(\frac{1}{2\pi^2}\right)\frac{\Delta x\;\Delta y;\Delta z}{8}\sum_{i,j,k}^{N_x-1,N_y-1,Nz-1}[B_0]_{i,j,k}+[B_0]_{i+1,j,k}+[B_0]_{i,j,k+1}+[B_0]_{i+1,j,k+1}\\
&+ [B_0]_{i,j+1,k}+[B_0]_{i,j+1,k}+[B_0]_{i,j+1,k+1}+[B_0]_{i+1,j+1,k+1}\,,
\end{aligned} \tag{5.32}$$

where Δx, Δy and Δz are the grid spacings of the three-dimensional mesh. We then sum the B_I to determine the final value of B.

Following Sec. 4.4.2, we compute the following locally defined energy densities: 1) total, T_{00}; 2)

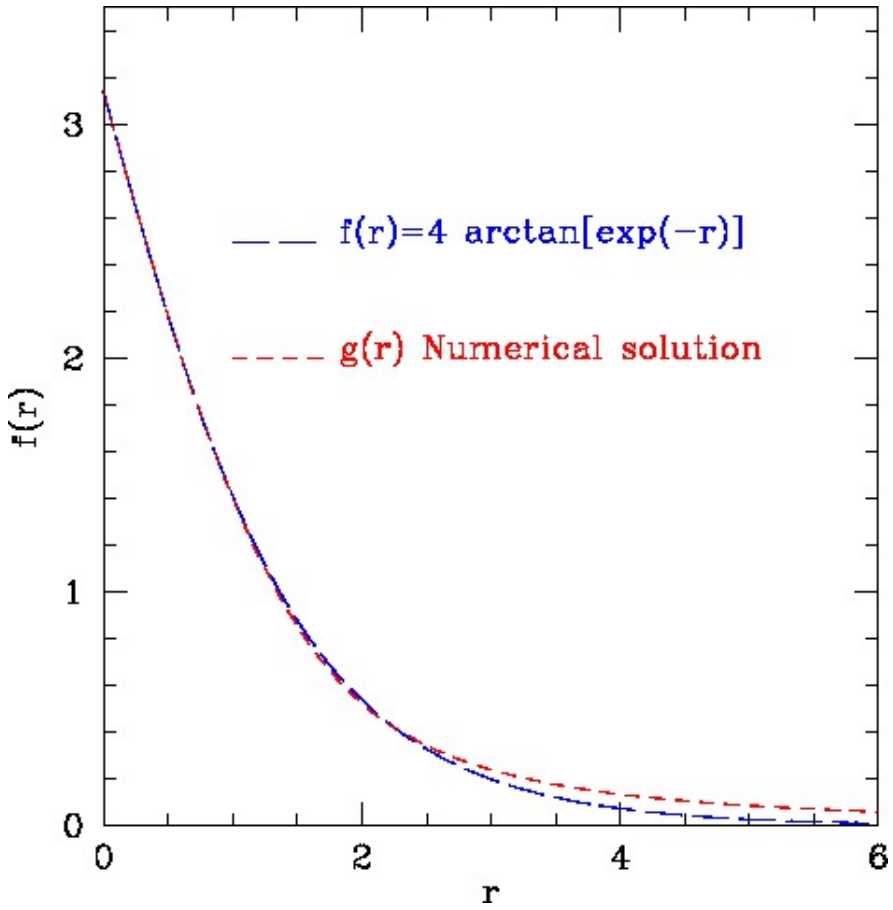

Figure 5.2: This figure displays the closed form radial profile function, $f(r)$ (5.19) (blue), and the numerical profile, $g(r)$ (red). The latter is calculated with a shooting parameter $g' = dg/dr = -2.008$ (with boundary condition at the origin $g_0 = \pi$). The $g(r)$ plot shows a subset of the full computations, which generally comprise discrete collections of points, r_p, $p = 1, \ldots, N$, where N is of the order of 1300, $r_1 = 0$ and $r_N \equiv r_{\max} \approx 300$ (i.e. only a small portion of the radial integration domain is shown here). The LSODA error tolerance is of the order of 1.0×10^{-7} which guarantees that the error in the profile function (r) is much smaller than the error of the evolved finite difference solutions that we subsequently generate. Note that the functions are almost identical near the origin. Both then rapidly fall off for $r \gtrsim 5$, departing from each other as $r \to \infty$, where the tail of $f(r)$ decays more rapidly than that of $g(r)$. The form of these profiles demonstrates manifestly the localized (particle-like) nature of the skyrmions. As for baby skyrmions, a natural length scale is defined by the size of the skyrmion, which appears to be ≈ 5 in radius (10 in diameter). We use this size to determine acceptable dimensions for our computational domains, noting that, as usual, the meaning of high (or low) resolution for a finite difference grid will always be relative to the natural scale.

kinetic, T and 3) potential, P. We also evaluate the integrals of these quantities over the solution domain, yielding values denoted by E, K and U, respectively. Computing the local energy density, T_{00}, is accomplished by first calculating the energy-momentum tensor, $\mathcal{T}_{\mu\nu}$, of the model using (4.44). As usual, $\mathcal{T}_{\mu\nu}$ describes the density and flow of the (local) 4-momentum. The local energy density, T_{00}, is then given by (5.33),

$$T_{00} = \mathcal{T}_{\mu\nu} U^{\mu} U^{\nu} = \mathcal{T}_{00} \,, \tag{5.33}$$

where $U^{\mu} = (1, 0, 0, 0)$ is the 4-velocity of a coordinate-stationary observer [141]. The calculation of the kinetic K and potential U energy densities follow from the decomposition of the Lagrangian density of the full Skyrme model (5.6) as $\mathcal{L} = K - U$, which is usually expressed in terms of the right $SU(2)$ valued-current R_{μ} introduced in Sec. 5 [155],

$$K = \int d^3x \;\; -\frac{1}{2}\mathrm{Tr}(R_0 \; R_0) - \frac{1}{4}\mathrm{Tr}([R_0 R_i, R_0 R_i]))\,, \tag{5.34}$$

and[33]

$$U = \int d^3x \;\; -\frac{1}{2}\mathrm{Tr}(R_i \; R_i) - \frac{1}{8}\mathrm{Tr}([R_j R_i, R_j R_i]))\,, \tag{5.35}$$

where the Latin index $i \ldots = 1, 2, 3$ runs over the spatial dimensions. Again, the specific expressions for T_{00}, K and U are calculated using symbolic manipulation—with currents R_{μ} written in terms of our sigma model dynamical fields, ϕ_a, as prescribed in Sec. 5.2—and then exported to Fortran 77, to be computed as separate grid functions in our code.

The total energy, E, is then calculated in complete analogy with the computation of B described above. Sub-integrals, E_I, are given by

$$\begin{aligned} E_I \;\; &= \;\; \int d^3x \;\; E = \frac{\Delta x \; \Delta y; \Delta z}{8} \sum_{i,j,k}^{N_x-1, N_y-1, N_z-1} [T_{00}]_{i,j,k} + [T_{00}]_{i+1,j,k} + [T_{00}]_{i,j,k+1} \\ &+ \;\; [T_{00}]_{i+1,j,k+1} + [T_{00}]_{i,j+1,k} + [T_{00}]_{i,j+1,k} + [T_{00}]_{i,j+1,k+1} + [T_{00}]_{i+1,j+1,k+1}\,, \end{aligned} \tag{5.36}$$

and then the E_I are summed to yield the value of E. Correspondingly, the subintegrals for K and

[33] The potential energy U is the sum of the spatial gradients and the potential function V.

U are calculated via

$$K_I = \int d^3x \;\; T = \frac{\Delta x \; \Delta y; \Delta z}{8} \sum_{i,j,k}^{N_x-1,N_y-1,N_z-1} [T]_{i,j,k} + [T]_{i+1,j,k} + [T]_{i,j,k+1} + [T]_{i+1,j,k+1} + [T]_{i,j+1,k} + [T]_{i,j+1,k} + [T]_{i,j+1,k+1} + [T]_{i+1,j+1,k+1} \,, \quad (5.37)$$

$$U_I = \int d^3x \;\; P = \frac{\Delta x \; \Delta y; \Delta z}{8} \sum_{i,j,k}^{N_x-1,N_y-1,N_z-1} [P_{00}]_{i,j,k} + [P_{00}]_{i+1,j,k} + [P_{00}]_{i,j,k+1} + [P_{00}]_{i+1,j,k+1} + [P_{00}]_{i,j+1,k} + [P_{00}]_{i,j+1,k} + [P_{00}]_{i,j+1,k+1} + [P_{00}]_{i+1,j+1,k+1} \,. \quad (5.38)$$

The K_I and U_I are summed to yield the values of K and U.

5.3 General Features of Skyrmion Scattering: Previous Work

This section provides a detailed summary of previous $3+1$ skyrmion numerical studies; these have been mentioned previously in Sec. 1.4.1. We will adopt the following notation to refer to the most common type of scattering that we consider here and in subsequent sections. SS denotes the collision of two skyrmions, each with topological charge B, while $S\bar{S}$ refers to the scattering of a skyrmion with charge B and an anti-skyrmion with charge $-B$.

We first need to say a few words about units. The values of the constants F_π and e, which appear in our Lagrangian density (5.3), are not relevant for our calculations, since we scaled them out in Sec. 5.2. However, we need their values when we compare with other works, which usually express length scales in femtometers (fm), and energy in MeV. To complicate matters, F_π and e vary greatly in the literature, depending on the phenomenological context of the model at hand. We will adopt the values of Sommermann et al. [86], i.e. $F_\pi = 128$ MeV and $e = 5.4$. Therefore, our time and length units (as stated before, $c = 1$ throughout this thesis) are $2/eF_\pi = 0.57$ fm, and for energy, $F_\pi/4e \approx 6$ MeV.

The most relevant numerical work in $3+1$ dimensions for this thesis includes (in chronological order):

- Verbaarschot, Walhout and Wambach (1986) [84] performed the first numerical work on

SS and $S\bar{S}$ collisions in axisymmetry, and included a pion mass term. Their choice of symmetry effectively reduces the problem to one in two spatial dimensions, and they adopt cylindrical coordinates, (ρ, z) for their calculations. Their motivation is to determine when collisions cease to show purely classical behaviour. They argue that the Skyrme model is a semi-classical approximation, and therefore, at sufficiently high energy, non-classical internal degrees of freedom are excited at a critical velocity $v^\star$—signalling semi-classical effects—and remain in this state after the interaction. By analyzing the elasticity of collisions as a function of the velocity, they determined the $v^\star$ when kinetic energy is no longer conserved.

Their implementation adopts a leap-frog scheme for the time evolution of the Hamiltonian equations of motion. The canonical momenta of the Skyrme fields are promoted to independent dynamical variables. However, no details about the finite difference discretization are provided. The chiral constraint is imposed by means of a Lagrange multiplier term.

Numerical experiments consisted of head-on encounters with initial velocities 0.2, 0.4 and 0.6. They discovered that elasticity is maintained below $v^\star = 0.39$ (150 MeV) [34] for SS collisions, and 75 MeV for $S\bar{S}$ pairs.

Calculations were performed on a grid with a resolution of 100×80 points in (ρ, z), with a mesh spacing $h = 0.075$, yielding a domain with dimensions $[0, 7.5]\times[-3, 3]$. The starting locations of the solitons were $z = -3$ and $z = 3$. The configurations evolved were the hedgehogs studied formerly by Adkins and Nappi [156], where the radius of the skyrmion is ≈ 5 [157, 27]. They report that stability restricts the Courant number to smaller values as one goes to higher energy. For instance, $\lambda = 0.1$ for $v = 0.2$–0.4 (35 and 150 MeV respectively) and $\lambda = 0.05$ for $v = 0.6$ (390 MeV). In an effort to improve stability, artificial viscosity is introduced. However, this modification results in undesirable side effects, such as the dissipation of E, which prevents the meaningful monitoring of the conservation of energy.

Radiation is observed at $v = 0.6$, and is dubbed "mesonic" waves. An important observation is that a $S\bar{S}$ pair with the internal phase $\Psi_1 = 0$ (see Sec. 5.2.4) does not annihilate, but forward scatters, while a value of $\Psi_1 = \pm\pi$ causes the configuration to end in annihilation (these results are consistent with ours in Sec. 4.9). It is customary to refer to the latter choice

[34] Its is customary for scattering calculations of the Skyrme model, in three dimensions, to characterize the collisions in terms of center of mass energy (i.e. the lab frame where our experiments are described) expressed in MeV. We will adopt this standard, and will also specify the velocity of the collisions. We remind the reader that, in this chapter, unless we clearly state that we using MeV, the default units of energy are the ones adopted in Sec. 5.2, $F_\pi/4e$.

of internal phase as the *annihilation channel*.

- Allder, Koonin, Seki and Sommermann (1987) [85] pioneered the first true $3+1$ numerical calculations of head-on SS collisions, motivated by the possibility of computing cross sections for baryon resonance and meson production. They study SS collisions at various impact parameters, for center-of-mass energies of 157 MeV ($v = 0.402$), 432 MeV ($v = 0.603$), and 885 MeV ($v = 0.75$). Their main result is that the inelasticity of the interaction is a function of the impact parameter, b, as is the deflection angle. Head-on SS collisions appear to be elastic, while off-axis encounters excite rotational and vibrational modes.

  Similarly to [84], they formulate their equations of motion from a Hamiltonian, and spatially discretize in a uniform Cartesian grid using second order centred stencils. Time stepping is achieved by means of a staggered leap-frog method. A Lagrange multiplier term is added to the Lagrangian density to impose the chiral constraint. No pion mass or potential terms are included. By (chiral) symmetry arguments, they restrict the computation to just one quadrant of the total domain. The mesh size in this quadrant is $41 \times 41 \times 21$, with $h = 0.084$ fm (0.14 in our units), corresponding to dimensions $[0, 3.36] \times [0, 3.36] \times [0, 1.68]$ fm ($[0, 5.89] \times [0, 5.89] \times [0, 2.94]$ in our units). From the information provided we can infer that their total domain dimensions are $[0, 11.78] \times [0, 11.78] \times [0, 2.94]$. They do not specify the size of their skyrmion, but from their references it is likely they used a radius $\approx$ 2–3 fm ($\approx$ 3.5–5 in our units). The baryon number density of the skyrmion shown has a diameter of ≈ 1 fm (1.7 our units). As reported by Verbaarschot et al [84], the Courant number λ is constrained to small values in the range from 0.075 to 0.013, in order to keep the evolution stable.

  Wambach [28] discusses Allder et al's [85] physics and numerical setup in further detail, and from a pedagogical perspective.

- Crutchfield and Bell (1991) [1] represents one of the studies most relevant for this thesis, and was largely motivated by the numerical instabilities observed in Allder et al [85] and Verbaarschot et al [84]. We have already described this work in detail in Sec. 4.5.

- Crutchfield, Snyderman and Brown (1992) [83] simulated the classical evolution of bound-state $B = 2$ solutions, with the aim of reproducing properties of the deuteron. They found that pairs of skyrmions (SS) in the maximally attractive channel ($\Psi = 1$) form bound states after some time, allowing the detailed measurement of certain phenomenological parameters.

Their calculations use a numerical grid with $56 \times 56 \times 28$ points, which translates to a domain box with dimensions $[0, 8] \times [0, 8] \times [0, 4]$. Following Allder et al [85], they take advantage of symmetry properties to reduce the actual computational domain dimensions to $[0, 4] \times [0, 4] \times [0, 4]$, with $h = 0.07$ and a Courant number $\lambda = 0.5$. They implemented the predictor-correct scheme developed in [1] (See Sec. 4.5). The radius of the skyrmion used can be inferred from information in the paper to be ≈ 2 fm (≈ 3.5 our units). The use of viscous "attenuation" is briefly mentioned. Notwithstanding the low velocity of these interactions, they are illustrative of the trends in numerical methods in this area, since stability is largely improved, allowing for larger values of the Courant number, λ.

- Battye and Sutcliffe (1996) [25] is an important reference for us, since our initial data setup (Sec. 5.2.4) and equations of motion (Sec. 5.2) follows their work closely. They studied scattering of multi-soliton skyrmions for $B = 1, 2, 3$ and 4, with spherical, toroidal and tetrahedral baryon density topologies. Right angle scattering is observed in SS collisions of $B = 1$ skyrmions with an internal phase difference (See Sec. 5.2.4) of $\Psi_1 = \pi$. An intermediate $B = 2$ toroidal bound state is formed at the collision point, before the skyrmions separate and exit at right angles. The interaction is basically elastic, with little or no radiation observed. Additional experiments are shown, notably a collision among three $B = 1$ skyrmions (which we may denote SSS), each located at a different vertex of an equilateral triangle. The end state consists of a $B = 1$ spherical skyrmion, and a $B = 2$ toroidally shaped one. The focus of this work is to obtain end state configurations of minimal energy, as potential candidates for approximations to nuclei (as well as for other applications). A dissipative term added to the equations of motion guarantees that such configurations can relax in a computationally reasonable time.

  The Lagrangian equations of motion are discretized with fourth order finite difference stencils in space, and a leap-frog time stepping method is used. The fields equations are cast in first order form, using auxiliary fields $\pi_a = \dot{\phi}_a$. Dirichlet conditions are used, and the chiral constraint is imposed through a combination of reprojection and a Lagrange multiplier term (see Sec. 5.2.3).

  Collisions were performed between pairs of identical skyrmions with different values of total baryon number B, and starting locations of their centres at $(0, 0, 1.5)$ and $(0, 0, -1.5)$. Velocities are restricted to $v = 0.17$ and $v = 0.3$, a choice justified by the authors in light of the

breakdown of hyperbolicity conjectured by Crutchfield and Bell [1].

The dynamical domain is discretized by means of uniform Cartesian meshes, of sizes $70 \times 70 \times 70$ and $100 \times 100 \times 100$ lattice points, with a grid spacing $h = 0.1$, and Courant numbers in the interval $0.1 \leq \lambda \leq 0.2$. This again corresponds to maximum domain sizes of $[-5, 5] \times [-5, 5] \times [-5, 5]$. A priori, this appears puzzling, since as we have noted above (see Fig. 5.2), the radius of the static skyrmion is ≈ 5. The size of the computational domain thus does not seem large enough to contain two well-separated skyrmions. However, it is possible that the authors were only concerned with the size as defined by the localization of the baryon density, which is significantly smaller.

- Battye and Sutcliffe (2001) [26] studied clusters of static skyrmions with a total $B \leq 22$, producing complex end states resembling Fullerenes [26]. A dissipative term is added to the equations of motion in order to remove kinetic energy of the system, thus allowing a quick relaxation of the skyrmion clusters into Fullerene structures, which are the focus of their work.

  Other than the above considerations, their numerical setup is identical to the one described in [25]. Results were obtained on Cartesian grids $100 \times 100 \times 100$ and $200 \times 200 \times 200$ lattice points, a Courant number of $\lambda = 0.1$, and grid spacings $h = 0.1$ and $h = 0.2$. This corresponds to a maximum domain size $[-10, 10] \times [-10, 10] \times [-10, 10]$. Again, the size (in radius) of the skyrmion is ≈ 5.

5.4 Skyrmion Head-on Collisions

In this section we describe our AMR calculations of SS head-on scattering of skyrmions in three spatial dimensions. We perform computations in both the attractive ($\Psi_1 = \pi$) and repulsive ($\Psi = 0$) channels. Our aim is to describe the generic phenomenology of these interaction types. Again, we stress that these results are preliminary, in the sense that we do not have the same evidence for convergence as we do for the $2 + 1$ case. Specifically, lack of sufficient computer resources has prevented us from establishing definitive convergence behaviour for our computations, and, as described in Sec. 3.6, it is difficult for us to perform convergence tests when AMR is used.

Fig. 5.3 shows the evolution of the baryon number density, $B_0(t, x, y, 0)$ (i.e. the $z = 0$ plane of the 3D data set), for a SS head-on collision in the repulsive channel ($\Psi_1 = 0$). A boost

factor $\gamma = 1.6$ ($v = 0.8$) was used for each skyrmion. Fixing other parameters, we performed computations for several velocities, ranging from $v = 0.3$ to $v = 0.9$. In all cases we found the same generic phenomenology, i.e. forward scattering with no visible radiation present.

We then carried out runs in the attractive channel ($\Psi_1 = \pi$) using the same interval of velocities. In this case we found right-angle scattering for all initial boosts, again with minimal or no radiation present. Fig. 5.4 shows $B(t, x, y, 0)$ for $\gamma = 1.6$: results for the other values of γ used appear very similar.

The calculations described above, for both the repulsive and attractive channels, were performed with a relatively large truncation error threshold of $\tau_{\max} = 1 \times 10^{-2}$. These generated a hierarchy of grids with a finest level $L_f = 5$, (Figs.5.6 and 5.5), with a base grid of $65 \times 65 \times 65$. Not surprisingly, setting a more stringent value of $\tau_{\max} = 6 \times 10^{-3}$ causes the AMR algorithm to introduce additional levels so that, as illustrated in Fig. 5.7, the finest level is $L_f = 7$.

5.5 Conclusions and Future Developments

In summary, we have performed a preliminary study of head-on skyrmion-skyrmion collisions. The computations involved both the attractive and repulsive channels and were carried out for a range of initial velocities. The observed phenomenology is consistent with that reported in previous work [25, 85, 28]. It is also similar to what we have seen for the scattering of $2 + 1$ baby skyrmions as described in Chap. 4. It would be interesting to extend our studies to include skyrmion-antiskyrmion $S\bar{S}$ scattering, as well as more general off-axis collisions.

Once more we emphasize that these results are preliminary, since limitations in computer resources have prevented us from establishing definitive convergence of our unigrid computations. This naturally provides one direction for future improvement of our code. Specifically we could try to optimize those portions of the code which dominate execution time.

Clearly the issue of a transition from pure hyperbolic to mixed elliptic-hyperbolic behaviour is still of central interest—as it was for the baby Sykrme case—not least since the "full" model is actually of phenomenological interest. Our experience is that high resolution is essential in firmly establishing any such transition, through, for example, monitoring of the behaviour of the total energy. Thus, although the results from Chap. 4, as well as the experiences of other researchers, suggest that we should expect a breakdown of hyperbolicity, additional work with our code could

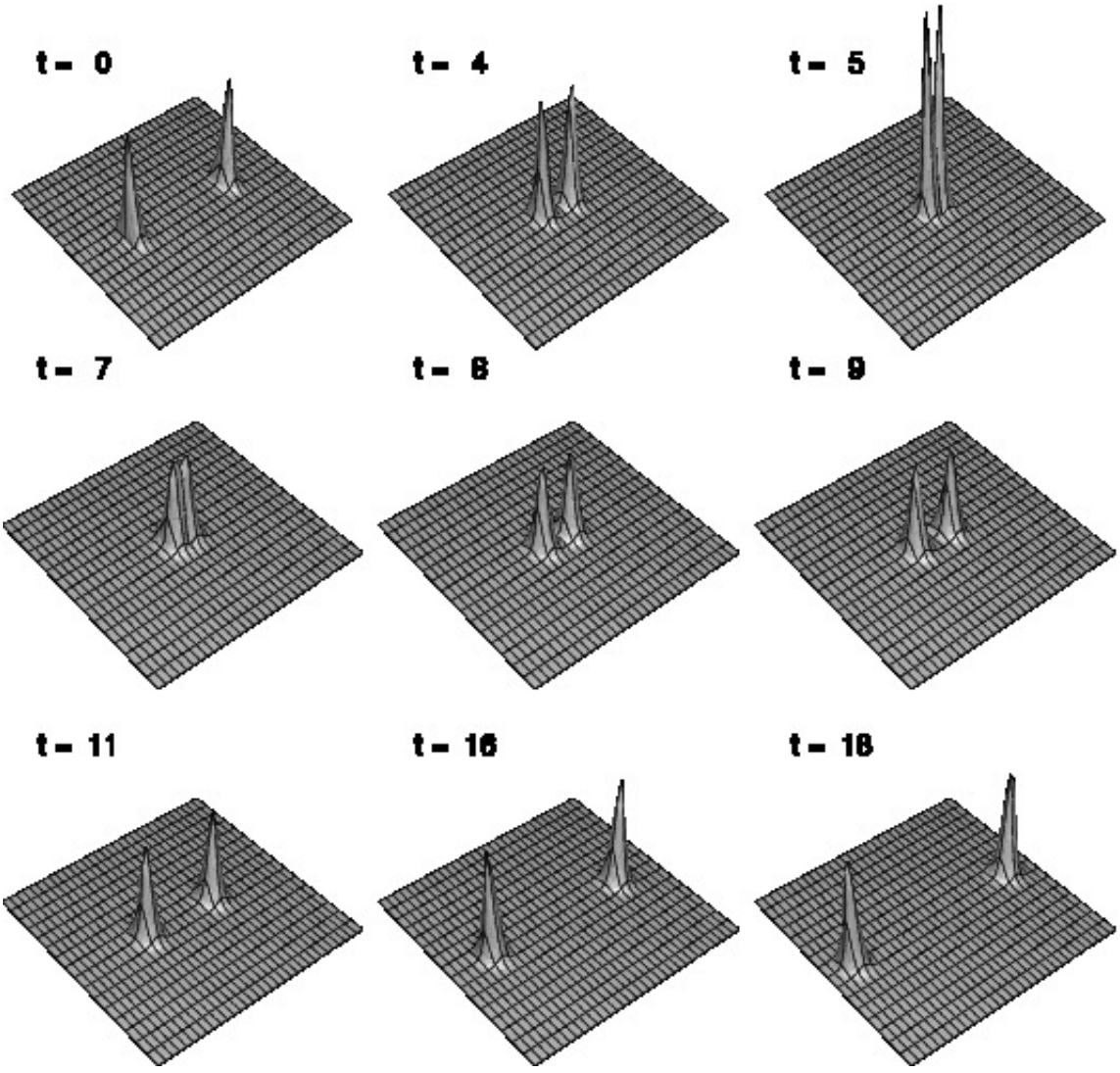

Figure 5.3: AMR calculation of the evolution of the baryon number density, $B_0(t, x, y, 0)$ (i.e. the $z = 0$ plane), for a SS head-on collision in the repulsive channel, $\Psi_1 = 0$, at $\gamma = 1.6$ ($v = 0.8$). The interaction displays forward scattering, and no radiation is visible. A maximum of 5 AMR levels ($L_f = 5$) was used in the calculation. The domain is $[-9, 9] \times [-9, 9] \times [-9, 9]$, and at this velocity the skyrmions have a diameter ≈ 6.25 in the x direction. We used $\tau_{\max} = 1 \times 10^{-2}$ on a $65 \times 65 \times 65$ base grid, with Dirichlet boundary conditions. Other parameters for the run are: $\epsilon_{\rm KO} = 0.4$, and $\lambda = 0.1$. The skyrmions are initially centred at $(x_0^{(1)}, y_0^{(1)}, z_0^{(1)}) = (-4.5, 0, 0)$ and $(x_0^{(2)}, y_0^{(2)}, z_0^{(2)}) = (4.5, 0, 0)$.

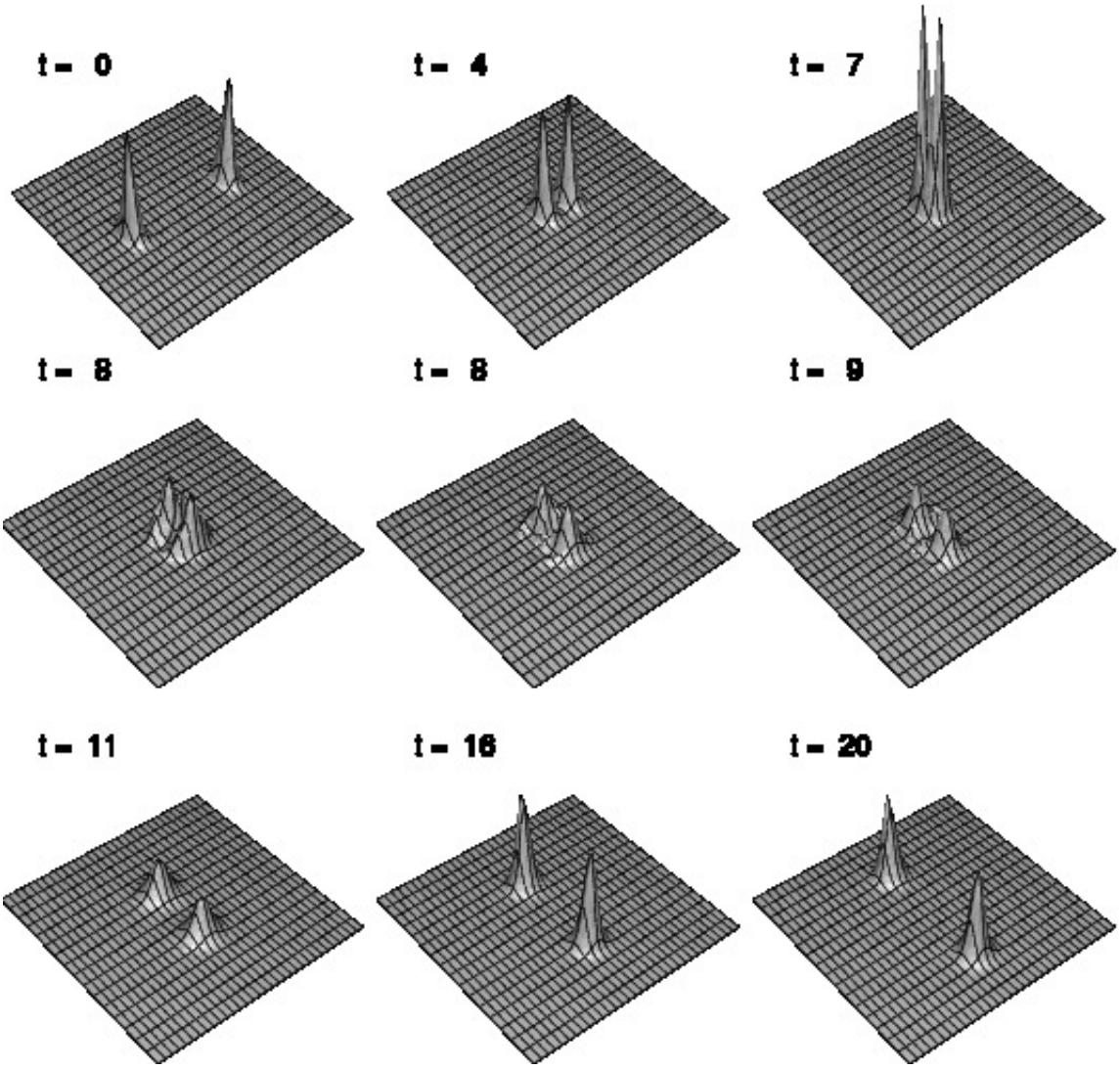

Figure 5.4: AMR calculation of the evolution of the baryon number density, $B_0(t, x, y, 0)$ (i.e. the $z = 0$ plane), for a SS head-on collision in the attractive channel, $\Psi_1 = \pi$, at $\gamma = 1.6$ ($v = 0.8$). The interaction displays forward scattering, and no radiation is visible. All additional parameters for the run are identical to those described in the caption of the previous figure (Fig. 5.3).

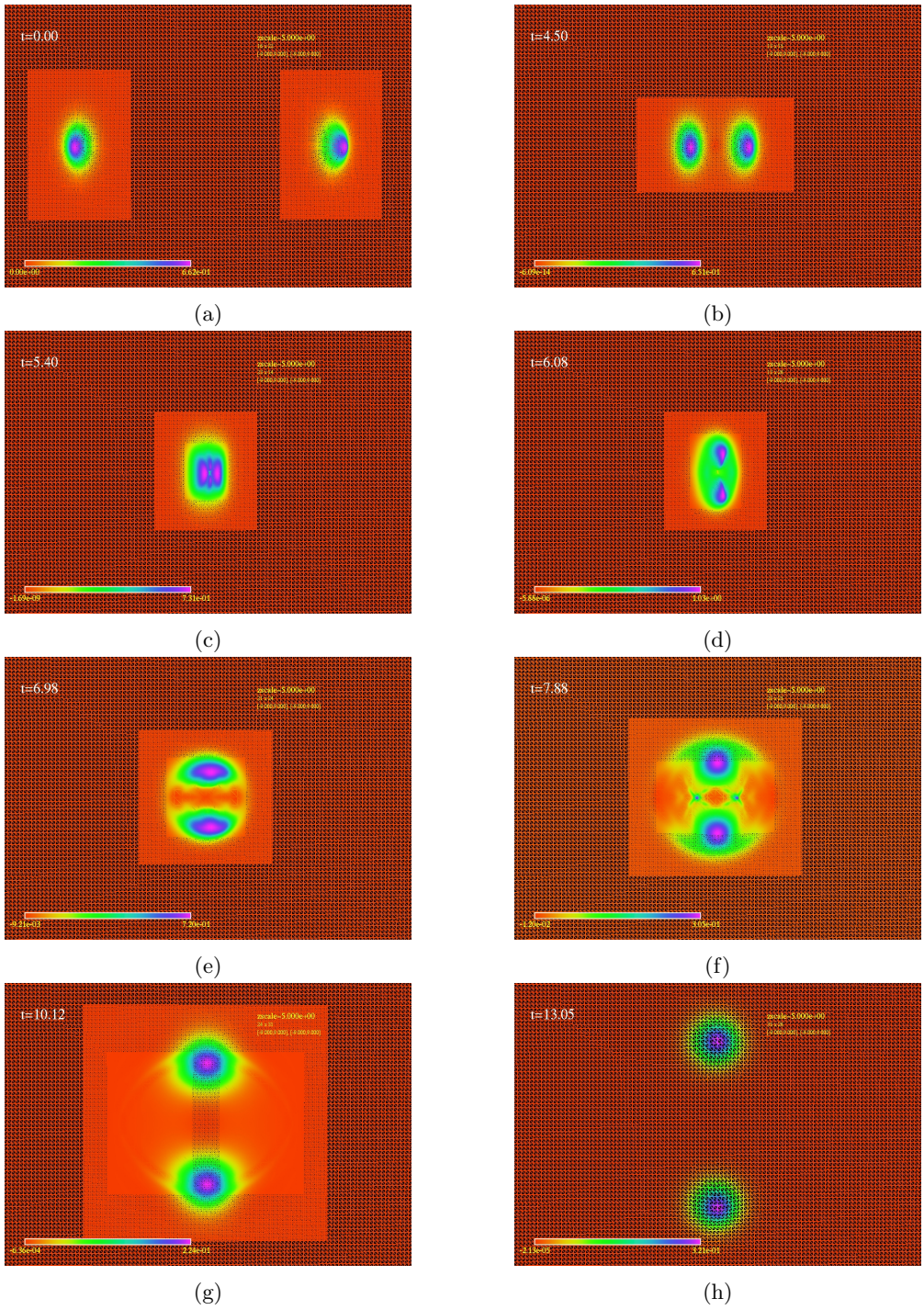

Figure 5.5: Wire-mesh contour plot of the evolution of the baryon density, B_0, as previously shown in Fig. 5.4. The slice corresponding to the collision plane $z = 0$ is shown. The figure shows the time-development of a typical adaptive mesh refinement hierarchy. Finer level grids are difficult to distinguish due to resolution limitations of the figure, as well as the fact that finer grids generally have small extent. For instance, we can identify 3 different levels in images (c)–(g), while there are actually $L_f = 5$ levels at that time.

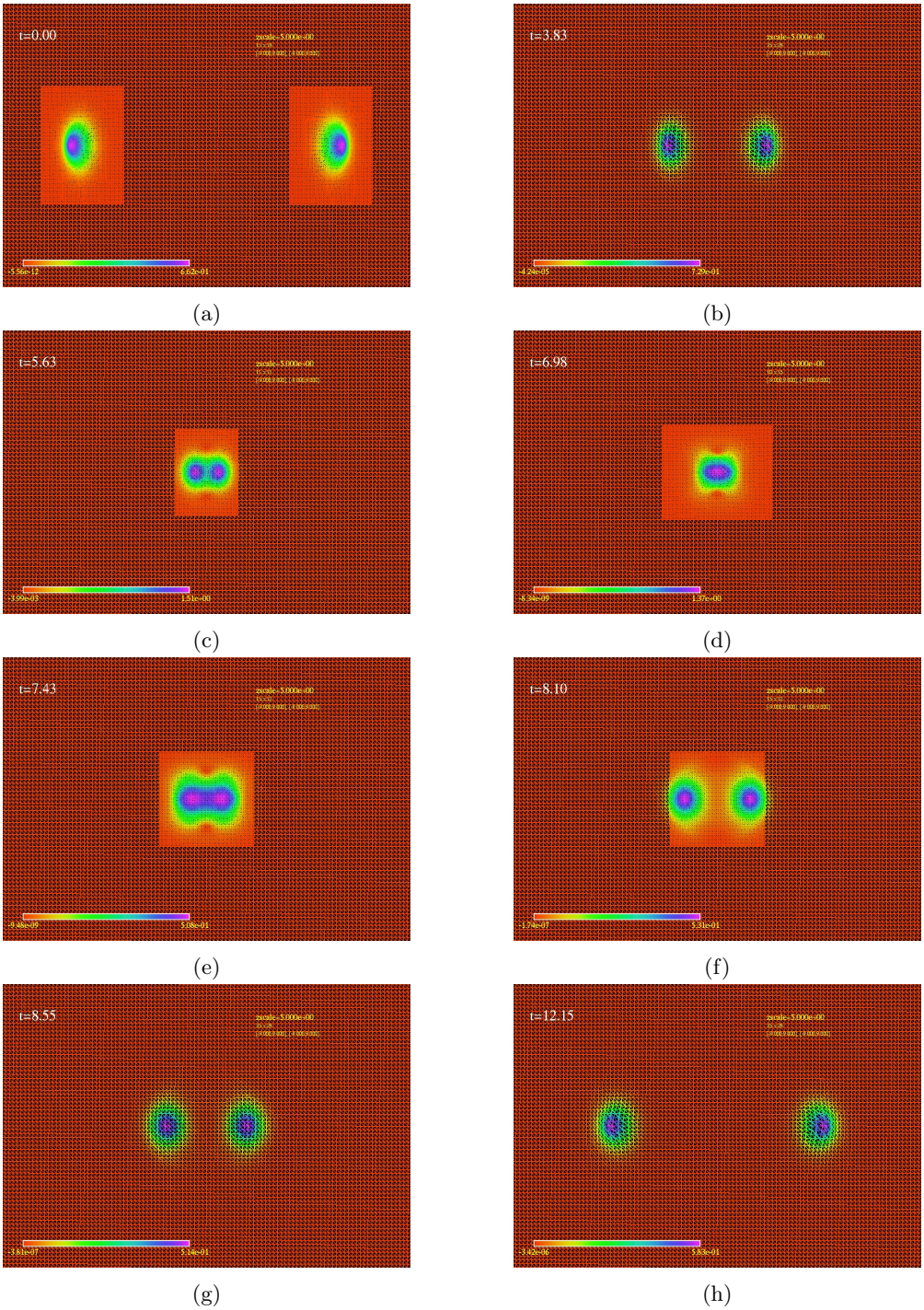

(a) (b) (c) (d) (e) (f) (g) (h)

Figure 5.6: Wire-mesh contour plot of the evolution of the baryon density, B_0, as previously shown in Fig. 5.3. Comments made in the caption of the previous figure (Fig. 5.5) also apply here.

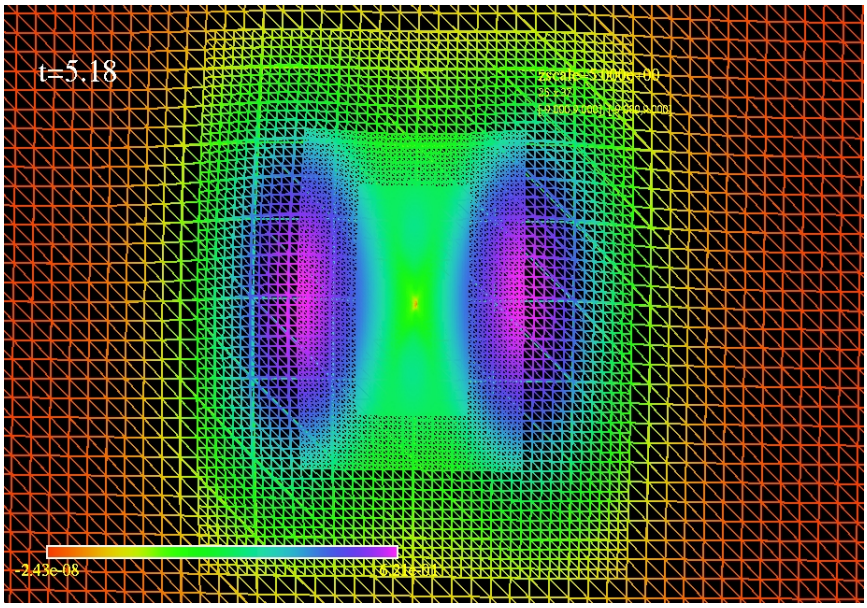

(a)

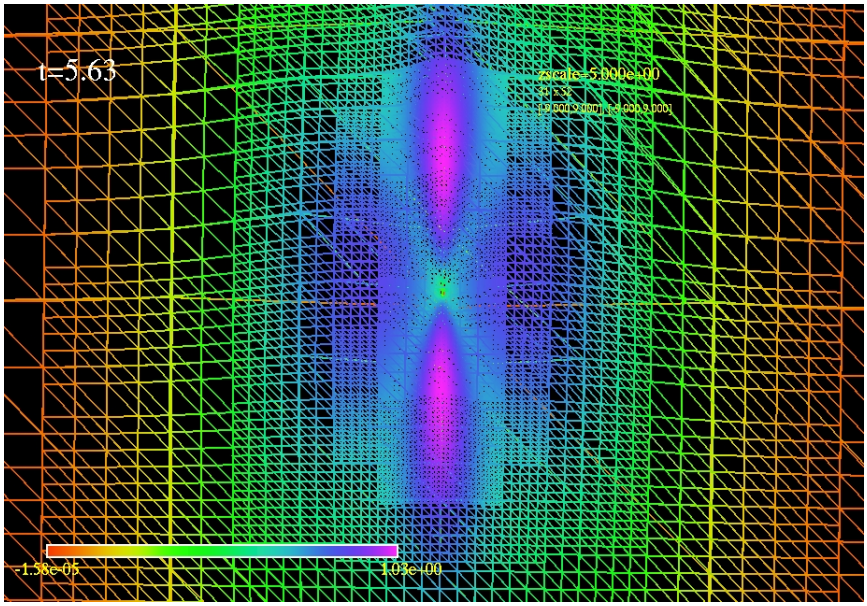

(b)

Figure 5.7: These figures illustrate the AMR hierarchy of grids at two instants of time for the initial data described in Fig. 5.3. Here, however, we have computed with a truncation error threshold $\tau_{\max} = 6 \times 10^{-3}$, and the maximum level of refinement is $L_f = 7$. All additional parameters are as listed in the caption of Fig. 5.3.

shed more light on the subject.

CHAPTER 6

CONCLUSIONS

We now summarize the main results and conclusions stemming from the work reported in this thesis.

Chap. 2 described the development of a computational framework used to construct finite-difference codes for the approximate solution of hyperbolic PDEs. Parallelization and adaptive mesh refinement (AMR) capabilities were provided by the incorporation of a specific implementation of the Berger-Oliger algorithm [120, 121, 107, 108].

Primarily to test this framework, in Chap. 3 we studied a theory describing the dynamics of a complex scalar field theory that possesses stable, localized (solitonic) solutions called Q-balls. We analyzed some aspects of the dynamics of Q-balls, focusing on two main scenarios: collisions between Q-balls having opposite charges, $Q^+\ Q^-$, and those between configurations with the same charge, $Q^+\ Q^+$. The observed interactions during the collision were qualitatively different for the two scenarios: $Q^+\ Q^-$ interactions exhibited purely constructive interference, whereas $Q^+\ Q^+$ collisions showed destructive interference patterns. Some phenomenology of $Q^+\ Q^+$ scattering had been previously reported [18], and we were able to reproduce these results. However, to the best of our knowledge, the $Q^+\ Q^-$ work was original. Our key findings were that the $Q^+\ Q^-$ collisions resulted in bound states for $v \lesssim 0.4$, while producing purely forward scattering at any higher velocity.

We also investigated the dynamics of Q-balls for different values of their charge. We found that right-angle scattering was completely absent from the dynamics of sufficiently low-charge Q-balls. Additionally, we studied scattering of Q-balls against potential obstructions, and we discovered that it was characterized by a combination of transmission and reflection of the soliton.

Chap. 4 reports our main contributions; these come from a detailed study of the dynamics of the baby Skyrme model. Particular emphasis was placed on the exploration of the rich phenomenology of the collisions of two baby skyrmions or of a baby skyrmion-antiskyrmion pair. The investigation of a loss of hyperbolicity (well-posedness) for certain configurations—as suggested by Crutchfield

and Bell [1, 26, 95]—was of central interest. By monitoring the behavior of the total energy, and by directly examining the numerical solutions, we provided strong evidence that the evolution of highly boosted baby skyrmion collisions becomes ill-posed. As discussed in App. C.2, corroborating evidence for the loss of hyperbolicity was provided by the appearance of complex eigenvalues computed in the context of a normal mode analysis for a particular linearization of the equations of motion.

Our experiments also suggest that consideration of global and local values of energy quantities alone is not sufficient to determine when well-posedness is lost. We present this chiefly as an observation: claims in the literature (see e.g Crutchfield and Bell's [1]) are not obviously inconsistent with what we have seen.

Importantly, since we demonstrated that our code converged in strong-field cases where hyperbolicity was maintained, but where small changes in initial data parameters (i.e. the initial boost parameter, γ) resulted in a loss of convergence, we are confident that the observed behavior with respect to well-posedness is not due to the finite-difference scheme that was used (i.e. it is not a "numerical artifact").

As previously emphasized by Crutchfield and Bell, the loss of hyperbolicity implies a breakdown of the physical applicability of the Skyrme model. At least heuristically, one can argue that this is perhaps not unexpected given that the model can be viewed as an effective-field approximation of a more fundamental underlying theory, in which high-frequency degrees of freedom have been integrated out. Whether or not hyperbolicity can be restored through modifications of the (effective) Lagrangian and, if so, whether the resulting models will produce a more accurate description of nucleon interactions, remain open questions.

In addition, our experiments provided further understanding of the general phenomenology of collisions in the baby Skyrme model. For instance, previous studies had indicated that the highest-energy skyrmion collisions (before the evolutions become ill-posed) were not very elastic, since they were apparently always accompanied by the emission of large amounts of radiation. However, our calculations with AMR showed reduction of these effects relative to unigrid computations, suggesting that at least some of the previously observed non-elasticity was due to insufficient finite-difference resolution.

In Sec. 4.3.3 we studied two different techniques for maintaining the constraint, $\phi^a \phi^a = 1$, that must be satisfied by the baby Skyrme fields. One was a simple reprojection that was found to

be very robust and which was used almost exclusively in our numerical experiments. The other was based on the idea of constraint damping and, provided that the two adjustable parameters characterizing the method were chosen judiciously, also worked well.

Finally, in Chap. 5 we presented preliminary results for the head-on scattering of skyrmions in three spatial dimensions. Although computer resource limitations prevented us from establishing definitive convergence behaviour for unigrid computations, the phenomenology that we observed (using AMR calculations) was consistent with previous studies [85, 28, 26].

In terms of the numerical schemes employed, the use of an implicit two-level Crank-Nicholson scheme for the temporal discretization of the equations of motion (for all the models studied in this thesis), yielded good stability properties. In particular, our unigrid calculations were stable for Courant numbers as large as $\lambda = 0.5$. This is an improvement relative to some of the earlier numerical work [85, 84], where use of explicit schemes restricted the Courant number to excessively small values.

We note that our methodology and computational infrastructure could be readily adapted to study similar phenomena in theories including 1) sigma models (oscillons [80] and sphalerons [158]), and 2) extensions of the Skyrme model, such as the Skyrme-Fadeev-Hopf theory [159]. In particular, it is reasonable to expect that solutions in the latter case will also exhibit a configuration-dependent breakdown of hyperbolicity: investigation of this conjecture would be worthwhile.

The Einstein-Skyrme model in spherical symmetry [160] has been shown to display interesting behaviour at the threshold of black-hole formation (critical phenomena), and our studies can be seen as a preliminary step towards extension of those calculations to the full 3D case.

We conclude by observing that topological skyrmions continue to be studied vigorously, and that detailed numerical experimentation will become an increasingly valuable tool in such work. For example, skyrmions emerge as holographic baryons in certain limits of five-dimensional gravity-gauge duals, and provide a calculational framework for the strong coupling regime [46]. Branes with low energy (effective) descriptions in terms of solitons have also been studied intensively in recent years [161]. Finally, it is not unreasonable to expect that a thorough understanding of collisions of self-gravitating relativistic skyrmions—or similar solitons—may shed light on many issues at the crossroads of space-time singularity formation, astrophysics and exotic nonlinear physics [162].

BIBLIOGRAPHY

[1] William Y. Crutchfield and John B. Bell. Instabilities of the Skyrme model. *J. Comput. Phys.*, 110:234–241, 1994.

[2] Thierry Dauxois and Michel Peyrard. *Physics of Solitons*. Cambridge, UK: Univ. Pr. (2006) 422 p.

[3] Alan C. Newell. *Solitons in Mathematics and Physics*. SIAM (1985) 245 p.

[4] A.T. Filippov. *The Versatile Soliton*. 2000.

[5] Johnson R.S. Drazin, P.G. *Solitons, an Introduction*. Cambridge Texts in Applied Mathematics, UK: Univ. Pr. (1989) 226 p.

[6] J. Scott Russell. Report on Waves. *Report of the fourteenth meeting of the British Association for the Advancement of Science, York, September 1844*, London:311–390, Plates XLVII–LVII, 1845.

[7] Markus Heyerhoff. The history of the early period of soliton theory. 1997. http://www.solitons.de/Review.htm, Retrieved May 28, 2013.

[8] Zabusky Norman J. Hu Bambi Porter, Mason A. and David K Campbell. Fermi, Pasta, Ulam and the Birth of Experimental Mathematics. *American Scientist*, 97(3):214, 2009.

[9] Thierry Dauxois. Fermi, Pasta, Ulam and a mysterious lady. *Physics Today*, 61(1):55–57, 2008.

[10] N. J. Zabusky and M. D. Kruskal. Interaction of "solitons" in a collisionless plasma and the recurrence of initial states. *Phys. Rev. Lett.*, 15:240–243, Aug 1965.

[11] R. MacKenzie, (ed.), Manu B. Paranjape, (ed.), and W. J. Zakrzewski. *Solitons: Properties, dynamics, interactions, applications. Proceedings, Workshop, Kingston, Canada, July 20-26, 1997*. New York, USA: Springer (1999) 312 p.

[12] E.A. Kuznetsov, A.M. Rubenchik, and V.E. Zakharov. Soliton Stability in Plasmas and Hydrodynamics. *Phys.Rept.*, 142:103–165, 1986.

[13] Constantin A. and D. Henry. Solitons and Tsunamis. *Z. Naturforsch*, 64a:65–68, 2009.

[14] T. H. R. Skyrme. A Unified Field Theory of Mesons and Baryons. *Nucl. Phys.*, 31:556–569, 1962.

[15] V. G. Makhankov, Y. P. Rybakov, and V. I. Sanyuk. *The Skyrme model: Fundamentals, methods, applications*. Berlin, Germany: Springer (1993) 265 p. (Springer series in nuclear and particle physics).

[16] Valery I. Sanyuk. Genesis and evolution of the Skyrme model from 1954 to the present. *Int. J. Mod. Phys.*, A7:1–40, 1992.

[17] E.M. Nyman and D.O. Riska. Low-Energy Properties of Baryons in the Skyrme Model. *Rept.Prog.Phys.*, 53:1137–1182, 1990.

[18] Minos Axenides, Stavros Komineas, Leandros Perivolaropoulos, and Manolis Floratos. Dynamics of nontopological solitons: Q balls. *Phys. Rev.*, D61:085006, 2000.

[19] T. H. R. Skyrme. A Nonlinear field theory. *Proc. Roy. Soc. Lond.*, A260:127–138, 1961.

[20] N. S. Manton and P. Sutcliffe. *Topological solitons*. Cambridge, UK: Univ. Pr. (2004) 493 p.

[21] A. Alonso Izquierdo et al. Lectures on the mass of topological solitons. 2007.

[22] Alfred Seeger. Solitons. pages 702–716, 2009.

[23] Sidney R. Coleman. Classical Lumps and their Quantum Descendents. *Subnucl. Ser.*, 13:297, 1977.

[24] Tanmay Vachaspati. *Kinks and domain walls: An introduction to classical and quantum solitons*. Cambridge, UK: Univ. Pr. (2006) 176 p.

[25] Richard A. Battye and Paul M. Sutcliffe. Multi-soliton dynamics in the Skyrme model. *Phys. Lett.*, B391:150–156, 1997.

[26] Richard A. Battye and Paul M. Sutcliffe. Skyrmions, fullerenes and rational maps. *Rev. Math. Phys.*, 14:29–86, 2002.

[27] I. Zahed and G. E. Brown. The Skyrme Model. *Phys. Rept.*, 142:1–102, 1986.

[28] J. Wambach. From skyrmions to the nucleon-nucleon potential. In H. von Geramb, editor, *Quantum Inversion Theory and Applications*, volume 427 of *Lecture Notes in Physics*, pages 365–381. Springer Berlin / Heidelberg, 1994.

[29] G. H. Derrick. Comments on Nonlinear Wave Equations as Models for Elementary Particles. *Journal of Mathematical Physics*, 5:1252–1254, September 1964.

[30] R.H. Hobart. On the instability of a class of unitary field models. *Proceedings of the Physical Society*, 82(2):201, 1963.

[31] R. Rajaraman. *Solitons and Instantons. An introduction to Solitons and Instantons in Quantum Field Theory*. Amsterdam, Netherlands: North-holland (1982) 409p.

[32] Yang Yi Song. *Solitons in Field Theory and Non-linear Analysis*. Springer monographs in mathematics. Springer, New York, NY, 2001.

[33] Alexander M. Polyakov and A. A. Belavin. Metastable States of Two-Dimensional Isotropic Ferromagnets. *JETP Lett.*, 22:245–248, 1975.

[34] John Preskill. Vortices and Monopoles. Lectures presented at the 1985 Les Houches Summer School, Les Houches, France, Jul 1 - Aug 8, 1985.

[35] T. Weidig. The baby Skyrme models and their multi-skyrmions. *Nonlinearity*, 12:1489–1503, November 1999.

[36] M. Nakahara. *Geometry, topology and physics*. Boca Raton, USA: Taylor and Francis (2003) 573 p.

[37] S. V. Ketov. *Quantum nonlinear sigma models: From quantum field theory to supersymmetry, conformal field theory, black holes and strings*. Berlin, Germany: Springer (2000) 420 p.

[38] Nicholas S. Manton. Solitons as elementary particles: a paradigm scrutinized. *Nonlinearity*, 21(11):T221–T232, Nov 2008.

[39] J. K. Perring and T. H. R. Skyrme. A Model unified field equation. *Nucl. Phys.*, 31:550–555, 1962.

[40] Ivan Christov and C.I. Christov. Physical dynamics of quasi-particles in nonlinear wave equations. *Physics Letters A*, 372(6):841 – 848, 2008.

[41] Igor R. Klebanov. The Skyrme model. 1997. Lectures, QCD and Hadron Structure, June 9th-llth, 1992, Kloster Banz, Germany.

[42] Robert Vihn Mau. The theory of the nucleon-nucleon interaction. pages 1–38, 2001.

[43] Edward Witten. Baryons in the 1/N Expansion. *Nucl. Phys.*, B160:57, 1979.

[44] Gregory S. Adkins, Chiara R. Nappi, and Edward Witten. Static Properties of Nucleons in the Skyrme Model. *Nucl.Phys.*, B228:552, 1983.

[45] Michal Praszalowicz. Pentaquark in the Skyrme model. *Phys.Lett.*, B575:234–241, 2003.

[46] Gerald E. Brown and Mannque Rho. *The Multifaceted Skyrmion*. 2009.

[47] Michael P. Mattis and Marek Karliner. Baryon spectrum of the Skyrme model. *Phys. Rev. D*, 31:2833–2848, Jun 1985.

[48] J. Schechter and H. Weigel. The Skyrme model for baryons. 1999. Invited review article for INSA-Book-2000.

[49] Herbert Weigel. Chiral Soliton Models for Baryons. *Lect.Notes Phys.*, 743:1–274, 2008.

[50] Timothy S. Walhout and Jochen Wambach. From Skyrmions to the nucleon-nucleon potential. *Int. J. Mod. Phys.*, E1:665–738, 1992.

[51] Yu.P. Rybakov and V.I. Sanyuk. Topological Skyrmions. 1981.

[52] N. S. Manton. Classical Skyrmions – Static Solutions and Dynamics. 2011.

[53] G. Holzwarth and B. Schwesinger. Baryons in the Skyrme Model. *Rept. Prog. Phys.*, 49:825, 1986.

[54] Juha Jaykka and Martin Speight. Easy plane baby skyrmions. *Phys. Rev.*, D82:125030, 2010.

[55] B. M. A. G. Piette, B. J. Schroers, and W. J. Zakrzewski. Dynamics of baby skyrmions. *Nucl. Phys.*, B439:205–238, 1995.

[56] A. E. Kudryavtsev, B. Piette, and W. J. Zakrzewski. Mesons, baryons and waves in the baby Skyrmion model. *Eur. Phys. J.*, C1:333–341, 1998.

[57] Frank Wilczek and A. Zee. Linking Numbers, Spin, and Statistics of Solitons. *Phys.Rev.Lett.*, 51:2250, 1983.

[58] W. J. Zakrzewski. *Low Dimensional Sigma Models*. Bristol, UK: Hilger (1989) 289p.

[59] A. M. Din and W. J. Zakrzewski. Skyrmion Dynamics in $(2+1)$-Dimensions. *Nucl. Phys.*, B259:667, 1985.

[60] R.S. Ward. Sigma models in 2+1 dimensions, 1994.

[61] R. A. Leese. Q lumps and their interactions. *Nucl. Phys.*, B366:283–314, 1991.

[62] X. C. Xie and Song He. Skyrmion excitations in quantum Hall systems. *Phys. Rev. B*, 53:1046–1049, Jan 1996.

[63] Oliver Schwindt and Niels R. Walet. Towards a phase diagram of the 2D Skyrme model. *Europhys. Lett.*, 55:633–639, 2001.

[64] Carsten Timm. A new twist in a ferromagnet. *Physics*, 2:35, May 2009.

[65] S. M. Girvin. Course 2: The Quantum Hall Effect: Novel Excitations and Broken Symmetries. In A. Comtet, T. Jolicoeur, S. Ouvry, & F. David, editor, *Topological Aspects of Low Dimensional Systems*, page 53, 1999.

[66] Niels R. Walet and Tom Weidig. Full 2D Numerical Study of the Quantum Hall Skyrme Crystal. 2001.

[67] A. Neubauer, C. Pfleiderer, B. Binz, A. Rosch, R. Ritz, P. G. Niklowitz, and P. Böni. Topological hall effect in the *a* phase of mnsi. *Phys. Rev. Lett.*, 102:186602, May 2009.

[68] Sidney R. Coleman. Q Balls. *Nucl. Phys.*, B262:263, 1985.

[69] Erick J. Weinberg. Classical solutions in quantum field theories. *Ann. Rev. Nucl. Part. Sci.*, 42:177–210, 1992.

[70] T. D. Lee and Y. Pang. Nontopological solitons. *Phys. Rept.*, 221:251–350, 1992.

[71] Michael Dine and Alexander Kusenko. The origin of the matter-antimatter asymmetry. *Rev. Mod. Phys.*, 76:1, 2004.

[72] Richard Battye and Paul Sutcliffe. Q-ball dynamics. *Nucl. Phys.*, B590:329–363, 2000.

[73] Alexander Kusenko. Q-balls in the mssm. *Nuclear Physics B - Proceedings Supplements*, 62(1-3):248 – 252, 1998. Proceedings of the Fifth International Conference on Supersymmetries in Physics.

[74] Z. Nussinov and S. Nussinov. Non-Relativistic Bose-Einstein Condensates, Kaon droplets, and Q- Balls. *eprint arXiv:cond-mat/0409094*, September 2004.

[75] K. Enqvist and M. Laine. Q-balls in atomic Bose-Einstein condensates. *JCAP*, 0308:003, 2003.

[76] M. Deshaies-Jacques and R. MacKenzie. Q-balls in Maxwell-Chern-Simons theory. *Phys. Rev.*, D74:025006, 2006.

[77] Eugen Radu and Mikhail S. Volkov. Existence of Stationary, Non-Radiating Ring Solitons in Field Theory: Knots and Vortons. *Phys.Rept.*, 468:101–151, 2008.

[78] Alexander Kusenko. Small Q balls. *Phys.Lett.*, B404:285, 1997.

[79] Tuomas Multamaki. *On the Properties and Cosmology of Q-balls*. PhD thesis, 2001.

[80] Petja Salmi. *Oscillons*. PhD thesis, 2000.

[81] Tuomas Multamaki and Iiro Vilja. Analytical and numerical properties of Q-balls. *Nucl. Phys.*, B574:130–152, 2000.

[82] Eric Braaten. Nucleon-Nucleon scattering amplitudes and the classical scattering of skyrmions. *Phys. Rev.*, D37:2026, 1988.

[83] W. Y. Crutchfield, N. J. Snyderman, and V. R. Brown. Deuteron in the Skyrme model. *Phys. Rev. Lett.*, 68(11):1660–1662, Mar 1992.

[84] J. J. M. Verbaarschot, T. S. Walhout, J. Wambach, and H. W. Wyld. Scattering of skyrmions in an axially symmetric system. *Nucl. Phys.*, A461:603, 1987.

[85] A. E. Allder, S. E. Koonin, R. Seki, and H. M. Sommermann. Dynamics of Skyrmion Collisions in (3+1)-Dimensions. *Phys. Rev. Lett.*, 59:2836, 1987.

[86] H. M. Sommermann, R. Seki, S. Larson, and S. E. Koonin. Baryon-antibaryon annihilation in the Skyrme model. *Phys. Rev. D*, 45(11):4303–4306, Jun 1992.

[87] R. D. Amado, M. Á. Halász, and P. Protopapas. Two skyrmion dynamics with ω mesons. *Phys. Rev. D*, 61:074022, Mar 2000.

[88] Adam Miklos Halasz and R. D. Amado. Skyrmion anti-Skyrmion annihilation with omega mesons. *Phys. Rev.*, D63:054020, 2001.

[89] Wojciech J. Zakrzewski. Soliton Like Scattering in the O(3) Sigma Model in (2+1)-Dimensions. 1990.

[90] Robert A. Leese, Michel Peyrard, and Wojciech J. Zakrzewski. Soliton Scattering in some Relativistic Models in $(2 + 1)$- Dimensions. *Nonlinearity*, 3:773–808, 1990.

[91] P M Sutcliffe. The interaction of Skyrme-like lumps in (2+1) dimensions. *Nonlinearity*, 4(4):1109, 1991.

[92] Michel Peyrard, Bernard Piette, and Wojciech J. Zakrzewski. Soliton scattering in the Skyrme model in (2+1)- dimensions. 1. Soliton-soliton case. *Nonlinearity*, 5:563–583, 1992.

[93] B. M. A. G. Piette, B. J. Schroers, and W. J. Zakrzewski. Multi-solitons in a Two-dimensional Skyrme Model. *Z. Phys.*, C65:165–174, 1995.

[94] Daniel A. Dwyer and Krishna Rajagopal. Collision-induced decay of metastable baby skyrmions. *Phys. Rev.*, D62:105028, 2000.

[95] W. Wai-Yeung Wong. Regular hyperbolicity, dominant energy condition and causality for Lagrangian theories of maps. *Classical and Quantum Gravity*, 28(21):215008, November 2011.

[96] G. W. Gibbons. Causality and the Skyrme model. *Phys. Lett.*, B566:171–174, 2003.

[97] Tuomas Multamaki and Iiro Vilja. Q-ball collisions in the MSSM: Gravity-mediated supersymmetry breaking. *Phys. Lett.*, B482:161–166, 2000.

[98] J. C. Collins and W. J. Zakrzewski. The scattering of a skyrmion configuration on asymmetric holes or barriers in a model Landau-Lifshitz equation. 2009.

[99] Jassem H. Al-Alawi and Wojtek J. Zakrzewski. Q-ball Scattering on Barriers and Holes in 1 and 2 Spatial Dimensions. *J. Phys.*, A42:245201, 2009.

[100] M. Alcubierre. *Introduction to 3+1 Numerical Relativity.* Oxford University Press, 2008.

[101] Jacques Hadamard. *Lectures on Cauchy's problem in linear partial differential equations.* Yale University Press, 1923.

[102] J. Shatah. Weak Solutions and the Development of singularities in SU(2) Sigma Models. *Comm. Pure Appl. Math.*, 41:459–469, 1988.

[103] J. Shatah and A.S. Tahvildar-Zadeh. On the Cauchy Problem for Equivariant Wave Maps. *Comm. Pure Appl. Math.*, 47:719–751, 1994.

[104] J. Shatah and M. Struwe. *Geometric Wave Equations.* Courant Lecture Notes in Mathematics, New York University, 1998.

[105] James Isenberg and Steven L. Liebling. Singularity formation in 2+1 wave maps. *J.Math.Phys.*, 43:678–683, 2002.

[106] S.W. Hawking and G.F.R. Ellis. The Large scale structure of space-time. 1973.

[107] F. Pretorius. http://laplace.physics.ubc.ca/Doc/pamr/AMRD_ref.pdf. Retrieved May 28, 2013.

[108] F. Pretorius. http://laplace.physics.ubc.ca/Doc/pamr/PAMR_ref.pdf. Retrieved May 28, 2013.

[109] Joseph Oliger Marsha J Berger. Adaptive mesh refinement for hyperbolic partial differential equations. *Journal of Computational Physics*, 53:484–512, March 1984.

[110] M. Choptuik. Unpublished Numerical Relativity Lecture Notes (1997).

[111] M. W. Choptuik. *Lectures for VII Mexican School on Gravitation and Mathematical Physics, Numerical Analysis for Numerical Relativists*, (2006).

[112] B. Coutinho Mundim. *A Numerical Study of Boson Star Binaries*. PhD thesis, The University of British Columbia, (2008).

[113] P. D. Lax and R. D. Richtmyer. Survey of the stability of linear finite difference equations. *Communications on Pure and Applied Mathematics*, 9(2):267–293, 1956.

[114] L. F. Richardson. The approximate arithmetical solution by finite differences of physical problems involving differential equations, with an application to the stresses in a masonry dam. *Philosophical Transactions of the Royal Society of London. Series A*, **210**:307–357, (1911).

[115] J. Crank and P. Nicolson. A practical method for numerical evaluation of solutions of partial differential equations of the heat-conduction type. *Advances in Computational Mathematics*, 6:207–226, 1996. 10.1007/BF02127704.

[116] M.W. Choptuik. Critical behaviour in scalar field collapse. In D. Hobill, A. Burd, and A. Coley, editors, *Deterministic Chaos in General Relativity*, pages 155–175. Springer, (1994).

[117] R.L. Marsa and M.W. Choptuik. Black hole scalar field interactions in spherical symmetry. *Phys.Rev.*, D54:4929–4943, 1996.

[118] H. Kreiss and J. Oliger. Methods for the approximate solution of time dependent problems. *Publication Series No. 10*, 1973.

[119] Saul A. Teukolsky. Stability of the iterated Crank-Nicholson method in numerical relativity. *Phys. Rev. D*, 61:087501, Mar 2000.

[120] Frans Pretorius and Matthew W. Choptuik. Adaptive Mesh Refinement for Coupled Elliptic-Hyperbolic Systems. *J. Comput. Phys.*, 218:246–274, 2006.

[121] F. Pretorius. *Numerical Simulations of Gravitational Collapse*. PhD thesis, The University of British Columbia, (2002).

[122] Samuel Bieri. Stability of the soliton in the broken $O(3)$ nonlinear model in $2+1$ dimensions. 2004. Diploma Work. Institute for Theoretical Physics, Swiss Federal Institute of Technology Lausanne EPFL.

[123] R.L. Burden and J.D. Faires. *Numerical analysis*. Thomson Brooks/Cole, 2005.

[124] W H Press, S A Teukolsky, W T Vetterling, and B P Flannery. *Numerical recipes in FORTRAN. The art of scientific computing*, volume 6. Cambridge University Press, 1992. http://portal.acm.org/citation.cfm?id=563041.

[125] http://www.netlib.org/odepack. Retrieved May 28, 2013.

[126] http://www.netlib.org/lapack. Retrieved May 28, 2013.

[127] M. Choptuik and R. L. Marsa. http://laplace.physics.ubc.ca/People/matt/Rnpl/index.html. Retrieved May 28, 2013.

[128] http://www.maplesoft.com. Retrieved May 28, 2013.

[129] M. Choptuik. ftp://laplace.physics.ubc.ca/pub/TensorV6/.

[130] Jr Giblin, John T., Lam Hui, Eugene A. Lim, and I-Sheng Yang. How to Run Through Walls: Dynamics of Bubble and Soliton Collisions. *Phys.Rev.*, D82:045019, 2010.

[131] Edmund J. Copeland, M. Gleiser, and H.-R. Muller. Oscillons: Resonant configurations during bubble collapse. *Phys.Rev.*, D52:1920–1933, 1995.

[132] Mustafa A. Amin. Inflaton fragmentation: Emergence of pseudo-stable inflaton lumps (oscillons) after inflation. arxiv:1006.3075.

[133] Gragor Leiler and Luciano Rezzolla. On the iterated Crank-Nicolson for hyperbolic and parabolic equations in numerical relativity. *Phys.Rev.*, D73:044001, 2006.

[134] Marek Karliner and Itay Hen. Review of Rotational Symmetry Breaking in Baby Skyrme Models. 2009. 0901.1489.

[135] A.E. Kudryavtsev, B.M.A.G. Piette, and W. J. Zakrzewski. Skyrmions and domain walls in (2+1) dimensions. *Nonlinearity*, 11:783–795, 1998.

[136] B. Piette and W. J. Zakrzewski. Numerical Integration of (2 + 1) Dimensional PDEs for S^2 Valued Functions. *Journal of Computational Physics*, 145(1):359 – 381, 1998.

[137] Robert Owen. Constraint Damping in First-Order Evolution Systems for Numerical Relativity. *Phys. Rev.*, D76:044019, 2007.

[138] Carsten Gundlach, Jose M. Martin-Garcia, Gioel Calabrese, and Ian Hinder. Constraint damping in the Z4 formulation and harmonic gauge. *Class. Quant. Grav.*, 22:3767–3774, 2005.

[139] Robert Leese. Low-Energy Scattering of Solitons in the CP^1 Model. *Nucl. Phys.*, B344:33–72, 1990.

[140] G. W. Gibbons, C. M. Warnick, and W. W. Wong. Non-existence of Skyrmion-Skyrmion and Skyrmion-anti- Skyrmion static equilibria. *J. Math. Phys.*, 52:012905, 2011.

[141] Robert M. Wald. *General Relativity.* Chicago, Usa: Univ. Pr. (1984) 491p.

[142] Ramon J. Cova. Skyrmions scattering in (2+1)-dimensions. *Helv.Phys.Acta*, 68:282–296, 1995.

[143] Robert A. Leese, Michel Peyrard, and Wojciech J. Zakrzewski. Soliton Stability in the O(3) Sigma Model in (2+1)-Dimensions. *Nonlinearity*, 3:387–412, 1990.

[144] R. Leese. Discrete Bogomolny Equations for the non-linear $O(3)$ Sigma Model in (2+1)-Dimensions. *Phys.Rev.*, D40:2004–2013, 1989.

[145] Minoru Eto, Toshiaki Fujimori, Muneto Nitta, Keisuke Ohashi, and Norisuke Sakai. Dynamics of non-abelian vortices. *Phys. Rev. D*, 84:125030, Dec 2011.

[146] R. S. Ward. Slowly Moving Lumps in the CP^1 Model in $(2 + 1)$-Dimensions. *Phys. Lett.*, B158:424, 1985.

[147] Carl Rosenzweig and Ajit Mohan Srivastava. Towards a qualitative understanding of the scattering of topological defects. *Phys. Rev. D*, 43:4029–4041, Jun 1991.

[148] Parvin Eslami, Wojtek J. Zakrzewski, and Mohsen Sarbishaei. Baby Skyrme models for a class of potentials. 2000.

[149] Michel Peyrard, Bernard Piette, and Wojciech J. Zakrzewski. Soliton scattering in the skyrme model in (2+1)-dimensions. 2. More general systems. *Nonlinearity*, 5:585–600, 1992.

[150] J. C. Collins and W. J. Zakrzewski. Scattering of a two skyrmion configuration on potential holes or barriers in a model Landau-Lifshitz equation. *Journal of Physics A Mathematical General*, 42(16):165102–+, April 2009.

[151] Bernard Piette, W. J. Zakrzewski, and Joachim Brand. Scattering of topological solitons on holes and barriers. *J. Phys.*, A38:10403–10412, 2005.

[152] Jassem H. Al-Alawi and Wojtek J. Zakrzewski. Scattering of Topological Solitons on Barriers and Holes in Two $\lambda\phi^4$ Models. *J. Phys.*, A40:11319–11332, 2007.

[153] J. C. Collins and W. J. Zakrzewski. Scattering of a two skyrmion configuration on potential holes of barriers in a model Landau-Lifshitz equation. *J. Phys.*, A42:165102, 2009.

[154] Marcus Berg, Ethan Honda, Rob Jones and Eric Hirschmann,. Critical Collapse of Self-Gravitating Skyrmions. 1998. http://www.physto.se/ mberg/physics/p387g2/skyr.html. Retrieved May 28, 2013.

[155] B.J. Schroers. Dynamics of moving and spinning Skyrmions. *Z.Phys.*, C61:479–494, 1994.

[156] Gregory S. Adkins and Chiara R. Nappi. Stabilization of Chiral Solitons via Vector Mesons. *Phys. Lett.*, B137:251, 1984.

[157] J.F. Donoghue, E. Golowich, and Barry R. Holstein. Dynamics of the Standard Model. *Camb.Monogr.Part.Phys.Nucl.Phys.Cosmol.*, 2:1–540, 1992.

[158] Ya Shnir and D.H. Tchrakian. Axially-symmetric Sphaleron Solutions of the Skyrme Model. *J.Phys.Conf.Ser.*, 284:012053, 2011.

[159] J. Jäykkä J. Hietarinta, J. Palmu and P. Pakkanen. Scattering of knotted vortices (Hopfions) in the Faddeev-Skyrme model. *New Journal of Physics*, 14(1):013013, 2012.

[160] Piotr Bizoń and Tadeusz Chmaj. Formation and critical collapse of skyrmions. *Phys. Rev. D*, 58:041501, Jun 1998.

[161] Jose J. Blanco-Pillado, Handhika S. Ramadhan, and Noriko Shiiki. Skyrme Branes. *Phys. Rev.*, D79:085004, 2009.

[162] Matthew W. Choptuik and Frans Pretorius. Ultra Relativistic Particle Collisions. *Phys. Rev. Lett.*, 104:111101, 2010.

[163] J.W. Thomas. *Numerical Partial Differential Equations: Finite Difference Methods.* (1995), Springer-Verlag New York, Inc., Sec. 2.4.

[164] Oscar A. Reula. Hyperbolic Methods for Einstein's Equations. *Living Reviews in Relativity*, 1(3), 1998. http://www.livingreviews.org/lrr-1998-3, Retrieved May 28, 2013.

[165] Ronald S Irving. *Integers, Polynomials, and Rings:A Course in Algebra*. (2004), Springer-Verlag New York, Inc., Chapter 10 ex.10.14.4 and 10.17.4, pp.154156.

[166] Steven H. Schot. Eighty years of Sommerfeld's radiation condition. *Historia Mathematica*, 19(4):385 – 401, 1992.

[167] M. Choptuik. Unpublished. explorations in gravitational physics (numerical relativity) lecture notes (2010). http://laplace.phas.ubc.ca/2010-pi-nr/lec/week1/Lec1.pdf.

APPENDIX A

FINITE DIFFERENCING: FURTHER DETAILS

A.1 Stability of a Numerical Approximation Scheme

As mentioned in 2.1, the concept of stability of a finite difference scheme captures the notion that a numerical solution must not "blow-up" in time unless the continuum solution does so. There are a variety of definitions of stability in the literature, but the following [163] will suffice for our purposes.

We assume that our finite difference scheme has been written in the two-level form

$$\mathbf{u}^{n+1} = Q\,\mathbf{u}^{n}\,, \tag{A.1}$$

where $\mathbf{u}^n$ and $\mathbf{u}^{n+1}$ are the numerical approximations at the current and advanced discrete times, respectively, and Q is the finite difference update operator. We further restrict attention to the case of one spatial dimension—the extension to additional dimensions is trivial—and assume that the finite difference mesh has spacings Δx and Δt in the spatial and temporal directions, respectively. Then we say that the scheme (A.1) is stable with respect to some norm $\|\cdot\|$ if there are positive constants Δx_0 and Δt_0, and non-negative constants K and β such that

$$\|\mathbf{u}^{n+1}\| \leq K e^{\beta t} \|\mathbf{u}^{0}\|\,, \tag{A.2}$$

for $0 \leq t \equiv (n+1)\Delta t$, $0 < \Delta x \leq \Delta x_0$ and $0 < \Delta t \leq \Delta t_0$.

We note that the possibility for exponential growth of the numerical solution implied by (A.2) allows for a corresponding growth rate in the continuum, and is a matter of convention. Should it be known that the growth of the exact solution relative to the initial data can be bounded with a less-rapidly growing function (including a constant), then the definition of stability can be adjusted accordingly.

A.2 The Courant Number, λ

We consider the usual wave equation with unit propagation speed

$$u(t,x)_{tt} = u_{xx}\,, \tag{A.3}$$

and finite-difference using the standard $O(h^2)$ *time explicit* approximation on a uniform mesh with spacings Δx and Δt in the x and t directions, respectively.

$$\frac{u_i^{n+1} - 2u_i^n + u_i^{n-1}}{\Delta t^2} = \frac{u_{i+1}^n - 2u_i^n + u_{i-1}^{n-1}}{\Delta x^2}\,. \tag{A.4}$$

The Courant factor (or number), λ, is defined by

$$\lambda \equiv \frac{\Delta t}{\Delta x}\,. \tag{A.5}$$

For explicit schemes such as (A.4), λ must be generally satisfy a restriction $\lambda < \kappa$, with κ some positive constant, to ensure stability. This restriction can be understood physically from considerations of the dependence of the advanced solution, u^{n+1}, on the retarded values, u^n and u^{n-1}, and is perhaps easiest to understand in pictorial form.

Consider then Fig. A.1, which shows two finite difference meshes, one with $\lambda < 1$ (Fig. A.1a (a)), the other with $\lambda > 1$ (Fig. A.1b (b)). Solid lines denote the physical cones of dependence for the advanced value u_j^{n+1}, while the dotted lines show the numerical cones of dependence. The structure of the latter reflects the fact that the scheme (A.4) connects only nearest neighbours. The key observation is that if the numerical cone does not properly contain the physical one then not all of the information necessary to determine the solution value u_j^{n+1} is available, and the numerical solution will be unstable. In the current case, this translates to the well-known limit, $\lambda \leq 1$. This restriction can also be obtained easily using a Von Neumann mode analysis.

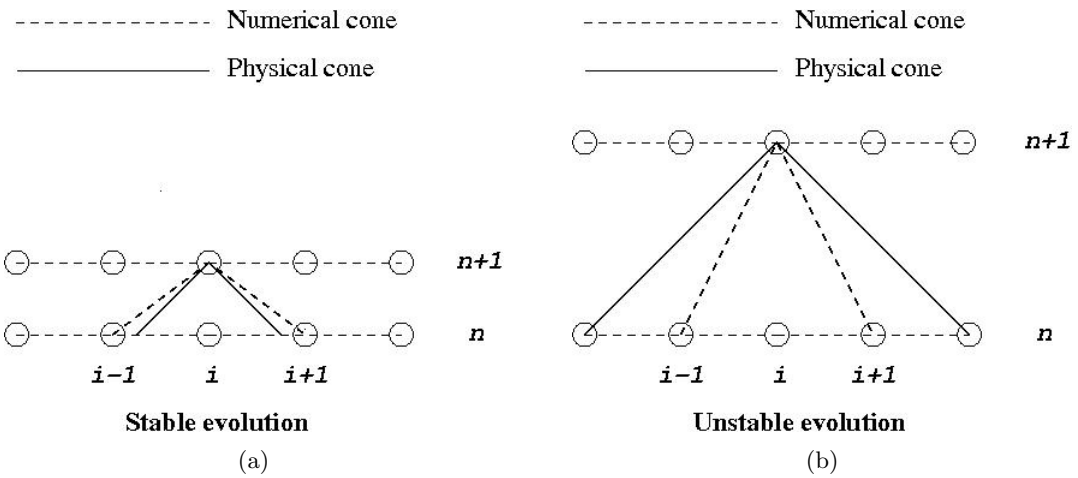

Figure A.1: Physical and numerical domains of dependence. Shown are two finite difference grids with differing values of the Courant number, $\lambda \equiv \Delta t/\Delta x$. In plot (a) we have $\lambda < 1$, the physical light cone is properly contained with the numerical cone, and the explicit scheme (A.4) is stable. Conversely, in (b), where $\lambda < 1$, the physical light cone lies outside the numerical cone and the scheme is unstable.

APPENDIX B

MISCELLANEOUS Q-BALL CALCULATIONS

B.1 Variation of the Q-ball Action

The $2+1$ model of a complex scalar field ϕ that is studied in Chap. 3 has a Lagrangian

$$\mathcal{L} = \frac{1}{2}\partial_\mu\phi^*\partial^\mu\phi - \frac{1}{2}|\phi|^2 + \frac{1}{3}A|\phi|^3 - \frac{1}{4}B|\phi|^4\,, \tag{B.1}$$

where Greek indices $\mu, \ldots$ run over the spacetime values $0, 1, 2$ (where 0 is the time index). Here we have adopted the specific choice of potential

$$U(|\phi|^2) = \frac{1}{2}|\phi|^2 - \frac{1}{3}A|\phi|^3 + \frac{1}{4}B|\phi|^4\,, \tag{B.2}$$

in which the mass, m, of the field is set to unity and A and B are constants.[35]

If we write the modulus of the field in terms of the field, ϕ, and its complex conjugate, ϕ^*, i.e. $|\phi| = \sqrt{\phi^*\phi}$, we have

$$\mathcal{L} = \frac{1}{2}\partial_\mu\phi^*\partial^\mu\phi - \frac{1}{2}\phi^*\phi + \frac{1}{3}A(\phi^*\phi)^{3/2} - \frac{1}{4}B(\phi^*\phi)^2\,. \tag{B.3}$$

Variation with respect to $\partial_\mu\phi^*$ and ϕ^* yields

$$\frac{\partial\mathcal{L}}{\partial(\partial_\mu\phi^*)} = \frac{1}{2}\partial^\mu\phi\,, \tag{B.4}$$

and

$$\frac{\partial\mathcal{L}}{\partial\phi^*} = -\frac{1}{2}\phi + \frac{1}{2}A\phi\sqrt{\phi^*\phi} - \frac{1}{2}B\phi(\phi^*\phi)\,. \tag{B.5}$$

[35] As discussed in Sec. 3.2, without loss of generality we can also set $A = 1$ by a suitable rescaling, but we will not do so here

Thus, the Euler-Lagrange field equations of motion are

$$\partial_\mu \frac{\partial \mathcal{L}}{\partial(\partial_\mu \phi^*)} - \frac{\partial \mathcal{L}}{\partial \phi^*} = \frac{1}{2}\partial_\mu \partial^\mu \phi + \phi - A|\phi|\phi + B|\phi|^2\phi = 0\,. \tag{B.6}$$

B.2 General Arguments for the Existence of Q-balls

In this section we discuss in more detail the manner in which the particular properties of the potential function, $U(|\phi|^2)$, determine the existence of Q-ball solutions. Our discussion follows closely the works of Coleman [68], Kusenko [78], Multamaki [79] and Salmi [80].

The charge of a d-dimensional Q-ball—where d is the spatial dimensionality—is defined by (3.3)

$$Q = \frac{1}{2i}\int d^d x \;\; (\phi^* \dot{\phi} - \phi \dot{\phi^*})\,. \tag{B.7}$$

The energy, E, is given by (3.4)

$$E = \int d^d x \;\; \left[\frac{1}{2}|\dot{\phi}|^2 + \frac{1}{2}|\nabla\phi|^2 + U(|\phi|^2)\right], \tag{B.8}$$

where we have adopted the notation $\dot{\phi} = \partial_0 \phi$ for time derivatives. We seek to minimize the energy (B.8) for fixed charge. We thus introduce a Lagrange multiplier, ω, and minimize

$$E_\omega = E + \omega\left[Q - \frac{1}{2i}\int d^d x \;\; (\phi^* \dot{\phi} - \phi \dot{\phi^*})\right] \tag{B.9}$$

with respect to ϕ. Substituting (B.8) in (B.9) and regrouping terms yields

$$E_\omega = \int d^d x \;\; \left[\frac{1}{2}|\dot{\phi}|^2 + \frac{1}{2}|\nabla\phi|^2 + U(|\phi|^2)\right] + \omega Q - \frac{\omega}{2i}\int d^d x \;\; \left[(\phi^* \dot{\phi} - \phi \dot{\phi^*})\right]. \tag{B.10}$$

Separating time and spatial terms we have

$$E_\omega = \int d^d x \;\; \left[\left(\frac{1}{2}|\dot{\phi}|^2 - \frac{\omega}{2i}(\phi^* \dot{\phi} - \phi \dot{\phi^*})\right) + \left(\frac{1}{2}|\nabla\phi|^2 + U(|\phi|^2)\right)\right] + \omega Q\,. \tag{B.11}$$

Factoring and reordering gives

$$E_\omega = \int d^d x \;\; \left[\frac{1}{2}\left(|\dot{\phi}|^2 + \omega i \phi^* \dot{\phi} - \omega i \phi \dot{\phi^*}\right) + \left(\frac{1}{2}|\nabla\phi|^2 + U(|\phi|^2)\right)\right] + \omega Q\,. \tag{B.12}$$

Now we complete the square of the time-dependent term,

$$E_\omega = \int d^d x \ \left[\frac{1}{2}\left(|\dot{\phi}|^2 + \omega i\phi^*\dot{\phi} - \omega i\phi\dot{\phi^*} + \omega^2|\phi^2| - \omega^2|\phi^2|\right) + \left(\frac{1}{2}|\nabla\phi|^2 + U(|\phi|^2)\right)\right] + \omega Q\,, \tag{B.13}$$

and since $|\phi|^2 = \phi^*\phi$ we can write

$$E_\omega = \int d^d x \ \left[\frac{1}{2}(\dot{\phi} - i\omega\phi)(\dot{\phi^*} + i\omega\phi^*) - \frac{1}{2}\omega^2|\phi^2| + \left(\frac{1}{2}|\nabla\phi|^2 + U(|\phi|^2)\right)\right] + \omega Q\,. \tag{B.14}$$

Defining the *effective potential*, $U_\omega(|\phi|^2)$, by

$$U_\omega(|\phi|^2) = U(|\phi|^2) - \frac{1}{2}\omega^2|\phi^2|\,, \tag{B.15}$$

we have [78, 79, 80],

$$E_\omega = \int d^d x \ \left[\frac{1}{2}|\dot{\phi} - i\omega\phi| + \frac{1}{2}|\nabla\phi|^2 + U_\omega(|\phi|^2)\right] + \omega Q\,. \tag{B.16}$$

We now adopt a time-harmonic stationary ansatz for the solution $\phi(t, x^i)$ (see Sec. 3.2),

$$\dot{\phi} - i\omega\phi = 0 \quad \rightarrow \quad \phi(t, x^i) = e^{i\omega t}\sigma(x^i)\,, \tag{B.17}$$

where $\sigma(x^i)$ is a static, positive, real-valued profile function with dependence on the spatial dimensions of spacetime x^i, with $i = 1, 2, \ldots d$. Using this form for the solution we obtain a configuration with charge

$$Q = \omega \int d^d x \ \ \sigma(x^i)^2\,, \tag{B.18}$$

and energy

$$E = \int d^d x \ \ \left[\frac{1}{2}|\nabla\sigma(x^i)|^2 + U_\omega(\sigma(x^i)^2)\right] + \omega Q\,. \tag{B.19}$$

The extremization of (B.19) with respect to two parameters, namely σ and ω, is simplified by noting that we seek localized solutions that vanish at infinity. It has been shown [78, 79, 80] that, for ω in some range(s), there exist configurations with monotonically decreasing $\sigma(r)$ which satisfy the boundary condition $\sigma(r) \to 0$ as $r \to 0$. A subset of these are precisely the static solutions that we want. By extremizing the energy functional (B.19) with respect to σ we derive the governing

ODE for the profile function:

$$\nabla^2\sigma = -\frac{\partial U_\omega(\sigma^2)}{\partial\sigma}\,. \tag{B.20}$$

Assuming spherical symmetry (circular symmetry for the $d = 2$ case), we have

$$\frac{d^2\sigma}{dr^2} + \frac{(d-1)}{r}\frac{d\sigma}{dr} - \frac{dU_\omega(\sigma^2)}{d\sigma} = 0\,, \tag{B.21}$$

where $U_\omega(\sigma^2) \equiv U(\sigma^2) - \omega^2\sigma^2/2$. There are certain restrictions on the potential, $U(\sigma)$, in order that (B.21) admit regular, finite-energy solutions. Specifically, $U(\sigma)$ must be $U(1)$-symmetric and the origin in potential space must be a global minimum; i.e. $U(0) = 0$. Further, Coleman [68] showed that the most important condition for the existence of Q-ball solutions in the theory is that the effective potential, $U_\omega(\sigma^2)$, have an (additional) minimum where $\sigma \neq 0$.

The last requirement can easily be fulfilled through the choice of an appropriate polynomial potential, such as the one adopted in Chap. 3:

$$U(|\phi|^2) = \frac{1}{2}|\phi|^2 - \frac{1}{3}A|\phi|^3 + \frac{1}{4}B|\phi|^4\,. \tag{B.22}$$

The need for a second minimum of $U_\omega(\sigma^2)$, with $\sigma \neq 0$, can be understood heuristically through an analogy from classical mechanics—also proposed by Coleman [68]—who realized that (B.21) has the functional form of the equation of a particle moving in an (inverted) effective potential $V_\omega^{\rm eff}(\sigma^2) \equiv -U_\omega(\sigma^2)$. We emphasize that here we are viewing ω as an adjustable parameter. In contrast, in the computation of Q-ball solutions described in Sec. 3.2, ω is an eigenvalue whose value is determined by a specific choice of $\sigma \equiv \sigma_0$.

Now, in the single-particle interpretation, σ plays the role of the particle's position, while r represents time, so that the governing ODE (B.21) becomes

$$\frac{d^2\sigma}{dt^2} + \frac{(d-1)}{t}\frac{d\sigma}{dt} + \frac{dV_\omega^{\rm eff}}{d\sigma} = 0\,. \tag{B.23}$$

The second term in (B.23) acts as a frictional force that is proportional to velocity and inversely proportional to time. Thus, except for the $d = 1$ case, the particle energy is not conserved; i.e. the system is dissipative. Continuing with the analogy, the boundary conditions we seek, namely $\sigma(r \to \infty) = 0$ and $\sigma'(0) = 0$, correspond to $\sigma(t \to \infty) = 0$ and $d\sigma/dt(0) = 0$. In other words, any Q-ball solution can be identified with the motion of a particle that starts at rest at some location,

$\sigma = \sigma_0(\omega)$, and that ends up at rest at the origin, $\sigma = 0$.

Now consider Fig. B.1 which shows a plot of $V_\omega^{\rm eff}(\sigma^2)$ for our choice of potential—which is representative of the type of $V_\omega^{\rm eff}$ that *will* produce Q-balls—and for the specific choice $\omega = 0.7739293$. Clearly, due to the presence of friction we must release the particle at some position σ_0 such that $V_\omega^{\rm eff}(\sigma_0^2) > V_\omega^{\rm eff}(0)$. Moreover, since the frictional term is inversely proportional to time, we can make the dissipation arbitrarily small by starting the particle arbitrarily close to the maximum of $V_\omega^{\rm eff}$. By continuity there must be some σ_0—as displayed in the figure—such that the particle arrives at rest at the origin.

For a general potential, Q-ball solutions will exist only for values of ω in a finite range (equivalently, values of σ_0 in some finite interval). In our case we have

$$V_\omega^{\rm eff} = \frac{1}{2}(\omega^2 - 1)\sigma^2 + \frac{A}{3}\sigma^3 - \frac{B}{4}\sigma^4 \,. \tag{B.24}$$

Since $V_\omega^{\rm eff}$ must have a minimum at some $\sigma = \sigma_{\rm min}$, with $\sigma_{\rm min} \neq 0$ and $V_\omega^{\rm eff}(\sigma_{\rm min}^2) < 0$, the effective potential must have two zero-crossings (at least) in the interval from $\sigma = 0$ and the global maximum. Setting the right hand side of (B.24) to zero and dividing by σ^2 then yields

$$-\frac{B}{4}\sigma^2 + \frac{A}{3}\sigma + \frac{1}{2}(\omega^2 - 1) = 0 \,. \tag{B.25}$$

The discriminant condition for the existence of two additional (real) zeros is thus $A^2/9 + B(\omega^2 - 1)/2 > 0$, which leads to the condition,

$$1 < \omega^2 < 1 - \frac{2A^2}{9B} \,, \tag{B.26}$$

or for the specific values $A = 1$, $B = 1/2$ adopted in Chap. 3,

$$1 < \omega^2 < \frac{5}{9} \,. \tag{B.27}$$

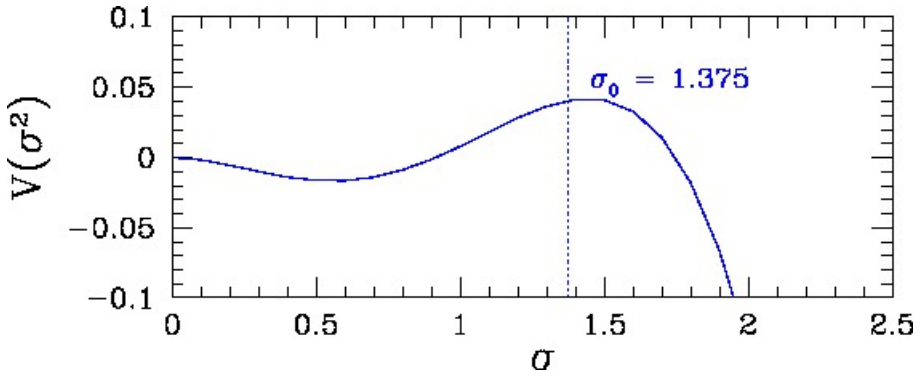

Figure B.1: Inverted effective potential $V_\omega^{\rm eff}(\sigma^2) \equiv -U_\omega(\sigma^2)$ for the specific choice $\omega = 0.7739293$. In the mechanical analog, when the particle is released from rest at $\sigma = \sigma_0 = 1.375$, it will arrive at the origin, $\sigma = 0$, also at rest.

APPENDIX C

HYPERBOLICITY AND LINEARIZED ANALYSIS

C.1 Hyperbolicity and Well-posedness of Time-dependent PDEs

In this section we provide further details concerning the issues of hyperbolicity and well-posedness that were discussed briefly in Sec. 1.5.2. We closely follow the presentations of Reula [164] and Alcubierre [100], which we emphasize provide *reviews* of the relevant theory that are directed at numerical relativists and those working in related fields.

The canonical example of a hyperbolic system is the wave equation in one space variable,

$$\partial_{tt} u(t,x) = \partial_{xx} u(t,x)\,, \tag{C.1}$$

where the solution, $u(t,x)$, describes free propagation with unit velocity. The adjective hyperbolic originates from the hyperbolic conoid that delimits causally connected regions that are defined with respect to any given point in the spacetime domain. More generally, and in heuristic terms, a hyperbolic system of PDEs is one in which all signals propagate with finite speed.

We now consider a general set of PDEs of evolutionary type having linear constant coefficients. Such a system can be cast in the form

$$u_t = Lu(t,x^i)\,, \tag{C.2}$$

where $u \equiv [u_1(t,x^i), u_2(t,x^i), \ldots, u_n(t,x^i)]^T$ is an n-component vector of dependent variables (fields), the index $i = 1,\ldots,d$ labels the spatial dimensions, and L is an operator whose components depend smoothly on the spatial derivatives of u. The issue of central interest is to determine

under what conditions initial data $u(0, x^i) \equiv u_0(x_i)$ will generate a unique solution, $u(t, x^i)$: this is known as the *Cauchy* or *initial value* problem for (C.2). If such conditions exist, then we say that (C.2) is *well-posed*. Conversely, if there are no such conditions—so that even for short times $t > 0$ there is no unique solution for specified u_0—then we say that the system is *ill-posed*. Clearly, any physically meaningful model characterized by a set of evolutionary PDEs must be well-posed.

Again, restricting attention to the case of systems having linear constant coefficients, precise mathematical definitions of hyperbolicity for (C.2) (there are, as we shall immediately see, several types of hyperbolicity) are expressed as algebraic conditions on the coefficients. We further assume that L depends only on first space derivatives so that we can write

$$\frac{\partial u}{\partial t} + A^i \frac{\partial u}{\partial x^i} = 0\,. \tag{C.3}$$

Here, each of the A_i is an $n \times n$ matrix of smooth constant coefficients. We define the *principal symbol* of the system (C.3) as the matrix $P(n_i) \equiv A^i n_i$, where n_i an arbitrary unit vector. The system (C.3) is *strongly hyperbolic* if $P(n_i)$ has real eigenvalues and a complete set of eigenvectors for all n_i. If $P(n_i)$ has real eigenvalues for all n_i, but lacks a complete set of eigenvectors, then the system is only *weakly hyperbolic*. The system is *symmetric hyperbolic* if all the A^i are symmetric. The most restrictive type of hyperbolicity requires that the eigenvalues of $P(n_i)$ be not only real, but also distinct for all n_i. Since $P(n_i)$ is diagonalizable in this case, we note that strict hyperbolicity implies strong hyperbolicity. It is well known that the eigenvalues of $P(n_i)$ are degenerate for most physical models. Therefore, strict hyperbolicity is quite an unusual condition. A key result of interest here is that it can be shown that strongly hyperbolic systems are well-posed, whereas weakly hyperbolic ones are not.

In contrast, for an elliptic system of PDEs, all the eigenvalues of $P(n_i)$ are *complex*. Physically this means that the speed of propagation of small perturbations is infinite (superluminal) and thus incompatible with relativistic dynamics.

For our purposes, the most important observation is that a system of the form (C.3) which has a $P(n_i)$ with at least one complex eigenvalue will *not* be well-posed. That is, it will not have an initial-value formulation where initial data $u_0(x^i)$ yields a unique solution $u(t, x^i)$. Furthermore, in the main body of the thesis we use the terminology *mixed hyperbolic-elliptic* to refer to a system where $P(n_i)$ has both real and complex eigenvalues. Once more, in this case we cannot expect

well-posedness.

For illustrative purposes, and again following [100], we analyze the hyperbolicity of the three dimensional wave equation. We have

$$\partial_{tt}\phi(t,x,y,z) - v^2\nabla^2\phi = 0\,, \tag{C.4}$$

where v is the speed of propagation. (C.4) can be recast as a system of first-order-in-time equations through the introduction of auxiliary variables, $\Pi(t,x,y,z)$ and $\Phi_i(t,x,y,z)$, $i = 1,2,3$:

$$\Pi \equiv \partial_t\phi\,, \tag{C.5}$$

$$\Psi_i \equiv v\partial_i\Psi_i\,. \tag{C.6}$$

With these definitions (C.4) becomes

$$\partial_t\Pi - v\partial_i\Psi_i = 0\,, \tag{C.7}$$

$$\partial_t\Psi_i - v\partial_i\Pi = 0\,. \tag{C.8}$$

Taking an arbitrary unit vector n_i we thus have

$$P(n_i) = v\begin{pmatrix} 0 & -n_x & -n_y & -n_z \\ -n_x & 0 & 0 & 0 \\ -n_y & 0 & 0 & 0 \\ -n_z & 0 & 0 & 0 \end{pmatrix}. \tag{C.9}$$

Using the fact that $n_x^2 + n_y^2 + n_z^2 = 1$, we find that the eigenvalues of $P(n_i)$ are

$$\lambda_1 = +v\,, \tag{C.10}$$

$$\lambda_2 = -v\,, \tag{C.11}$$

$$\lambda_3 = 0\,, \tag{C.12}$$

$$\lambda_4 = 0\,. \tag{C.13}$$

Since two of the eigenvalues are degenerate, the system is not strictly hyperbolic. On the other

hand, $P(n_i)$ *does* have a complete set of eigenvectors, given in column form by

$$R(n_i) = \begin{pmatrix} 1 & 1 & 0 & 0 \\ -n_x & n_x & -n_z & -n_y \\ -n_y & n_y & 0 & n_x \\ -n_z & n_z & n_x & 0 \end{pmatrix} . \tag{C.14}$$

Thus the wave equation (C.4) is strongly hyperbolic and, consequentially, is well-posed.

Finally, we reiterate that we have only discussed here the issues of hyperbolicity and well-posedness for the case of linear constant coefficient systems. For quasi-linear PDEs of evolutionary type, such as those describing the Skyrme models (as well as more general nonlinear systems), the theory is much less developed. We thus adopt the assumption that, at a *minimum*, the equations that result from freezing and linearizing coefficients must be hyperbolic/well-posed in order for the full systems to have equivalent properties.

C.2 Linearized Mode Analysis of the Baby Skyrme Equations

As emphasized in the main body, one of the principal goals of our current work is to study in detail the previously reported claim [1, 26] that, dependent on the nature of the initial data, the equations of motion for Skyrme models may become of mixed hyperbolic-elliptic type, rather than purely hyperbolic. This would then imply a breakdown of the initial-data formulation of the governing PDEs which, numerically, would presumably be manifested by non-convergence of any possible (consistent) differencing of the PDEs.

In the numerical experiments that we described in Chapter 4, we have used monitoring of the behaviour of the total energy E, as well as direct inspection of the grid functions, as diagnostic tools for detecting transitions from purely hyperbolic (well-posed) to mixed hyperbolic-elliptic (ill-posed) behaviour. We now discuss an additional method based on a characteristic (normal mode) analysis of the linearized equations of motion that provides corroborating evidence for these transitions.

The nonlinear PDEs (4.16) that describe our model can be converted into a system with linear constant coefficients by "freezing" the coefficients of the highest-derivative terms. As discussed above (App. C.1), it is then relatively straightforward to determine if the system is (strongly)

hyperbolic and thus well-posed, and this is precisely the approach adopted by Crutchfield and Bell [1].

In Crutchfield and Bell's analysis it was found that under certain conditions unstable modes (i.e. complex eigenvalues of the linearized system) could appear for both the baby and full $3+1$ Skyrme models. On the basis of this analysis the authors concluded that the models could then exhibit non-hyperbolicity which, in numerical simulations, would be manifested as unstable oscillatory solutions.

We now perform an analysis that parallels that in [1], but restrict attention to the baby Skyrme model in $2+1$ dimensions. Thus, Latin indices such as $a, b, c...$ label the 3 real components of the field, i.e. $\phi_a = (\phi_1, \phi_2, \phi_3)$, Greek indices label the dimensions of space-time, $\mu, \nu = 0, 1, 2$, and indices such as $i, j, k...$ range over the spatial coordinates. Again, summation conventions apply to all index types.

We begin by observing that we can write the equations of motion of the model (4.16) in the form [1, 26, 35],

$$(M_{ab}\partial_t\phi_b)_{,t} - (C_{ab}\partial_i\phi_b)_{,i} = 0\,, \tag{C.15}$$

where we ignore the Lagrange multiplier term in (4.16) since it has no relevance for the characteristic structure analysis (i.e. the calculation does not involve actual evolution of the fields).

Here, the coefficient matrices, M_{ab} and C_{ab}, can be written as [36]

$$M_{ab} = \delta_{ab}\left(\frac{1}{4} + [\partial_i\phi_c]^2\right) - \partial_i\phi_a\partial_i\phi_b\,, \tag{C.16}$$

$$C_{ab} = \delta_{ab}\left(\frac{1}{4} + [\partial_\mu\phi_c]^2\right) - \partial_\mu\phi_a\partial_\mu\phi_b\,. \tag{C.17}$$

The field equations (C.15) can then be rewritten as

$$M_{ab}\partial_{tt}\phi_b - C_{ab}\partial_{ii}\phi_b = (C_{ab})_{,i}\partial_i\phi_b - (M_{ab})_{,t}\partial_t\phi_b = 0\,. \tag{C.18}$$

It is convenient to write the terms on the right-hand side of (C.18) so that all second order deriva-

[36] It is worth mentioning that all matrix manipulations in the present analysis are performed using symbolic computation. Given the Lagrangian of the model as input, the coefficients M_{ab} and C_{ab} are computed using Maple procedures and then converted to Fortran code. Thus, confidence is high that the numerical calculations related to the linear analysis are reliable.

tives of the field variables are manifest [1]:

$$M_{ab}\partial_{tt}\phi_b - C_{ab}\partial_{ii}\phi_b = -G_{ab,i}\phi_{b,it} + J_{ab,i}\phi_{b,it} - H_{ab,ij}\phi_{b,ij}\,, \tag{C.19}$$

where the matrices $G_{ab,i}, J_{ab,i}$ and $H_{ab,ij}$ are given by

$$\begin{aligned} G_{ab,i} &= -\delta_{ab}\phi_{\tau,i}\phi_{\tau,i} - \phi_{a,i}\phi_{b,t} + 2\phi_{a,t}\phi_{b,i}\,, \\ J_{ab,i} &= \delta_{ab}\phi_{\tau,i}\phi_{\tau,i} - 2\phi_{a,i}\phi_{b,t} + \phi_{a,i}\phi_{b,t}\,, \\ H_{ab,ij} &= \delta_{ab}\phi_{\tau,j}\phi_{\tau,i} + \phi_{a,j}\phi_{b,i} - 2\phi_{a,i}\phi_{b,j}\,. \end{aligned} \tag{C.20}$$

The next step in our analysis is to obtain linearized equations of motion for small perturbations, $\delta\phi_a$, of the Skyrme fields. To that end we write

$$\phi_a = \phi_a^{(0)} + \delta\phi_a = \phi_a^{(0)} + \exp(-\boldsymbol{i}[\vec{k}\cdot\vec{r} - \omega t])\,, \tag{C.21}$$

where $\phi_a^{(0)}$ is a background field, and $\boldsymbol{i} = \sqrt{-1}$. We now substitute (C.21) in (C.18) and evaluate to lowest order in $\delta\phi_a$. This leads to the following *dispersion relation*,

$$(M\omega^2 + G_i\omega k_i - J_i\omega k_i + H_{ij}k_ik_j - Ck_ik_i)\delta\phi_a = 0\,, \tag{C.22}$$

where the matrices M, G_i, J_i, H_{ij} and C are to be evaluated using the values of $\phi_a^{(0)}$ defined at any instant of time. However, an important simplification in the calculation of the modes defined by the dispersion relation (C.22) is achieved by assuming that the small perturbations $\delta\phi_a$ propagate only along one of the coordinate directions, x or y. Assuming arbitrarily that this is the x direction, we have

$$\phi_a = \phi_a^{(0)} + \exp(-\boldsymbol{i}[\vec{k_x}\cdot\vec{r} - \omega t])\,. \tag{C.23}$$

The dot product in (C.23) between the wave vector $\vec{k_x}$ and the position vector $\vec{r}$ is easily evaluated:

$$\vec{k_x}\cdot\vec{r} = (k_x\hat{x}, 0)\cdot(x\hat{x}, y\hat{y}) = k_x x\,. \tag{C.24}$$

Thus, if the perturbation (C.23) *only depends on* x, all terms with mixed spatial derivatives in (C.21) vanish, while those involving spatial-temporal derivatives cancel. The result is that

$G_{ab,i}, J_{ab,i}$ and $H_{ab,ij}$ vanish, and we are left with the simplified dispersion relation

$$(M\omega^2 - Ck_xk_x)\delta\phi_a = 0\,. \tag{C.25}$$

This in turn yields the *characteristic equation*

$$\det(M\omega^2 - Ck_xk_x) = 0\,, \tag{C.26}$$

where, again, M and C are evaluated using the values of $\phi_a^{(0)}$ at any given time. Equation (C.26) leads to a sixth-order polynomial characteristic equation in ω. We perform the change of variable,

$$z = \omega^2\,, \tag{C.27}$$

and obtain a *cubic* equation of the type

$$az^3 + bz^2 + cz + d = 0\,. \tag{C.28}$$

The nature of the roots of (C.28) can be determined [165] by calculating the sign of the discriminant, Δ, given by

$$\Delta = 18abcd + b^2c^2 - 4ac^3 - 4b^3d - 27a^2d^2\,. \tag{C.29}$$

There are three possible cases:

1. $\Delta > 0$: the equation has three distinct real roots.
2. $\Delta = 0$: the equation has three real roots; either a double plus single, or a triple.
3. $\Delta < 0$: the equation has one real root and two roots which are complex conjugates of each other.

Noting that complex z implies complex ω, we observe that, from the point of view of this linearized analysis, we can expect a breakdown in hyperbolicity (well-posedness) whenever $\Delta \leq 0$. We also observe that it is straightforward to evaluate Δ on all mesh points at any discrete time.

We looked for the appearance of complex ω in our numerical calculations by performing simulations of head-on baby skyrmion collisions—similar to those described in Sec. 4.7—for several values of the boost factor γ, and using initial configurations in both the repulsive and attractive channels.

As also discussed in Sec. 4.7, for both the repulsive- and attractive-channel cases we find critical boost parameters, $\gamma^\star$, above which we see an apparent breakdown in hyperbolicity/well-posedness that is signalled by a loss of conservation of energy and the development of growing, high-frequency modes on the finite difference mesh. For the computations with $\gamma > \gamma^\star$ we *did* find grid points with $\Delta < 0$. Conversely, when $\gamma < \gamma^\star$ we found that Δ was strictly positive at all times, and throughout the computational domain. Thus, the appearance of complex roots in the dispersion relation is apparently correlated with the loss of conservation of energy and smoothness that we use as our primary indications of loss of hyperbolicity.

Finally, we also performed calculations involving generic smooth initial data, similar to the Gaussian pulses evolved in Sec. 4.4.4, but with the time derivatives set to very large values at $t = 0$, as discussed in Sec. 4.9.1. As for the highly boosted collisions described above, we detected complex eigenvalues during the evolutions. The loss of conservation of energy also appears to be correlated with the observation of $\Delta < 0$ for this type of initial data.

APPENDIX D

MISCELLANEOUS SKYRMION CALCULATIONS

D.1 The Hobart-Derrick Argument

The Hobart-Derrick argument [29, 15, 30, 31] provides a criterion for the existence of static solutions of minimal energy in a theory, according to dimensionality and field content. We apply this theory in the contexts of Q-balls, baby skyrmions and skyrmions and view it primarily as providing justification for the forms of the Lagrangian in the skyrmion cases.

Consider a static solution that minimizes the energy associated with one of the three models being studied—the Lagrangian for each can be written in the form (4.3), and is a functional of the fields $\phi = \phi(x^i)$, $i = 1, 2 \dots d$, where d is the number of spatial dimensions.[37] It is straightforward to show [122, 15] that if we apply a rescaling on the spatial coordinates, $\tilde{x}^i \to \eta x^i$, so that $\phi'(\tilde{x}^i) = \phi(\eta x^i)$ where η a real number, the effect on the energy contributions in each term of the Lagrangian (4.3) is [122, 15]

$$\begin{aligned} \partial_\mu \phi_a \partial^\mu \phi_a \equiv \epsilon_2 \qquad & \epsilon_2 \to \eta^{2-d} \epsilon_2 \,, \\ \tfrac{1}{2}(\partial_\mu \phi_a \partial^\mu \phi_a)^2 + \tfrac{1}{2}(\partial_\mu \phi_a \partial_\nu \phi_a)(\partial^\mu \phi_b \partial^\nu \phi_b) \equiv \epsilon_4 \qquad & \epsilon_4 \to \eta^{4-d} \epsilon_4 \,, \\ -V(\phi_a) \qquad & V \to \eta^{-d} V \,. \end{aligned} \tag{D.1}$$

With respect to the rescaling, the static energy, ϵ_{static}, is therefore,

$$\epsilon_{\text{static}} = \eta^{2-d} \epsilon_2 + \eta^{4-d} \epsilon_4 + \eta^{-d} V \,. \tag{D.2}$$

[37] Here we are suppressing internal indices for the skyrmion cases—this has no impact on the argument.

By assumption, the energy is minimized for $\eta = 1$. It thus follows that

$$\frac{d\epsilon_{\text{static}}}{d\eta}\Big|_{\eta=1} = (2-d)\epsilon_2 + (4-d)\epsilon_4 - dV = 0\,. \tag{D.3}$$

For the Q-ball case, $d = 2$ and $\epsilon_4 = 0$: thus (D.3) appears to imply that for the existence of a stable static solution we must have $V = 0$.[38] However, we know from Chap. 3 (as well as previous work, of course) that this is not the case. The solution to this apparent paradox is to realize that the argument only applies to *static* solitons, and is not valid for *stationary* objects (i.e. solutions with an internal time dependence) such as Q-balls. On the other hand, for baby skyrmions, where $d = 2$, (D.3) provides a condition for the existence of a stable static solution: both the fourth-order Skyrme term and a non-zero potential are needed for such a configuration. Finally, for the original Skymre model, where $d = 3$, (D.3) dictates that stable solitons can exist when $\epsilon_2 + 3V = \epsilon_4$. Thus even for $V = 0$, we can have a stable minimum provided that $\epsilon_2 = \epsilon_4$.

D.2 Explicit Form of the Lagrange Multiplier

In this section we calculate explicitly the Lagrange multiplier term that we add to the Lagrangian density of the baby Skyrme model in (4.14). We begin by contracting (4.15) with ϕ_a:

$$\begin{aligned}\phi_a\Big[(1 \;+\; & \partial_\mu\phi_a\partial^\mu\phi_a)\Box\phi_a + \partial_\mu\partial_\nu\phi_b\partial^\mu\phi_b\partial^\nu\phi_a - \partial^\mu\phi_b\partial^\nu\phi_b\partial_\mu\partial_\nu\phi_a - \Box\phi_b\partial^\nu\phi_b\partial_\nu\phi_a + \lambda_{LM}\phi_a \\ - \; & \frac{dV(\phi_3)}{d\phi_a}\delta_{a3}\Big] = 0\,.\end{aligned} \tag{D.4}$$

Since the derivative of the constraint $\phi_a\phi_a = 1$ with respect to any space-time coordinate μ vanishes—i.e. $\phi_a\partial_\mu\phi_a = 0$—we find that

$$(1 + \partial_\mu\phi_a\partial^\mu\phi_a)\phi_a\Box\phi_a - (\partial^\mu\phi_b\partial^\nu\phi_b)\phi_a(\partial_\mu\partial_\nu\phi_a) + \lambda_{LM}\phi_a\phi_a - \frac{dV(\phi_3)}{d\phi_a}\delta_{a3}\phi_a = 0\,. \tag{D.5}$$

From the second derivative of the constraint we get

$$\phi_a\partial_\mu\partial^\mu\phi_a + \partial_\mu\phi_a\partial^\mu\phi_a = 0\,, \tag{D.6}$$

[38] Establishing that a solution is stable requires consideration of the second variation with respect to λ—as in Derrick's original argument—so the development here can be viewed as providing *necessary* conditions for stable, static solutions.

which can be rewritten as

$$\phi_a \Box \phi_a = -\partial_\mu \phi_a \partial^\mu \phi_a \,, \tag{D.7}$$

and the second term in (D.5) can be expressed as

$$\begin{aligned} & (\partial^\mu \phi_b \partial^\nu \phi_b)\phi_a(\partial_\mu \partial_\nu \phi_a) = (\partial^\mu \phi_b \partial^\nu \phi_b)\phi_a(\eta_{\nu\mu}\partial_\mu \partial^\mu \phi_a) = \partial^\mu \phi_b \partial^\nu \phi_b \eta_{\nu\mu}\phi_a \Box \phi_a \\ = \;& \partial^\mu \phi_b \partial^\nu \phi_b \eta_{\nu\mu}(-\partial_\mu \phi_a \partial^\mu \phi_a) = \partial^\mu \phi_b \partial^\nu \phi_b(-\partial_\mu \phi_a \partial_\nu \phi_a)\,. \end{aligned} \tag{D.8}$$

Substituting (D.7) and (D.8) in (D.5) we find

$$(1 + \partial_\mu \phi_a \partial^\mu \phi_a)(-\partial_\mu \phi_a \partial^\mu \phi_a) - \partial^\mu \phi_b \partial^\nu \phi_b(-\partial_\mu \phi_a \partial_\nu \phi_a) + \lambda_{LM}\phi_a \phi_a - \frac{dV(\phi_3)}{d\phi_a}\delta_{a3}\phi_a = 0\,. \tag{D.9}$$

Setting $\phi_a \phi_a = 1$ and solving (D.9) for λ_{LM} finally yields

$$\lambda_{LM} = (1 + \partial_\mu \phi_a \partial^\mu \phi_a)(\partial_\nu \phi_a \partial^\nu \phi_a) - (\partial_\mu \phi_a \partial_\nu \phi_a)(\partial^\mu \phi_b \partial^\nu \phi_b) + \frac{dV(\phi_3)}{d\phi_3}\phi_3\,. \tag{D.10}$$

The calculation of the Lagrange multiplier in three spatial dimensions is completely analogous, except that we must set $V(\phi_a) = 0$.

D.3 The W-formalism, or Rational Ansatz

Belavin and Polyakov [33] suggested that the $\mathbb{CP}^1$ model be expressed in terms of a complex field $W(t, x, y) = W(z) = W(\bar{z})$ given by a *rational* function of the fields, $\phi_a, a = 1, 2, 3$. Specifically,

$$W(z) = \frac{\phi_1 + i\phi_2}{1 + \phi_3}\,, \tag{D.11}$$

where $z = x + iy$ is the complex coordinate in the spatial plane. The Lagrangian density (4.1) then takes the form

$$\begin{aligned} \mathcal{L} \;=\; & \frac{|W_0|^2 - |W_x|^2 - |W_y|^2}{(1 + |W|^2)^2} - 2\theta_1 \frac{(W_0^* W_y - W_0 W_y^*)^2 + (W_0^* W_x - W_0 W_x^*)^2}{(1 + |W|^2)^4} \\ + \;& 2\theta_1 \frac{(W_x^* W_y - W_x W_y^*)}{(1 + |W|^2)^4} - 4\theta_2 \frac{1}{(1 + |W|^2)^4}\,. \end{aligned} \tag{D.12}$$

Solutions of the Euler-Lagrange equations derived from (D.12) are described in [61, 139, 89, 90, 91, 92, 149] (see Sec. 4.5 for more details). The inverse mapping of (D.11) is given by the stereographic projection of the sphere S^2—defined in (ϕ_1, ϕ_2, ϕ_3) space—onto the complex plane, yielding

$$\phi_1 = \frac{W + W^*}{1 + |W|^2} \quad \phi_2 = \frac{W - W^*}{1 + |W|^2} \quad \phi_3 = \frac{1 - |W|^2}{1 + |W|^2}\,. \tag{D.13}$$

Specific static solutions of the equations derived from (D.12), which are reported in [92, 149], are

$$W(z) = W(x, y) = \lambda(x + iy) \qquad \text{with} \quad \lambda = \left(\frac{\theta_2}{2\theta_1}\right)^{1/4}, \tag{D.14}$$

where λ is a parameter that fixes the size of the soliton. The corresponding anti-skyrmion is given by

$$W(\bar{z}) = W(x, y) = \lambda(x - iy)\,, \tag{D.15}$$

and initial data for two baby skyrmions positioned at $\pm a$ is given by,

$$W = \lambda \frac{(x + iy - a)(x + iy + a)}{2a} \tag{D.16}$$

For the single baby skyrmion case, the explicit form of the solution with topological charge $B = 1$ is [54]

$$\begin{pmatrix} \phi_1(x, y) \\ \phi_2(x, y) \\ \phi_3(x, y) \end{pmatrix} = \frac{1}{\lambda^2(x^2 + y^2) + 1} \begin{pmatrix} \lambda^2(x^2 + y^2) - 1 \\ 2\lambda x \\ -2\lambda y \end{pmatrix}. \tag{D.17}$$

D.4 Variation of the Skyrme Action

The Lagrangian density for either of the Skyrme models considered in this thesis can be written as

$$\mathcal{L} = \frac{1}{2}\partial_\mu \phi_a \partial^\mu \phi_a + \frac{1}{4}(\partial_\mu \phi_a \partial_\nu \phi_a)^2 - \frac{1}{4}(\partial_\mu \phi_a \partial_\nu \phi_a)(\partial^\mu \phi_b \partial^\nu \phi_b) + V(\phi_3) + \lambda_{\mathrm{LM}}(\phi_a \phi_a - 1)\,. \tag{D.18}$$

where it is understood that 1) spacetime and internal indices range over $0, 1, 2$ and $1, 2, 3$ for the baby skyrmion case, and $0, 1, 2, 3$ and $1, 2, 3, 4$ for the original Skyrme model; 2) there is no potential term in the latter instance. The variational procedure sketched here is thus suitable for

both models.

To obtain the equations of motion from (D.18), we follow the Euler-Lagrange prescription [32]:

$$\partial_\mu \left(\frac{\partial \mathcal{L}}{\partial_\mu \phi_a} \right) - \frac{\partial \mathcal{L}}{\partial \phi_a} = 0 \,. \tag{D.19}$$

First, we find

$$\frac{\partial \mathcal{L}}{\partial_\mu \phi_a} = \partial^\mu \phi_a + (\partial_\nu \phi_b \partial^\nu \phi_b) \partial^\mu \phi_a - \partial_\nu \phi_a (\partial^\mu \phi_b \partial^\nu \phi_b) \,. \tag{D.20}$$

Applying ∂_μ to the above yields

$$\begin{aligned} (1 \;+\; & \partial_\nu \phi_b \partial^\nu \phi_b) \Box \phi_a + \partial^\mu \phi_a \partial_\nu \phi_b \partial_\mu \partial^\nu \phi_b + \partial^\mu \phi_a \partial^\nu \phi_b \partial_\mu \partial_\nu \phi_b \\ - \; & (\partial^\mu \phi_a \partial_\nu \phi_b \partial_\mu \partial^\nu \phi_b - \partial_\nu \phi_a \partial^\mu \phi_b) \partial_\mu \partial^\nu \phi_b - \partial_\nu \phi_a \partial^\nu \phi_b \Box \phi_b \,. \end{aligned} \tag{D.21}$$

Performing some index manipulation (recall that the flat metric $\eta_{\mu\nu}$ is used to raise and lower all indices) and reordering of terms, we obtain the desired result:

$$\begin{aligned} (1 \;+\; & \partial_\mu \phi_a \partial^\mu \phi_a) \Box \phi_a + \partial_\mu \partial_\nu \phi_b \partial^\mu \phi_b \partial^\nu \phi_a - \partial^\mu \phi_b \partial^\nu \phi_b \partial_\mu \partial_\nu \phi_a - \Box \phi_b \partial^\nu \phi_b \partial_\nu \phi_a \\ + \; & \lambda_{\mathrm{LM}} \phi_a - \frac{dV(\phi_3)}{d\phi_a} = 0 \,. \end{aligned} \tag{D.22}$$

D.5 Regularity of a Hedgehog Configuration at the Origin

Consider a spherically-symmetric hedgehog configuration in three spatial dimensions, as given by (5.16):

$$\phi_a = \begin{pmatrix} \sin f(r) \;\; \sin\theta \;\; \cos(\varphi) \\ \sin f(r) \;\; \sin\theta \;\; \sin(\varphi) \\ \sin f(r) \;\; \cos\theta \\ \cos f(r) \end{pmatrix} . \tag{D.23}$$

Here, we have adopted the usual spherical polar coordinates (r, θ, φ). The profile function, $f(r)$, is given by (5.19),

$$f(r) = 4 \tan^{-1} \exp(-r) \,. \tag{D.24}$$

As $r \to 0$ we have

$$f(r) = 4\tan^{-1}\exp(-r) \sim \pi - 2r + O(r^3)\,. \tag{D.25}$$

We want to show that (D.23) describes a configuration that is regular at the origin, even though the profile function $f(r)$ is not.

Using elementary trigonometric identities we have

$$\begin{aligned}\sin(\pi - 2r) &= \sin(\pi)\cos(-2r) + \cos(\pi)\sin(-2r) = -\sin(-2r)\,, \\ \cos(\pi - 2r) &= \cos(\pi)\cos(-2r) - \sin(\pi)\sin(-2r) = -\cos(-2r)\,.\end{aligned} \tag{D.26}$$

and for $r \to 0$, $-\sin(-2r) \to 2r$ and $-\cos(-2r) \to -1$. Thus, we find

$$\lim_{r\to 0}\phi_a = \lim_{r\to 0}\begin{pmatrix} 2r\cos\phi\sin\theta \\ 2r\sin\phi\sin\theta \\ 2r\cos\theta \\ -1 \end{pmatrix} = \begin{pmatrix} 2x \\ 2y \\ 2z \\ -1 \end{pmatrix} \tag{D.27}$$

Thus the components, ϕ_a, are all regular at the origin, as claimed (a completely analogous argument holds in the baby Skyrme case).[39]

[39] We thank Frans Pretorius for supplying this argument.

APPENDIX E

BOUNDARY CONDITIONS

We begin by emphasizing that the PDEs studied in this thesis are most naturally posed as true initial-value (Cauchy) problems, wherein the spatial domain is unbounded. Computationally, however, and unless we resort to some form of compactification, the spatial domain must be truncated at some finite distance from the central region where the dynamics of interest unfold. The PDEs must then be solved as initial-boundary value problems, and appropriate boundary conditions must be imposed on the dynamical variables to generate a unique solution from given initial data.

For the calculations reported in this thesis, we have adopted two types of conditions that we now describe briefly.

E.1 Dirichlet (Reflective) Boundary Condition

A Dirichlet boundary condition specifies the value of a function on the boundary of the solution domain. This type of condition is trivially implemented in our numerical computations.

E.2 Sommerfeld (Outgoing Radiation) Boundary Condition

This condition was first proposed in 1912 by Arnold Sommerfeld (see, e.g. [166]) in relation to the Helmholtz equation and some uniqueness theorems for partial differential equations in mathematical physics [166, 167]. The condition is most easily understood in the $1+1$ context, where it is based on the fact that a wave (radiation) can be written as a linear combination of right- and left-moving pieces. Given that our initial data always describe configurations that are localized near the center of the computational domain, and which generically lead to dynamics in which radiation is emitted, it is physically appropriate to demand that there be no *incoming* radiation from any of the boundaries for any $t \geq 0$.

To see how the Sommerfeld condition works in the $1+1$ case, we consider a field, $\phi(t,x)$, with time derivative, $\pi(t,x) \equiv \partial_t \phi(t,x)$, that satisfies the wave equation

$$\partial_{tt}\phi = \partial_{xx}\phi\,. \tag{E.1}$$

Here, we have set the speed of propagation to unity as usual. The radiation condition means that at $x = x_{\rm min}$ we must have only left-moving signals, so that $\phi(t,x) \approx \phi(x+t)$ and $\pi(t,x) \approx \pi(x+t)$, or

$$\begin{aligned} \phi_t(t,x_{\rm min}) &= \phi_x(t,x_{\rm min})\,, \\ \pi_t(t,x_{\rm min}) &= \pi_x(t,x_{\rm min})\,. \end{aligned} \tag{E.2}$$

Similarly, at $x = x_{\rm max}$ we require only right-moving waves, so that $\phi(t,x) \approx \phi(x-t)$ and $\pi(t,x) \approx \pi(x-t)$, or

$$\begin{aligned} \phi_t(t,x_{\rm max}) &= -\phi_x(t,x_{\rm max})\,, \\ \pi_t(t,x_{\rm max}) &= -\pi_x(t,x_{\rm max})\,. \end{aligned} \tag{E.3}$$

For problems in higher spatial dimensionality, wave amplitudes will generally diminish as the radiation propagates outwards. Given the dimensionality, and assuming that the propagation of the waves is roughly spherical about some origin, $r = 0$, we can deduce an approximate rate of fall-off for $r \to \infty$. For example, in $2+1$ circular symmetry, which is the case studied most extensively in this thesis, and assuming that the asymptotic solution is of the form

$$\phi(t,r) \approx r^{\alpha} f(t-r)\,, \tag{E.4}$$

we find that $\phi \approx 1/\sqrt{r}$, i.e. that $\alpha = -1/2$. Thus, at $r = r_{\rm max}$ we should impose

$$\frac{\partial(\sqrt{r}\phi)}{\partial t}(t,r_{\rm max}) = -\frac{\partial(\sqrt{r}\phi)}{\partial t}(t,r_{\rm max})\,. \tag{E.5}$$

We can then use the chain rule to express this last condition in Cartesian coordinates:

$$\frac{\partial(\sqrt{r}\phi)}{\partial t} = -\frac{x}{r}\frac{\partial(\sqrt{r}\phi)}{\partial x} - \frac{y}{r}\frac{\partial(\sqrt{r}\phi)}{\partial y}\,. \tag{E.6}$$

This condition is also straightforward to implement computationally by using forward and backward difference approximations, as appropriate, for the spatial derivatives.